INFORMATION TO USERS

This manuscript has been reproduced from the microfilm master. UMI films the text directly from the original or copy submitted. Thus, some thesis and dissertation copies are in typewriter face, while others may be from any type of computer printer.

The quality of this reproduction is dependent upon the quality of the copy submitted. Broken or indistinct print, colored or poor quality illustrations and photographs, print bleedthrough, substandard margins, and improper alignment can adversely affect reproduction.

In the unlikely event that the author did not send UMI a complete manuscript and there are missing pages, these will be noted. Also, if unauthorized copyright material had to be removed, a note will indicate the deletion.

Oversize materials (e.g., maps, drawings, charts) are reproduced by sectioning the original, beginning at the upper left-hand corner and continuing from left to right in equal sections with small overlaps. Each original is also photographed in one exposure and is included in reduced form at the back of the book.

Photographs included in the original manuscript have been reproduced xerographically in this copy. Higher quality 6" x 9" black and white photographic prints are available for any photographs or illustrations appearing in this copy for an additional charge. Contact UMI directly to order.

UMI®

Bell & Howell Information and Learning
300 North Zeeb Road, Ann Arbor, MI 48106-1346 USA
800-521-0600

NOTE TO USERS

This reproduction is the best copy available

UMI

Dynamic Analysis of a Tracked Snowplowing Vehicle and Assessment of Ride Quality

Kun Wang

A Thesis

in

The Department

of

Mechanical Engineering

Presented in Partial Fulfillment of the Requirements
For the Degree of Master of Applied Science at
Concordia University
Montreal, Quebec, Canada

August 1998

NOTE TO USERS

Page(s) not included in the original manuscript are unavailable from the author or university. The manuscript was microfilmed as received.

ii

This reproduction is the best copy available.

ABSTRACT

DYNAMIC ANALYSIS OF A TRACKED SNOWPLOWING VEHICLE AND ASSESSMENT OF RIDE QUALITY

Kun Wang

Tracked snowplow vehicles, designed for removing snow from the sidewalks, pose severe ride environment for the drivers, primarily arising from road wheel-track-terrain interactions. The drivers of such vehicles are thus exposed to a comprehensive magnitude of low frequency whole-body vibrations. Exposure to such large amplitude low frequency vibration limits the performance abilities of the driver and thus the vehicle mobility.

The ride dynamics of a modern snowplowing vehicle is analyzed through systematic considerations of the track dynamics, track-terrain interaction, road wheel suspension, snowplowing forces, road wheel-track interactions, secondary suspension and biodynamic behavior of the driver. An in-plane twelve-degrees-of-freedom ride dynamic model of the vehicle is developed.

The ride dynamic response of the model is analyzed under deterministic and random road excitations, during transit and plowing operations. The validity of the analytical model is demonstrated by comparing the response characteristics with the measured data. The ride quality of the vehicle is assessed in relation to the proposed guidelines upon applying the recommended frequency-weighting filters.

The influence of variations in design and operating variables on the ride

performance of the vehicle is investigated through a comprehensive parametric study. The variations in operating conditions include the speed, road roughness, the nature of task, and snow parameters. The parametric study on design variables includes the variations in secondary and primary suspension, geometry, track tension and elasticity, and road wheel parameters. The results of the study are discussed to highlight the contributions of these parameters on the ride quality and to identify most desirable design and operating conditions.

ACKNOWLEDGEMENTS

TABLE OF CONTENTS

CHAPTER 1

INTRODUCTION, LITERATURE SURVEY, AND OBJECTIVES

CHAPTER 2

DEVELOPMENT OF RIDE DYNAMIC MODEL

CHAPTER 3

RESPONSE EVALUATIONS OF THE VEHICLE MODEL

CHAPTER 4

RIDE QUALITY ANALYSIS AND PARAMETRIC STUDY

CHAPTER 5

CONCLUSIONS AND RECOMMENDATION FOR FUTURE WORK

LIST OF FIGURES

LIST OF TABLES

NOMENCLATURE

SYMBOL	DESCRIPTION
a_{bl}	Horizontal distance between blade lower mount and hull c.g. (m)
a_{b2}	Horizontal distance between blade lower mount and hull c.g. (m)
a_c	Horizontal distance between rubber mounts (m)
a_{cf}	Horizontal distance between front mount and cab c.g (m)
a_{co}	Horizontal distance between rear mounts and hull c.g (m)
a_{hf}	Horizontal distance between sprocket c.g. and hull c.g.(m)
a_{hr}	Horizontal distance between walking beam c.g. and hull c.g. (m)
a_o	Distance between cab c.g. and seat base (m)
a_{23f} , a_{23r}	Horizontal distance between second road wheel c.g. and walking beam center (m)
a_{rwl}	Horizontal distance between torsion bar center and wheel c.g. (m)
a_{wl}	Horizontal distance between torsion bar center and hull c.g. (m)
B	Half of the clearance between the bump stops of seat suspension (mm)
b_b	Vertical distance between two mounts of blade (m)
b_{bl}	Vertical distance between torsion bar and hull c.g. (m)
b_{b2}	Vertical distance between upper mount and hull c.g. (m)
b_c	Vertical distance between cab mounts and cab c.g.(m)
b_{hc}	Vertical distance between cab c.g. and hull c.g. (m)
b_{hf}	Vertical distance between walking beam c.g. and hull c.g.(m)
b_{rwl}	Vertical distance between torsion bar and wheel c.g. (m)

b_{23f}, b_{23r}	Vertical distance between wheel c.g. and walking beam center (m)
C_1	Damping coefficient of the human body model (Ns/m)
C_A	Bleeding damping coefficient (Ns/m)
C_B	Blow-off damping coefficient (Ns/m)
C_{bw1}	Damping coefficient of the bump stop (Ns/m)
C_c	Damping coefficient of cushion (Ns/m)
C_{cxi}	Horizontal damping coefficient of the cab mount (Ns/m)
C_{czi}	Vertical damping coefficient of the cab mount (Ns/m)
C_{rw1}	Damping coefficient of the road wheel (Ns/m/rad)
C_{tw1}	Torsional damping coefficient of the rubber suspension (Nms/rad)
F_c	Cushion dynamic force (N)
F_{CD}	Magnitude of Coulomb friction (N)
F_D	Seat suspension shock absorber force (N)
F_k	Seat suspension spring force (N)
F_f	Linkage friction force (N)
F_{hn}	Normal force acting on the road wheel (N)
F_{hx}, F_{hz}	Horizontal and vertical forces acting on the drive sprocket (N)
F_{wx}^i, F_{wz}^i	Horizontal and vertical forces acting on the road wheel (N) (i=1,3)
F_s	Force due to bump stops of the seat (N)
F_{SEAT}	Force developed by suspension seat (N)
F_{wi}	Bump stop force (N)

F_{wn}	Net footprint force acting at road wheel (N)
I_B	Mass moment of inertia of blade. (kg m^2)
I_{yc}	Mass moment of inertia of cab (kg m^2)
I_{w1}	Mass moment of inertia of first road wheel arm (kg m^2)
I_{w23}	Mass moment of inertia of walking beam (kg m^2)
K_1	Stiffness coefficient of the human body model (N/m)
K_{bwi}	Stiffness coefficient of bump stop (kN/m)
K_c	Stiffness coefficient of cushion (N/m)
K_{cxi}	Horizontal stiffness coefficient of cab mount (kN/m)
K_{cL}	Stiffness coefficient of hydraulic cylinder (kN/m)
K_{czi}	Vertical stiffness coefficient of cab mount (kN/m)
K_g	Stiffness coefficient of blade spring (kN/m)
K_s	Stiffness coefficient of seat suspension (kN/m)
K_{st}	Spring rate of bump stop (kN/m)
K_{rw}	Spring constant of road wheel (kN/m)
K_t, K_{tr}	Vertical and longitudinal stiffness of track (kN/m)
K_{tr}	Longitudinal stiffness of track belt (kN/m)
K_{tw1}	Torsional stiffness coefficient of first road wheel suspension (Nm/rad)
K_w	Equivalent spring constant for road wheel (kN/m)
K_{wi}	Radial stiffness coefficient of road wheel (kN/m/rad)
L_{b1}	Distance between hydraulic force acting point and pivot point (m)

L_{b2}	Distance between ground supporting force and pivot point (m)
L_h	Length of track supported on drive sprocket and the third road wheel (m)
L_{fr}	Length of first road wheel arm (m)
L_{23f}, L_{23r}	Length of front and rear walking beam arm (m)
L_{23fr}	Length of walking beam (m)
L_j	Length of jth track segmentt between adjacent wheels (m)
L_{tr}^o, L_{tr}	Free and instantaneous track length (m)
MH	Static mid-ride height (m)
HD	Horizontal projection of shock absorber end points (m)
m_l	The human upper body mass (kg)
m_b	Blade mass (kg)
m_c	Cab mass (kg)
m_o	The human lower body mass (kg)
m_s	Seat suspension mass (kg)
M_{wl}	Suspension torque due to torsion bar
R_{bwi}	Radius distance pivot center and bump stop (m)
R_h, R_{wi}	Radius of drive sprocket wheel, and i^{th} road wheel (m)
T_{tr}^o	Track pre-tension (kN)
T_{tr}	Overall track tension (N)
V_s	Transition velocity (m/s)
x_c, x_h	Horizontal displacement of cab and hull (m)

X_h, Y_h	Cartesian coordinates of hull wheel center (m)
X_{wi}, Y_{wi}	Cartesian coordinates of ith road wheel center (m)
y_i	Relative vertical displacement between z_i and z_{i-1} (i=3) (m)
z_i	Vertical displacement of the human upper body, lower body and seat sprung mass (m)
z_c, z_h	Vertical displacement of cab and hull (m)
α	Shock absorber inclination angle (deg)
α_b	Hydraulic force inclination angle (deg)
α_w	One-half if wheel-contact patch (rad)
$\theta_b, \theta_c, \theta_h$	Pitch angle of blade, cab and hull (rad)
$\theta_{w1}, \theta_{w23}$	Pitch angle of first road arm and walking beam (rad)
δ_i	Radial deflection (m)
β_i	Wheel contact patch (rad)
β_{wi}	Angle between bump stop and road wheel arm (deg)
$\varepsilon_1^j, \varepsilon_2^j$	Horizontal inclinations of jth track segment at its ends (rad)
ϕ_h, ϕ_i	Track wrap angle around hull wheel, and i^{th} road wheel (rad)

CHAPTER 1

INTRODUCTION, LITERATURE SURVEY AND OBJECTIVES

1.1   INTRODUCTION

Tracked sidewalk snowplow vehicles are employed for removing the snow from the sidewalks in many urban areas. Such vehicles are designed with flexible tracks to achieve adequate traction on snow or ice-covered surfaces. From a dynamic analysis point of view, the tracked nature of theses vehicles poses many complex challenges to the designers, and only few studies on the dynamics of such vehicles have been reported in the last two decades. Dynamic interactions between the track and randomly rough sidewalks, and dynamic pushing forces coupled with dynamics of the vehicle pose a complex ride vibration environment for the drivers. The magnitudes of such ride vibrations are known to be quite severe. During heavy snowfalls, the drivers perform the snow clearing and sanding tasks over prolonged durations. Prolonged occupational exposure to high magnitudes of whole-body ride vibration is known to affect the health, safety and productivity of the drivers in an adverse manner. The analysis and enhancement of ride vibration environment of such vehicles thus forms an important design task.

It is essential to keep the vibration levels within comfortable limits under all environmental and terrain conditions, so as to ensure the comfort of the operators, as well as to prevent any harmful consequences to the operator's health. Performance characteristics of a road vehicle, in general, relate to its traction/braking, handling, directional control and ride quality. The scope of this dissertation research primarily

1

relates to the ride quality of the vehicle, which is a complex function of many factors, including: seated posture, work-station design, visibility, steering effort requirements, temperature, humidity, shock and vibration environment etc. While many efforts have been mounted to design driver-friendly work-stations, only limited efforts have been made to enhance the shock and vibration environment for the drivers. Furthermore, until recent years, side-walk snowplow vehicles were designed with no primary and secondary suspension, with the exception of vertical suspension seat. The drivers of such vehicles were thus exposed to low frequency and high magnitudes of ride vibration and shock arising from dynamic terrain-track interactions. Prolonged exposure to such low frequency and large amplitude ride vibrations of vehicles causes operator bodily discomfort, physiological damage and inefficient performance, and thus the mobility performance of the vehicle is limited. Poor performance rate of the vehicle operator has been attributed to various effects of vehicle vibration: namely, operator's slow reaction time, errors in compensatory tracking, loss of foot pressure constancy and visual [1].

The scope of the dissertation research is thus to analyze the ride vibration environment of a modern sidewalk snowplow vehicle through system model development and analyses. A typical sidewalk snowplow vehicle is shown in Figure 1.1. In order to improve the ride quality of snowplows, a comprehensive mathematical model of the vehicle, comprising elastic cab mounts and primary suspension is developed. The ride dynamics of the vehicle is evaluated under dynamic interactions of the track with randomly rough sidewalk surfaces. The analytical model is verified using field measured data acquired under a wide range of operating conditions. A parametric study is performed to illustrate the influence of vehicle suspension and track parameters on the

Figure 1.1: A pictorial view of a sidewalk snowplow.

ride dynamics of the snowplow vehicle. Accordingly, a literature search is carried out to understand the existing state of the art and to determine the necessary investigations in order to improve the ride quality of snowplow vehicles.

1.2   REVIEW OF RELEVANT LITERATURE

Reported studies on dynamics of tracked vehicles, field measurements, ride comfort assessment and tolerance criteria are thoroughly reviewed to enhance the focus of the study and to identify appropriate analytical methods. The highlights of the reported studies are grouped under different relevant topics and briefly described in the following sections.

1.2.1   Analytical Models of Tracked Vehicle

The drive towards increased power-to-weight ratio and mobility of vehicles employed in military, resource and service sectors has evolved into the design of tracked vehicles. The reported studies on these vehicles include a diversity of emphasis concerning the tractive performance, gradability, directional response, stability, braking, etc. While majority of the studies have been directed towards mobility of high performance military vehicles, the ride dynamics of such vehicles have been addressed only in a limited number of studies. These studies, however, have established that track-terrain interactions affect the dynamics of the vehicle in a significant manner.

In 1971, Eppinger et al. [2] developed and analyzed an in-plane model of a six-wheeled tracked vehicle to illustrate the effects of dynamic track loads on the ride response of the vehicle. The tracked vehicle was modeled as a two-degrees-of-freedom

4

(bounce and pitch motions of the hull) dynamical system, incorporating nonlinear suspension characteristics and wheel lift-off, as shown in Figure 1.2. Influence of running gear components, such as road wheel suspension and track on the dynamic response of the hull was investigated. The track was modeled as a massless elastic band capable of transmitting only tensile forces considered linearly proportional to change in the total track length. The terrain was assumed to be a non-deformable continuous profile, and was described through horizontal and vertical coordinates of successive points, where intermediate points were determined based on linear interpolation. The analytical model was validated against the measured response of a one-tenth scale laboratory model of a tank with and without the track. The analytical and experimental acceleration response at the center of gravity of the vehicle with and without the track, due to excitation from a trapezoidal-shaped bump, revealed that addition of the track increases the severity of the hull dynamic response considerably.

In 1972, Lessem and Murphy [3] developed a mathematical model based on data compiled from field tests of different tracked vehicles to study the influence of track on the ride dynamic response of high speed tracked vehicles. An in-plane model was developed incorporating the degrees-of-freedom associated with bounce and pitch motions of hull as well as bounce motion of each road wheel and axle assembly. Figure 1.3 illustrates an eight-degrees-of-freedom model of the six-wheeled M60 A1 battle tank. The torsion bar suspension configuration was modeled as a parallel combination of vertical spring and damper. The road wheel tires were modeled as radially segmented discrete springs, where each segmented spring is assumed to deflect independent of its neighbor as it enters the wheel-terrain contact zone. The total contact force was thus
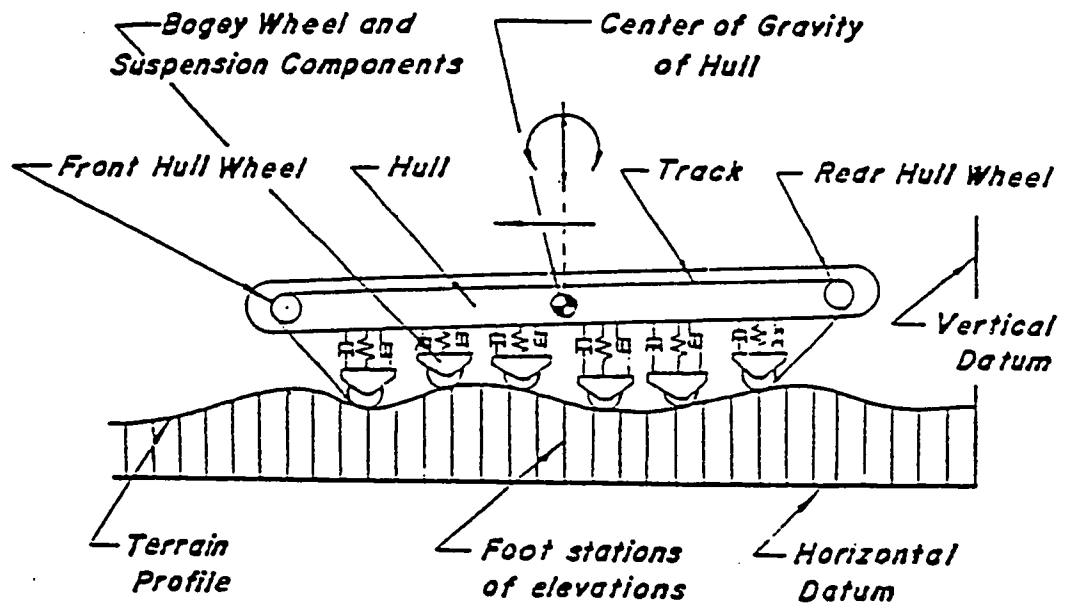
Figure 1.2: An in-plane model of a six-wheeled tracked vehicle [2].
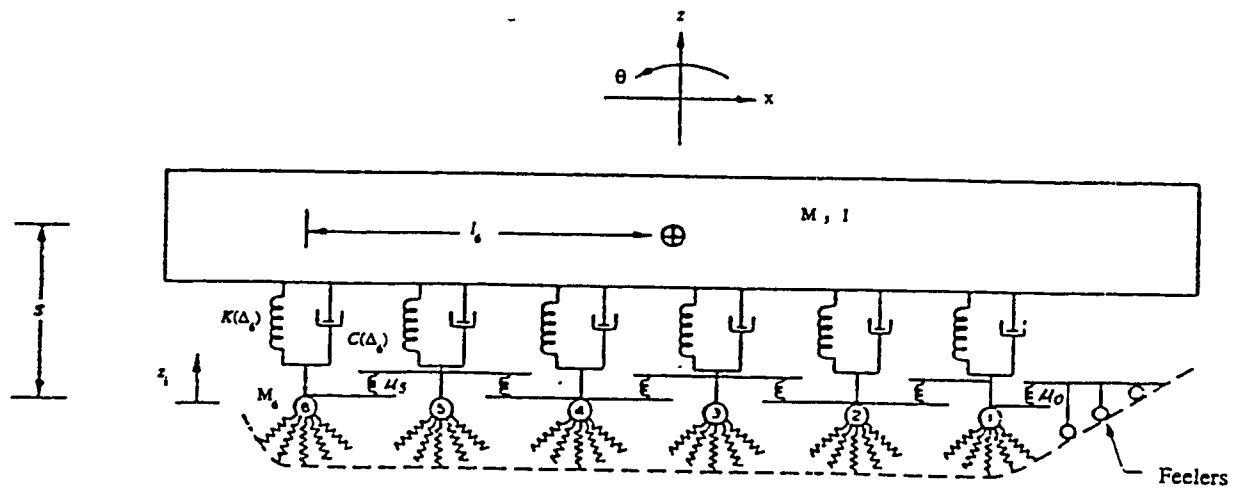
Figure 1.3: Schematic representation of M60 A1 battle tank model [3,6].

expressed as the sum of segment forces, and the horizontal tire forces were used to determine the longitudinal response of the hull. The contributions due to track tension effects were modeled as local tensioning effects, while neglecting the overall track tension. Track tension was represented by interconnecting linear springs between each road wheel, where the spring constant is determined based on the weight of each road wheel against the track. Thus, this track tension model effectively generated a vertical force as a linear function of the displacement between the wheels. The spring constant of the track segment between the sprocket and the first road wheel is determined using three massless feelers placed against the track. The ride acceleration data of four military tracked vehicles of different weights and running gear, namely, M29, M113, M114 and M4 vehicles which were towed with and without the track over an assortment of half-round rigid obstacles and ditches, were acquired. Results obtained via computer simulation are compared with the experimental results. The analytical and experimental studies revealed that the interactions of the track were strongly dependent on vehicle speed. While the track produced a smoothing effect at low speeds, the ride quality at higher speeds is deteriorated due to track interactions.

Murphy et al.[4] further adopted the ride model configuration and extended it to develop a Vehicle Ride Dynamic Module (VEHDYN) for general use in support of the Army Mobility Code (AMC-74). VEHDYN's primary purpose was to predict the ride and shock limiting vehicle speeds for typical high speed wheeled or tracked off-road vehicles. Four basic configurations: rigid or unsprung, independent, walking beam and bogie suspensions, were considered to formulate the ride simulation model used in VEHDYN. The cyclic chordal action of the track, defined as variation in velocity of the

7

track as it passes over a sprocket or the road wheel, was analyzed by Lee [5] using a receptance technique. It was established that low frequency noise and vibration is experienced in the vehicle compartment when the track leaves the last road wheel to engage with the idler and the sprocket due to cyclic chordal action of the track [6]. These studies on dynamic forces acting on the idler supports have been employed to describe favorable idler wheel configuration, compliance of the idler arm and geometry of the track shoe assembly to minimize the vibrations arising from the track-idler interactions.

Wheeler [7] developed a comprehensive simulation package for an in-plane ride dynamics of XM1 tank subjected to non-deformable terrain input. The ride model considered pitch and bounce degrees-of-freedom associated with vehicle sprung mass and an additional degree-of-freedom for each road wheel, as shown in Figure 1.4. Overall track tension was considered to account for track dynamic effects, and the input at the wheel-terrain interface was restricted to be only vertical. The forces acting on a road wheel were thus assumed to be vertical only, and included road arm force, contact force due to wheel deflection, and force due to track restricting the downward motion of the wheel. The horizontal forces incorporated in the model were only due to track tension in the inclined front and rear track segments, but were assumed to be statically balanced. The package employed MIMIC simulation language for the solution of equations of motion, which allowed for variation in the vehicle parameters such as: number and location of road wheels, spring rates, damping characteristics, road arms length, vehicle speed, sprung weight, pitch mass moment of inertia, etc. The predicted response time histories were compared with field measurements with some apparent success. Although
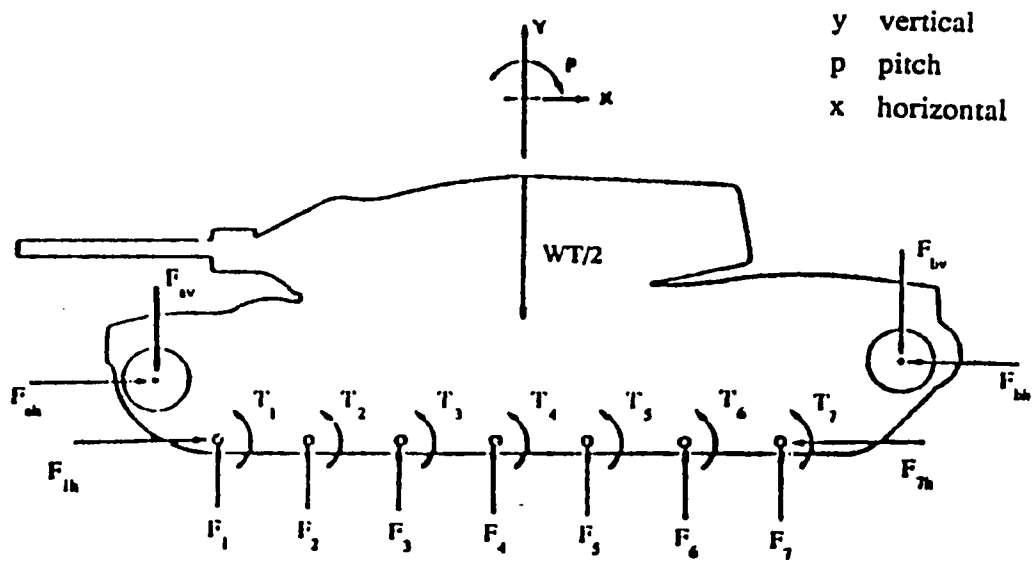
Figure 1.4: Schematic of a multi-degree-of-freedom XM1 tank model [7].
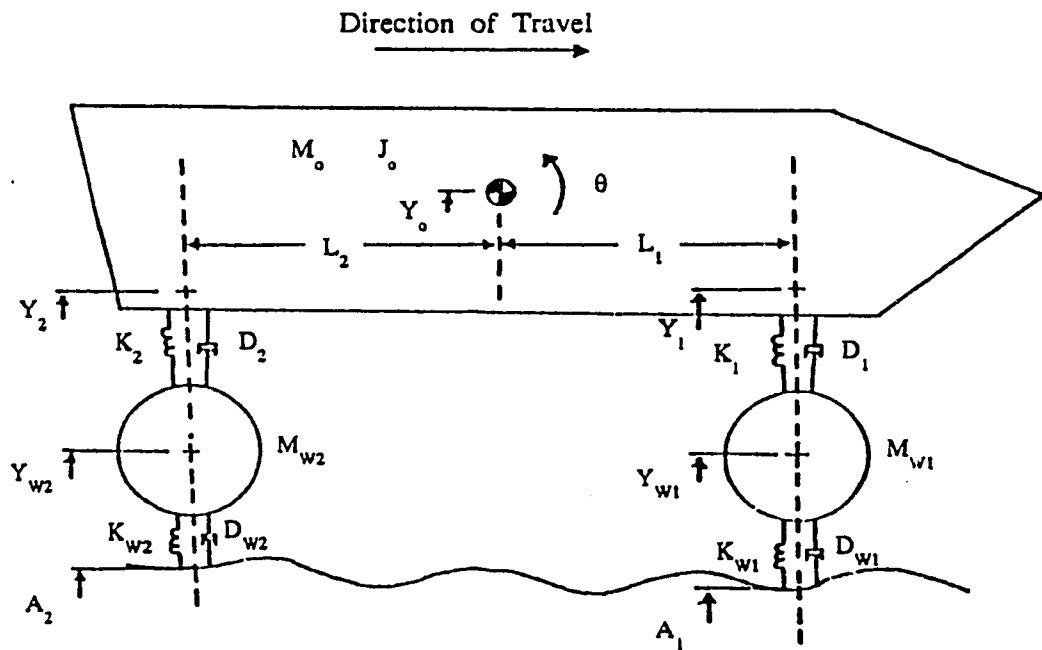
Figure 1.5: Ride dynamic model of a tracked vehicle [9].

program was developed for tank dynamics, it has been applied to a ¾-ton truck and combat tracked vehicle signature duplicator, CTVSD. Meachom et al. [8] proposed analytical methods to predict vibration modes of the track, chordal effects, dynamic track tension and path, energy dissipation, tension during negotiation of an obstacle, distribution of track tension, pin/bushing stresses and deflections, temperature buildup, and end connector tightening effectiveness.

While majority of above mentioned studies emphasized on the contributions of the track tension and dynamics, few other studies have specifically investigated the ride dynamics of such vehicles. Hoogterp [9] developed a ride model to simulate tracked vehicles while ignoring track dynamics. The ride simulation model incorporated vertical and pitch motions of the sprung mass as well as vertical motion of each road wheel, as shown in Figure 1.5. The vehicle suspension and road wheels were modeled as linear vertical springs and dampers. The ride model also included a pair of wheels to be joined in tandem arrangement and a fifth wheel type trailer hitch with full pitch freedom. Computer simulations of two military tracked vehicles crossing over various rough terrains were validated through field tests in terms of driver's comfort limiting velocity as a function of terrain roughness. Results indicated the obvious that comfort limiting velocity decreases for rougher terrains.

In 1979, Beck and Wehage [10] conducted a study to investigate the use of force feedback servo control mechanisms to improve the man-machine interactions and the response of an articulated tracked vehicle. The DADS (Dynamic Analysis and Design System) software, was utilized to formulate the equations and geometric constraints describing two identical M113 tracked vehicles coupled by an electro-hydraulic servo-

controlled articulation joint. The primary objective of this study was to investigate the potential of the controlled articulation and to compare mobility performance of the articulated and the single vehicle, specifically in view of obstacle crossing characteristics. In order to improve the suspension performance of tracked vehicles, various researchers have conducted feasibility analyses involving fluidically-controlled suspension systems [11,12].

The ride dynamics of military tracked vehicles operating on deformable off-road terrains are strongly dependent upon the shearing and compaction of the terrain. Bekker [13,14] presented insight on the theory of soil mechanics and the interrelationship with tracked vehicles such as rut making and ground compaction including snow, and how these constraints result in higher locomotive resistance which lowers fuel economy. In 1980, Wong et al. [15] presented an analytical framework for predicting the ground pressure distribution and tractive performance of tracked vehicles. The prediction of ground pressure distribution under the track has become of vital importance since vehicle sinkage and motion resistance is critical to vehicle mobility. It is also important to the steering dynamics of the vehicle since turning resistance depends on the ground pressure. The above terramechanics studies have concentrated on vehicle mobility and environmental protection, however, information pertaining to track-terrain interactions may be acquired and used for ride dynamic response analysis of the vehicle crossing over deformable terrains.

In 1983, Maclaurin [16] described a computer system (the AD-Applied Dynamics) used by British researchers for military tracked vehicle simulation. The digital computer with multiprocessing capability, specifically designed for high speed simulation

of complex dynamic systems was used to analyze suspension models, including active suspension. The military tracked vehicle was modeled in the pitch and bounce plane and accounted for the various nonlinearities in springs, dampers, Coulomb friction, tire stiffness, wheel/terrain separation, sprocket and idler terrain contact. The track was modeled by equating the peripheral length, catenary action and track tension. Maclaurin [16] also conducted analytical and experimental studies to determine the influence of suspension characteristics on mobility performance of battle tanks. An MCV (Mechanised Combat Vehicle) fitted with torsion bars and rotary vane hydraulic damper, and the Challenger fitted with the hydrogas suspension, were tested on various terrains. Results revealed that the Challenger yields higher limiting speeds with acceptable vibration levels than the MCV.

In 1984, Galaitsis [17] presented a method to predict dynamic loads due to the track that occur in high speed M113 vehicles. The two-dimensional mathematical model incorporated dynamics of all the road wheels, the track loop, rigid suspension and flat ground profile, emphasizing the interactions between the track shoes and road wheels of the tracked vehicle. When developing the equations of motion of the track loop, the inertia of the shoes, stiffness and damping characteristics of the rubber bushings inserted between each shoe was considered. The shoe-wheel interactions are taken into account by considering the properties of shoe pads and the friction forces exerted by the wheel on the pads. The track tension and track bending moment established by the analytical model were validated via experimental investigations.

Garnich and Grimm [18] proposed an in-plane ride simulation model of the M60 A1 battle tank with trailing arm suspension, as shown in Figure 1.6. The tracked vehicle
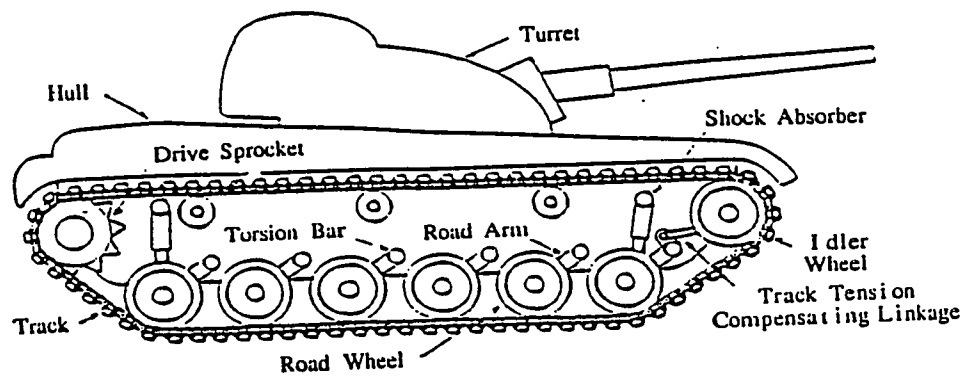
(a) Schematic of the M60 battle tank.
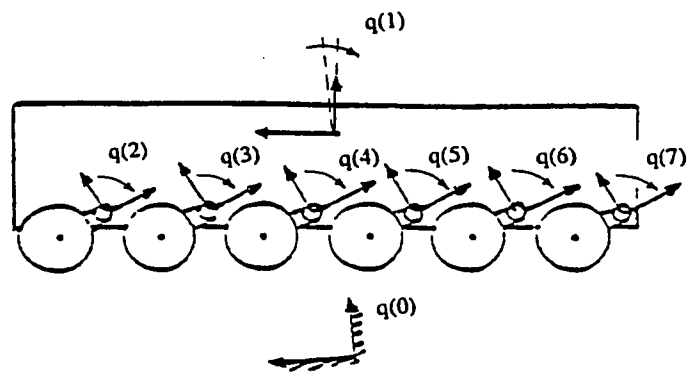
(b) Generalized coordinates and frames of reference of the model.
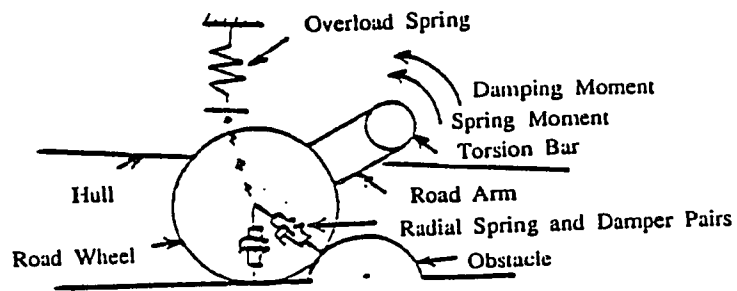
(c) The road wheel model.

Figure 1.6: Schematic representation of the M60 tank and its ride model [18].

was modeled as an eight-degrees-of-freedom discrete dynamical system, incorporating the vertical and pitch motions of hull, and rotational motion for all six road arm and wheel assemblies. The torsion bar suspension configuration connecting the road arm and road wheel to the hull chassis was modeled as a constant rate torsional spring, while the inclined shock absorber mounted at the first and the last road wheels were replaced by equivalent viscous torsional dampers in parallel with torsional springs. The road wheels were represented by discrete radial springs and dampers, while overloading springs were used to represent bump stops. The contributions of the track loads to the vehicle dynamics was accounted for by considering four different types of track tension: (i) *Global Track Tension* - a uniform overall track tension caused by stretching of the track belt, where the bridging effect involves the track creating a flexible bridge spanning terrain concavities; (ii) *Drive Sprocket Induced Tension* - estimated from an average applied torque as the vehicle passes over a half-round obstacle; (iii) *Track Bridging Effect* - caused by the track creating a flexible bridge spanning terrain discontinuities; and (iv) *Tension due to Track Compensating Linkage* - induced by a compensating link between idler and adjacent road wheel, so that as road wheel moves up, idler moves forward to take up slack in the track. The analytical results established for deterministic excitations were validated via an array of experimental investigations, varying from simple static deflection checks to track effects which influence the individual road wheels. The global track tension was found to cause substantial changes in vehicle dynamic response to large discrete obstacle, which created high track tension magnitude and significant road wheel-terrain separation.

McCullough and Haug [19] extended the concept of super-element representation of recurring subsystem in mechanical system to model a typical high mobility tracked vehicle. The running gear subsystem, including the track, drive sprocket, idler, road wheels and road arms, were defined as super-elements. The model incorporated the track tension, suspension forces, track-wheel-ground forces, track connectivity and bridging of the track. In particular, the track tension was obtained based on the catenary equation by approximating the relationship between track tension and the length of track hanging between drive sprocket and idler. The track belt stretching was also accounted for in conjunction with a simple relaxation of ideal catenary equation. The super-element modeling strategies were used in conjunction with the multi-body computer code DADS for the purpose of simulation and shown to be much faster than the conventional multi-body approach. The absorbed power of the vertical acceleration at the driver location is established via simulation and experimentation for a military armoured personnel carrier crossing a 20cm semicircular obstacle. It was shown that the inclusion of track bridging in the track model contributed to an improved ride quality.

Also in 1985, Krupka [20] developed a comprehensive three-dimensional mathematical model of a military battle tank. The tank was treated as three distinct bodies, each having six-degree-of-freedom: the hull, the turret, and the main gun. The equations of motion were derived using Lagrange's formulation. All three rigid bodies were connected by a set of kinematic constraints, which provided the physical interface of the system. The main emphasis of proposed model was to study the dynamics associated with gun, such as gun bending effects. However, this study did not report any simulation results.

In 1986, Creighton [21] reported a revised ride prediction module, referred to as VEHDYN II. It is an improved version of the AMC-74 Vehicle Ride Dynamic Module, VEHDYN [4]. Like VEHDYN, VEHDYN II predicts the gross motions of a tracked or wheeled vehicle traversing an arbitrary non-deformable terrain at a constant forward speed, and computes the average absorbed power (ride performance criterion) and peak vertical acceleration at the driver's location or any other specified location in the vehicle (shock performance criterion). Although the basic vehicle-terrain simulation model is the same as in VEHDYN, the analytical models for sub-systems, such as suspension spring and damping characteristics, and dynamic wheel-track-terrain interactions were modified. In particular, the dynamic wheel/track-terrain interface was modeled using the concept of a continuous ring of radial springs instead of discrete radially segmented group of springs. The dynamic track tensioning effects were further enhanced by incorporating track feeler-terrain interaction, which employed a hypothetical linear spring placed perpendicular to the feeler at the location of maximum displacement due to interaction with terrain profile. In addition, the height of the vehicle and horizontal force effects were incorporated.

Afonso [22] investigated the ride quality of a military armored personnel carrier (M113 APC) through a systematic study of the ride dynamics of the tracked vehicle. The ride dynamics was studied through four mathematical models characterizing the dynamics of the wheeled as well as tracked vehicles, including: (i) ride dynamic model of a multi-wheeled vehicle with idealized suspension, which was formulated upon neglecting track loads and kinematics of the linkage suspension, as shown in Figure 1.7; (ii) a second model was developed assuming track tension as restoring forces acting on
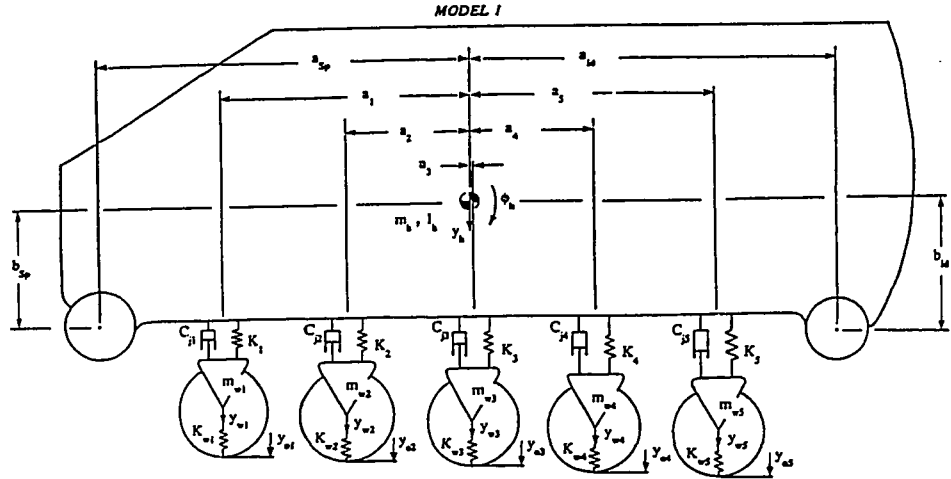
Figure 1.7 Schematic of M113 multi-wheeled vehicle model with idealized suspension (Model I) [22].
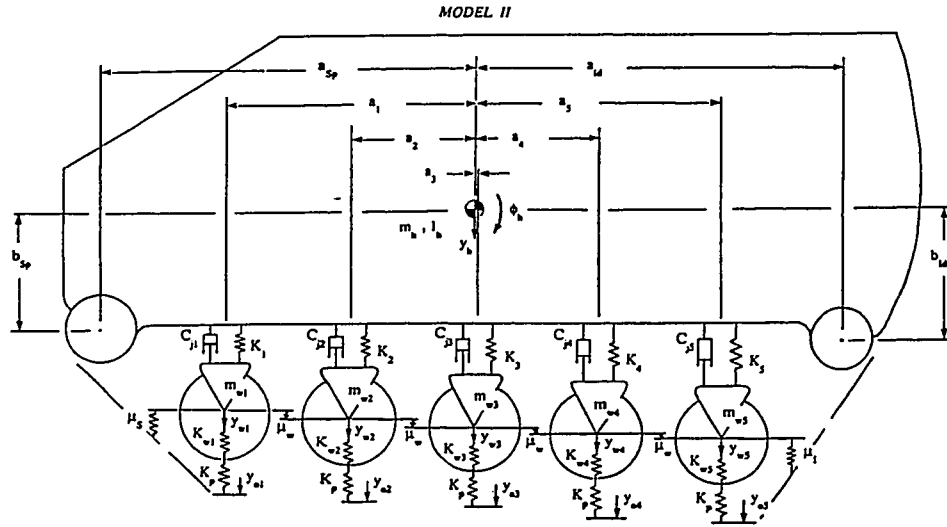
Figure 1.8 Schematic of the M113 tracked vehicle model with idealized suspension (model II) [22].

the road wheels, as shown in Figure 1.8; (iii) the ride dynamic model of a multi-wheeled

vehicle with trailing arm torsion-bar suspension shown in Figure 1.9, incorporating road

wheels supported by swing arms individually splined to torsion bars which extend over

the width of the hull chassis; and (iv) Model IV was developed to include the dynamic

effects of the track on the ride performance of the tracked vehicle, as shown in Figure

1.10. The ride dynamics of these four models were investigated for deterministic and

random terrain excitations. Transient acceleration response at the driver's location was

evaluated for deterministic excitations, arising from semicircle and block obstacles, via

direct integration of the nonlinear differential equations of motion. It was concluded that

the linkage suspension model provided superior ride response as compared to the

idealized suspension. The addition of the track improved ride response significantly.

Absorbed power at the driver location increased considerably with increasing roughness

of the terrain and a decrease in torsion bar stiffness resulted in the improvement of ride

quality of the M113 vehicles.

Rakheja et al. [23] performed the dynamic analysis of tracked vehicles with

trailing arm suspension to assess ride vibrations environment. A ten road wheel tracked

vehicle with independent trailing arm suspension where each road wheel was mounted on

a road arm splined to a torsion bar extending over the width of the chassis was modeled

and analyzed. Shock absorbers were mounted between the road arm and hull chassis to

prevent road wheel interference with the track. The ten road wheel tracked vehicle was

modeled as an in-plane seven-degrees-of-freedom dynamical system, incorporating the

kinematic relations as implied by the linkage assembly comprised of torsion bars, road

arms, shock absorbers and dynamics of the track. Each road wheel was attached to the
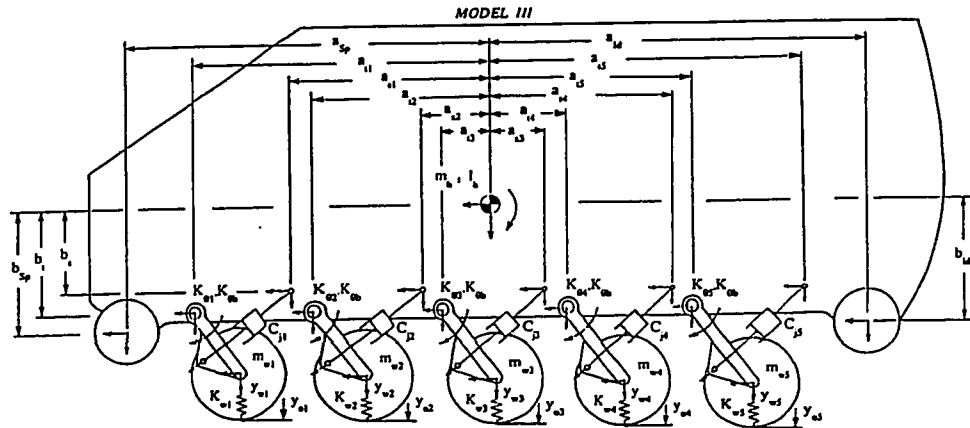
MODEL III

Figure 1.9: Schematic of the M113 multi-wheeled vehicle model with linkage suspension (Model III) [22].
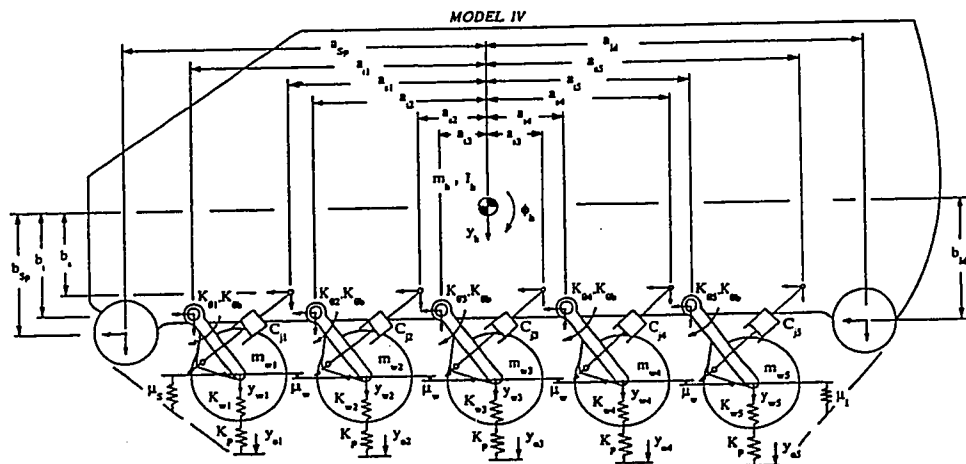
MODEL IV

Figure 1.10: Schematic of the M113 tracked vehicle model with linkage suspension (Model III) [22].

chassis through a trailing arm suspension. The track tension caused by the relative displacement of a road wheel with respect to the adjacent road wheel was modeled as a restoring force proportional to the relative motion of the wheel. Ride vibration response at driver's location was evaluated for random excitations arising from Belgian Pave, ploughed field, pasture and MVEE random course. Vertical and horizontal ride vibration at the driver location were assessed via average absorbed power. Absorbed power quantities and the ride quality of tracked vehicle was computed and discussed in terms of vehicle speed, terrain roughness, suspension parameters and track tension. Results showed that soft road wheel suspension may cause excessive road wheel motion leading to interference with the track. The variation in track tension does not alter vehicle ride considerably, although a slight improvement in vertical as well as horizontal vehicle ride quality can be achieved by increasing track tension.

Dhir [24] presented a computational procedure for establishing zero-force and static-equilibrium configurations of a typical multi-wheeled/tracked off-road vehicle, which were required for the purpose of ride dynamics simulation. The in-plane ride dynamic model of a high mobility tracked vehicle (M113APC) was described by "2+N" degrees-of-freedom, incorporating the bounce and pitch motions of hull and angular orientation of the N road arms with respect to the hull frame. Each road wheel was independently attached to the hull through a trailing or road arm splined to a transverse torsion bar. The wheel model was based on the concept of a continuous ring of radial springs uniformly distributed over the wheel-ground footprint, and an equivalent damper. The track was modeled as a continuous belt loop capable of transmitting static tensile loads, which were evaluated considering the sag due to the track segment hanging

between hull wheels (sprocket and idler), and appropriate wheel-track connectivity. The zero-force configuration was established by shifting the vehicle upward based on the static suspension and wheel deflections. The suspension and wheel loads required for determining these deflections were evaluated using a simplified approach. The vehicle's static equilibrium was assured by allowing the vehicle to settle under its own weight from the zero-force datum. An iterative stiffness method was employed for the vehicle settlement, where the static deflections computed earlier for defining the zero-force configuration served as the starting value. The settled configuration was validated against the measured configuration of the vehicle sitting on a flat surface. The computational procedure presented required minimal input vehicle data, and accurately predicted the settled vehicle configuration. A comprehensive computer simulation model of a typical tracked vehicle was further developed to predict its ride vibration environment [25, 26]. Field testing of a conventional armored personnel carrier traversing over a random course was carried out to validate the simulation model. The comparison of measured and predicted results exhibited a good agreement. In addition, the effectiveness of the simulation model in terms of accuracy of response predictions, was demonstrated by comparing with VEHDYN II, the ride prediction module of the NATO Reference Mobility Model (NRMM) [21].

A multi-purpose ride dynamic simulation model (RIDSIM) was further developed to investigate the ride dynamic aspects of high mobility wheeled/tracked off-road vehicles, as shown in Figure 1.11 [27]. The development of RIDSIM was primarily based on the modeling strategies adopted for the ride model formulation of a typical high-speed

21

Figure 1.11: In-plane model representation of a typical high mobility tracked vehicle [27].

22
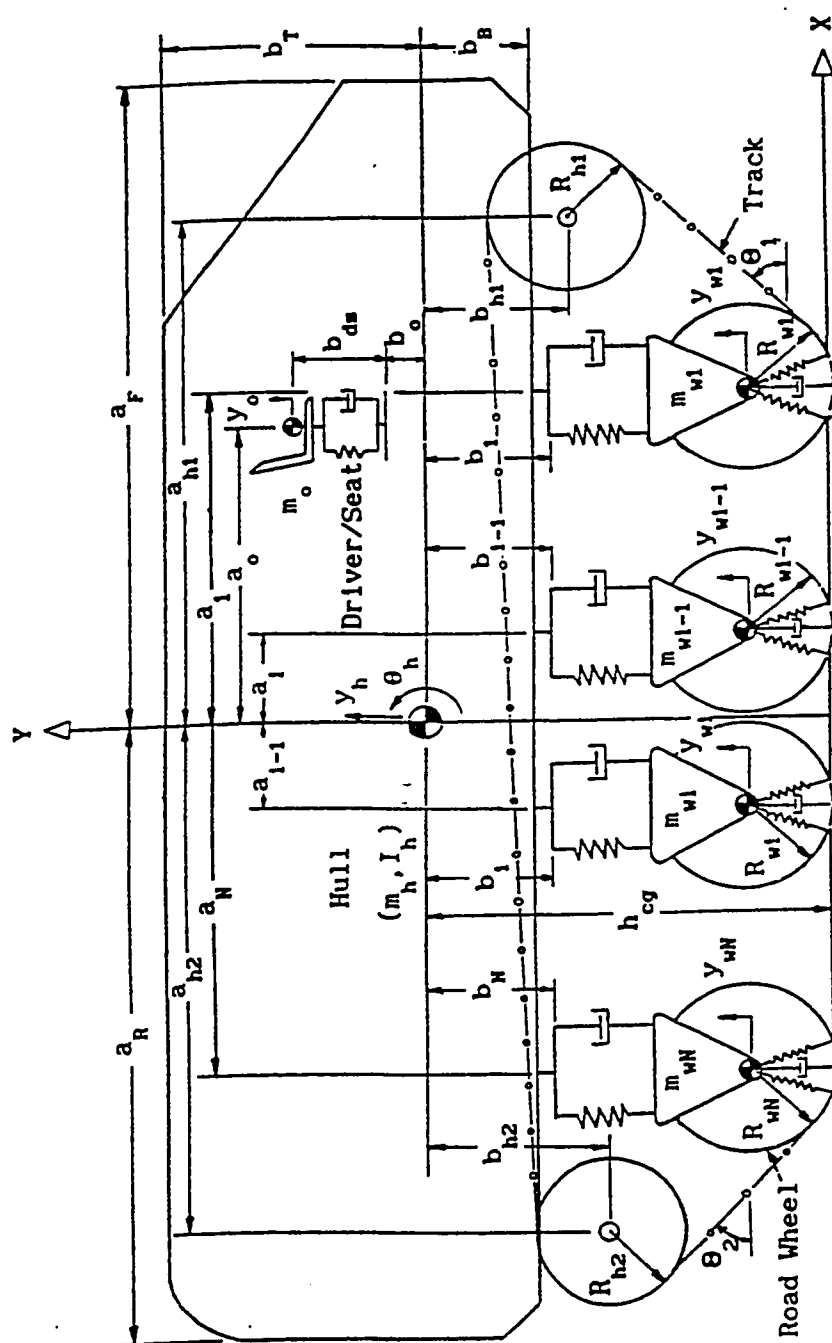
multi- wheeled tracked vehicle (an armoured personnel carrier: M113 APC), which was selected as a candidate vehicle for this study. The candidate vehicle ride model was conceived based on three formulations of varying complexities: Model I, Model II, and Model III. The Model I incorporated idealized independent suspension representation of the tracked vehicle's torsion bar/trailing arm suspension system, an idealized continuous radial spring/equivalent damper model for wheel/track-terrain interaction, and dynamic track loads computed based on track belt extensibility and pre-tension. Model II was a refined model in view of the sub-system modeling strategies. The refinements included an adaptive formulation of the idealized continuous radial spring model for the wheel/track-terrain interaction, dynamic track loads evaluated based on an improved track model, and equations of motion re-derived based on an improved representation of the idealized independent suspension unit. The Model III was re-formulated considering a realistic representation of the vehicle's trailing arm/torsion bar suspension system, incorporating the detailed kinematics of trailing arm/torsion bar suspension system, incorporating the detailed kinematics of trailing arm and shock absorber linkage in addition to the refined wheel and track sub-models used in Model II. It was concluded that ride predictions derived from Model I generally revealed a good agreement with field measurements. The ride predictions evaluated using Model II showed an improved correlation with the field test data, while the Model III resulted in smoother ride and even closer correlation with the field measured data.

Dhir [28] presented various modeling strategies to account for the track dynamics in the ride dynamic simulation of high mobility tracked vehicles negotiating rough off-road terrains. The mathematical model of a tracked vehicle, proposed in previous studies,

was used and four different analytical track representations of varying complexities were formulated. The overall track tension, in the preliminary model was computed as track pre-tension and tension due to the stretching of the track belt. The total track length, which was continuously dependent on generalized coordinates associated with road wheels and hull, and the terrain profile, was computed at each integration step by summing up the various segments which constitute the entire circumference of the track. The track bridging effects were also enhanced in view of an appropriate definition of track inclination angles around road wheels. The track sag was further represented using an ideal catenary-based approach in the third wheel. This approach was based on the assumption that the lowermost point was always located at the mid-point of the hanging track.

The final track model was based on the model employed in VEHDYN [21], where the dynamic track tensioning effects were modeled as local tensioning effects, while neglecting the overall track tension. The intermediate track segments (between road wheels) were modeled as vertical springs interconnecting each adjacent road wheel pair as proposed earlier by Afonso [22], which restricted the relative vertical motion of the road wheels. The ride response predictions of the test vehicle for a few representative test conditions were evaluated in conjunction with different track models, and the results were directly compared against the field-measured ride data. Based on the comparative study, it was observed that the ride predictions based on the first three track models were very similar, and showed good agreement with the field measurements, whereas the ride predictions based on track model # 4 exhibited relatively poor agreement.

1.2.2 Ride Comfort Assessment Criteria

Ride quality is concerned with driver's sensation of the terrain-induced vibration environment of a vehicle, and is generally difficult to assess. Numerous studies have been conducted to establish the ride assessment criteria for preservation of driver comfort, health, safety, and performance. Two different methods are frequently used to evaluate the whole body vibration: subjective and objective. Subjective methods are often based upon subjective response of vehicle ride comfort on an absolute scale and used to assess relative ride ranking of a group of vehicles, operator tolerance in relation to productivity, vibration interference with normal operator control tasks, health aspects to vocational exposure, competitive significance and cost/benefit ratio of potential ride improvement [29]. Subjective methods, however, often lead to misleading information due to a multitude of inconsistencies dependent upon age, preferences, and moods of the subject at the time of experiment. Alternatively, objective methods provide an assessment methodology based on direct measure of physical quantities such as velocity, acceleration, absorbed power, and jerk over the frequency range of interest. Over the years, numerous objective ride comfort criteria have been proposed, however, a generally acceptable criterion is yet to be established. Some of the proposed ride criteria are summarized below.

Earlier studies on human body response to vehicle vibration were primarily carried out using subject-shake table [30]. Dieckman [31] proposed constants related to comfort zones and fatigue time limits for passenger car vibrations. A constant, K, is proposed based on levels of constant acceleration upto 5 Hz, constant velocity from 5-50

Hz, and constant displacement above this frequency. The Dieckman's criterion proposed

three different comfort zones based upon the constant value, which are defined as:

$$K = \begin{cases} 0.1-1 & : \text{imperceptible to slightly uncomfortable} \\ 1-10 & : \text{slightly disagreeable to disagreeable with} \\ & \quad \text{a fatigue time of 1 hour} \\ 10-100 & : \text{very disagreeable to exceedingly disagreeable} \\ & \quad \text{with a fatigue time of 1 minute} \end{cases} \qquad (1.1)$$

Goldman [32] analyzed the vibration data acquired from several sources, and

deduced three comfort levels in the vertical mode in terms of acceleration and frequency

contents. The comfort levels were referred to as *perceptible, unpleasant,* and *intolerable.*

The vibration data used by Goldmann were obtained from a variety of experiments where

the subjective and physical environments varied considerably. Janeway [33]

recommended exposure limits for vertical vibration of passenger cars in terms of

maximum jerk in the frequency range of 0-6 Hz, and maximum acceleration for middle

frequency range of 6-20 Hz. The safe limits of vibration exposure were proposed based

on the survey of subjective tolerance data, which represented an attempt to set a level at

which no discomfort is experienced by the most sensitive passenger.

A comparison of the Dieckmann, Janeway and Goldman ride criteria revealed that

the human is most sensitive to vertical vibration below 20 Hz [34]. Since the above ride

assessment criteria have been established based on sinusoidal vibrations at a constant

frequency, their application to assess the vehicle's random ride vibrations is questionable.

Von Eldick Thieme [35] and Butkunas [36], however have outlined methods for applying

existing ride comfort criteria (including those mentioned above) to random vibration

environment of vehicles. In Germany, the K-factor was proposed as a measure of

vibration intensity, based on subjective assessment [37]. The K-factor can be evaluated

from the frequency and rms acceleration, velocity or displacement amplitude as follows:

$$k = \alpha \frac{x_1}{\sqrt{1 + (f / f_o)^2}}$$

$$k = \nu \frac{x_2 f}{\sqrt{1 + (f / f_o)^2}}$$ (1.2)

$$k = \sigma \frac{x_3 f^2}{\sqrt{1 + (f / f_o)^2}}$$

where α is rms acceleration in m/s^2, ν is rms velocity in mm/s, σ is rms displacement

in mm. f_0, x_1, x_2 and x_3 are constant given by:

$$f_0 = 10 \text{ Hz} \qquad\qquad x_1 = 18 \frac{k}{m/s^2}$$

$$x_2 = 0.112 \frac{k}{mm/s^2} \qquad\qquad x_3 = 0.71 \frac{k}{mm/s^2}$$

Lee and Pradko [38, 39] proposed a scalar quantity called *absorbed power* to

measure the average rate of energy dissipated by the complex damped elastic properties

of the human anatomy. The proposed measure was developed based on a purely

mechanical approach (ride simulator tests) while excluding subjective evaluation. The

average absorbed power is determined from the intensity and frequency of the input

vibration as:

$$P = \sum_{i=1}^{n} K_i a_i^2$$ (1.3)

where P is average absorbed power, a_i is rms acceleration at a frequency 'i' in m/s^2, K_i

is absorbed power constant of the body at frequency 'i', and n is the number of discrete

by the scalar sum of absorbed powers associated with each of three translational axes. The absorbed power criterion has been extensively used to assess military vehicle ride due to its simplicity. It provides a single number rating of the ride environment, which is function of the vibratory modes, intensities, frequency contents, body orientation, posture, etc. The absorbed power criterion is also supported by the Janeway recommended safe limits [33], particularly in the low frequency range, i.e., the 2.7 W power curve coincides very closely with the Janeway limit up to about 5 Hz. Average absorbed power in the range of 6-10 W, is considered acceptable for off-road vehicles, and has been extensively used to assess military vehicle ride.

A general guide for defining the human tolerance to whole body vibration has been proposed in the International Standard, ISO2631(1978) [40,41]. This guide is recommended for the evaluation of vibration environments in transport vehicles as well as in the industry, and defines three distinct limits for whole-body vibration in the frequency range of 1-80 Hz: (i) Exposure limits related to the preservation of safety (or health) and should not be exceeded without special justification; (ii) Fatigue or decreased proficiency boundaries related to the preservation of working efficiency, which apply to such tasks as driving a road vehicle or a tractor; and (iii) Reduced comfort boundaries concerned with the preservation of comfort. Figure 1.12 illustrate the fatigue or decreased proficiency boundaries for exposure to vertical and horizontal vibration, which are defined in terms of root mean square values (rms) of acceleration as a function of
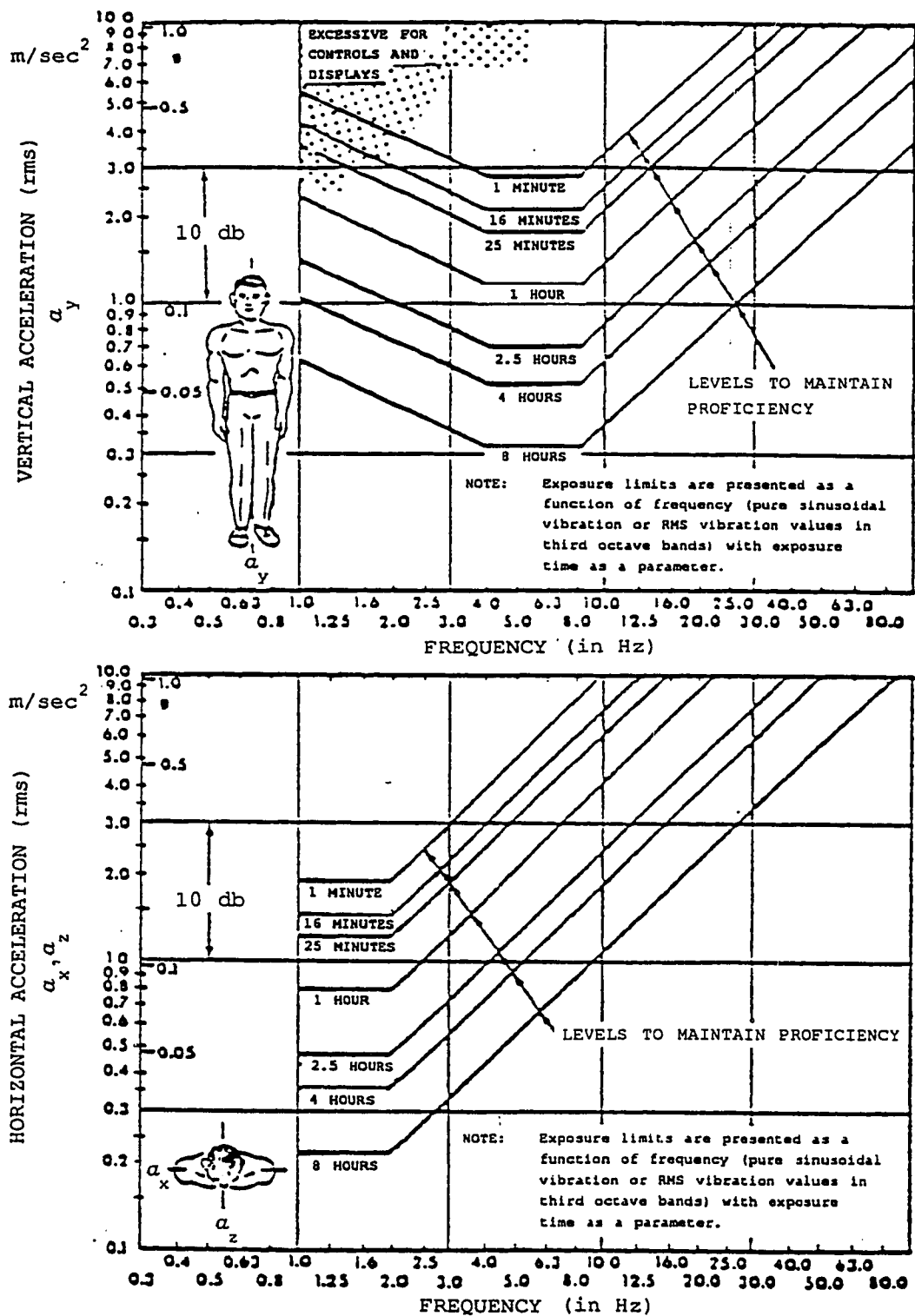
Figure 1.12: Limits of whole-body vibration for fatigue or decreased proficiency in vertical and horizontal direction recommended by ISO [40].

frequency and exposure time. It can be seen that the exposure limits are reduced as the average daily exposure time increases. When vibration takes place in more than one direction simultaneously, corresponding boundaries apply to each vectorial component in the three axes. The exposure limits for safety (or health) reasons are obtained by raising the fatigue for decreased proficiency boundaries by a factor of two (6 dB higher), whereas the reduced comfort boundaries are obtained by lowering the boundaries by a factor of 3.15 (10 dB lower).

In 1976, Smith [42] proposed a procedure to convert the (ISO -2631, 1978) limits to a form usable for direct comparison with ride vibration data presented in power spectral density (PSD) form. The ISO-2631 [40] ride assessment criteria is most widely accepted, and is applicable to whole-body vibration. However, this standard fails to quantify ride criteria under rotational modes of vibration. ISO has recently proposed revised weighting factors and methodology in order to quantify the ride quality by a single number along the translational and rotational axes [43]. This method of assessing the ride is gaining popularity due to its simplicity. However, there have been many concerns associated with the measurement procedures, and vibration limits proposed in the revised ISO-2631. The methods can be applied for evaluating the exposure to vibration containing occasional high peaks (high crest factors, the ratio of peak value to the overall rms acceleration). For vibration with crest factors below or equal to 9, the basic evaluation method is normally considered adequate. For certain types of vibrations, especially those containing occasional shocks, the basic evaluation method may understimate the severity with respect to discomfort even when the crest factor is not greater than 9. In cases of doubt it is therefore recommended to use and report additional

greater more than 9. The first method, referred to as the running rms method, takes into account occasional shocks and transient vibration by use of a short integration time constant. The vibration magnitude is defined as a maximum transient vibration value (MTVV), $a_w(t_o)$ given by:

$$a_w(t_o) = \left\{ \frac{1}{\tau} \int_{t_o-\tau}^{t_o} [a_w(t)]^2 \, dt \right\}^{1/2}$$ (1.4)

where $a_w(t)$ is the instantaneous frequency-weighted acceleration, τ is the integration time for running averaging, t is the time and t_o is the time of observation. The second method, referred to as the fourth power vibration dose method, is more sensitive to occasional peak vibration than the basic evaluation method by using the fourth power instead of the second power of the acceleration time history as the basis for averaging. The fourth power vibration dose value (VDV) in meters per second to the power 1.75 ($m/s^{1.75}$), or in radians per second to the power 1.75 ($rad/s^{1.75}$) , is defined as:

$$VDV = \left\{ \int_0^T [a_w(t)]^4 \, dt \right\}^{1/4}$$ (1.5)

where T is the duration of measurement. The "fourth power" criteria has been recently accepted for inclusion in the new draft of ISO-2631 guide (1997) [43].

1.3 SCOPE OF THE PRESENT RESEARCH WORK

1.3.1 Objectives

The overall objective of this thesis is to contribute to the improvement of ride quality performance of tracked snowplow vehicles, through systematic study of primary and secondary suspension, and track-terrain interactions. The specific objectives of the dissertation research are as follows:

1. To develop a comprehensive mathematical model of a sidewalk snowplow vehicle incorporating nonlinear models of the cab mounts, driver, suspension seat and road wheels suspension.

2. To characterize the wheel/track-terrain interactions, using an adaptive foot-print model.

3. To evaluate the ride vibration response of the snowplow vehicle subject to deterministic obstacle and random terrain excitations.

4. To validate the simulation model using field test data.

5. To assess the ride quality of the snowplow vehicle.

6. To carry out comprehensive parametric sensitivity analyses to illustrate the influence of vehicle suspension and track parameters on the ride dynamics of the snowplow vehicle.

1.3.2 Organization of the Thesis

In Chapter 2, various configurations of the snowplow vehicle adopted for this study, are described. A ride dynamic model of the snowplow vehicle is developed employing simplified yet credible mathematical formulations of subsystems of the vehicle-terrain dynamical system. Details and assumptions associated with the modeling of driver-seat-suspension system, cab and vehicle suspension system, wheel, and track are provided.

In Chapter 3, field measurement methodology and the measured data are briefly reviewed and the deterministic as well as random excitations are discussed. Free vibration analysis, transient response analysis and random response analysis of the vehicle are carried out. The ride dynamic response of the snow plow vehicles to random terrains and deterministic obstacles are presented. Field validation of the ride dynamic model is also carried out.

In Chapter 4, the ride quality of the snowplow vehicle is analyzed using the guidelines proposed in ISO 2631. A parametric sensitivity analysis is carried out to study the influence of various operating conditions and design parameters such as track stiffness, wheel suspension stiffness, cab mounts stiffness, damping, seat suspension and track terrain on the ride quality of the vehicle.

The conclusion drawn from the study and the recommendations for future work are finally presented in Chapter 5.

CHAPTER 2

DEVELOPMENT OF RIDE DYNAMIC MODEL

2.1   INTRODUCTION

The vibration environment of a snowplow vehicle is primarily dominated by the road wheel suspension, track-terrain interactions and the driver-seat suspension. A comprehensive mathematical model of the snowplow vehicle thus must identify and characterize the dynamics associated with the track and wheel suspension. During the modeling stage, it is usually desirable to develop a simple and credible model such that the dynamics of the vehicle is fully described. Simplicity of the model is determined by the number of its degrees-of-freedom, whereas the credibility of the vehicle model is demonstrated by its capability to simulate the vehicle behavior realistically within the desired accuracy.

From the analytical modeling point of view, snowplow is a tracked vehicle which is a complex dynamical system, and requires special modeling considerations. Although ride model of a tracked vehicle is similar to that of a wheeled vehicle, it requires certain special considerations of the track. In this chapter, a sidewalk snowplow vehicle is described, and the dynamic loads arising from the track, blade, road wheels, suspension and terrains are identified. This mathematical model includes: systematic identification of the static and dynamic properties of the track, tires, and cab mounts; development of an adaptive contact track-road interaction model; characterization and analytical representations of the trailing-arm front wheel suspension, and tandem rear wheels suspension; characterization and analytical representation of blade contact forces arising

from the road and plowing. The systematic development of the ride model is presented along with the underlying assumptions.

2.2 DESCRIPTION OF A SIDEWALK SNOWPLOW VEHICLE

The ride vibration environment of modern snowplowing vehicles is related to many design and operating factors. Both the design and operating factors are known to vary considerably. The track-terrain interactions, plowing forces and thus the ride vibration environment vary significantly with the nature of task, road surface, speed, depth and density of snow, and temperature. Furthermore the modern vehicle configurations offer considerable design variations with respect to the major components, such as track, road wheel suspension, cab suspension, and weights and dimensions. While conventional vehicles do not employ primary and secondary suspension with the exception of a vertical seat suspension, the more advanced designs may include elastically mounted cab, road wheel suspension and an elastic track. The ride vibration environment of these vehicles may thus vary significantly with the design configurations. Furthermore, these vehicles may employ solid rubber road wheels or pneumatic tires. The track designs also vary from those consisting of relatively rigid links to continuous elastic belt. Figure 2.1 illustrates a schematic view of a modern sidewalk snowplowing vehicle. The vehicle consists of trailing arm first road wheel suspension and tandem rear wheels. The track is a continuous elastic track and its tension can be adjusted by positioning the rear road wheels. All the road wheels are made of solid rubber. The driver cab is mounted on four rubber mounts, while the drive train is installed in the rear of the hull.

35
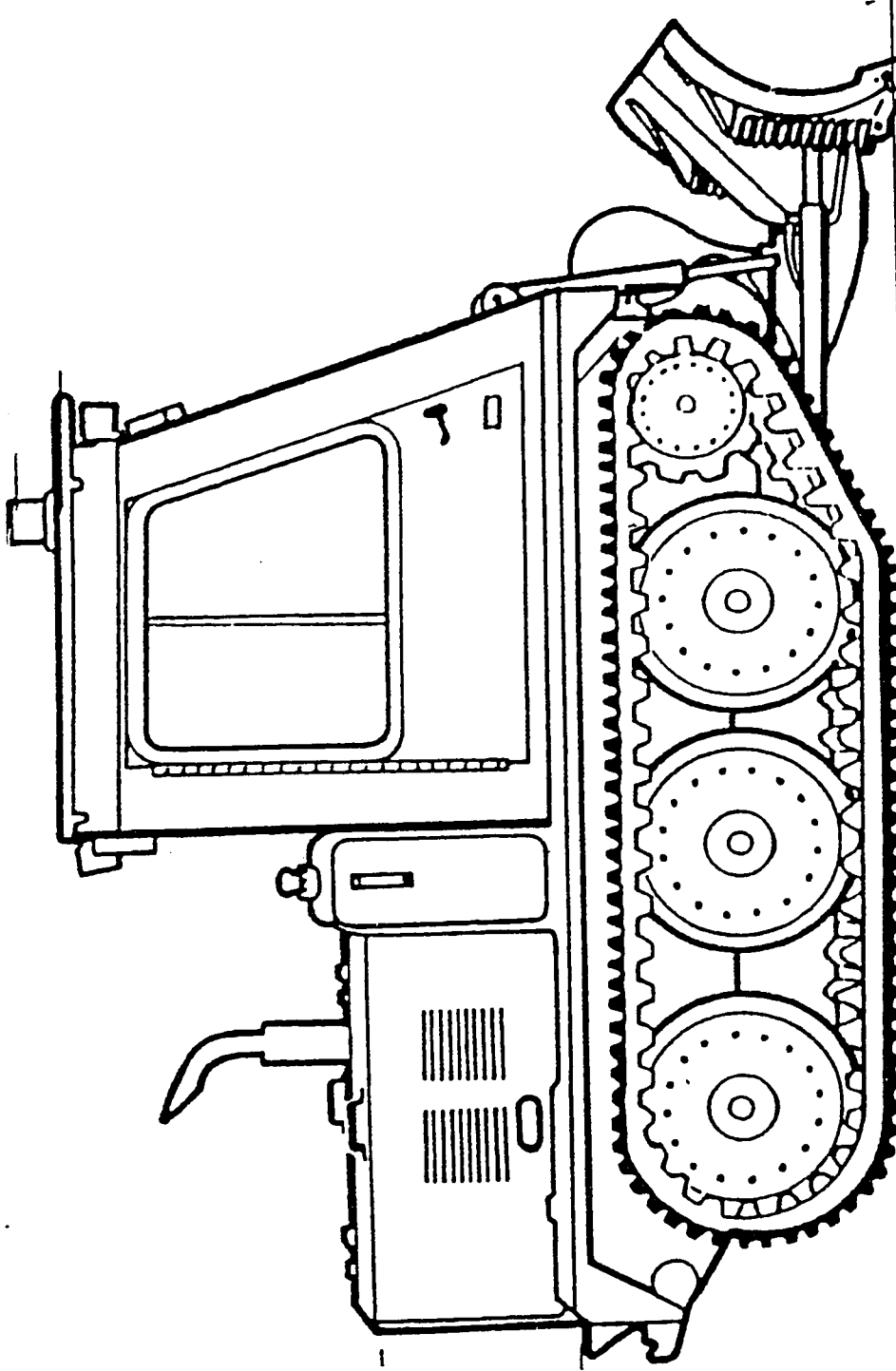
Figure 2.1: A schematic of a sidewalk snowplow vehicle, manufactured by Bombardier Inc.

36

2.3   DEVELOPMENT OF NONLINEAR RIDE DYNAMIC MODEL

In general, a snowplow vehicle can be analytically represented through three-dimensional mathematical model incorporating six degrees-of-freedom for vehicle body, appropriate number of degrees-of-freedom for road wheel assemblies, and an additional degree-of-freedom for driver and seat dynamical system and/or any other vehicle components considered as separate bodies. However, the width of the snowplow vehicle is very small compared to its length, and previous studies have demonstrated that an in-plane model provides sufficient information for detailed analysis of the suspension dynamics, and associated shock and vibration environment of the vehicle [2-17]. An in-plane ride dynamic simulation model of a snowplow vehicle traversing an arbitrary but specified non-deformable terrain at a constant forward speed is thus developed in the following sub-sections.

For the purpose of dynamic modeling, a sidewalk snowplow vehicle can be divided into six major components: driver and seat suspension; cab suspension; road wheels suspension; hull; blade; and track. A building block modeling approach is employed to formulate the analytical model of the vehicle-terrain by integrating the above component models, as illustrated in Figure 2.2.

Assuming negligible roll, while traversing undeformable sidewalks, an in-plane ride dynamic model of snowplow vehicle is formulated with symmetry about a plane defined by a vertical axis and the vehicle's longitudinal axis. The analytical model is formulated to describe the longitudinal, bounce and pith motions associated with the vehicle sprung body (hull) and the cab. The vertical driver-seat-suspension system is
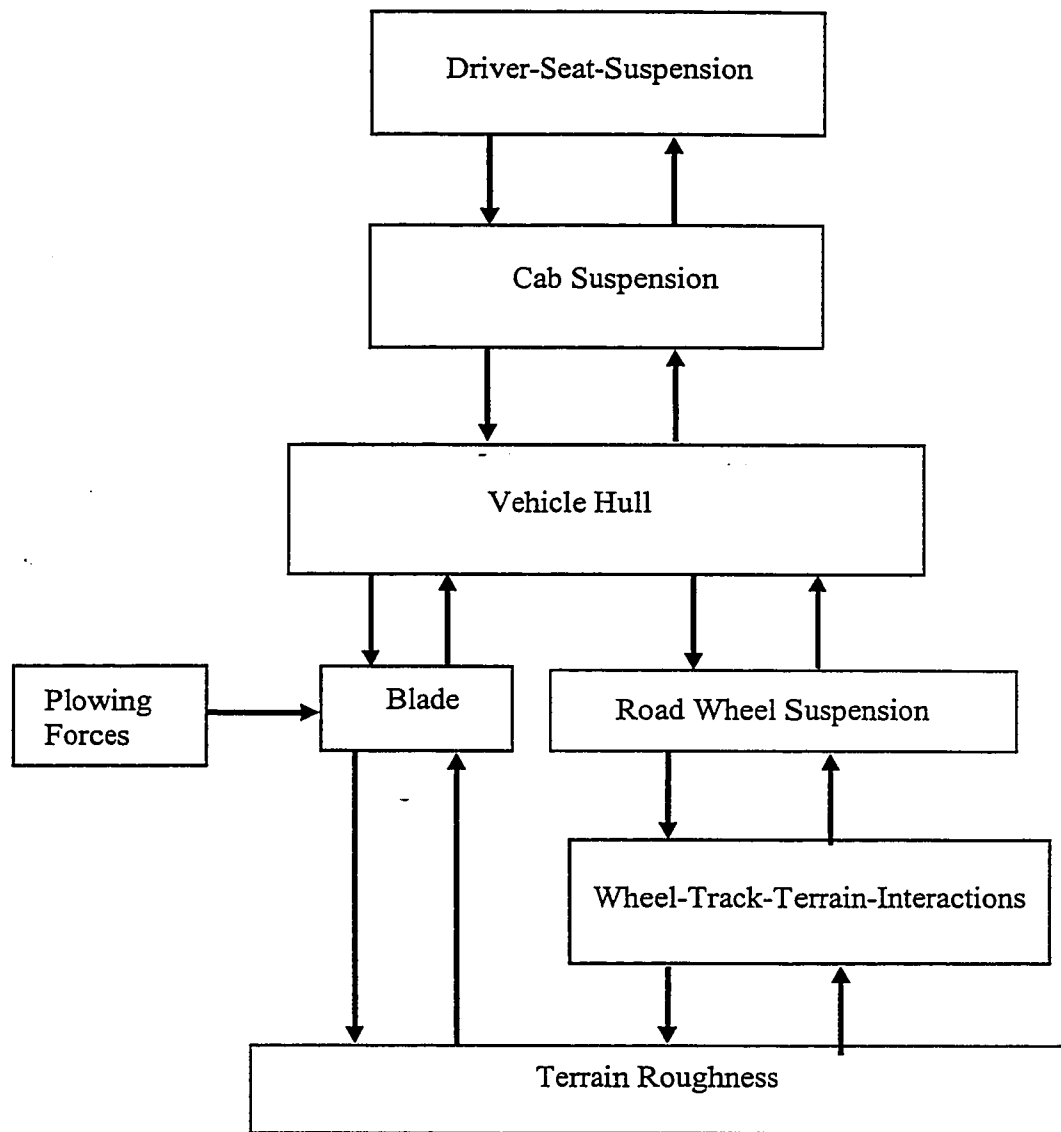
Figure 2.2: Building block simulation approach for the tracked snowplow vehicle.

developed upon integrating a single-degree-of-freedom (DOF) driver model to a two-DOF seat suspension, incorporating nonlinearities due to shock absorber damping, linkage friction and bump stops. The first road wheel and axle assembly is represented by a lumped mass with a trailing arm that undergoes a pitch rotation. The second and third road wheel, arranged in a tandem configuration, are represented by a walking beam with pitch DOF. Each road wheel resting on the track is represented by a continuous radial spring and an equivalent viscous damper model. The drive sprocket is also treated in a similar manner, when it comes in contact with the terrain under certain severe irregularities. The track is modeled as a continuous elastic belt capable of transmitting only tensile forces. The blade-road contact and plowing actions transmit considerable magnitudes of vertical and horizontal forces to the blade and the vehicle. The front blade assembly is thus represented by a rigid body with pitch rotation. The entire vehicle ride model is thus developed as a 12-DOF dynamic system, as illustrated in Figure 2.3.

The differential equations of motion of the snowplow vehicle model are derived using d'Alembert's principle upon identifying the various forces acting on the seat, cab, hull and the road wheels. The static deflections of the suspension springs, tires and tracks, due to the vehicle sprung and unsprung weights are computed from the static force balance, assuming that the sprung weight is uniformly distributed over the wheels. The total ride dynamic model of the vehicle is formulated upon developing and integrating the six different component models with appropriate considerations of the constraint forces. These components include: (i) driver and seat; (ii) cab and cab mounts; (iii) road wheels; (iv) blade; (v) hull; and (vi) the track-terrain interactions. The component models together with the major simplifying assumptions are described in the following sections.

Figure 2.3: In-plane ride dynamic model of a snowplow vehicle.

40
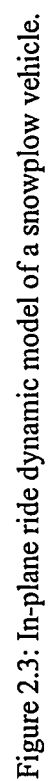
2.4 ANALYTICAL MODEL OF THE DRIVER-SEAT-SUSPENSION SYSTEM

The suspension at the seat has been considered as the simplest and most effective option for ride improvement of off-road vehicles [44, 45]. Considerable efforts have been expended to reduce the discomfort experienced by the driver through improved postural support and vibration attenuation performance of the seat [45-47]. Since the vertical vibration have been recognized among the most severe ones, majority of the studies focus on the vertical seat-suspension with rigid body representation of the driver. Although, the lateral vibrations of off-road vehicles have also been recognized among the most severe ones, the efforts on developments of lateral seat-suspensions have been severely limited due to their predominance in the extremely low frequency region (around 1 Hz) [45]. Experimental studies conducted by Griffin [48] and Suggs *et al* [49] clearly illustrate that the characteristics of transmitted vibrations are strongly influenced by the dynamics of the seated human body. The ride performance analysis of a seat-suspension system, thus, necessitates appropriate considerations of dynamics due to the driver. A number of mechanical models of the seated driver, ranging from simple single-degree-of-freedom to many DOF models, have been reported in the literature. A recently reported review of thirteen different mechanical models concluded that the simple SDOF model, proposed by Griffin [48], can be effectively used to assess the driver-seat system performance in the low frequency range [50].

In this study, the vehicle seat-suspension system is characterized by a generalized nonlinear analytical model, incorporating nonlinear force-displacement and force-velocity characteristics due to shock absorber and restoring elements, and a SDOF seated occupant model.

2.4.1 Analytical Model of the Seat-Suspension

Suspension seat, in general comprises an air or mechanical spring, a double acting hydraulic damper, and either elastic or rigid compression and extension bump stops to prevent excessive relative motion of the low natural frequency suspension. Figure 2.4(a) illustrates a schematic of a typical under-the-seat suspension system, which consists of a cross-linkage mechanism, an inclined shock absorber, and either a coil or pneumatic spring. The vertical seat-suspension system, irrespective of the linkage and suspension type, can be characterized by a two-DOF dynamical system [51], while neglecting the dynamics of the driver, as illustrated in Figure 2.4(b). Additional degrees-of-freedom, however, need to be incorporated when the dynamics of the driver is considered.

(a) Schematic of an under-the-seat suspension system.

(b) A generalized two-DOF model of a seat-suspension model.
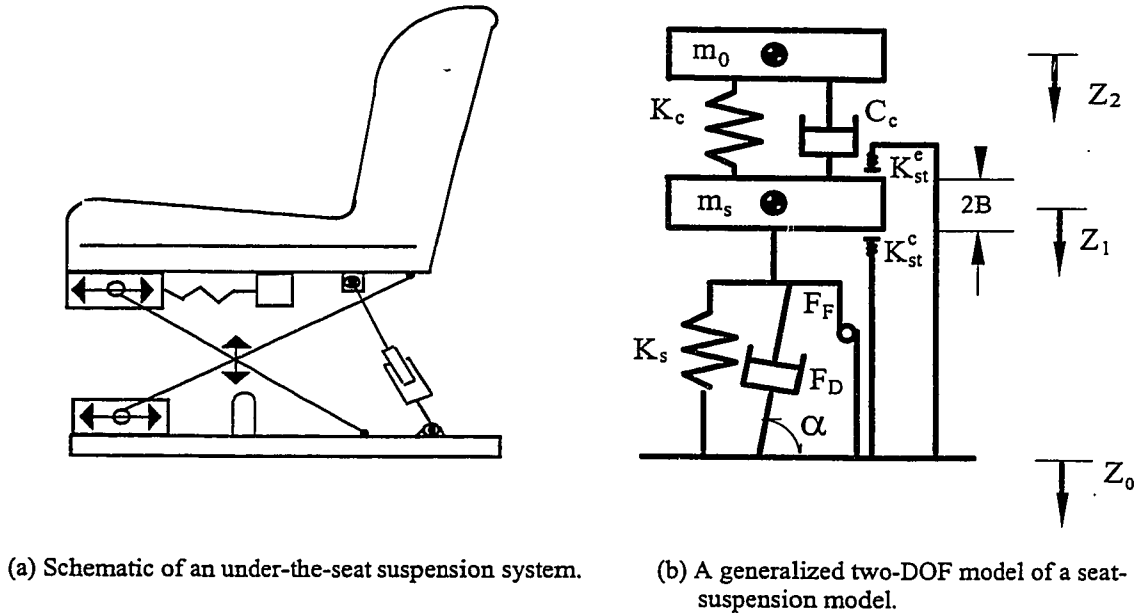
Figure 2.4: Seat-suspension system.

The primary assumptions implied in the modeling process are as follows:

(i)   Transverse stiffness of the cushion is assumed to be very high. The visco-elastic properties of the seat-cushion along the vertical axis are derived from measured force-deflection data [51], and characterized by equivalent linear stiffness and viscous damping coefficients within the operating range.

(ii)   Coulomb friction within the linkage mechanism is assumed to possess ideal characteristics.

(iii)   The resilient means, whether air or coil spring, is modeled as a vertical spring with linear coefficient in the operating range.

(iv)   The damper is assumed to yield symmetric forces in compression and rebound with relatively higher bleed damping at lower velocities.

In view of the complexities associated in developing a quantitative model of the human body and the fact that vehicle vibration dominate around low frequencies, a rigid body representation of the human driver may be considered appropriate. Impedance characteristics of human body, seated with semi-rigid envelope around the abdomen, reveal that human body subjected to whole-body vibration behaves similar to a rigid mass up to approximately 2 Hz [45,52]. Since the natural frequency of seat-suspension system is well below 2 Hz, a rigid mass representation of the driver may be used to analyze the seat-suspension systems. Such a seat-suspension model, however, may not accurately predict the suspension performance for excitation frequencies above 2 Hz. Based on the experimental studies conducted by Stikeleather [47], it is further assumed that only 5/7 of the driver mass is supported by the seat. The equations of motion for the nonlinear seat-suspension model with rigid driver mass, presented in Figure 2.4, can be expressed in the following manner:

$$m_s \ddot{z}_1 + F_s(y_1, B) + F_k(y_1) + F_d(\dot{y}_1, \alpha) + F_f(\dot{y}_1) - F_c(y_2, \dot{y}_2) = 0$$
$$m_0 \ddot{z}_2 + F_c(y_2, \dot{y}_2) = 0$$

(2.1)

where m_o is the effective operator mass supported by the seat, m_s is the sprung mass of the seat-suspension system. z_1 and z_2 are vertical displacement of the suspension and operator masses, respectively, and $y_1 = z_1 - z_o$; $y_2 = z_2 - z_1$. $F_c(y_2, \dot{y}_2)$ is the dynamic force developed by the cushion, given by:

$$F_c(y_2, \dot{y}_2) = K_c y_2 + C_c \dot{y}_2 \tag{2.2}$$

where K_c and C_c are linear stiffness and damping coefficients of the cushion, respectively. F_k, F_f, and F_s are the suspension forces due to suspension spring, linkage friction and bump stops, respectively, given by:

$$F_k(y_1) = K_s y_1; \qquad F_f(\dot{y}_1) = F_{CD}\, sgn(\dot{y}_1)$$
$$F_s(y_1, \alpha) = K_{st} S\, [y_1 - B sgn(y_1)] \tag{2.3}$$

where K_s is suspension spring rate, F_{CD} is magnitude of Coulomb friction, B is half the permissible suspension travel and K_{st} is spring rate of the bump stop, which may assume different values corresponding to compression (K_{st}^c) and extension (K_{st}^e), such that

$$K_{st} = \begin{cases} K_{st}^e ; & x_1 > B \\ K_{st}^c; & x_1 < -B \end{cases} \tag{2.4}$$

S and sgn(.) are nonlinear functions, given by :

$$sgn(\circ) = \begin{cases} +1 ; & (\circ) > 0 \\ -1 ; & (\circ) < 0 \end{cases} ; \quad \text{and } S = \begin{cases} 1 ; & |x_1| > B \\ 0 ; & |x_1| < B \end{cases} \tag{2.5}$$

In order to attain adequate vibration attenuation performance, the shock absorber is designed to generate high damping force due to bleed control corresponding to low piston velocity, and low damping force due to blow-off valves when piston velocity exceeds certain preset velocity. Assuming symmetric force-velocity characteristics

presented in Figure 2.5, the damping force, F_D developed along the shock absorber axis

is given by:
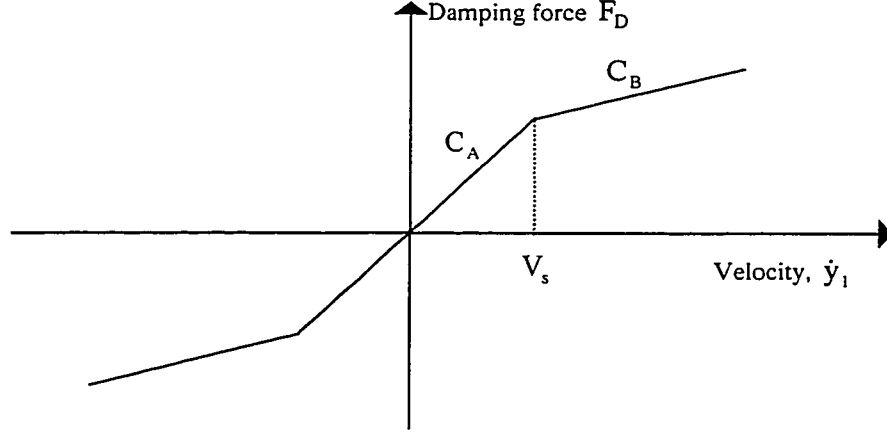
Figure 2.5: Symmetric force-velocity characteristics of a seat-suspension shock absorber.

$$F_D = \begin{cases} C_A V_r & ; \text{ if } |V_r| \leq V_s \\ C_A V_s \, \text{sgn}(V_r) + C_B [V_r - V_s \, \text{sgn}(V_r)] & ; \text{ if } |V_r| > V_s \end{cases} \qquad (2.6)$$

where V_s is preset or transition velocity, V_r is relative velocity across the shock

absorber, and C_A and C_B are damping coefficients corresponding to bleed and blow-off

stages. The suspension force, due to an inclined shock absorber, $F_d(\dot{y}_1, \theta)$, is derived

from its kinematic model, presented in Figure 2.6, as a function of its inclination α. The

relative velocity across the shock absorber is thus expressed as:

$$V_r = \dot{y}_1 \sin \alpha \qquad (2.7)$$

The angle of inclination α is expressed as a function of the motion of the

45
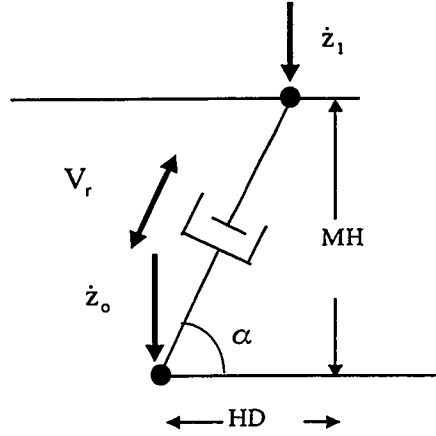
Figure 2.6: Kinematic model of the shock absorber.

suspension mass relative to the floor:

$$\alpha = \tan^{-1}\left[\frac{MH - y_1}{HD}\right] \tag{2.8}$$

where MH is the static mid-ride height and HD is horizontal projection of shock absorber

end points. The vertical suspension force due to shock absorber is then derived as:

$$F_d(\dot{y}_1, \alpha) = F_D \sin\alpha \tag{2.9}$$

Equations (2.1) through (2.9) describe the dynamics of a two degrees-of-freedom

driver-seat-suspension model incorporating geometric and suspension nonlinearities, and

rigid body model of the seated driver.

2.4.2 Seat-suspension model with one DOF driver model

The seat-suspension performance is affected not only by the suspension design

but also by the dynamics of the suspended drive. It is thus essential to develop an

acceptable human body model to investigate the performance characteristics of the total

driver-seat-suspension system. The impedance measurements performed on seated human

subjects illustrate that the upper torso and lower body resonate in the 4-6 Hz and 7-11 Hz excitation frequency ranges, respectively [49, 52]. Since off-road vehicle vibrations predominate at lower frequencies, a single-DOF model representing the dynamics of upper torso and lower body can be formulated. The buttocks and legs are treated as a rigid mass and lumped with the skeletal frame [52]. An analytical model of the seat-driver system can thus be developed by integrating the SDOF driver model to the seat-suspension model, as shown in Figure 2.7. The equations of motion for the three DOF driver-seat-suspension model are formulated as:
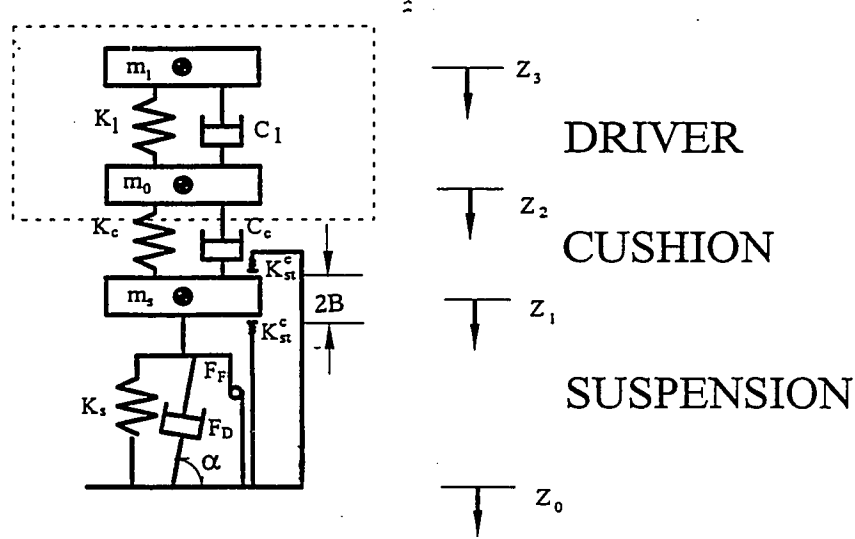
Figure 2.7: Three-DOF model of the driver-seat-suspension system.

$$m_s \ddot{z}_1 + F_s(y_1, B) + F_k(y_1) + F_d(\dot{y}_1, \alpha) + F_f(\dot{y}_1) - F_c(y_2, \dot{y}_2) = 0$$

$$m_o \ddot{z}_2 + F_c(y_2, \ddot{y}_2) - K_1 y_3 - C_1 \dot{y}_3 = 0 \qquad (2.10)$$

$$m_1 \ddot{z}_3 + K_1 y_3 + C_1 \dot{y}_3 = 0$$

In this case, m_o is mass of the seated driver's buttocks and legs supported by the seat. $y_3 = (z_3 - z_2)$, represents the relative displacement of the combined pelvis, abdomen, chest and head mass (m_1) with respect to mass m_o. $y_1 = (z_1 - z_0)$, represents

the relative displacement of the seat suspension mass and the cab floor. $z_o = z_c + a_o \theta_c$

(shown in Figure 2.8) is the vertical displacement of the cab floor. K_1 and C_1 are stiffness and damping coefficients of the human body model, derived from the impedance data.

2.5   DEVELOPMENT OF THE CAB SUSPENSION MODEL

Different concepts in secondary (cab and seat) suspensions have gained significant popularity due to their potentials for vehicle ride improvement. A suspension at the seat offers attenuation of vertical vibration alone and can lead to significant transient motions due to frequent contacts with the end stops. Alternatively, a suspension at the cab can attenuate ride vibrations along the vertical, pitch, roll, lateral and longitudinal directions, while the excessive relative deflection of the low natural frequency seat can be eliminated. In view of the ride improvement potentials of the cab suspension, a number of effective cab suspension designs have been developed by the automotive designers. Flower [53] presented a comparative ride performance of a number of cab suspensoin configurations. The ride performance characteristics of unique tilt cab system have been investigated analytically by Roley et al. [54] and Rakheja et al. [55]. The ride performance of vehicle cabs, in general is evaluated through lumped-mass models, while assuming negligible contributions due to structure deflection modes. The cab in the candidate vehicle is installed on four elastic mounts, which offer restoring forces along the radial and axial directions. Although elastic mounts do not yield significant attenuation of low frequency vehicular vibration, they offer considerable advantages in reducing high frequency vibration and noise, and structural vibration.

Figure 2.8 illustrates an in-plane model of the cab supported on four isolators, referred to as the "four-point configuration". The cab mounts are modeled as parallel combinations of spring-damper elements along the two orthogonal directions, as shown in longitudinal-bounce plane. The vertical spring-damper represents the tension/compression properties of the mount, while the longitudinal isolation is attributed to their shear properties. The cab is thus modeled as a three DOF system to incorporate the bounce (z_c), longitudinal (x_c) and pitch (θ_c) motions of the cab mass. The elastomer suspension are assumed to be linear and the seat is assumed to be fixed to the cab floor. The equations of motion describing the vibration of the three DOF cab suspension model are derived using Langrange's formulations, and expressed as:

$$m_c \ddot{x}_c + \sum_{i=1}^{2} F_{cx}^i = 0$$

$$m_c \ddot{z}_c - F_{SEAT} + \sum_{i=1}^{2} F_{cz}^i = m_c g \qquad (2.11)$$

$$I_{yc} \ddot{\theta}_c - F_{SEAT} a_o - F_{cz}^1 a_{cf} + F_{cz}^2 a_{cr} + b_c \sum_{i=1}^{2} F_{cx}^i = 0$$

where F_{cx}^i and F_{cz}^i (i=1,2) are the horizontal and vertical forces due to the cab mounts. Assuming linear stiffness and viscous damping due to the mounts, these forces can be derived from:

$$F_{cx}^i = 2K_{cxi}\{x_c + \theta_c b_c - x_h + \theta_h (b_{hc} - b_c)\} + 2C_{cxi}\{\dot{x}_c + \dot{\theta}_c b_c - \dot{x}_h + \dot{\theta}_h (b_{hc} - b_c)\}$$
$$F_{cz}^1 = K_{cz1}\{z_c - \theta_c a_{cf} - z_h + \theta(a_c + a_{co}) + z_{cst}\} + C_{cz1}\{\dot{z}_c - \dot{\theta}_c a_{cf} - \dot{z}_h + \dot{\theta}(a_c + a_{co})\}$$
$$F_{cz}^2 = K_{cz2}\{z_c + \theta_c a_{cr} - z_h + \theta a_{co} + z_{cst}\} + C_{cz2}\{\dot{z}_c + \dot{\theta}_c a_{cr} - \dot{z}_h + \dot{\theta} a_{co}\} \qquad (2.12)$$
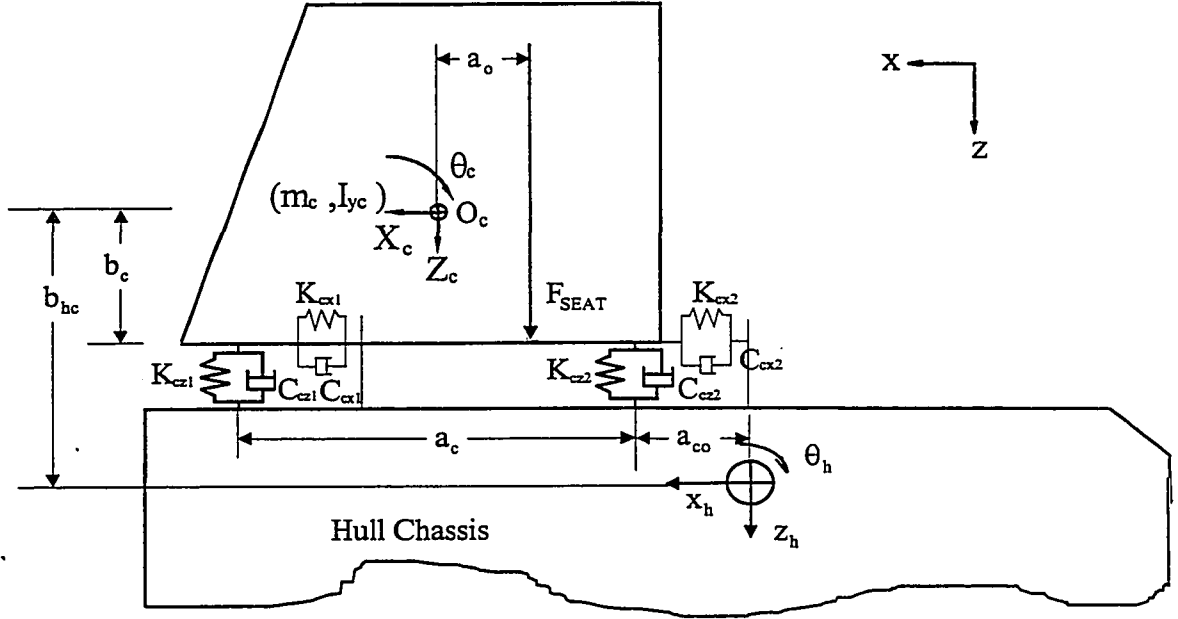
Figure 2.8: An in-plane model of the cab and cab mounts.

where K_{cxi} and K_{czi} are the linear vertical and horizontal stiffness coefficients of the cab

mounts, C_{cxi} and C_{czi} are the corresponding damping coefficients. z_{cst} is the static

deflection of cab mounts. m_c and I_{yc} represent cab mass and pitch mass moment of

inertia about the cab centre of gravity, respectively. Constants a_o, a_{cf}, a_{cr} a_{co}, b_{hc} and

b_c define the cab geometry, as shown in Figure 2.8, and $a_{cr} = a_c - a_{cf}$. F_{SEAT} is the force

developed by the suspension seat, which is derived from Equations (2.1):

$$F_{SEAT} = F_s(y_1, B) + F_k(y_1) + F_d(\dot{y}_1, \alpha) + F_f(\dot{y}_1) \tag{2.13}$$

2.6   DEVELOPMENT OF ROAD WHEEL SUSPENSION MODEL

The road wheel suspension comprises of four major components: torsion bar, road wheel arm, walking beam, and bump stop. The first road wheel is independently attached to the hull through a trailing road arm splined to a torsion bar. With this arrangement, the first road wheel is allowed to swing about the torsion bar center. The rear two wheels are supported in a tandem arrangement using a walking beam.

2.6.1   Dynamic Model of the First Road Wheel

The front road wheel suspension, referred to as "flexiride rubber suspension", employs an elastic rubber element in torsion. The rubber elastomer thus undergoes shear deformation which is technically considered superior to rubber in compression [57]. The wear and abrasion between the moving parts is considerably reduced leading to longer life and silent operation, since there is no relative movement between the metal and rubber surfaces. The first road wheel assembly is thus modeled as a trailing arm coupling the torsional stiffness due to torsion bar and a rigid unsprung mass due to the wheel as shown in Figure 2.9. The elastic bump stop employed to limit the wheel hop is represented by a parallel combination of clearance spring and viscous damping elements. The road wheel is further subject to horizontal and vertical forces F_{wx}^1 and F_{wz}^1, arising from the wheel-track-terrain interaction, which are described in the later section. The first road wheel assembly is thus modeled as a single-DOF dynamic system with pitch (θ_{w1}) degree-of-freedom. The differential equation of motion of the road wheel is derived as:

$$I_{w1}\ddot{\theta}_{w1} + M_{w1} + F_{wz}^1 a_{rw1} + F_{wx}^1 b_{rw1} + F_{w1}(\theta_{w1}, \beta_{w1})R_{bw1} = 0 \qquad (2.14)$$

51

where M_{w1} is the suspension torque due to elastic torsion bar. Assuming linear stiffness

(K_{tw1}) and damping (C_{tw1}) coefficients, the suspension torque is expressed as:

$$M_{w1} = K_{tw1}(\theta_{w1} - \theta_{w1st} - \theta_h) + C_{tw1}(\dot{\theta}_{w1} - \dot{\theta}_h) \qquad (2.15)$$

where θ_{w1} is the pitch rotation of the road wheel arm, θ_h is the pitch motion of the hull.

θ_{w1st} is the static deflection of the road wheel arm. I_{w1} is the pitch mass moment of

inertia of first road wheel about the road arm pivot. $F_{w1}(\theta_{w1}, \beta_{w1})$ is the force due to

motion limiting bump stop, given by:

$$F_{w1}(\theta_{w1}, \beta_{w1}) = -S_{w1}[K_{bw1}(|\theta_{w1} - \theta_{w1st} - \theta_h| - \beta_{w1}) + C_{bw1}(|\dot{\theta}_{w1} - \dot{\theta}_h|)] \qquad (2.16)$$

where $S_{w1} = \begin{cases} 1 ; & \theta_{w1} < 0 \text{ and } |\theta_{w1} - \theta_{w1st} - \theta_h| > \beta_{w1} \\ 0 ; & \text{otherwise} \end{cases}$ $\qquad (2.17)$

K_{bw1} and C_{bw1} are the linear stiffness and damping coefficients of the elastic bump stop,

respectively, and $\bar{\beta}_{w1}$ indicates the angular clearance between the bump stop and the static

road arm position. $a_{rw1} = L_{fr} \sin\alpha_o$ and $b_{rw1} = L_{fr} \cos\alpha_o$ of the wheel center along the

fixed x-z axis. α_o is the initial angle of the road wheel arm of flexiride rubber suspension

unit and L_{fr} is the length of road wheel arm.

2.6.2 Analytical Model of the Tandem Road Wheels

The second and third road wheels of the vehicle are supported by a walking beam

as schematically shown in Figure 2.10. The walking beam with wheel at each end is

attached to the hull through splining to a bar, which extends over the width of chassis and

is clamped on the other end. The walking beam is free to rotate about its pivot point. Two

Rotational bump stops are mounted to prevent the road wheels from hitting the hull
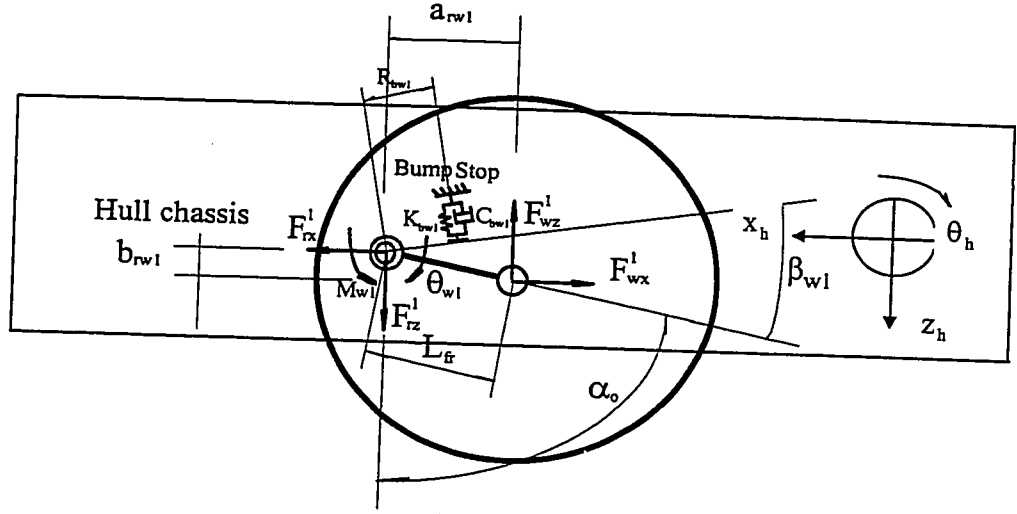
Figure 2.9: An analytical model of the flexiride first road wheel suspension.

chassis. The road wheels are further subject to horizontal and vertical forces arising from the wheel-track-terrain interactions, F_{wx}^2, F_{wx}^3, F_{wz}^2, F_{wz}^3, which are described in the later section. Thus the dynamics of walking beam assembly can be represented by its pitch DOF (θ_{w23}), and the differential equation of motion is derived as:

$$I_{w23}\ddot{\theta}_{w23} - F_{wz}^2 a_{23f} + F_{wz}^3 a_{23r} + F_{w2}(\theta_{w23},\beta_{w2})R_{bw2} + F_{w3}(\theta_{w23},\beta_{w3})R_{bw3}$$
$$- F_{wx}^2(b_{23f} + \theta_{w23}L_{23f}) + F_{wx}^3(\theta_{w23}L_{23r} + b_{23r}) = 0 \qquad (2.18)$$

where θ_{w23} is the pitch rotation of the road wheel arm, θ_h is the pitch motion of the hull. I_{w23} is the effective pitch mass moment of inertia of the walking beam assembly about its rotational center. $F_{wi}(\theta_{w23},\beta_{wi}),(i=2,3)$ are the forces due to motion limiting bump stops given by:
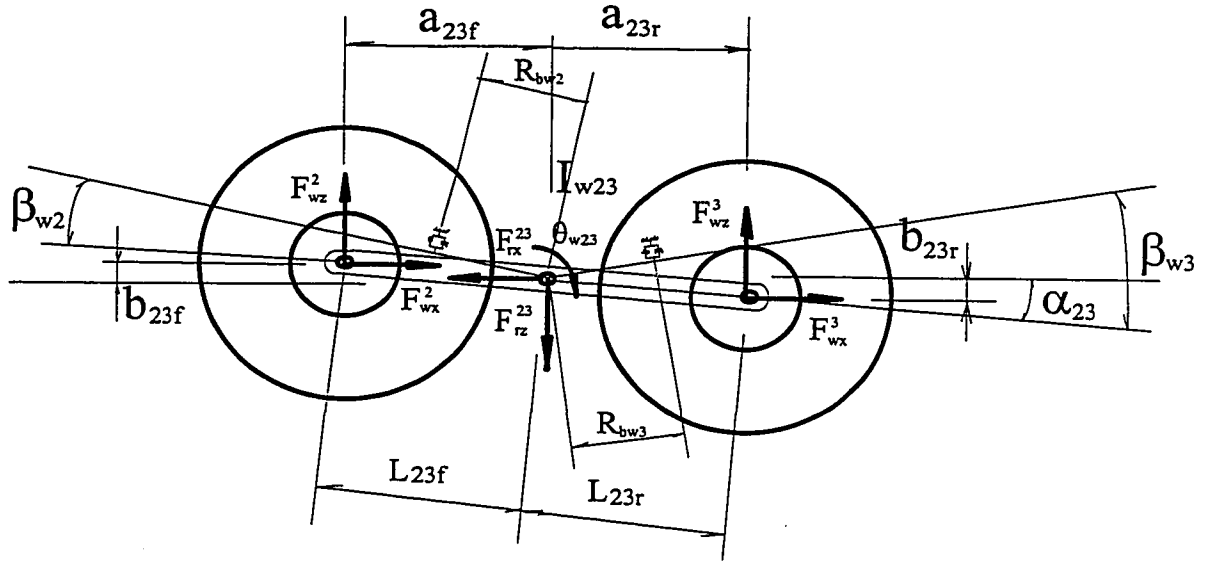
Figure 2.10: Road wheels and walking beam model.

$$F_{wi}(\theta_{w23}, \beta_{wi}) = S_{wi}[K_{bwi}(|\theta_{w23} - \alpha_{23} - \theta_h| - \beta_{wi}) + C_{bwi}(|\dot{\theta}_{w23} - \dot{\theta}_h|)]; \quad i = 2,3 \, (2.19)$$

$$\text{where } S_{w2} = \begin{cases} 1; & \theta_{w23} < 0 \text{ and } \theta_{w23} - \theta_h > \beta_{w2} \\ 0; & \text{otherwise} \end{cases}$$

and

$$S_{w3} = \begin{cases} -1; & \theta_{w23} < 0 \text{ and } |\theta_{w23} - \theta_h| > \beta_{w3} \\ 0; & \text{otherwise} \end{cases} \quad (2.20)$$

$K_{bw2}, K_{bw3}, C_{bw2}$ and C_{bw3} are the linear stiffness and damping coefficients of the elastic bump stops, respectively, and β_{w2} and β_{w3} indicate the angular clearance between the bump stops and the walking beam. $a_{23f} = L_{23f} \cos\alpha_{23}$ and $a_{23r} = L_{23r} \cos\alpha_{23}$, define the horizontal coordinates of the wheel center along the X axis. α_{23} is initial static angle of the walking beam, and L_{23f} and L_{23r} are the length of the walking beam.

2.7 ANALYTICAL MODEL OF THE BLADE

The blade of the snowplowing vehicle transmits forces and moments to the vehicle chassis during plowing tasks. The blade assembly is attached to the hull of snowplow through pin joints and a hydraulic actuator. The blade is subjected to a dynamic horizontal force (F_s), arising from the dynamic interaction of the blade with the accumulated snow, and a vertical force (F_g) arising from the cutting edge of the blade in contact with the ground. In this study, the contact force is derived assuming an elastic contact between the blade and the ground. The contact is thus modelled by a nonlinear spring K_g, as shown in Figure 2.11. The horizontal plow force is strongly related to the density and depth of snow. An analytical model of the snow plow force is thus derived as a function of the snow properties. The blade and its linkage assembly experience an angular motion under the application of contact and push forces. The equation of motion of the assembly can thus be derived using the generalized coordinate as its pitch rotation about the pivot O, and expressed as:

$$I_b \ddot{\theta}_b + F_{cL} L_{b1} \cos\alpha_b + m_b g L_{b2} + F_g L_{b3} + F_s b_s = 0 \qquad (2.21)$$

where I_b is the pitch mass moment of inertia of the blade about the pivot O, θ_b is the pitch coordinate of the blade, and F_{cL} is the force developed by the hydraulic cylinder. The cylinder force is considered to be negligible during plowing at a constant forward speed. The hydraulic cylinder, however, can develop certain dynamic force during the transport operation due to the compliance of the hydraulic column. Assuming constant stiffness due to hydraulic column, the cylinder force during transport operation may be expressed as:
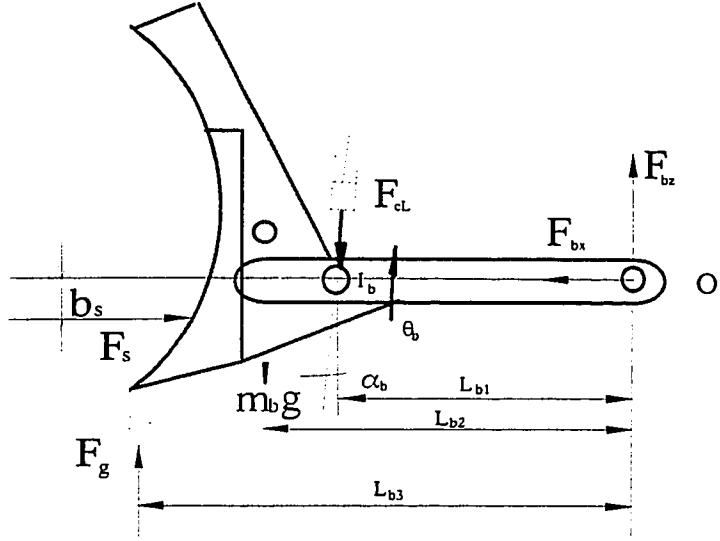
Figure 2.11: Forces acting on the blade assembly.

$$F_{cL} = K_{cL}[L_{b1}\theta_b - \theta_h(a_{b2} - a_{b1}) + \theta_h(b_{b2} - b_{b1})]\cos\alpha_b \qquad (2.22)$$

F_s is horizontal force acting on the blade arising from the plowing action, which is derived in section 3.4.2. This force is assumed to occur during the plowing operation. F_g is vertical contact force between the blade cutting edge and the terrain, which is also derived in section 3.4.2. F_{bx} and F_{bz} are the horizontal and vertical forces, respectively, acting between the blade and the hull. From the force-body diagram of the blade assembly, these forces are derived as follows:

$$F_{bz} = F_{cL}\cos\alpha_b - F_g + m_b g - m_b(L_{b2}\ddot{\theta})$$

$$F_{bx} = F_s - F_{cL}\sin\alpha_b \qquad (2.23)$$

2.8   DEVELOPMENT OF THE HULL MODEL

The vehicle hull, comprising chassis and drive train components, is subject to forces arising from the blade assembly (F_{bx} and F_{bz}), hydraulic cylinder force (F_{cL}), cab

mounts forces $(F^i_{cz}, F^i_{cx}, i = 1, 2)$, first road wheel arm (F^1_{rx}, F^1_{rz}), suspension torque due to

elastic torsionbar and force due to the walking beam mount $(F^{23}_{rx}, F^{23}_{rz})$. The hull, depicted

in Figure 2.12, is modeled as a rigid body with three DOF motion along the longitudinal

(x_h), vertical (z_h) and pitch (θ_h) coordinates. The differential equations of motion for

the hull model are derived as:

$$m_h \ddot{x}_h + F_{cL} \sin \alpha_b + F_{hx} + F^1_{rx} + F^{23}_{rx} + F_{bx} + F_{wx1} + F_{wx2} + F_{wx3} - \sum_{i=1}^{2} F^i_{cx} = 0$$

$$m_h \ddot{z}_h + F_{cL} \cos \alpha_b + F_{hz} + F^1_{rz} + F^{23}_{rz} - F_{bz} - F_{wz1} + F_{wz2} - F_{wz3} - \sum_{i=1}^{2} F^i_{cz} = 0$$

$$I_y \ddot{\theta}_h + F_{cL} \sin \alpha_b b_{b2} - F_{cL} \cos \alpha_b a_{b2} - F_{hz} a_{hf} + F_{hx} b_{hf} + F_{bz} a_{b1} + F_{bx} b_{b1}$$

$$- F^1_{rz} a_{w1} + F^1_{rx} b_{w1} + F^{23}_{rz} a_{hr} + F^{23}_{rx} b_{hr} + F^1_{cz} (a_c + a_{co}) + F^2_{cz} a_{co} - M_{w1} + F_{wz1} a_{wz1}$$

$$+ F_{wx1} b_{wx1} + F_{wz2} a_{wz2} + F_{wx2} b_{wx2} - F_{wz3} a_{wz3} + F_{wx3} b_{wx3} + \sum_{i=1}^{2} F^i_{cx} b_{hcs} = 0 \qquad (2.24)$$

where m_h is the mass corresponding to the vehicle hull and I_y is its pitch mass moment
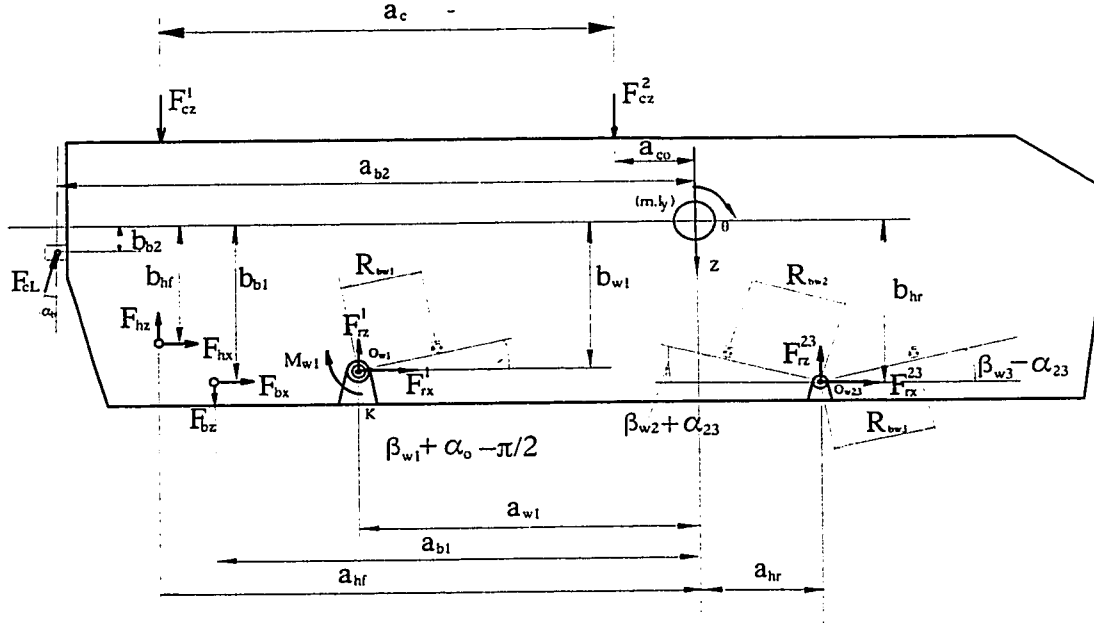
Figure 2.12: Forces and moments acting on the hull mass.

of inertia about the center of mass (c.g.). $F_{wx1}, F_{wx2}, F_{wx3}$ and $F_{wz1}, F_{wz2}, F_{wz3}$ are the horizontal and vertical components of the forces acting on the hull arising from three suspension bump stops, which are given by:

$$F_{wx1} = F_{w1}(\theta_{w1}, \beta_{w1}) \sin(\beta_{w1} + \alpha_0 - \frac{\pi}{2})$$

$$F_{wx2} = F_{w2}(\theta_{w23}, \beta_{w2}) \sin(\beta_{w2} + \alpha_{23})$$

$$F_{wx3} = F_{w3}(\theta_{w23}, \beta_{w2}) \sin(\beta_{w2} - \alpha_{23})$$

and

$$F_{wx1} = F_{w1}(\theta_{w1}, \beta_{w1}) \cos(\beta_{w1} + \alpha_0 - \frac{\pi}{2})$$

$$F_{wx2} = F_{w2}(\theta_{w23}, \beta_{w2}) \cos(\beta_{w2} + \alpha_{23}) \tag{2.25}$$

$$F_{wx3} = F_{w3}(\theta_{w23}, \beta_{w2}) \cos(\beta_{w2} - \alpha_{23})$$

where $a_{wz1}, a_{wz2}, a_{wz3}$ and $b_{wx1}, b_{wx2}, b_{wx3}$ are horizontal and vertical distances between the three bump stops and the hull c.g., given by:

$$a_{wz1} = a_{w1} - R_{bw1} \cos(\beta_{w1} + \alpha_0 - \pi/2)$$

$$a_{wz2} = a_{hr} - R_{bw2} \cos(\beta_{w2} + \alpha_{23})$$

$$a_{wz3} = a_{hr} + R_{bw3} \cos(\beta_{w2} - \alpha_{23})$$

and

$$b_{wx1} = b_{w1} - R_{bw1} \sin(\beta_{w1} + \alpha_0 - \pi/2)$$

$$b_{xz2} = b_{hr} - R_{bw2} \cos(\beta_{w2} + \alpha_{23}) \tag{2.26}$$

$$b_{wx3} = b_{hr} - R_{bw3} \cos(\beta_{w2} - \alpha_{23})$$

F_{hx} and F_{hz} are horizontal and vertical components of forces arising from the dynamic interactions of the track with the drive sprocket. These forces are derived in the following section.

2.9 DYNAMIC WHEEL-TRACK-TERRAIN INTERACTONS

A snowplow vehicle represents a complex dynamical system primarily due to the presence of track and dynamic wheel-track-terrain interactions. The ride dynamic model of a tracked vehicle thus differs considerably from that of a wheeled vehicle, due to unique wheel-track-terrain dynamics. The dynamics of the track have been investigated using different analytical models of varying complexities. Eppinger et al. [2] developed a two-DOF ride dynamic model of a tracked vehicle assuming the track as a continuous massless elastic band capable of transmitting tensile forces, which were considered linearly proportional to change in the total track length. Murphy et al.[4] and Rakheja et al.[23] developed vehicle dynamic models to predict ride-shock-limiting speeds for off-road vehicles, where the dynamic track loads were modeled by equivalent vertical springs interconnecting adjacent wheels. The track forces were thus developed as linear function of relative vertical displacement between the road wheels. Galaitsis[17] proposed a comprehensive model incorporating the inertias of each track shoe, stiffness and damping characteristics of the rubber bushings, and shoe-wheel interaction.

Garnich et al.[18] proposed an in-plane ride dynamic model for a M-60 battle tank where the dynamic track loads are modelled in view of four different track tensioning effects: global track tension, drive-sprocket induced track tension, track bridging effects, and tension due to track compensating linkage. The global track tension computed from change in the overall track length was found to cause substantial change in the vehicle dynamic response. McCullough et al.[19] utilized the concept of superelemnt representation to model a tracked vehicle, where the track tensioning effects were represented through catenary equations, track-wheel-ground forces, track connectivity

and bridging. Creighton [21] further enhanced the model developed by Murphy et al. [4] to include the height of the vehicle and horizontal force effects, where the interaction of inclined track feelers with rigid terrain profile was also improved. Dhir [28] presented four different track models of varying complexities employed in conjunction with an in-plane ride dynamic model of a tracked vehicle. In the first three track models, the dynamic track load is evaluated as an overall track tension, assuming the track as a continuous elastic belt, whose longitudinal extensibility is defined by a linear spring constant. The final track model is similar to that proposed earlier by Rakheja et al. [23], where the track loads are conceived as local tensioning effects generated by equivalent linear vertical springs interconnecting the adjacent wheel pairs.

All the above studies have concluded that dynamics of the tracked vehicle is strongly influenced by the dynamic track terrain. The dynamics derived on the basis of overall track terrain results in better correlation with the measured data. In this study, the track dynamics is thus incorporated through analysis of the overall tension of the continuous elastic track employed in snow vehicles. The dynamic wheel-track-terrain interactions are represented by integrating: (i) the wheel/track-terrain interactions to account for the ground normal force (net foot-print force) which is transferred to the wheel through the underlying track; and (ii) the dynamic track tensioning effects to account for the dynamic track load which is transferred to the wheel stations and the sprocket based on the geometric considerations of track segments around wheels and terrain profile. The net foot-print forces and dynamic track loads are derived in the following sub-sections.

2.9.1 Road Wheel Forces

Most commonly used wheel model is the "point-contact" model, which replaces the wheel by an equivalent vertical spring and damper assuming a single ground contact point directly beneath the wheel center [22]. The point contact modeling approach for such road wheels, generally, provides an over-estimate of the vertical ground force due to lack of ground-enveloping and does not adequately model the horizontal ground force [22]. The wheel model used in this study is based on the concept of a continuous ring of radial springs uniformly distributed over an adaptive wheel-ground footprint, and an equivalent damper[24]. The road wheel and the underlying track, however, are combined to form an equivalent elastic interface.

The road wheel-terrain interaction is represented by a radially distributed continuous spring taking into account the stiffness of the road wheel and the track, as shown in Figure 2.13. An equivalent damper is incorporated to account for the dissipative characteristics of the wheel and the track. Consider a differential element of the road wheel/track-terrain contact, shown in Figure 2.14, which represents a radial force dF_w,
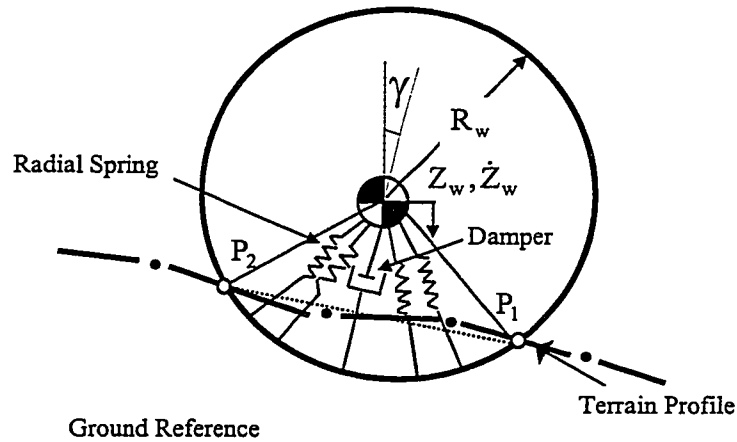
Figure 2.13: Analytical model for road wheel/track-terrain interactions.
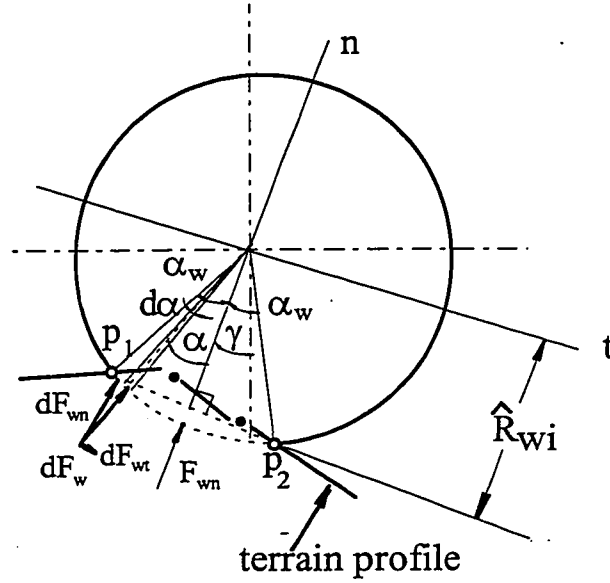
Figure 2.14: Deflection of an element of the road wheel in the
wheel-terrain contact patch.

applied at an angle α_i corresponding to the elemental radial deflection δ_i, due to

interaction with the undeformable terrain.

The element force is developed by radial deflection of the road wheel and the

track in the vicinity of the contact point. The radial spring force is then derived from

equivalent radial stiffness of the road wheel-track-ground interface in the following

manner:

$$dF_w = (K_w d\alpha)\delta_i \qquad (2.27)$$

where K_w is the equivalent spring constant derived from the radial spring constants of

the road wheel, K_{rw}, and the track, K_t:

$$K_w = \frac{K_{rw} K_t}{K_{rw} + K_t} \qquad (2.28)$$

Assuming an idealized wheel deflection characterized by a straight line joining the first and last wheel-terrain contact points on the lower wheel circumference ($\overline{P_1 P_2}$), the radial deflection δ_i of the element can be conveniently expressed as:

$$\delta_i = R_w - \frac{\hat{R}_{wi}}{\cos\alpha_i} \tag{2.29}$$

where $\hat{R}_{wi}$ is the deflected wheel radius around the element i. The normal and tangential components of the radial spring force are given as:

$$\begin{aligned} dF_{wn} &= dF_w \cos\alpha_i \\ dF_{wt} &= dF_w \sin\alpha_i \end{aligned} \tag{2.30}$$

Upon combining equations (2.27) to (2.30), and integrating over the entire contact patch $(-\alpha_w, \alpha_w)$, the resultant normal component of road wheel force can be expressed as:

$$F_{wn} = 2K_w R_w (\sin\alpha_w - \alpha_w \cos\alpha_w) \tag{2.31}$$

where α_w is one-half of the wheel-terrain contact patch, given as:

$$\alpha_w = \cos^{-1}\left(\frac{\hat{R}_w}{R_w}\right) \tag{2.32}$$

The radial spring constant, K_w, is established by measuring the static deflection of the wheel center, δ_w, on a flat ground due to the vertical static wheel load, P, as shown in Figure 2.15. Using equation (2.31):

$$K_w = \frac{P}{2R_w [\sin\alpha_{ws} - \alpha_{ws} \cos\alpha_{ws}]} \tag{2.33}$$
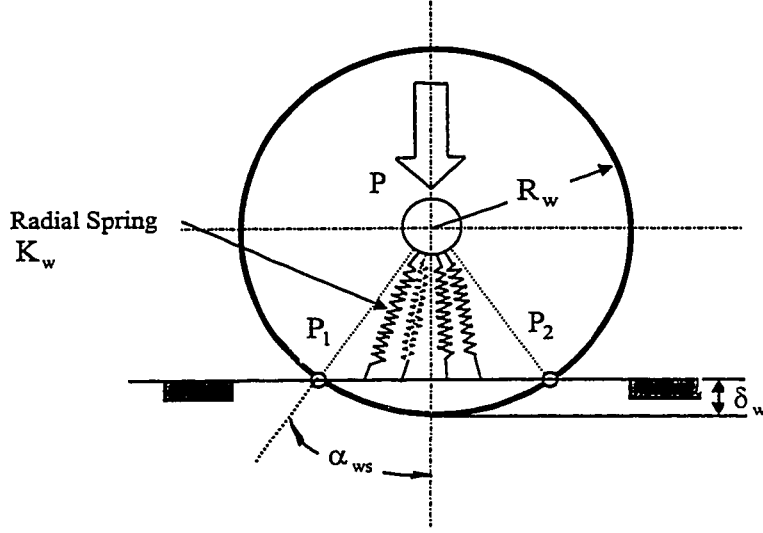
Figure 2.15: Road wheel deformation under a static force.

where α_{ws} is given as:

$$\alpha_{ws} = \cos^{-1}[\frac{R_w - \delta_w}{R_w}] \qquad (2.34)$$

The net tangential component of the road wheel-track force, however, is equal to zero due to assumed equilateral construction of the contact patch triangle, as shown in Figure 2.14. The normal component of the dissipative force developed by the interface can be derived as a function of the terrain-imposed vertical velocity input at the mid-point of wheel-terrain contact patch, which may be expressed as:

$$\dot{z} = V_x \tan\gamma \qquad (2.35)$$

where V_x is forward velocity of the vehicle, and term $\tan\gamma$ describes slope of terrain profile at the mid-point of contact patch. The wheel damping force is expressed as $F_{dw}^i = f(\dot{r}_{wi})$, where normal relative velocity, $\dot{r}_{wi}$, is given by:

$$\dot{r}_{wi} = (\dot{z} + \dot{z}_w)\cos\gamma + \dot{x}_w \sin\gamma = V_x \sin\gamma + \dot{z}_w \cos\gamma + \dot{x}_w \sin\gamma \qquad (2.36)$$

$\dot{x}_w$ and $\dot{z}_w$ are the longitudinal and vertical velocities of the wheel center, respectively. The total normal force developed at the wheel/track-ground interface can thus be expressed as:

$$F_{wn} = 2K_{rw}R_w(\sin\alpha_w - \alpha_w\cos\alpha_w) + F_{dw} \qquad (2.37)$$

2.9.2 Sprocket and Wheel-Track-Terrain Interaction

The drive sprocket of the vehicle, in-general, is subject to forces arising from track enveloping and tensioning effects. Under rough roads and excessive pitch motion of the vehicle, the sprocket can interact with the terrain. The sprocket may thus encounter forces arising from the track-terrain interactions, as shown in Figure 2.16. The horizontal (F_{hx}) and vertical (F_{hz}) forces acting at the drive sprocket can be derived from the track tension (T_{tr}) and the track-terrain interaction (F_{hn}):

$$F_{hz} = F_{hn}\cos\gamma_h - T_{tr}\sin\varepsilon_1^1 \qquad -$$

$$F_{hx} = F_{hn}\sin\gamma_h + T_{tr}(1 + \cos\varepsilon_1^1) \qquad (2.38)$$

where F_{hn} is the normal force acting at the center of the sprocket/track-terrain contact patch, represented by $\overline{P_1P_2}$. T_{tr} is the track tension, derived in section 2.9.3 and ε_1^1 is the instantaneous angle of the track leaving the sprocket with respect to fixed horizontal axis. The normal contact patch force is derived using the formulation presented in Equation (2.37). where the radial contact patch is described by $2\alpha_h$.

The vertical and horizontal components of forces acting on a road wheel and arising from the wheel-track-terrain interactions can be derived in a similar manner. The
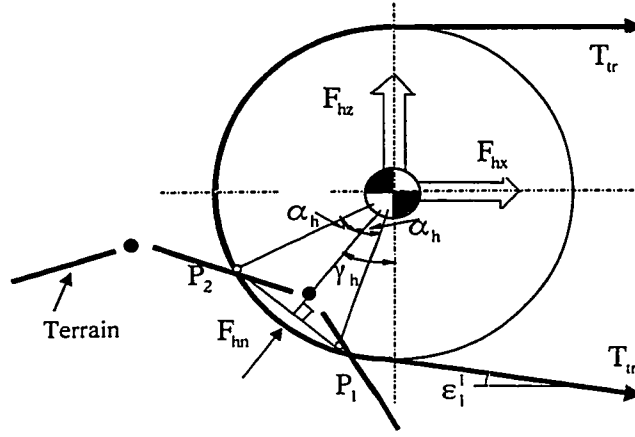
Figure 2.16: Forces acting on the drive sprocket.

first road wheel is subject to track tension T_{tr}, as shown in Figure 2.17. The road wheel is

further subject to forces arising from radial deformation of the track and wheel, F_{wn}, and

the trailing arm. While the trailing arm force is described in section 2.6.1, the normal

force from the contact patch can be derived using equation (2.37). The resultant

horizontal and vertical forces acting on the wheel can be expressed in the following

manner:

$$F_{wz}^1 = F_{wn}^1 \cos\gamma_{w1} + T_{tr}(\sin\varepsilon_1^2 + \sin\varepsilon_2^2)$$

$$F_{wx}^1 = F_{wn}^1 \sin\gamma_{w1} + T_{tr}(-\cos\varepsilon_2^2 - \cos\varepsilon_1^2) \qquad (2.39)$$

where T_{tr} is instantaneous track tension, and ε_1^2 and ε_2^2 are instantaneous angles of the

track in the leading and trailing edges of the contact patch, respectively, with respect to

the fixed horizontal axis. $2\alpha_{w1}$ describes the total radial contact patch of the road wheel

and the track in contact with the terrain.

The horizontal and vertical components of the forces acting on the two rear road

wheels are derived in a similar manner (Figure 2.18) and expressed as:
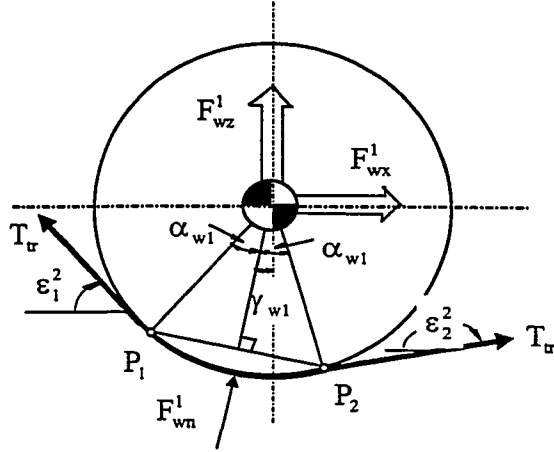
Figure 2.17: Forces acting on first road wheel.

$$F_{wz}^2 = F_{wn}^2 \cos\gamma_{w2} + T_{tr}(\sin\varepsilon_1^3 + \sin\varepsilon_2^3)$$

$$F_{wx}^2 = F_{wn}^2 \sin\gamma_{w2} + T_{tr}(-\cos\varepsilon_1^3 - \cos\varepsilon_2^3) \qquad (2.40)$$

$$F_{wz}^3 = F_{wn}^3 \cos\gamma_{w3} + T_{tr}\sin\varepsilon_1^4$$

$$F_{wx}^3 = F_{wn}^3 \sin\gamma_{w3} + T_{tr}(-\cos\varepsilon_1^4 - 1) \qquad (2.41)$$

where ε_1^3 and ε_2^3 are the instantaneous angles of the track in the leading and trailing edges, respectively, of the contact patch of the second road wheel, with respect to the fixed horizontal axis. ε_1^4 is the angle of the track at the leading edge of the contact patch of the last road wheel.

2.9.3 Wheel-Terrain Contact Patch

The computation of the net foot print force described in Equation (2.31) necessitates the determination of wheel-terrain contact patch. The total contact patch angle, β, can be derived from the coordinates of the terrain and line of contact $\overline{P_1 P_2}$, as
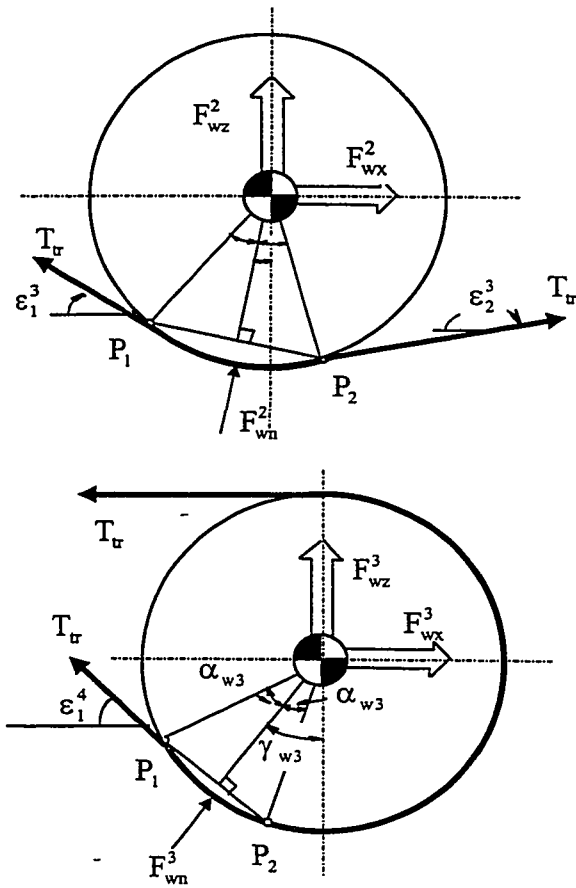
Figure 2.18: Forces acting on the rear road wheel.
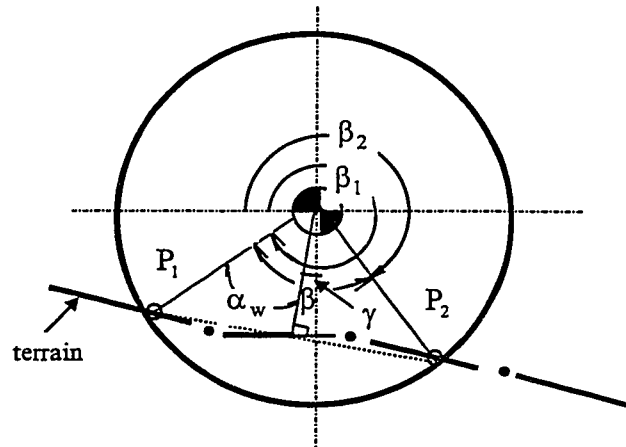
Figure 2.19: Wheel-terrain contact patch.

shown in Figure 2.19. Let β_{1i} and β_{2i} define the angles between the extreme contact

points P_1 and P_2, respectively, such that $\beta_i = \beta_{1i} - \beta_{2i}$, and

$$\beta_{1i} = \tan^{-1}((Y_1 - Y_w)/(X_1 - X_w)) \text{ and } \beta_{2i} = \tan^{-1}((Y_2 - Y_w)/(X_2 - X_w)) \quad (2.42)$$

where (X_w, Y_w), (X_1, Y_1) and (X_2, Y_2) represent the instantaneous coordinates of the

wheel center, noting that $\beta = 2\alpha_{wi}$, the angle of the mid-point of the contact patch, γ_i,

can be derived from:

$$\gamma_i = \beta_{2i} + \alpha_{wi} - 1.5\pi \quad (2.43)$$

2.9.4 Track Model

The snowplow vehicles are equipped with a rubber track, which can be modeled

as a continuous belt loop capable of transmitting static and dynamic tensile loads with

appropriate consideration of the kinematic constraints, track sag and appropriate wheel-

track connectivity. The track bridging or support as seen by the road wheels is modeled

considering appropriate track inclination angles around the road wheels, which are

described in the previous subsection. As shown in Figure 2.20, the track bridging around

the intermediate road wheels may be considered negligible when traversing on a flat

surface.

The dynamic track loads imposed on the road, primarily arise from the track pre-

tension and track belt extensibility. Assuming linear elastic properties of the track, the

track tension can be derived from its instantaneous length:
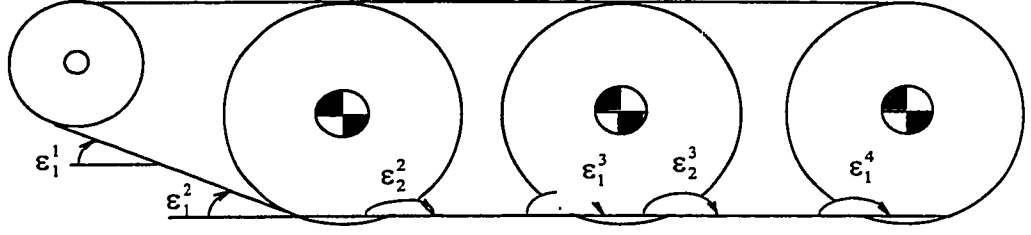
Figure 2.20: Orientation of the track and its bridging.

$$T_{tr} = \begin{cases} K_{tr}(L_{tr} - L_{tr}^0); & L_{tr} - L_{tr}^0 > 0 \\ 0 & ; L_{tr} - L_{tr}^0 \leq 0 \end{cases} \qquad (2.44)$$

where T_{tr} represents the track tension. L_{tr} is the instantaneous track length and L_{tr}^0 is the free length of the track. K_{tr} is the longitudinal stiffness coefficient characterizing the track extensibility. The track pre-tension T_{tr}^0 is computed from the track stiffness and initially installed length of the track (L_s) :

$$T_{tr}^0 = K_{tr}(L_s - L_{tr}^0) \qquad (2.45)$$

The total track length, which varies with the terrain profile, overall geometry, and coordinates of the road wheels and the hull. Referring to Figure 2.21, the instantaneous length of the track can be computed from:

$$L_{tr} = \sum_{i=1}^{3} \phi_i R_{wi} + \phi_h R_h + L_h + \sum_{j=1}^{3} L_j \qquad (2.46)$$

where L_j (j=1,2,3) are the length of track segments between the sprocket and first road wheel, and between the consecutive road wheels. The components $\phi_i R_{wi}$ and $R_h \phi_h$ represent the track wrap around the road wheel i, and the sprocket, respectively. L_h is the length of the track segment supported between drive sprocket and the third road wheel.

The track wrap angles ϕ_i and ϕ_h, track segment L_j and L_h are derived in the following section.
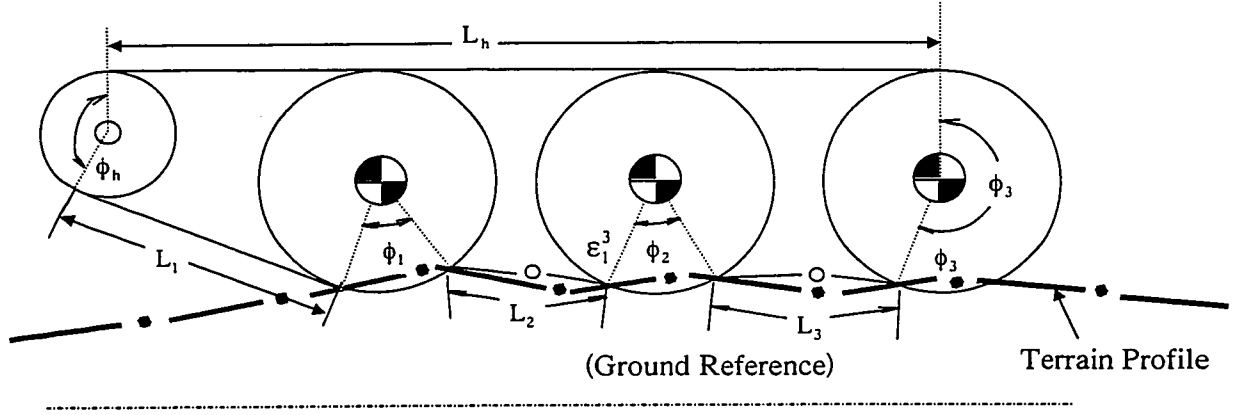
Figure 2.21: Dynamic track terrain interactions, and track wrap around
the sprocket and the road wheels.

Track Wrap Around i^{th} Road Wheel

The track wrap angle, ϕ_i, around i^{th} road wheel is assumed to be either equal to :

(i) β_i, the contact patch angle, for the road wheel in contact with terrain, as described in section 2.9.3 and illustrated in Figure 2.22, or

(ii) η_i, the angle defined by the track-wheel tangency points (P_1^T and P_2^T), when the road wheel lose contact with the terrain, as shown in Figure 2.23, given by:

$$\eta_i = \tan^{-1}((Y_2^T - Y_{wi}) / (X_2^T - X_{wi})) - \tan^{-1}((Y_1^T - Y_{wi}) / (X_1^T - X_{wi})) \qquad (2.47)$$

where, $P_1^T (X_1^T, Y_1^T)$ and $P_2^T (X_2^T, Y_2^T)$ are coordinates of leading and trailing tangency points, respectively.

The track-wheel tangency points are computed as the contact points of a line tangent to two given circles, whose center coordinates and radii are known. For front

road wheel in contact with the terrain, the coordinates of leading tangent point may need certain correction due to different height of the sprocket and the road wheel. The horizontal coordinates of wheel-terrain contact point X_l, and corresponding track-wheel tangency point X_l^T are analyzed to compute the correct track wrap angle, and/or to re-establish the correct point from which the track feeler is tangent to the sprocket. For instance, Figures 2.24 and Figure 2.25 illustrate two such situations, where the track wrap angle differs from that of the track inclination. Figure 2.24 shows that the track wrap angle around the front road wheel ϕ_l is equal to the wheel-terrain contact patch angle β_l. The front track feeler horizontal inclination is thus re-established based on the tangent line from $P_l(X_l, Y_l)$ to trailing contact point at the sprocket. Figure 2.25 shows a situation, where horizontal inclination of the track feeler is unchanged, while, the track wrap angle around the front road wheel ϕ_l is larger than the wheel-terrain contact patch angle β_l. The track wrap angle is thus computed as:

$$\phi_l = \beta_l - \tan^{-1}(Y_l^T - Y_l, X_l^T - X_l)$$ (2.48)

where, β is computed as given in equation (2.42).

Track Wrap Around the Sprocket

The track wrap angle, ϕ_h, around the sprocket is computed as:

$$\phi_h = \pi + \theta$$ (2.49)

where, θ is the horizontal inclination of the track feeler tangent to the sprocket which is derived from its horizontal inclination in conjunction with the connection illustrated in Figure 2.24.
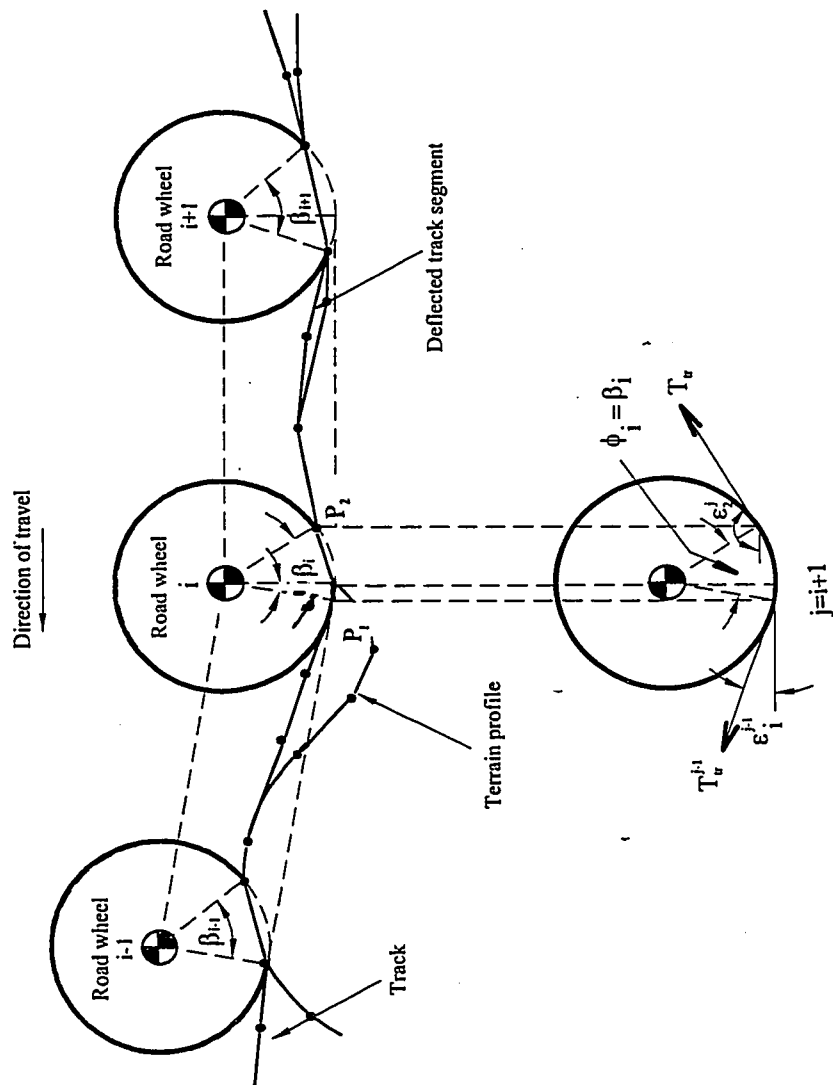
Figure 2.22: Orientation of the track for road wheels in contact with the terrain.

73
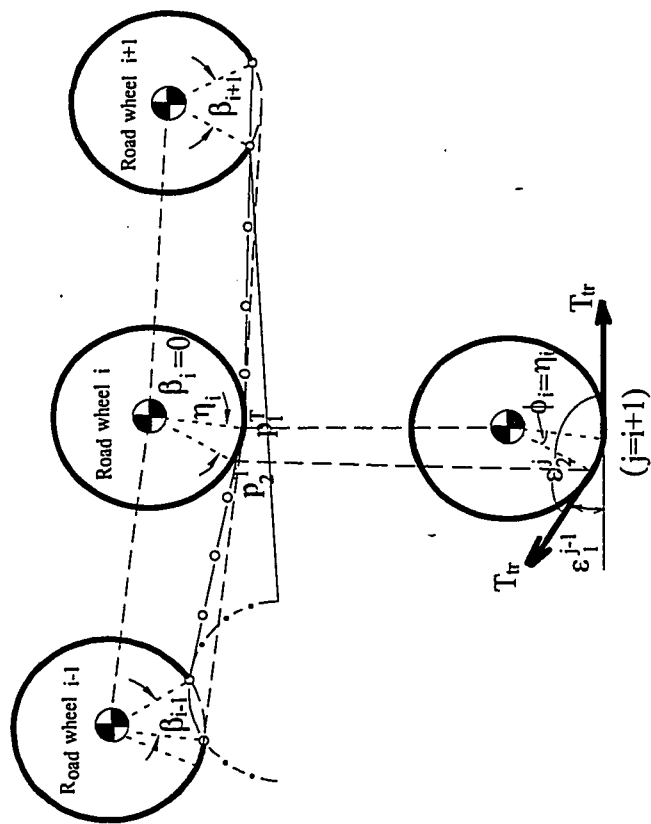
Figure 2.23: Coordinates of tangency points under loss of contact between road wheel and the terrain.

Track Segmental Lengths

L_h is the length of the track segment supported between drive sprocket and the third road wheel, which is assumed to be equal to $X_{w3} - X_h$, assuming relatively small inclination of the track segment.

Track-Terrain Contact Patch

The track-terrain contact patch represents the deflection of a track segment between adjacent wheels due to interactions with the non-deformable terrain profile, as illustrated in Figure 2.26. L_j is the resulting length of the jth track segment as it conforms or adapts to the local shape of the terrain profile. Consequently, each track segment (track feeler: $j=1$; between road wheels: $j=2,3$) is checked for deflection resulting from interactions with terrain profile. A computational procedure is devised to establish the lengths of deflected or stretched track segments:

(i)   As shown in Figure 2.27, the jth undeflected track segment spanning between $P_2(X_2^i, Y_2^i)$ and $P_1(X_1^{i+1}, Y_1^{i+1})$ is derived from the coordinates of the terrain profile and the track-tangent points, and the tangent feeler. The equation of the tangent line joining P_2^i and P_1^{i+1} can be expressed as:

$$\overline{Y}_{j\ell} = Y_2^i + m_j(X_2^i - \overline{X}_{j\ell}) ; \quad m_j = \frac{Y_1^{i+1} - Y_2^i}{X_1^{i+1} - X_2^i} \tag{2.50}$$

where $(\overline{X}_{j\ell}, \overline{Y}_{j\ell})$ are the coordinates of projections of the terrain profile points on the tangent line, where $l=M+1$, and M is the number of terrain profile segments, fully or partially covered within the segment, $j=2,3$. It should be noted that $\overline{X}_{j\ell} = X_{p\ell}$, where $X_{p\ell}$

75
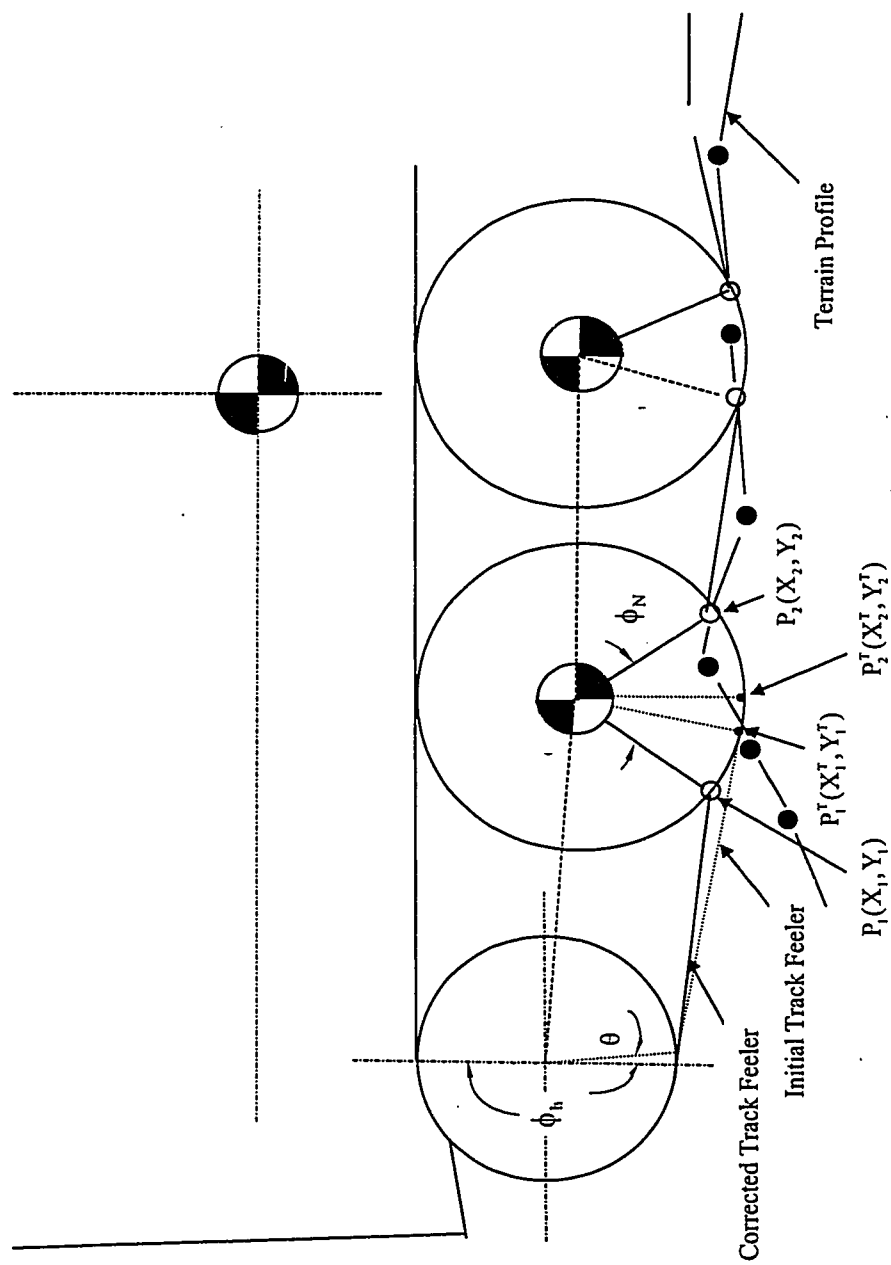
Figure 2.24: Corrected track feeler.

76
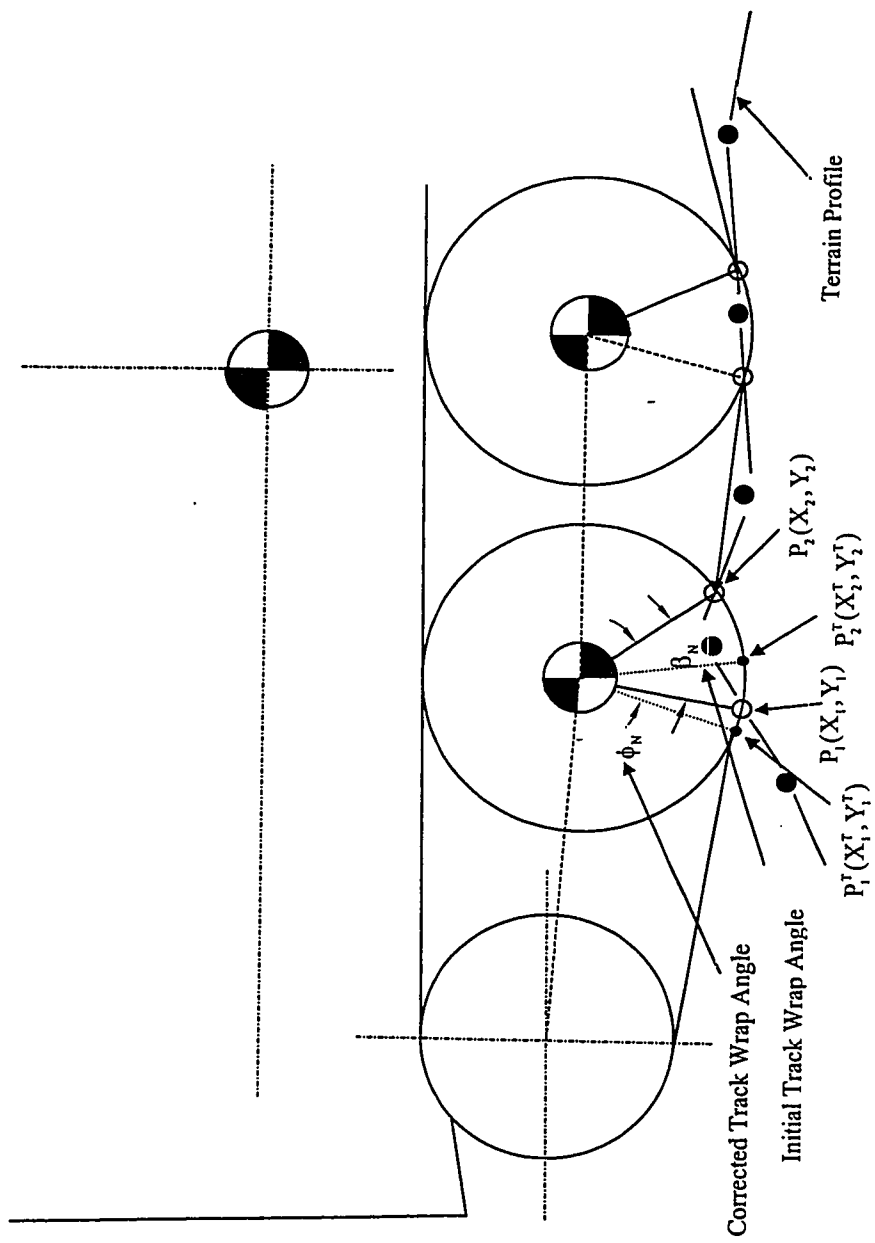
Figure 2.25: Corrected track wrap angle.

77

is the horizontal coordinate of the terrain profile points considered. The coordinates of the terrain profile including those of the wheel-track contact points are given as:

$$X_{p\ell} = \begin{cases} X_2^i \\ X_{s\ell} \\ X_\ell^i \end{cases} ; \quad Y_{pl} = \begin{cases} Y_2^i; & \ell = 1 \\ Y_{si}; & \ell = 2,...,M \\ Y_1^{i+1}; & \ell = M+1 \end{cases} \tag{2.51}$$

where $(X_{s\ell}, Y_{s\ell})$ are coordinates of the terrain profile within the segment, as defined in the lookup table.

(ii) The shape of the deflected track is determined by comparing the elevations of the tangent track $(\overline{Y}_{j\ell}, \ell = 2,...M)$ with those of the terrain profile $(Y_{p\ell})$ at respective horizontal locations $(\overline{X}_{j\ell})$. Let $Y_{j\ell}$ denote the elevations of points along the deflected track, such that

$$Y_{j\ell} = \begin{cases} Y_{p\ell}; & \text{for } (Y_{p1} - Y_{j1}) > 0; \ell = 2, ..., M \\ \overline{Y}_{j\ell} & ; \text{otherwise} \end{cases} \tag{2.52}$$

(iii) The maximum deviation between the actual and tangent tracks $(Y_{p\ell} \text{ and } \overline{Y}_{j\ell})$ along a direction normal to the tangent line is further determined as:

$$h_{max} = Max[(Y_{p1} - Y_{j1})\cos(\alpha_j)] \tag{2.53}$$

where, $\tan \alpha_j = m_j$, the slope of the tangent track.

The slopes of the lines joining the highest elevation point to the wheel-track contact points are then derived as:

$$m_2^i = \frac{Y_{jm} - Y_2^i}{\overline{X}_{jm} - X_2^i}; \quad m_1^{i+1} = \frac{Y_1^{i+1} - Y_{jm}}{X_1^{i+1} - \overline{X}_{jm}} \tag{2.54}$$
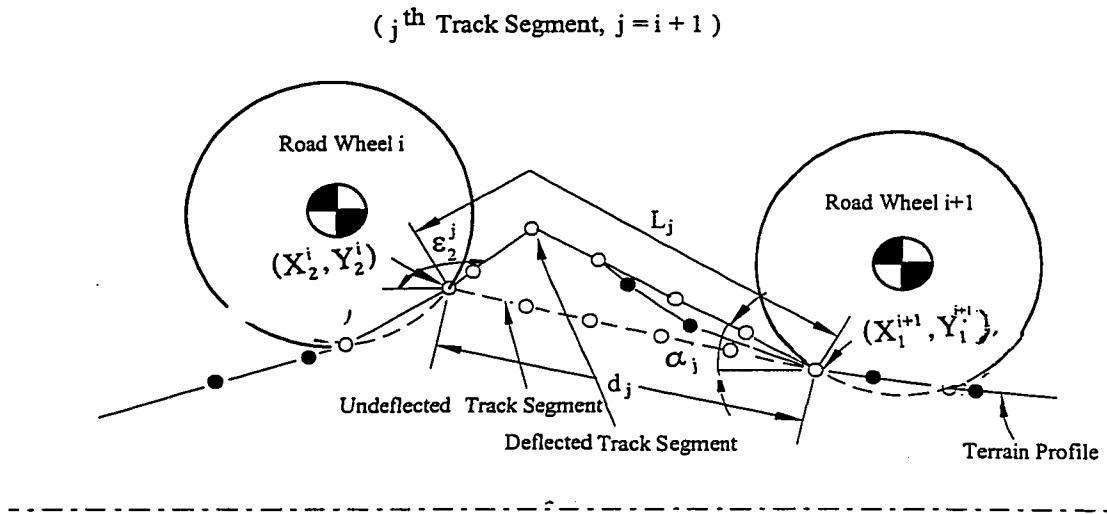
Figure 2.26: Track-terrain contact patch.

Maximum Deviation @ $[(Y_{p\ell} - Y_{j\ell}) \cos \alpha_j]_{\ell=m}$
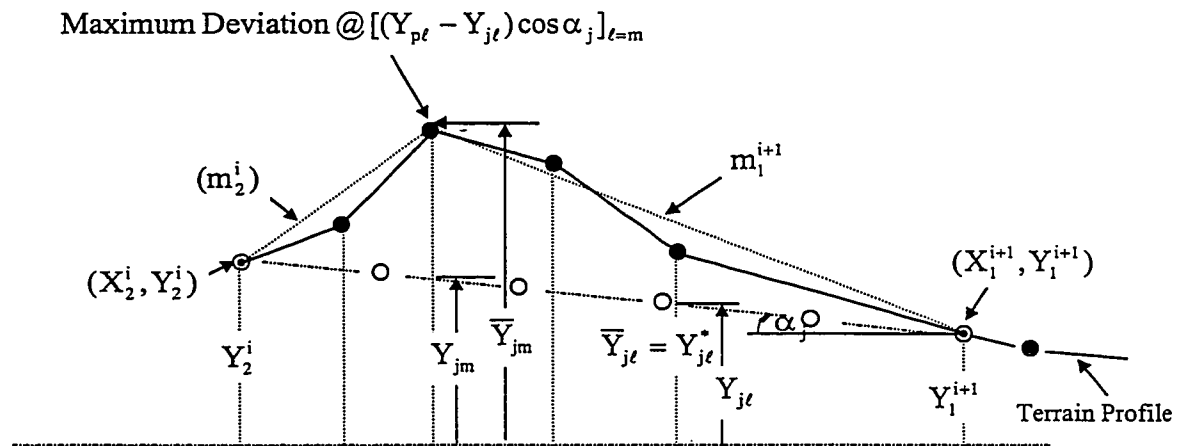
Figure 2.27: Determination of deflected/stretched track segment.

79

where, m_2^i and m_1^{i+1} are the slopes of lines jointing the highest elevation point to the ith and 'i+1' wheel contact points, respectively. Y_{jm}^* defines the elevation of the highest track-terrain contact point, and $\overline{X}_{jm}$ is the corresponding horizontal coordinate.

(iv)   Final step is to shift the vertical coordinates of the deflected track segment ($Y_{j\ell}^*$ in equation 2.52) such that a more accurate shape of the stretched track segment is obtained. It is carried out by computing the vertical coordinates of the sloped track (on each side of the maximum elevation point) at every specified horizontal location ($\overline{X}_{j1}$), and comparing it with corresponding terrain profile elevation. Consequently, vertical coordinates of the stretched track segment $Y_{j\ell}^*$ are defined as:

$$
Y_{j\ell}^* = \begin{cases} \begin{cases} Y_{j\ell} & ; \text{if } [Y_{p\ell} - (Y_2^i + m_2^i(\overline{X}_{j\ell} - X_2^i))] > 0 \\ Y_2^{i+1} + m_j^i(\overline{X}_{j1} - X_2^{i+1}); \text{if } [Y_{p\ell} - (Y_2^i + m_2^i(\overline{X}_{j\ell} - X_2^i))] < 0 \end{cases} & ; 2 \le \ell \le (m-1) \\ Y_{jm} & ; 1 = m \\ \begin{cases} Y_{j\ell} & ; \text{if } [Y_{p\ell} - (Y_1^{i+1} + m_1^{i+1}(\overline{X}_{j\ell} - X_1^{i+1}))] > 0 \\ Y_1^{i+1} + m_1^{i+1}(\overline{X}_{j\ell} - X_1^{i+1}); \text{if } [Y_{p\ell} - (Y_1^{i+1} + m_1^{i+1}(\overline{X}_{j\ell} - X_1^{i+1}))] < 0 \end{cases} & ; m+1 \le \ell \le M \end{cases}
$$

$$(2.55)$$

$$
Y_{j\ell}^* = \begin{cases} Y_1^{i+1} & ; \ell = M+1 \\ Y_2^i & ; \ell = 1 \end{cases}
$$

$$(2.56)$$

The total length of the stretched track segment is, then, obtained as:

$$
L_j = \sum_{\ell=1}^{M} [(\overline{X}_{j1+1} - \overline{X}_{j1})^2 + (Y_{j\ell+1}^* - Y_{j\ell}^*)^2]^{1/2}
$$

$$(2.57)$$

and horizontal inclinations of the deflected track segment at its both ends ($\varepsilon_1^j, \varepsilon_2^j$) are computed as:

$$\varepsilon_1^j = \tan^{-1}(Y_2^i - Y_{jm}^\bullet, X_2^i - \overline{X}_{jm}^\bullet)$$
$$\varepsilon_2^j = \tan^{-1}(Y_{jm}^\bullet - Y_1^{i+1}, \overline{X}_{jm} - X_1^{i+1})$$

<div align="right">(2.58)</div>

2.10 Summary

In this chapter, a mathematical model of a snowplow vehicle is developed to study its ride dynamic performance. The nonlinear 12-degrees-of-freedom in-plane ride dynamic model is formulated assuming constant forward speed and non-deformable arbitrary terrain profile. The highlights of the mathematical model include considerations of the biodynamic behavior of the nonlinear seat-suspension model, flexride and trailing arm road wheel suspension model, and an adaptive wheel-track-terrain interaction. In the following chapter, the excitations arising from road roughness and plowing tasks are characterized and analyses are performed to demonstrate the validity of the vehicle model.

CHAPTER 3

RESPONSE EVALUATIONS OF THE VEHICLE MODEL

3.1   INTRODUCTION

The nonlinear differential equations of motion developed for the 12-DOF model of the tracked snowplow are solved for excitations arising from the road surface and snowplowing. The evaluation of ride vibration response of the vehicle necessitates characterization of vehicle components and realistic input arising from the road roughness and the snowplowing. The performance characteristics of the track and suspension systems can be further enhanced through identification of various natural frequencies and associated modes of vibration. Since the driver is sensitive to both the magnitude and frequency of whole-body vibration, a knowledge of resonant frequencies can facilitate the assessment and appropriate tuning of the suspension system. In this chapter, deterministic and random undeformable ground profiles are discussed to derive the ride vibration response of the vehicle in terms of both the predominant frequencies and magnitudes. An analytical model of the snow and the blade is further developed to derive an estimate of push forces acting on the blade as a function of the snow depth and density. The analytical model is further evaluated for realistic road excitations and the response characteristics are compared with the field measured data to demonstrate validity of the proposed model.

3.2   ANALYTICAL METHODS

In general, two methods are available for analyzing the vehicle model developed

in Chapter 2, namely: frequency-domain method and time-domain method. The frequency-domain analysis utilizes Fourier transforms to represent the time dependent variables as frequency dependent variables. The time-domain analysis utilizes variables as functions of time and uses numerical integration algorithms to solve the differential equations of motion. In comparison, the frequency-domain technique reduces simulation time considerably as compared to the time domain analysis, and hence it is a convenient and economical option. However, the frequency-domain method is only suited for simulating vehicle ride models described through linear or linearized equations of motion. Consequently, one has to make a number of simplifying assumptions in the formulation of the ride model. Furthermore, majority of the proposed ride comfort assessment criteria describe the limits and methods based upon frequency spectra of the ride vibration [44-48]. The frequency-domain techniques have thus been widely used to study the ride dynamic behavior of road and off-road vehicles.

In this study, the ride dynamic simulation model subject to random irregular terrain excitations is formulated considering the non-linear dynamic wheel-track-terrain and blade-snow interactions. The analytical model thus leads to complex formulations, which may be characterized through a set of nonlinear coupled differential equations and solved in the time-domain using a direct integration technique.

3.3 CHARACTERIZATION OF SUSPENSION COMPONENTS

The validity of an analytical model is strongly dependent upon the appropriate characterization of various components or subsystem. The weights and dimensional data, supplied by the manufacturer [56], is thus thoroughly reviewed to identify various vehicle

parameters related to sprung and unsprung masses, geometry, and mass moments of inertia. The static and dynamic characteristics of the suspension and track are identified from the manufacturer data, test data available at Concave Research Center, and various published studies [51]. The properties of the seat-suspension components, including: cushion stiffness (K_c) and damping coefficient (C_c), suspension spring rate (K_s), coulombs friction (F_f), damping constants (C_A, C_B, V_s), bump stop stiffness (K_{st}) and the permissible travel (2B) are identified from the test data available at Concave [51]. The driver parameters $(m_o, m_1, K_1$ and $C_1)$ are identified from the seated driver model reported by Griffin [48]. The parameters for the driver and seat-suspension models are summarized in Table 3.1.

The properties of the cab mounts $(K^i_{cx}, K^i_{cz}, C^i_{cx}, K^i_{cz})$ are identified from the measured force-deflection characteristics supplied by Metalastick and Bombardier Inc. [56]. The force-deflection characteristics of elastic mounts, shown in Figure 3.1, exhibit nonlinear behavior when the magnitude of deflection is either extremely low or high. The measured data also reveals nearly constant stiffness in the vicinity of selected preload of 300 lb due to combined mass of the cab, seat and the driver. The radial stiffness properties of the mounts are assumed to be approximately three times the vertical stiffness (K^i_{cz}), while the damping is assumed to be small. The inertial and geometric properties of the cab and elastic properties of the mounts are summarized in Table 3.2.

The geometric and inertial parameters of the vehicle road wheel suspension, track and blade are extracted from the design drawings and specifications supplied by the manufacturer [56,57], and summarized in Tables 3.3 to 3.5.

84

Table 3.1: Parameters of the driver-seat-suspension model [51].

Description	Symbol	Value
Upper human body mass (kg)	m_1	35.1
Stiffness coefficient of upper human body (N/m)	K_1	27951.4
Damping coefficient of upper human body(Ns/m)	C_1	500.1
Lower human body mass (kg)	m_0	14.62
Seat suspension sprung mass (kg)	m_s	15.0
Cushion stiffness coefficient (N/m)	K_c	39375.0
Cushion damping coefficient (Ns/m)	C_c	139.8
Seat suspension stiffness coefficient (N/m)	K_s	5330
Magnitude of Coulomb friction (N)	F_{CD}	15
Bleed damping coefficient (Ns/m)	C_A	790
Blow-off damping coefficient (Ns/m)	C_B	672
Transition velocity (m/s) -	V_s	0.032
Shock absorber inclination angle (deg)	α	70
Spring rate of the upper bump stop (kN/m)	K_{st}^c	120
Spring rate of the lower bump stop (kN/m)	K_{st}^e	75
Clearance between the bump stops (mm)	2B	100
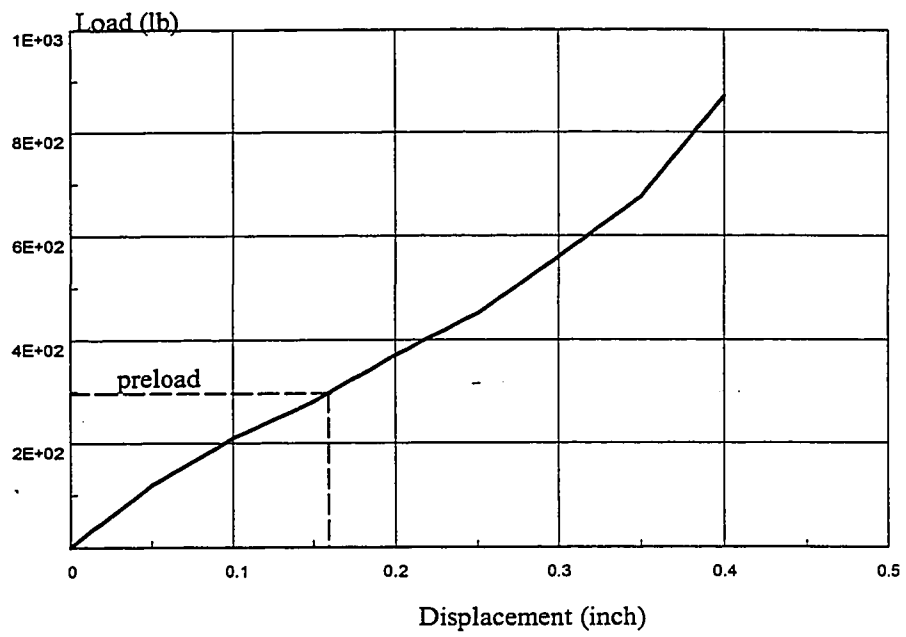
Figure 3.1: Static vertical force-deflection characteristics of elastic cab mounts [56].

Table 3.2: Parameters of the cab and cab mounts [56,57].

Description	Symbol	Value
Cab mass (kg)	m_c	453.6
Pitch mass moment of inertia of cab (kg m^2)	I_{yc}	800
Vertical stiffness coefficient of cab mount (kN/m)	K_{czi}	326.98
Horizontal stiffness coefficient of cab mount (kN/m)	K_{cxi}	980.94
Vertical damping coefficient of cab mount (Ns/m)	C_{czi}	200.0
Horizontal damping coefficient of cab mount (Ns/m)	C_{cxi}	500.0
Distance between cab c.g. and seat base (m)	a_o	0.20
Horizontal distance between rubber mounts (m)	a_c	1.308
Horizontal distance between front mount and cab c.g.	a_{cf}	0.760
Horizontal distance between rear mounts and hull c.g.	a_{co}	0.264
Vertical distance between cab mounts and cab c.g.	b_c	0.47
Vertical distance between cab c.g. and hull c.g.	b_{hc}	0.95

Table 3.3:Parameters of the road wheels and suspension[56,57].

Description	Symbol	Value
Mass moment of inertia of first road wheel arm (kg m^2)	I_{w1}	13.222
Mass moment of inertia of walking beam (kg m^2)	I_{w23}	54.014
Stiffness coefficient of bump stop (kN/m)	K_{bwi}	100.0
Radial stiffness coefficient of road wheel (kN/m/rad)	K_{wi}	612.9
Torsional stiffness coefficient of first road wheel suspension (Nm/rad)	K_{tw1}	9884.28
Damping coefficient of the bump stop (Ns/m)	C_{bw1}	10.0
Torsional damping coefficient of the rubber suspension (Nms/rad)	C_{tw1}	200.0
Damping coefficient of the road wheel (Ns/m/rad)	C_{rw1}	6.67
Radius of road wheel (m)	R_{wi}	0.321
Radial distance between torsion bar center and bump stop (m)	R_{bw1}	0.146
Radius distance between walking beam center and bump stop (m)	R_{bw2} R_{bw3}	0.240 0.118
Length of first road wheel arm (m)	L_{fr}	0.116
Length of the walking beam arms (m)	L_{23f} L_{23r}	0.406 0.324
Horizontal distance between torsion bar center and wheel c.g. (m)	a_{rw1}	0.113
Horizontal distance between second road wheel c.g. and walking beam center (m)	a_{23f}	0.404
Horizontal distance between third road wheel c.g. and walking beam center (m)	a_{23r}	0.323
Vertical distance between torsion bar and wheel c.g. (m)	b_{rw1}	0.0263
Vertical distance between second wheel c.g. and walking beam center (m)	b_{23f}	0.0354
Vertical distance between third wheel c.g. and walking beam center (m)	b_{23r}	0.0282
Angle between the bump stop and first road wheel arm (deg)	β_{w1}	26
Angle between bump stop and front arm of walking beam arms (deg)	β_{w2} β_{w3}	4.6 11.3

Table 3.4: Simulation parameters for the hull and the track [56,57].

Description	Symbol	Value
Hull mass (kg)	m_h	1430.9
Pitch mass moment of inertia (kg m^2)	I_{yh}	5218.5
Horizontal distance between sprocket c.g. and hull c.g.(m)	a_{hf}	1.525
Horizontal distance between walking beam c.g. and hull c.g. (m)	a_{hr}	0.51
Horizontal distance between torsion bar center and hull c.g. (m)	a_{w1}	0.937
Horizontal distance between blade lower mount and hull c.g. (m)	a_{b1}	1.072
Horizontal distance between blade lower mount and hull c.g. (m)	a_{b2}	1.680
Vertical distance between sprocket c.g. and hull c.g. (m)	b_{hf}	0.104
Vertical distance between walking beam c.g. and hull c.g.(m)	b_{hr}	0.160
Vertical distance between torsion bar and hull c.g. (m)	b_{w1}	0.168
Vertical distance between upper mount and hull c.g. (m)	b_{b1}	0.30
Vertical distance between lower mount and hull c.g. (m)	b_{b2}	0.28
Longitudinal stiffness of track (kN/m)	K_{tr}	300.0
Vertical stiffness of track (kN/m)	K_t	1500.0
Initial total track length (m)	L_{tr}^o	5.715
Track pre-tension (kN)	T_{tr}^o	10
Radius of drive sprocket (m)	R_b	0.215

Table 3.5: Simulation parameters for blade assembly [56,57].

Blade mass (kg)	M_B	158.75
Mass moment of inertia (kg m^2)	I_B	166.46
Vertical distance between two mounts (m)	b_b	0.15
Hydraulic actuate inclination angle (deg)	α_b	6.5
Stiffness coefficient of blade contact spring (kN/m)	K_g	300.0
Stiffness coefficient of hydraulic cylinder (kN/m)	K_{cL}	100.0
Horizontal distance between hydraulic actuator mount and pivot (m)	L_{b1}	0.621
Horizontal distance between blade contact point and pivot (m)	L_{b2}	1.646

3.4 CHARACTERIZATION OF INPUTS

Discrete undeformable ground profiles, such as semi-circle obstacles, sinusoidal course, granite blocks, etc., have been used to assess the vibration isolation performance of vehicle suspension and track dynamics. Various researchers have used these ground profiles to evaluate vehicle mobility performance. In most cases, the deterministic ground profiles have been used for assessment of transient response and validation of the analytical models [16-19]. In this study, a semi-circular obstacle is selected to analyze the transient ride response. A sidewalk snowplowing vehicle is subject to inputs arising from the randomly rough side-walks and blade forces when pushing the snow. Although the roughness profiles of sidewalks have not been reported, the roughness of various road surfaces have been extensively reported in the literature. The random road roughness is thus considered in this study to analyze the ride dynamics of the vehicle. The vehicle blade is subject to push forces that may depend upon the depth and density of the snow. The push forces are thus derived using a simplified model based upon the shearing of the snow, and is described in the following subsection.

3.4.1 Semicircle Obstacle

For analysis of the vehicle model presented in Chapter 2, a semicircle obstacle is selected as the deterministic input for transient response analysis as shown in Figure 3.2. The obstacle is characterized by its diameter and height, and excitations at the road wheels are determined from coordinates of the obstacle and the road wheels, vehicle speed and initial vehicle position.

3.4.2 Random Road Description

While many different deterministic inputs have been utilized to evaluate the vehicle mobility and transient ride dynamics, various studies have emphasized the significance of realistic terrain conditions. Numerous studies on mobility performance of tracked vehicle have been carried out for random off-road terrains [15,16]. Wheeler [7] and Hoogterp [9] used elevations of various random terrains to validate analytical models of different vehicles. A bumpy terrain course was established by Wheeler [7] to evaluate the vehicle mobility. The representation of realistic terrain forms an integral part of the studies involving ride dynamic analysis and dynamic wheel-track-terrain interactions. In this section, the random terrain is described and the method to determine the terrain coordinates within each contact patch is presented. The terrain profile is assumed to be non-deformable and is described by linear segments adjoining the horizontal and vertical coordinates of successive points on the profile. Consequently, the measured terrain profile is described through a look-up table containing horizontal and vertical coordinates of successive points, which are equally spaced at a spacing of 0.3m [63]. The intermediate profile points are determined based on linear interpolation assuming a continuous profile.

<u>Wheel-Terrain Contact Point</u>

It is apparent that determination of wheel-terrain contact points, P_1 and P_2, (section 2.9.3) along the lower circumference of a road wheel, is essential for computation of net foot-print force and track wrap around. An effective method is developed for fast and accurate computation of the wheel-terrain contact patch, based on
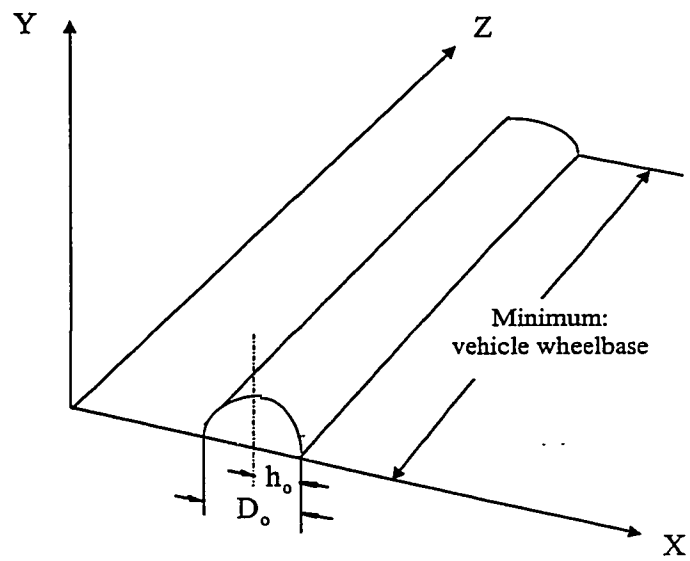
Figure 3.2: Geometry of semicircle
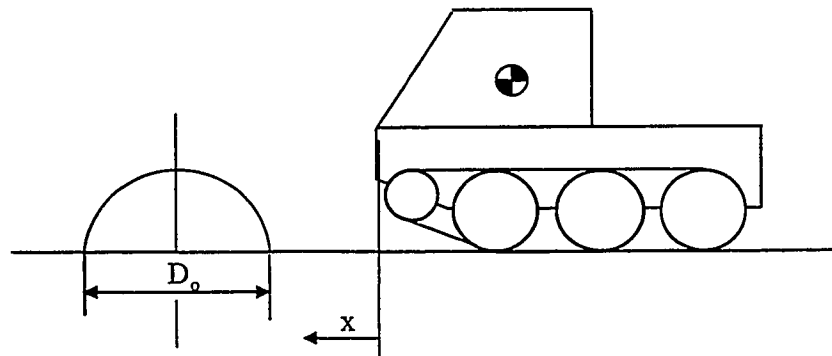
Figure 3.3: Schematic of snowplow vehicle negotiating semicircle obstacle.

the concept of a *circle-line* intersection of a circle, as shown in Figure 3.4. Two consecutive terrain profile points in the vicinity of the intersecting circumference on
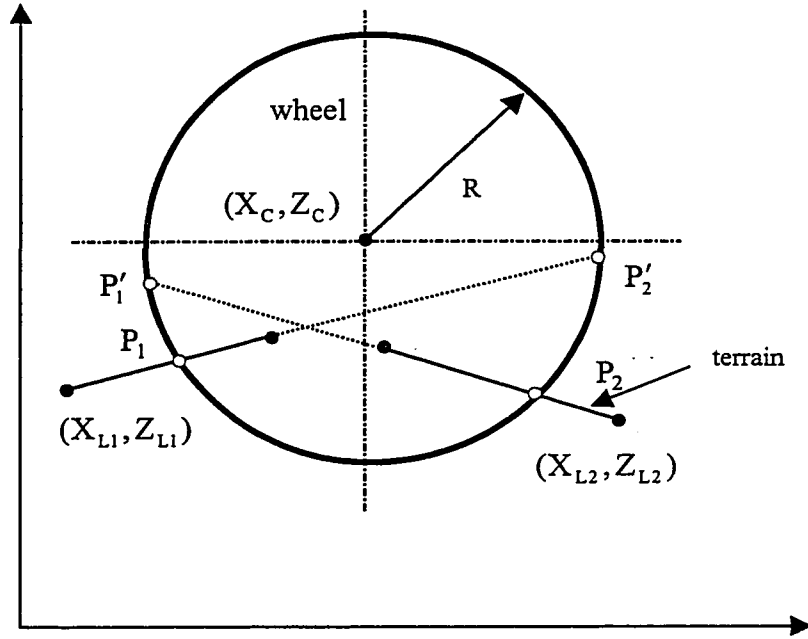
Figure 3.4: Circle-line intersection.

either side of the wheel center are identified to derive the intersection lines $\overline{P_1 P_2'}$ and $\overline{P_2 P_1'}$, as shown in the Figure. The equation of each line can thus be written as:

$$Z_1 = Z_{L1} + m_1(X_1 - X_{L1}); \quad Z_2 = Z_{L2} + m_2(X_2 - X_{L2}) \tag{3.1}$$

where (X_1, Z_1) and (X_2, Z_2) are coordinates of points on the two lines on the left and right-side of the wheel center, respectively. m_1 and m_2 are the slope of the lines $\overline{P_1 P_2'}$ and $\overline{P_2 P_1'}$, respectively. The equation of the circle describing the road wheel can be written as:

$$Z_c = Z_C \pm \sqrt{R^2 - (X_c - X_C)^2} \tag{3.2}$$

where (X_c, Z_c) refer to the coordinates of the intersection points on the circumference. The solution of equations (3.1) and (3.2) yields two values of Z_c, which correspond to elevations of arbitrary points located on upper- and lower-halves of the circumference at a longitudinal location, X_c. Since, the wheel-terrain contact occurs along the lower-half circumference only, the circle equation can be rewritten as:

$$Z_c = Z_C - \sqrt{R^2 - (X_c - X_C)^2} \qquad (3.3)$$

The coordinates of the intersection points, P_1 and P_2, are thus derived as:

$X_1 = X_c$ and $Y_1 = Y_c$.

3.4.3 Characterization of Blade Forces

When the snowplow vehicle is plowing the snow, the blade is subjected to horizontal and vertical forces arising from the plowing task and blade-road contact, respectively. Characterization of such forces poses many complexities due to extensive variations in the properties and depth of snow, speed, road surfaces, etc. While the vertical forces may be estimated assuming a uni-directional elastic contact between the blade and the road surface, the horizontal forces may be estimated through considerations of the plowing action and the nature of snow.

Horizontal Blade Force

Snow is a very complex composite of ice, water and air. The first snowplow force computational model was developed by Croce in Germany shortly before World War II

[58]. This model was based on an assumption that snow could be modeled as a fluid resulting in a Bernoulli type formulation for forces:

$$F = hw\varrho v^2 \qquad (3.4)$$

where F is total force required to plow the snow, h is depth of the snow, w is plow width, ϱ is snow density and v is the forward velocity. The resultant force F is resolved into three components acting along the longitudinal, lateral and vertical directions. It was established that Equation (3.4) yields a poor estimate of the plowing force and Mellor [59] proposed a correction factor C to achieve a better estimate. The resultant force was thus expressed as:

$$F = hw\varrho Cv^2 \qquad (3.5)$$

Kaku [60] developed the snow plowing force model by considering the conservation of momentum assuming that the snow behaves like a fluid. The model proposed that resultant plow force is proportional to square of the velocity, specific weight of the snow and a snow compression coefficient:

$$F = \frac{\gamma S \varepsilon v^2}{g} \qquad (3.6)$$

where γ is specific weight of the snow, S is cross sectional area of the plow, ε is the snow compression coefficient and g is acceleration due to gravity. The experimental studies performed, however, revealed that the snow does not behave like a fluid. Consequently, the proposed model could not provide a reasonable estimate of snow forces over a wide range of conditions. Alternatively, Walter [61] recently proposed a model to estimate the snow pushing force based upon systematic considerations of the compression of the snow. During snowplowing action, the snow may be considered to have four

95
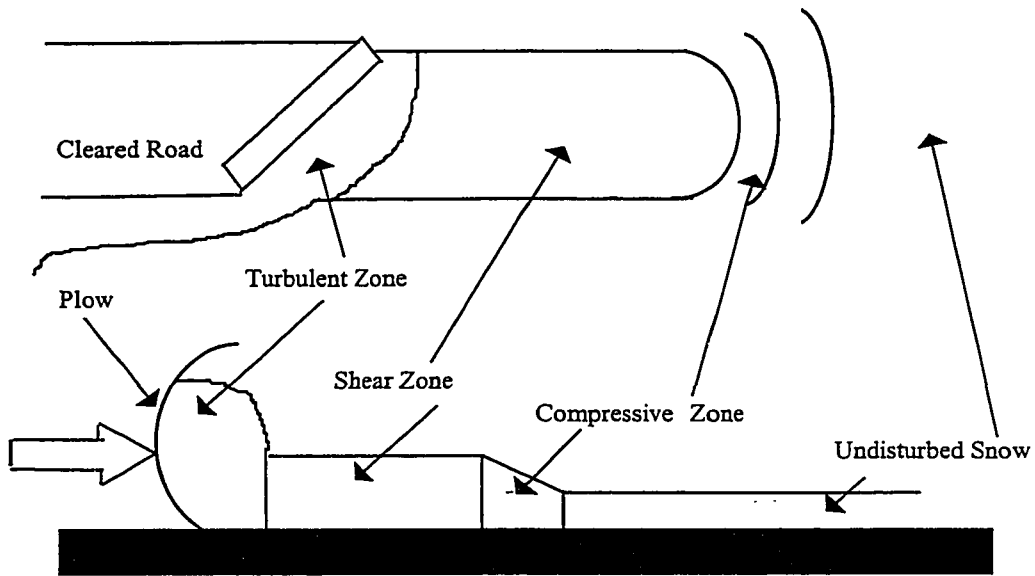
Figure 3.5: A schematic representation of four distinct snow zones
that may be realized during plowing.

distinct zones: turbulent zone, shear zone, compressive zone and undisturbed zone. Figure

3.5 illustrates various snow zones that may be realized during a plowing action.

Furthermore, the plow force depends strongly upon the weight, density and

compressive strength of snow, which may vary considerably. Fresh undisturbed snow

may vary in density from less than 0.09gm/cc to approximately 0.25gm/cc [61]. As the

snow ages in place, the density gradually increases depending on the barometric pressure

and temperature history over the aging period. The compressive strength of the snow also

varies with these factors. Under new fallen conditions the shear strength of the snow is

less than $0.01 kg/cm^2$. The strength increases with aging and variations in density and

temperature. While approximately 65% of the strength variance in snow can be attributed

temperature. While approximately 65% of the strength variance in snow can be attributed to changes in the density, only 20% variation is attributed to changes in the temperature. Assuming a constant temperature of -23.2°C, the following empirical relation describes the compressive strength of the snow [61].:

$$\sigma(\varrho) = \frac{-0.113227}{(-0.5+\varrho)} \tag{3.7}$$

where $\sigma(\varrho)$ is compressive strength and ϱ is density of the snow, which may vary from 0.09gm/cc to 0.4gm/cc. When snow is plowed, several distinct regions of snow are observed, each of which causes forces to be applied to the plow and subsequently to the snowplow frame, as illustrated in Figure 3.6. The undisturbed snow undergoes
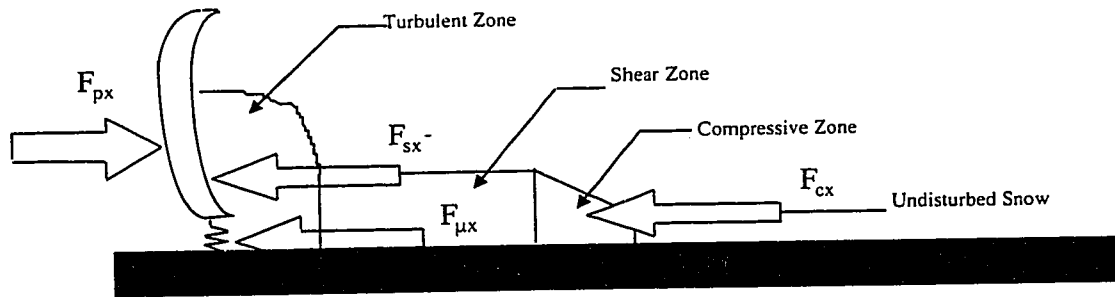
Figure 3.6: The forces developed during plowing action.

compression during the plowing operation, which is referred to as the compressive zone. Moving from the compression zone towards the plow, there is a shear block region in which compressed snow shears away from the undisturbed regions towards the sides. In the shear block region, there is little differential movement of the snow, the block thus moves at velocity equal to that of the plow. As a result, the only forces created are frictional forces at the sides and bottom of the block. It has been estimated that the

frictional forces of the shear are much smaller in magnitude than the compressive force [61]. In the final zone, as the snow reaches the plow, it is lifted by the rake angle of the plow and broken. At the same time snow is rolled over onto the lifted snow and the zone becomes turbulent. The turbulent zone is characterized by complex snow particle motions in which the shear zone block of snow loses its identity. This region is the most difficult to characterize for forces since particle motion is chaotic. Finally, the snow is cast away from the plow at the sides where it approaches rest position.

In the compressive zone, the density of fresh snow is as low as 0.09gm/cc, which increases to approximately 0.35gm/cc during plowing. Most of the compression force developed in this zone is caused by forcing of the air from the snow and by crushing of snow crystals. In this region, the undisturbed snow accelerates from rest to the plow velocity. Force due to compression of the snow, however, is strongly related to increase in snow density over the compression zone. Walter et al. [61] proposed a relation to estimate the pushing force associated with compression of the snow:

$$F_{cx} = \int_0^L hw(\varrho(x)a(x) + \sigma(x))dx \tag{3.8}$$

where F_{cx} is the horizontal force developed in the compressive zone, w is the plow width and h is the snow depth of the compressive zone. ϱ_x is density of the snow particles at a location x from the blade and a(x) is the acceleration. Since the forces developed due to friction in the shear zone are considered to be relatively small, the horizontal force F_s is considered to be equal to F_{cx}.

<u>Vertical Blade Force</u>

As show in Figure 3.6, the vertical blade-road contact force may be estimated assuming a uni-directional elastic contact between the blade and the road surface, such that:

$$F_g = S_w [K_g (Z_h - Z_g - a_{b1}\theta_h - L_{b3}\theta_b]$$ (3.9)

where Z_g is road elevation at the contact location, K_g is stiffness due to elastic contact, and F_g is vertical contact force, which occurs only during plowing operation. It is thus considered as zero during transit, sanding and loading operations. S_w is a nonlinear factor which describes the contact condition, and given by:

$$\begin{cases} S_w = 0; \ \text{if} \ \theta_b L_{b3} - z_h + \theta_h a_{b1} - z_g > 0 \\ S_w = 1; \ \text{if} \ \theta_b L_{b3} - z_h + \theta_h a_{b1} - z_g < 0 \end{cases}$$ (3.10)

3.5   FIELD MEASUREMENT OF VEHICLE VIBRATION

Field measurements were performed on a Bombardier snowplow vehicle comprising a suspended cab, first road wheel suspension, walking beam tandem configuration for the rear wheels, an elastic track and a suspended seat. The snowplow vehicle was instrumented with linear accelerometers, which were oriented to measure the vibration response at the cab floor. The measurements were performed by Institut de recherche en sante et securite du travail (IRSST) du Quebec for different operating conditions, such as plowing and transit operation, while the vehicle speed was selected by the driver.

A total of five accelerometers were installed on the cab floor, as shown in Figure 3.7. Accelerometers, 1, 2 and 3 are installed under the seat and oriented along x, y and z

axes, respectively. The accelerometers 4 and 5 are installed along the z axis in the rear section of the cab. The acceleration signals, acquired from accelerometers 3, 4 and 5 are manipulated to derive the pitch and roll accelerations of the cab, while accelerometers 1, 2 and 3 provide a direct measure of accelerations along X, Y and Z axes, respectively.
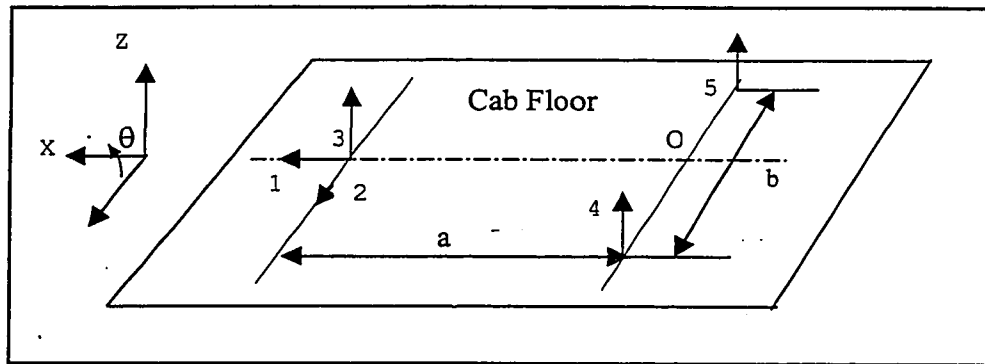
Figure 3.7: Location of accelerometers on the cab floor.

The pitch acceleration response characteristics of snowplow vehicle was derived from the measured vertical accelerations using the kinematics relations and assuming small angular motions. The acceleration signals 4 and 5 were manipulated to determine the vertical acceleration at a point O, located near the floor centerline. The acceleration signal 3 is then analyzed in conjunction with the acceleration at O to determine the pitch acceleration of the cab:

$$\ddot{\theta} = \frac{a_3 - a_o}{a}$$

(3.11)

Where a_3 and a_o are vertical accelerations recorded by accelerometer 3 and that derived at point O, $\ddot{\theta}$ is the pitch acceleration of the cab and a is the longitudinal distance between accelerometer 3 and the line connecting accelerometers 4 and 5. The field

measured longitudinal, vertical and pitch acceleration data were analyzed at Concave using the DSP software and expressed in terms of their power spectral density and 1/3-octave band rms acceleration spectra [63]. The measurements performed under varying operating conditions are further analyzed and the resulting spectra were presented in terms of their mean, minimum and maximum values in the 0-25 Hz frequency range.

Figure 3.8 to 3.10 illustrate minimum, maximum and mean values of power spectral density (PSD) and 1/3-octace band rms acceleration along the longitudinal, vertical and pitch coordinates measured in plowing operation. The corresponding results during a transit operation are illustrated in Figure 3.11 to 3.13. The measured data reveals predominant vibration peaks in the 1-2 Hz, 4-5 Hz, 9-11 Hz and 15-18 Hz frequency bands, which may be attributed to resonance associated with can pitch and suspension seat modes, cab vertical mode, chassis deflection modes and road wheel models, respectively.

3.6   VALIDATION OF THE ANALYTICAL MODEL

The analytical model of the snowplow vehicle, developed in Chapter 2, is validated using the field measured data. The validity of the model is initially examined by comparing its natural frequencies with the dominant ride frequencies identified from the field measured data. The ride dynamic model is further validated by comparing its vertical, longitudinal and pitch acceleration response at the cab with envelopes of the measured data presented in Figures 3.8 to 3.13.   It should be noted that field measurements were performed under varying speed and road roughness conditions.

Cab Longitudinal Acceleration PSD ((m/s²)²/Hz)

Cab Longitudinal 1/3 Octave Acceleration (m/s²)

Figure 3.8: PSD and RMS of longitudinal acceleration measured at the cab floor.
(task: plowing)

Cab Vertical Acceleration Psd ((m/s²)²/ Hz)

Frequency (Hz)

Cab Vertical 1/3 Octave Acceleration (m/s²)

Frequency (Hz)

Figure 3.9: PSD and RMS of vertical acceleration measured at the cab floor.
(task: plowing)

103
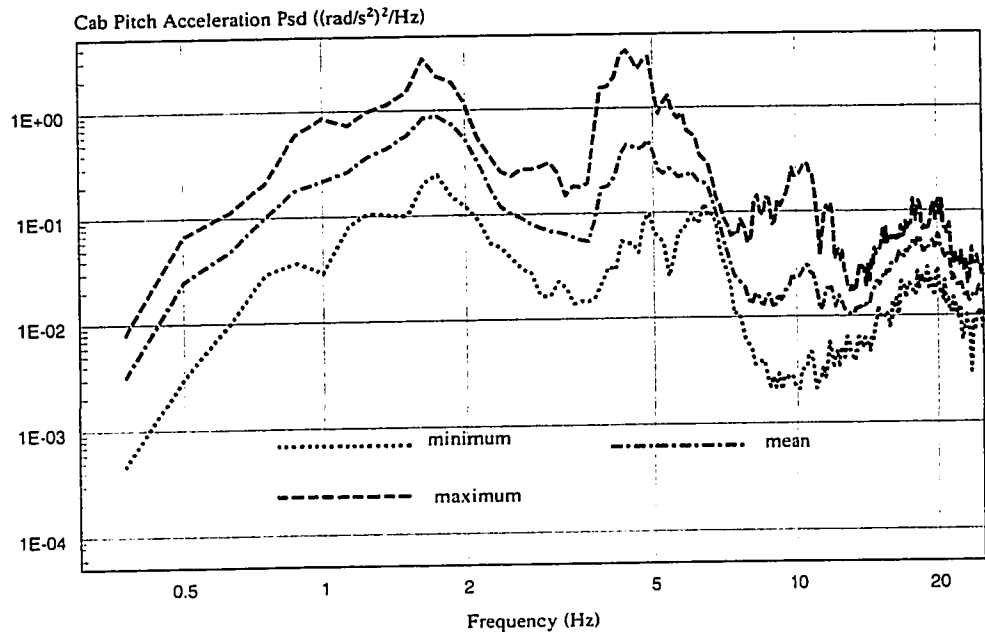
Figure 3.10: PSD and RMS of pitch acceleration measured at the cab floor.
(task: plowing)

104

Cab Longitudinal Acceleration PSD ((m/s²)²/Hz)

Cab Longitudinal 1/3 Octave Acceleration(m/s²)
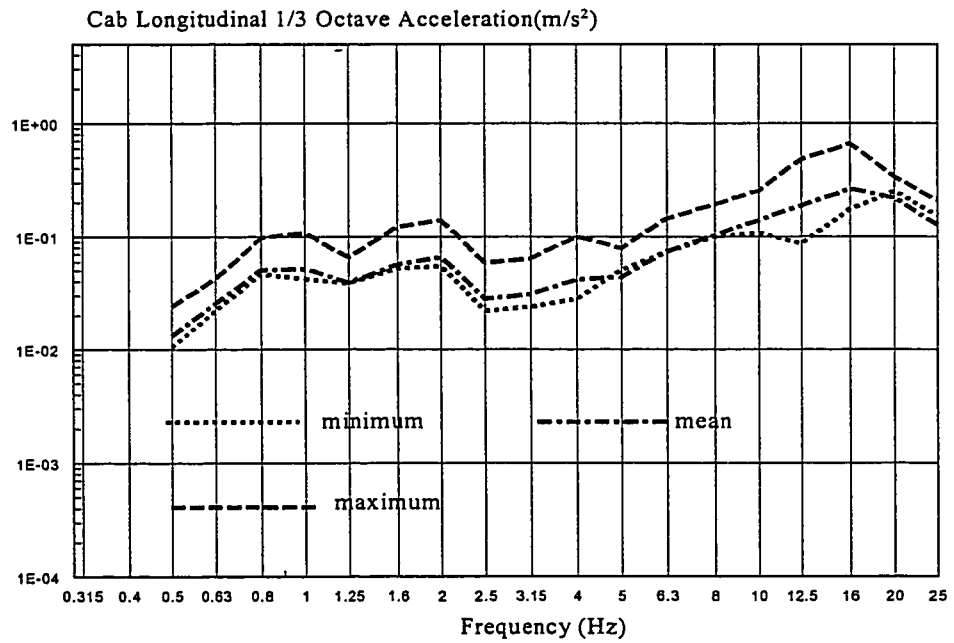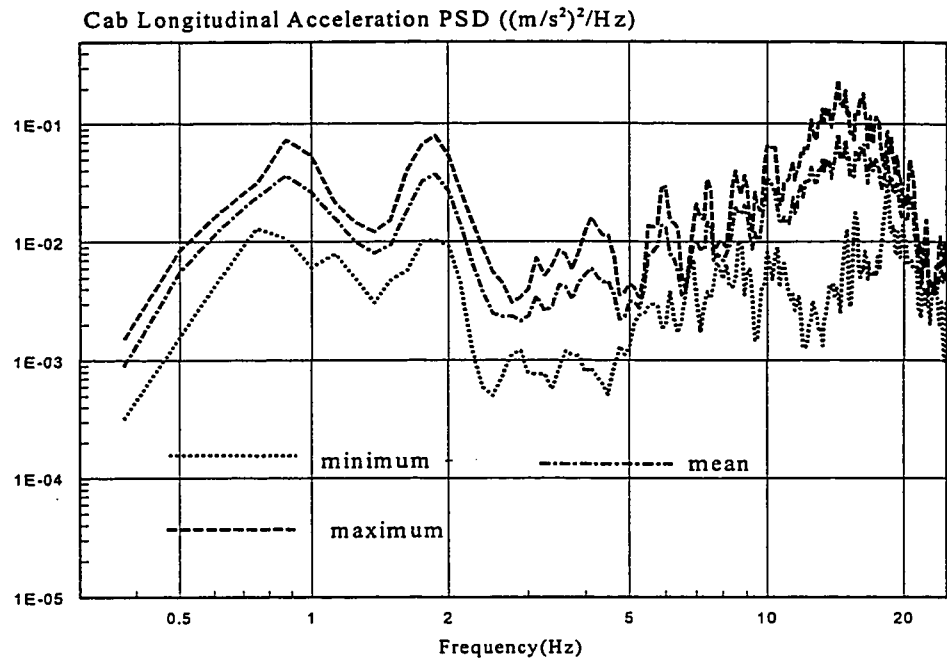
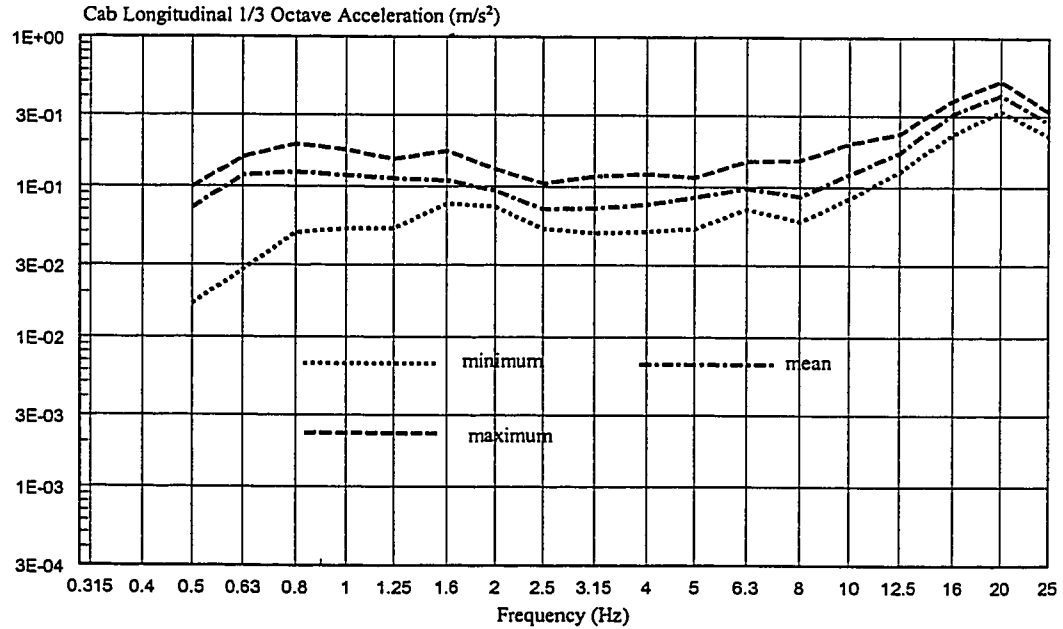Figure 3.11: PSD and RMS of longitudinal acceleration measured at the cab floor.
(task: transit)

Cab Vertical Acceleration PSD $((m/s^2)^2/Hz)$
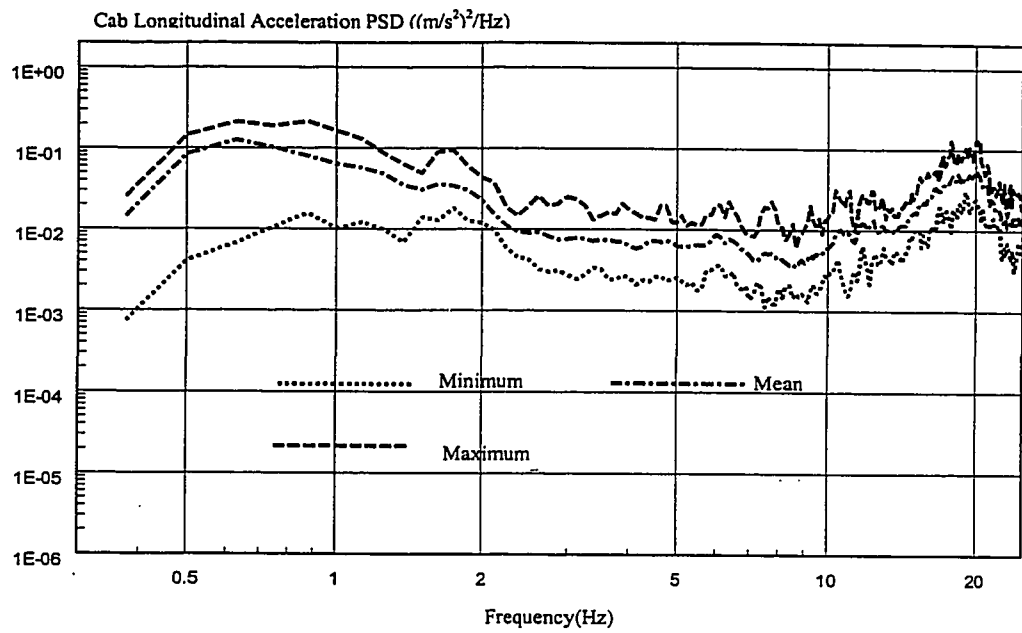

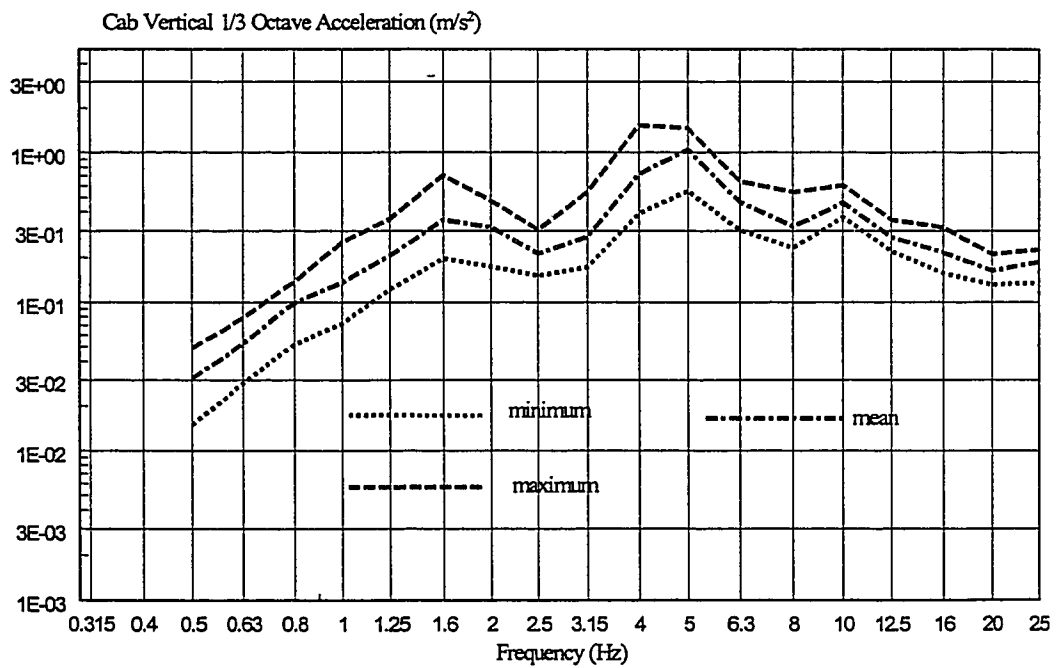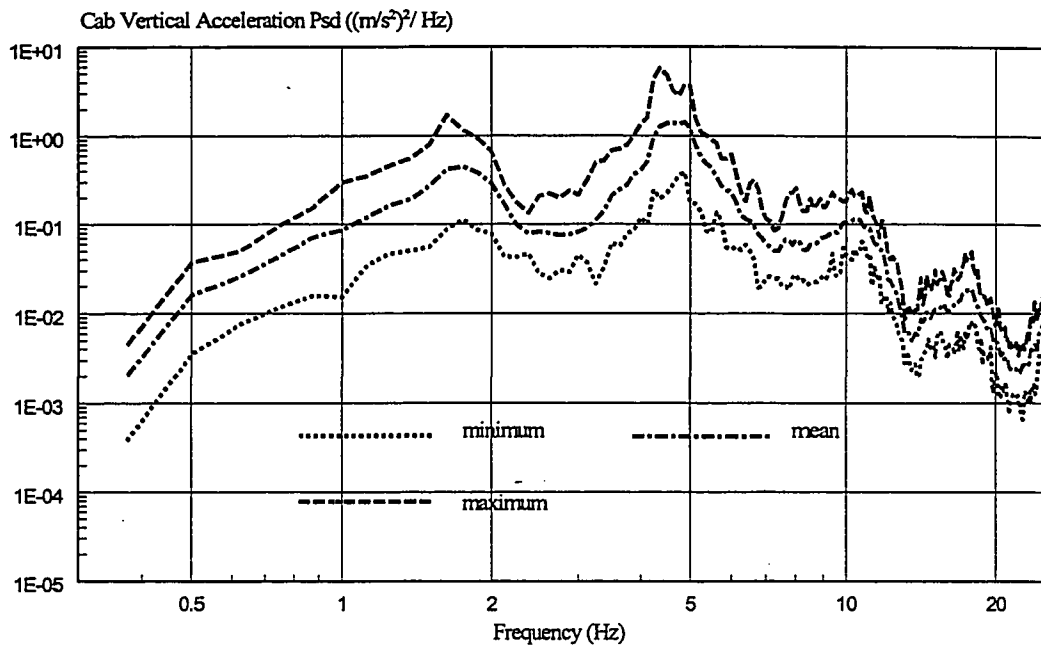**Cab Vertical 1/3 Octave Acceleration (m/s^2)**
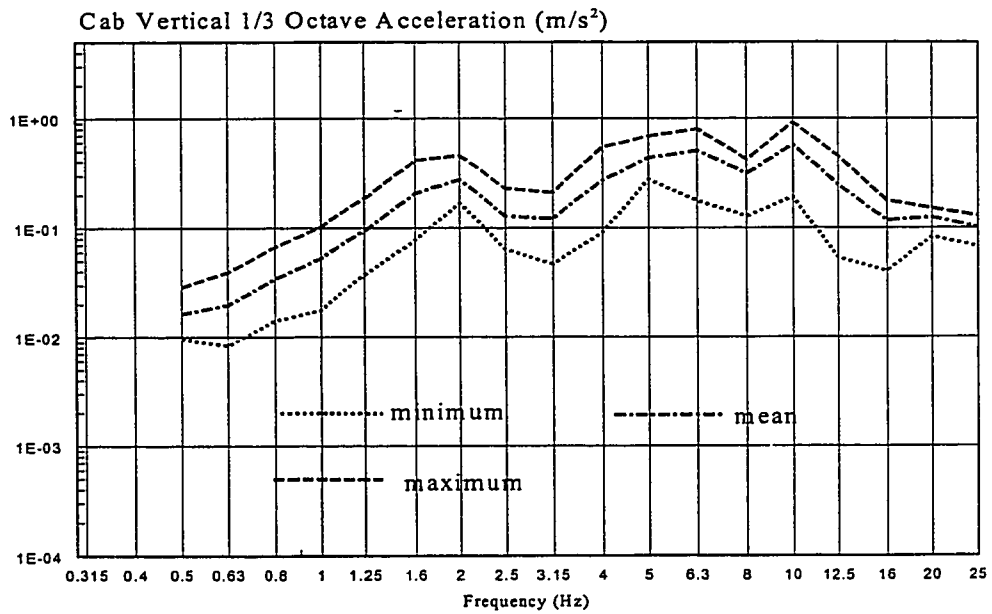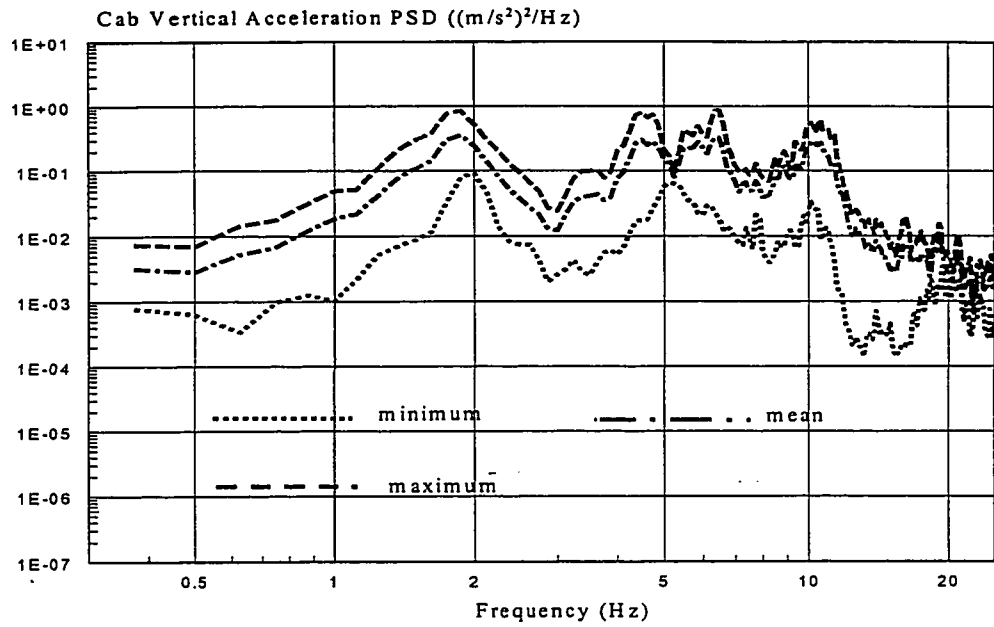
Figure 3.12: PSD and RMS of vertical acceleration measured at the cab floor. (task: transit)

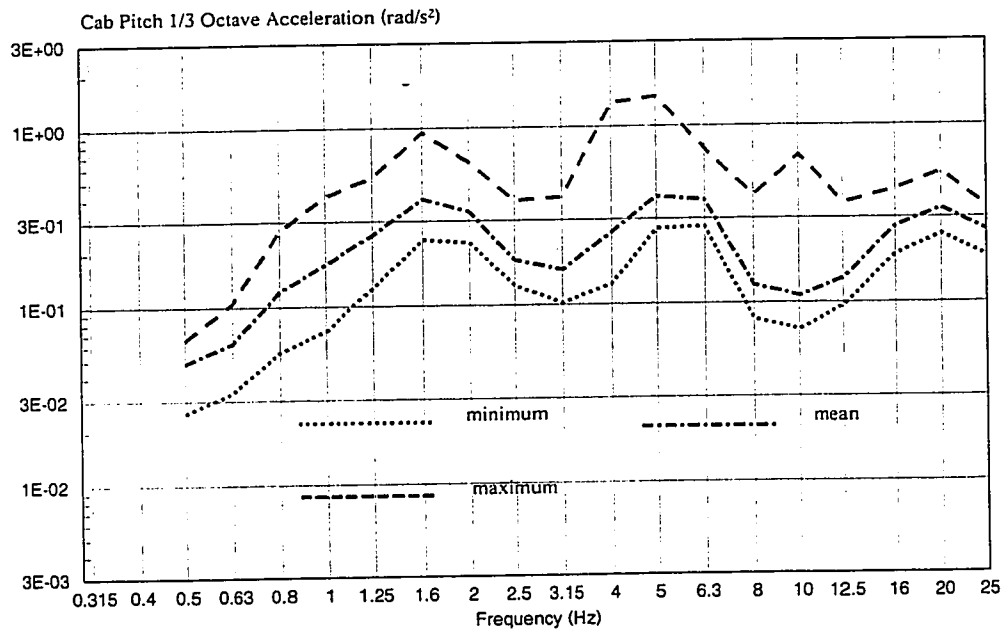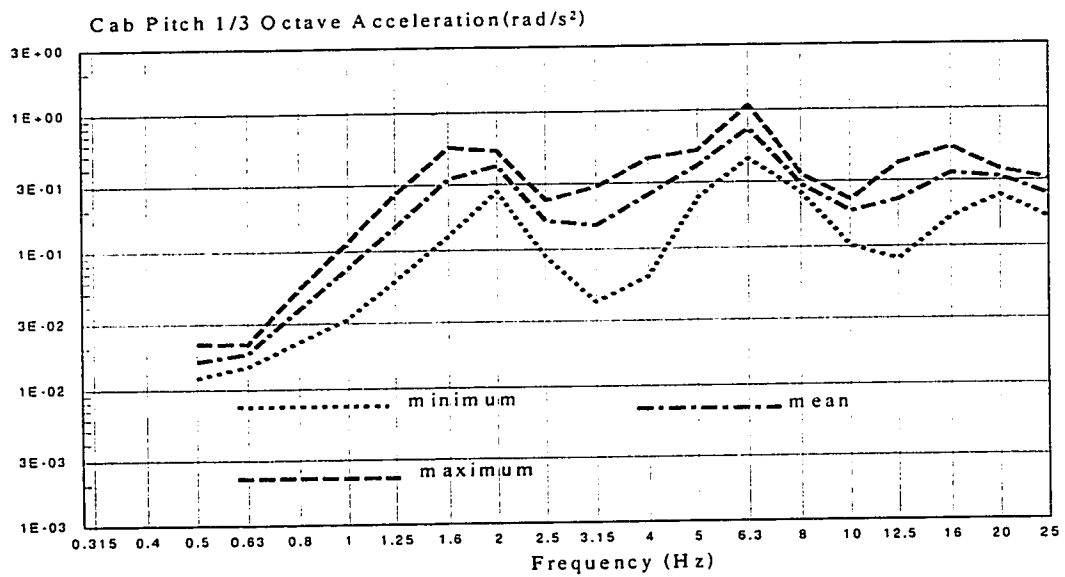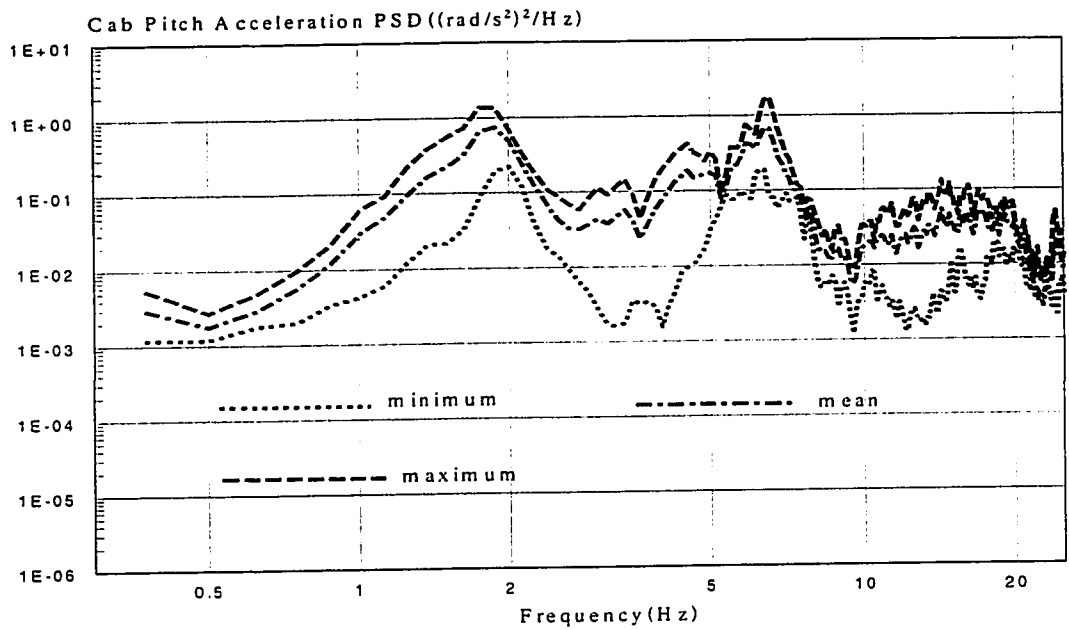Figure 3.13: PSD and RMS of pitch acceleration measured at the cab floor.
(Velocity: 8 km/h, task: transit)

107

The envelope curves of the PSD and RMS spectra are thus considered to represent the range of vibration response under a varying speeds and road conditions. Since the road roughness data is not available, the response analysis of the model is carried out using data available for a local road, as described in section 3.3. The ride vibration analyses are carried out for two specific operating conditions: transit operation where the horizontal snowplow force is suppressed; and snowplowing operation. The random response characteristics are compared with the measured data to demonstrate the validity of the simulation model.

In view of varying and unknown speed and road conditions, the validity of the simulation model is initially examined in terms of the dominant ride frequencies. Free vibration analysis of the vehicle model is performed to identify its resonant frequencies and deflection modes. An eigenvalue problem is formulated to derive the damped natural frequencies and deflection models of the vehicle, assuming linear properties of cab mounts, road wheel suspension and the track. The damped natural frequencies and the deflection modes thus derived are compared with dominant frequencies of vibration identified from the field measured data, as shown in Table 3.6.

An examination of the measured longitudinal, vertical and pitch acceleration spectra reveal predominance of ride vibration near 1.6 Hz, 4-6 Hz, 9-11 Hz and 17-20 Hz. The longitudinal ride vibration predominate in the 17-18 Hz frequency range, which correlates well with the longitudinal deflection mode of the cab (17.18 Hz). The measured vertical vibration reveal peak near 1.6 Hz, and in the 4.0-6.0 Hz, and 9.0-11.0 Hz bands, which correlate well with the natural frequencies associated with seat

suspension and cab pitch mode, cab vertical, and chassis and road wheel vertical and

pitch modes.

Table 3.6: Comparison of natural frequencies of the model with predominant
frequencies of measured response.

Dominant Deflection Mode	Damped Natural Frequencies (Hz)	Dominant Ride Frequencies (Hz) (measured data)
θ_c	1.61	1.6-2.0
z_s	1.70	
z_c	4.65	4.0-6.0
θ_h	5.95	
z_1	6.39	
θ_{w1}	7.07	9.0-11.0
x_h	7.89	
z_h	8.56	
θ_{w23}	8.78	
z_0	13.04	17-20.0
x_c	17.18	

The simulation model is further validated through direct comparison of model and

field measured acceleration response spectra. Equations (2.11) and (2.24) are solved to

determine the PSD and RMS of acceleration response at the cab floor along the vertical,

longitudinal and pitch coordinates. Analyses are performed for two different operations:

plowing large accumulations of snow; and transit operation. The ride response

characteristics of the vehicle model are further analyzed to derive the PSD and 1/3 band

rms acceleration of the longitudinal, vertical and pitch vibration of the cab. The resulting

spectra are compared with those derived from the measured data to examine the validity

of the model.

Figures 3.14 to 3.19 illustrate comparison of the measured and analytical ride

vibration response characteristics of the snowplow vehicle employed in two operations:

transit and plowing. The results presented in these Figures, in general, exhibit a reasonably good correlation with the measured response data. Figure 3.14 and 3.17 illustrate a comparison of analytical and measured PSD and 1/3 Octave RMS of longitudinal acceleration response of cab during plowing and transit operation, respectively. The longitudinal acceleration response of the cab derived from the analytical model, correlates well with the lower bound of the measured response in majority of the frequency range. The response spectra reveal predominance of longitudinal vibration near 1 Hz, 1.6 Hz and in the 17-20 Hz range. While the low frequency vibration near 1 Hz are believed to be due to road excitation. A comparison of Figure 3.14 and Figure 3.17 further reveals that the ride response along the longitudinal axis is higher when vehicle is plowing the snow, which can be attributed to the snow pushing force.

Figure 3.15 and 3.18 illustrate a comparison of computed and measured vertical acceleration response of the cab under plowing and transit operation, respectively. Both the analytical and measured response reveal peak in the vicinity of 1.6 Hz, attributed to the natural frequency of the seat suspension, and in the 4-6 Hz band, attributed to the vertical mode natural frequencies of the cab and first road wheel suspension. While the analytical response in the low frequency range (below 3 Hz) is close to the lower bound of the measured data, the response at higher frequency if closer to the upper bound. The results further show that the horizontal plowing force also contribute to the vertical ride vibration encountered at the cab floor.

The PSD and rms of the pitch vibration response of the model are also compared with the measure data, as shown in Figure 3.16 and Figure 3.19, respectively, for the
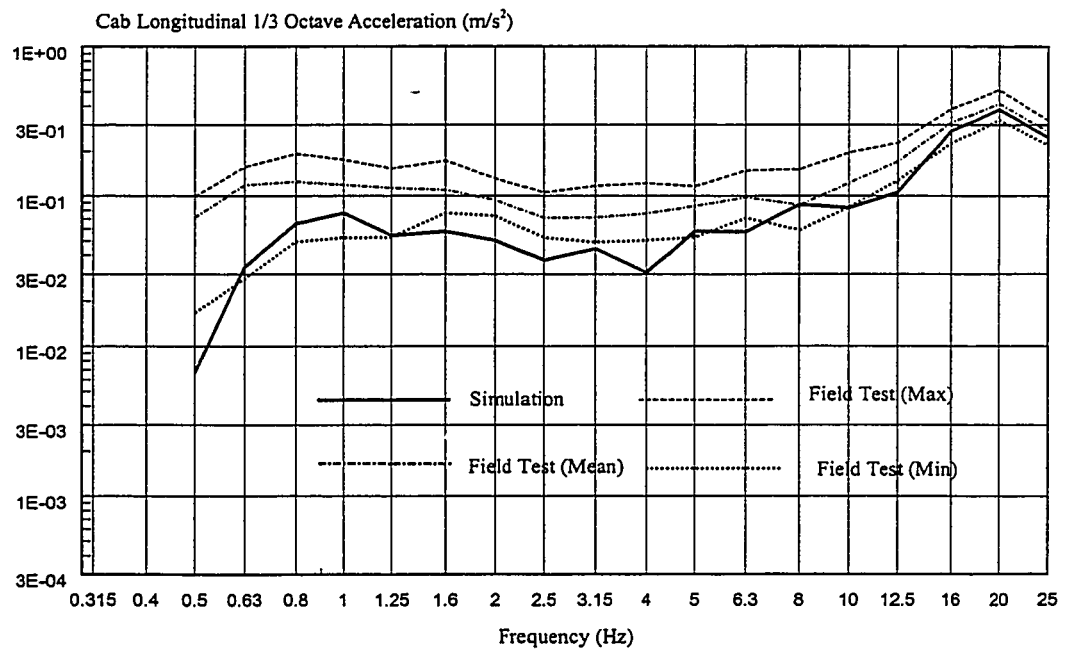
Figure 3.14: Field validation of simulation model-longitudinal of cab.
(Velocity: 8 km/h, task: plowing)
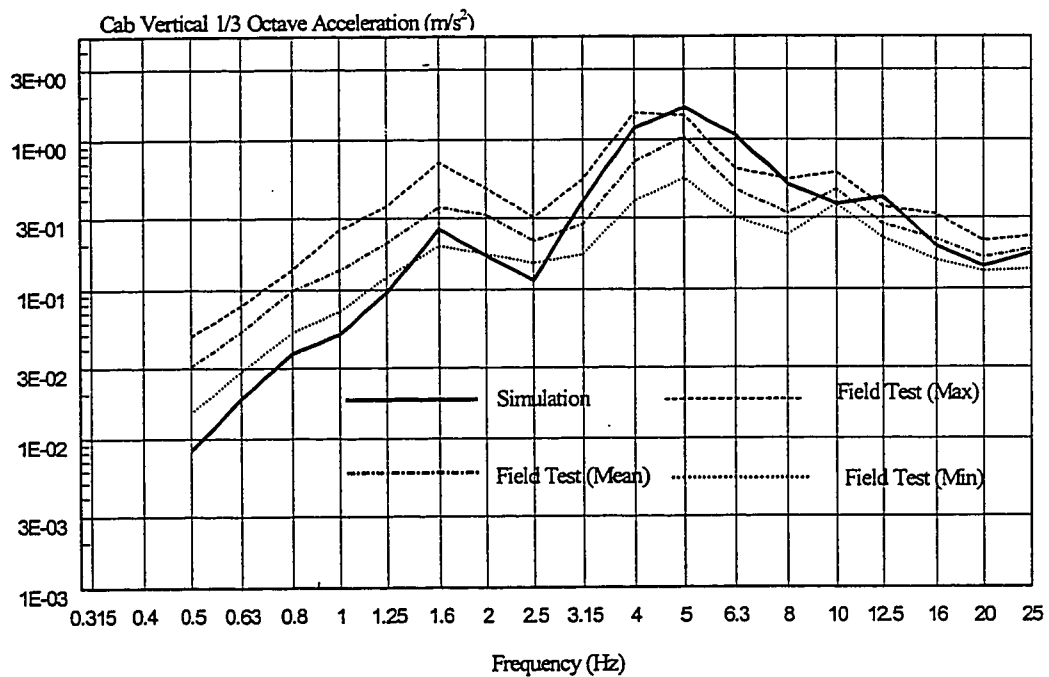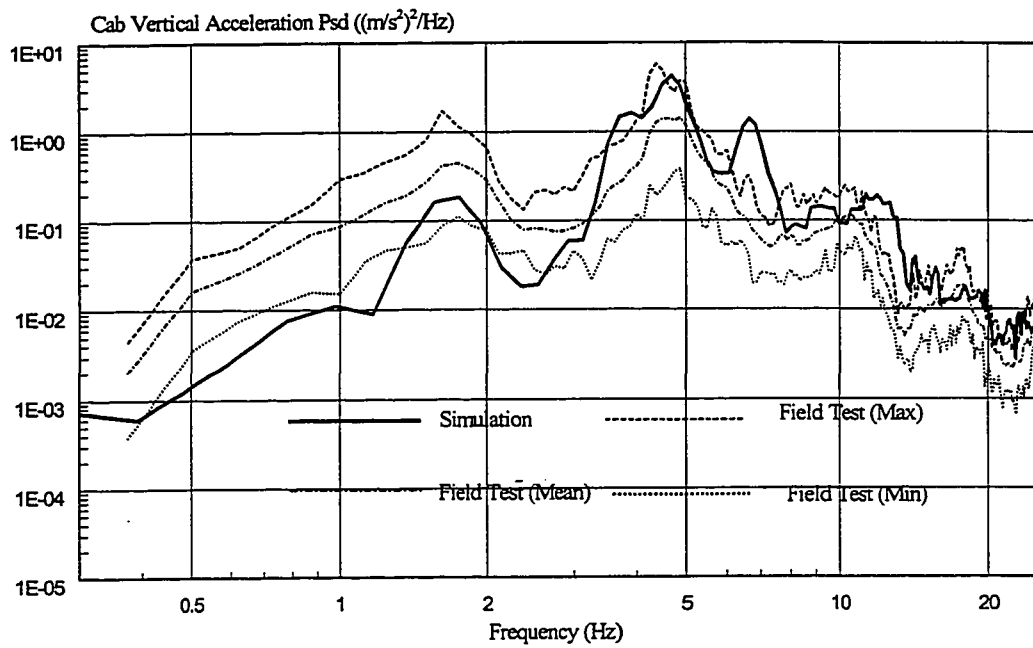
Figure 3.15: Field validation of simulation model-vertical of cab.
(Velocity: 8 km/h, task: plowing)

Cab Pitch Acceleration Psd ((rad/s²)²/Hz)

Simulation

Field Test (Max)

Field Test (Mean)

Field Test (Min)

Frequency (Hz)

Cab Pitch 1/3 Octave Acceleration (rad/s²)

Simulation

Field Test (Max)

Field Test (Mean)

Field Test (Min)

Frequency (Hz)
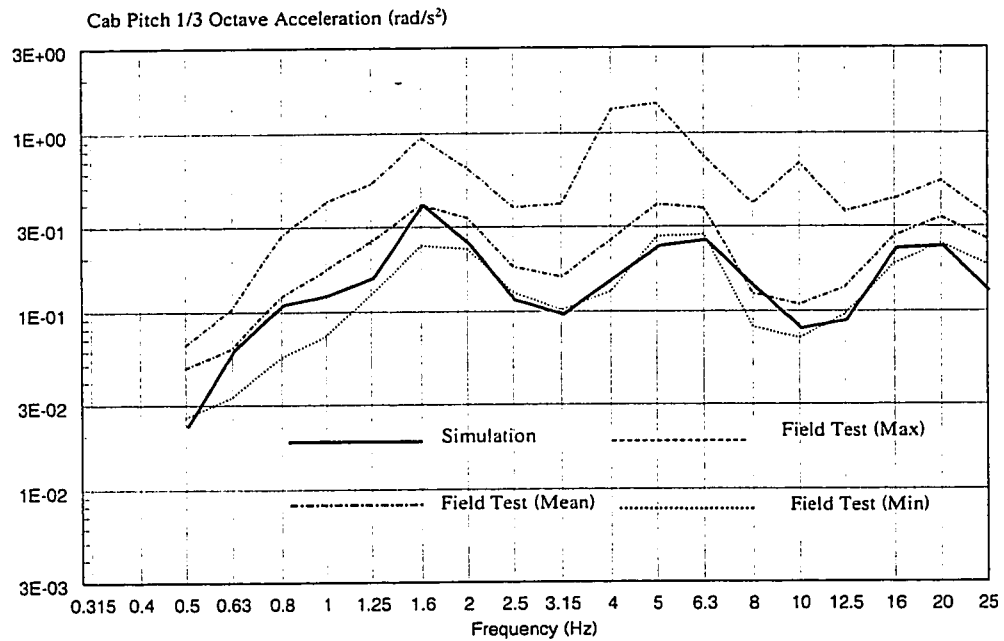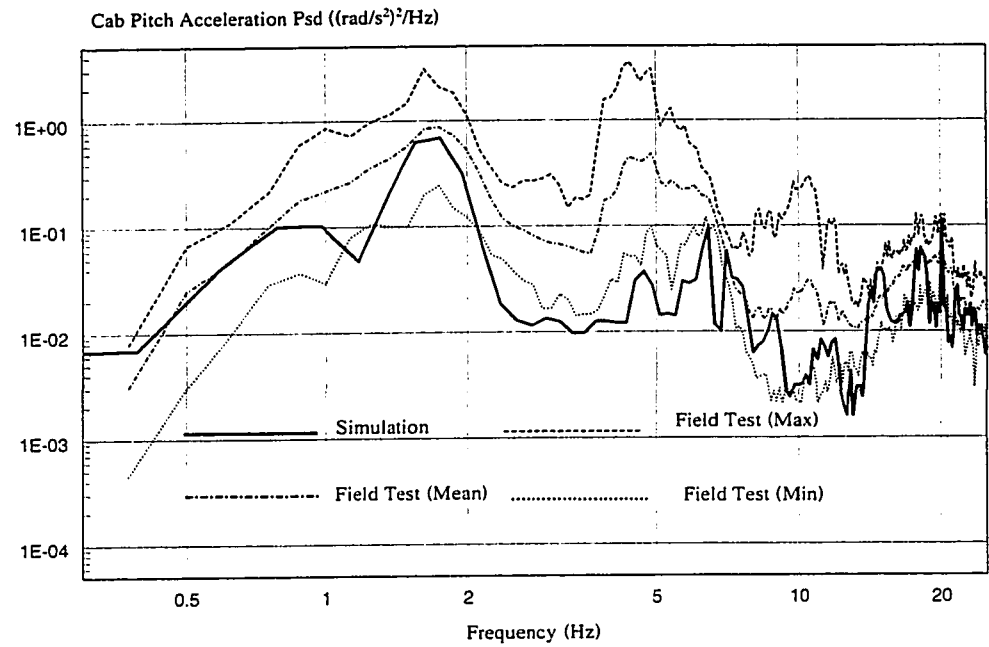
Figure 3.16: Field validation of simulation model-pitch of cab.
(Velocity: 8 Km/h, task: plowing)

113

Cab Longitudinal Acceleration PSD ((m/s²)²/Hz)

Frequency(Hz)

Cab Longitudinal 1/3 Octave Acceleration(m/s²)

Frequency (Hz)
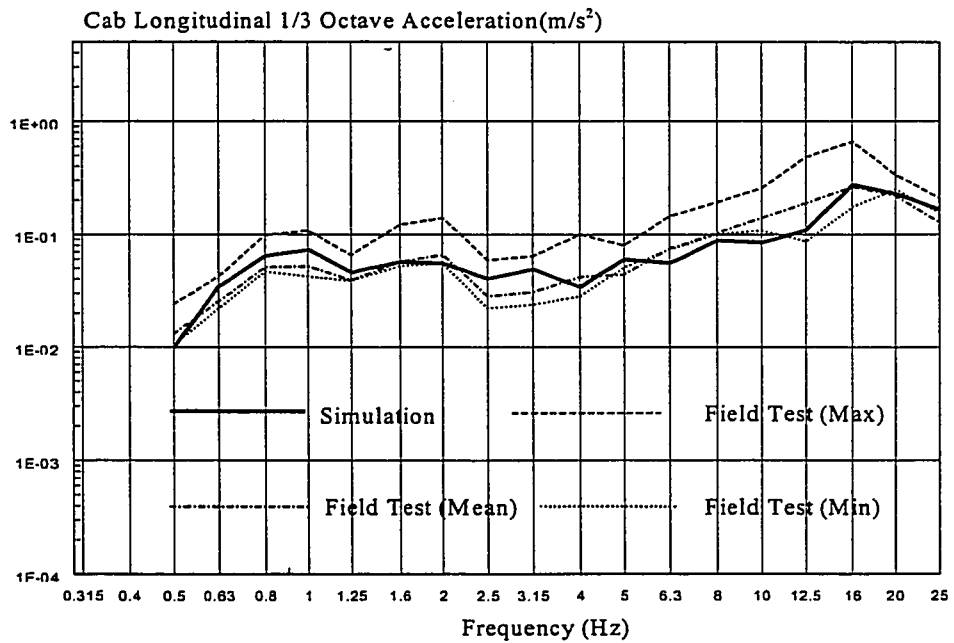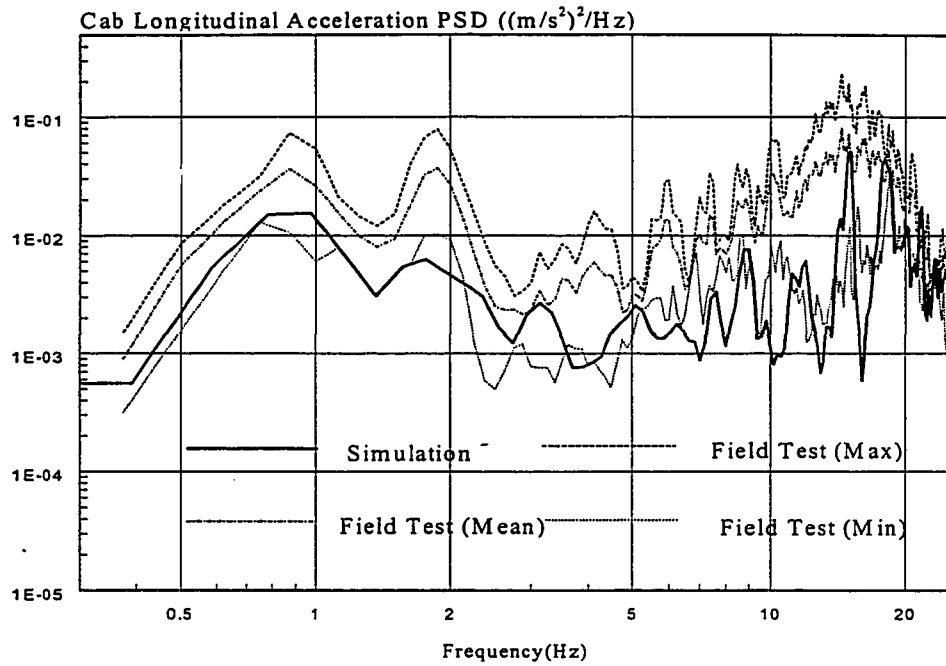
Figure 3.17: Field validation of simulation model-longitudinal of cab.
(Velocity: 8 km/h, task: transit)

Cab Vertical Acceleration PSD ((m/s²)²/Hz)

Cab Vertical 1/3 Octave Acceleration (m/s²)
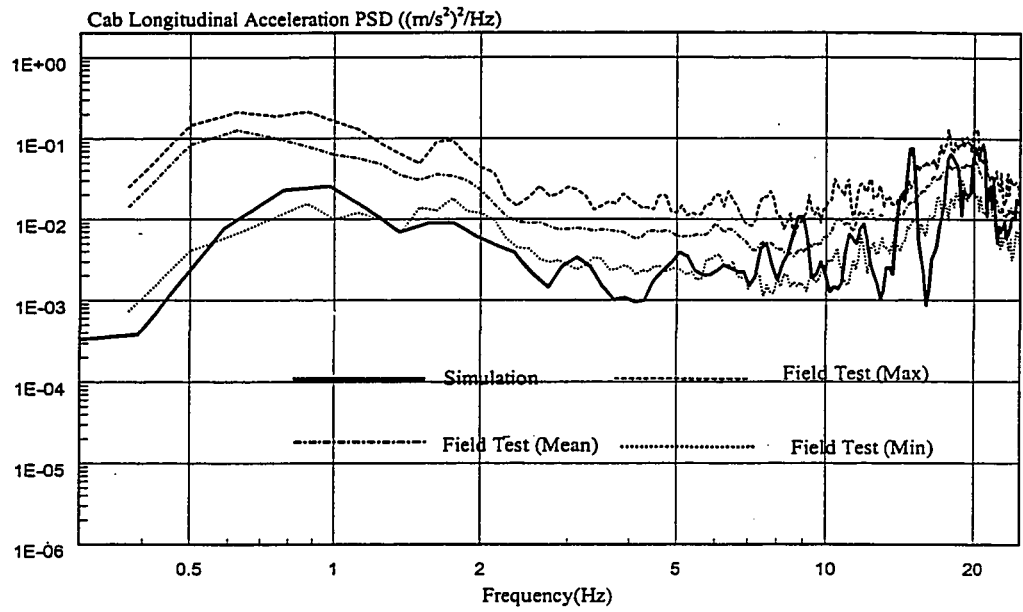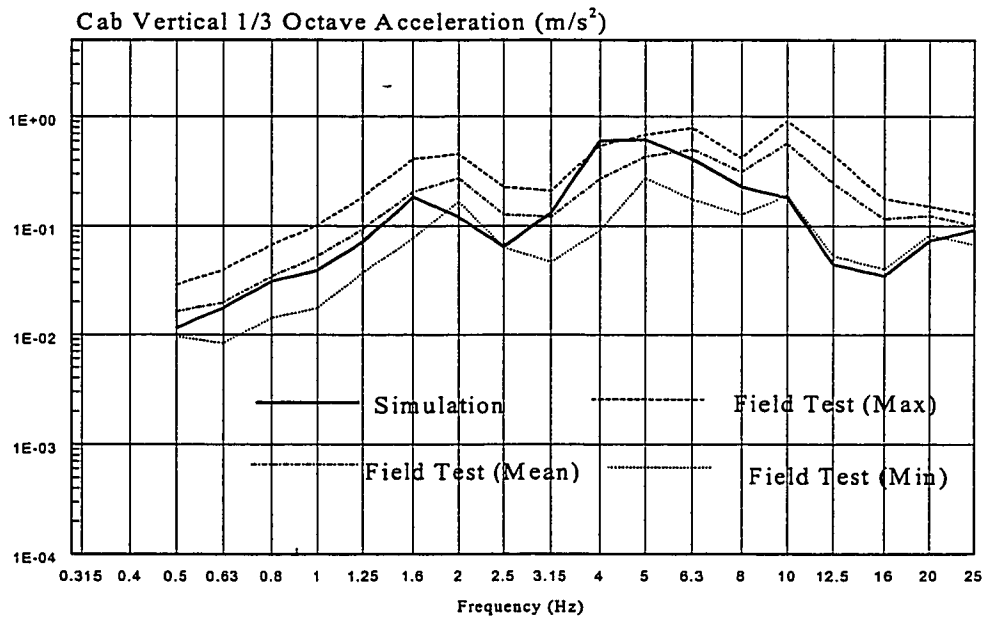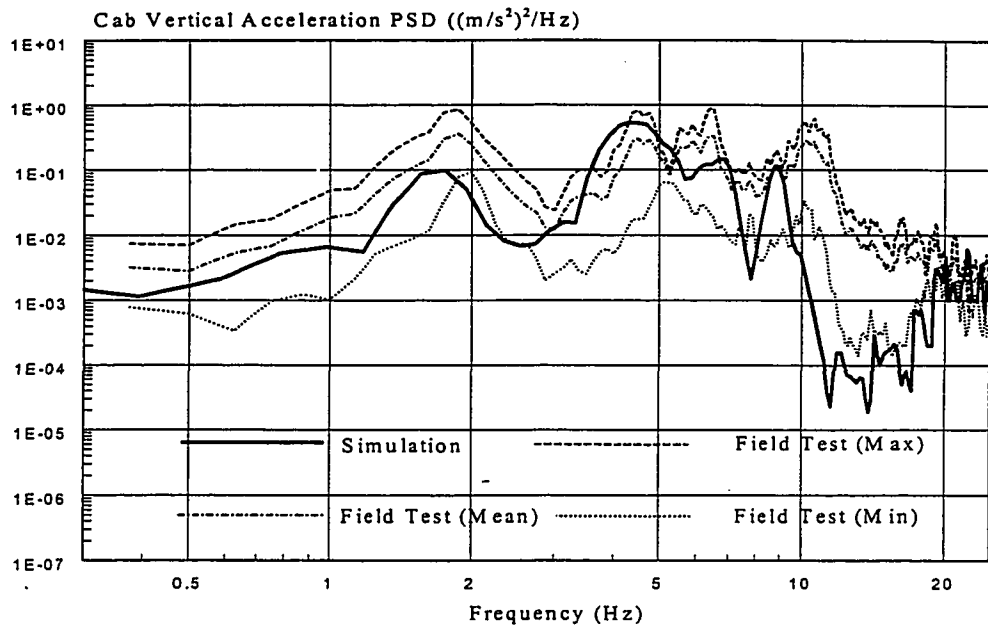

Figure 3.18: Field validation of simulation model-vertical of cab.
(Velocity: 8 km/h, task: transit)

115
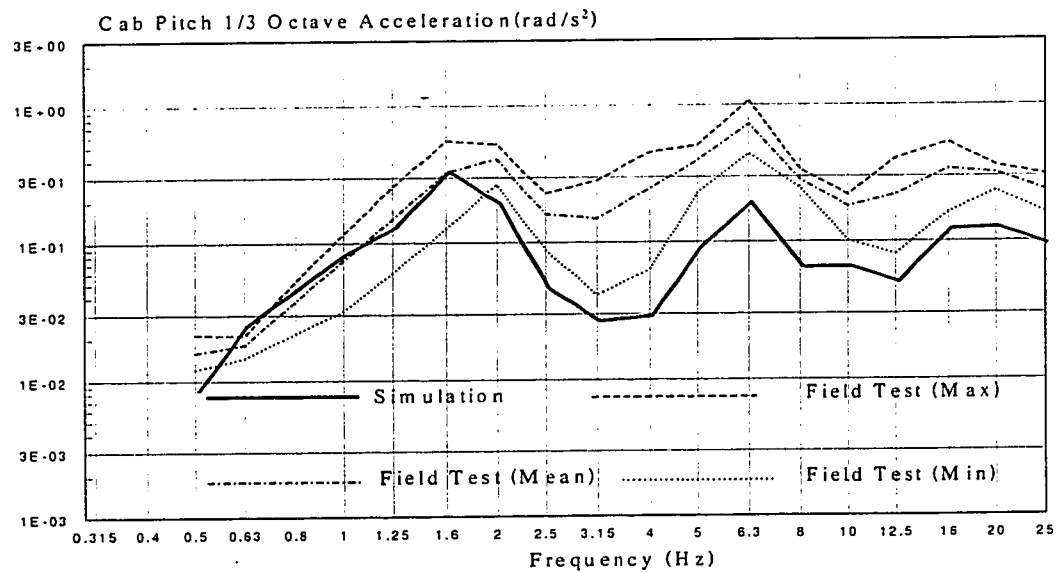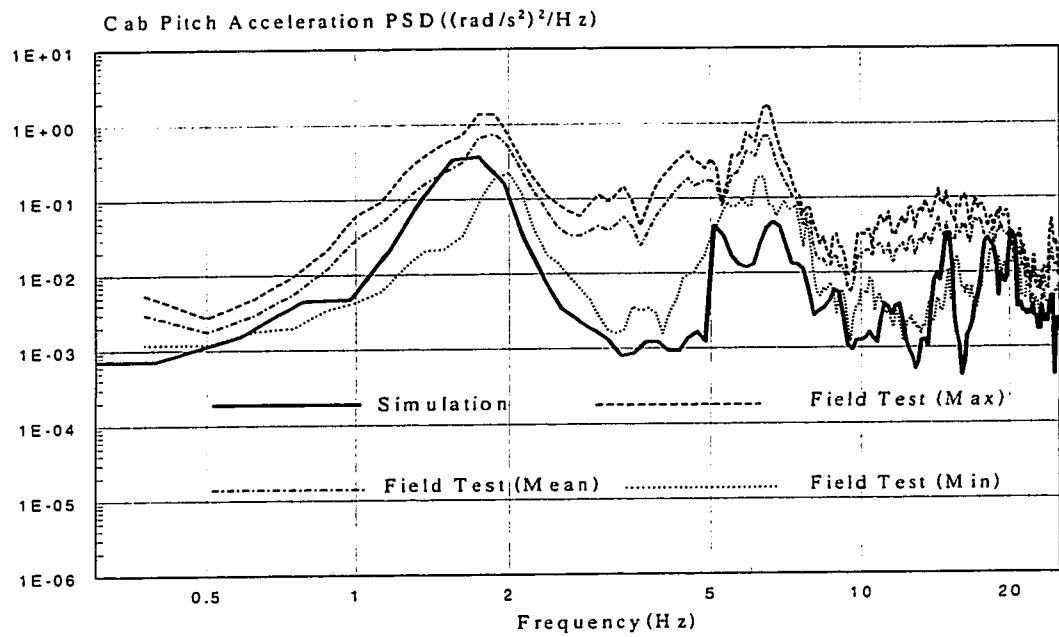
Figure 3.19: Field validation of simulation model-pitch of cab.
(Velocity: 8 km/h, task: transit)

116

plowing and transit operation. The spectra are similar to those obtained for vertical vibration. It should be noted that a sidewalk snowplow is frequently subject to transient excitations due to discontinuities in the sidewalk. Such excitations predominantly cause pitch motion of the vehicle at relatively high frequencies associated with the pitch mode vibration of the road wheel suspensions (θ_{w1} and θ_{w23}) and structural modes. Under plowing operation, the pitch vibration of the cab is also observed to higher than those encountered along transit operations. The comparison of the analytical and measured response reveals reasonably good correlation, although the model response lies in the vicinity of the lower bound of the measured data.

3.7 SUMMARY

In this chapter, a general overview of the field tests performed by IRSST and Concave is presented and the measured data is presented in the form of envelope curves of PSD and 1/3 –Octave band rms accelerations. The envelope curves are considered to represent the range of most probable ride vibration during plowing and transit operation. The analytical model is analyzed under excitation arising from a medium rough road and horizontal push force arising from the plowing task. Free vibration analysis is performed and the natural frequencies of the vehicle model are compared with the dominant measured ride frequencies. The vehicle response characteristics in terms of PSD and rms acceleration of cab pitch, longitudinal and vertical acceleration are compared with the measured data. It is concluded that the analytical response correlates reasonably well with the measured data.

CHAPTER 4

RIDE QUALITY ANALYSIS & PARAMETRIC STUDY

4.1 INTRODUCTION

The ride quality of snowplow vehicles is strongly related to the properties of the suspension at the seat and the cab, track properties, track-terrain interaction, wheel suspension and the nature of tasks. Assessment of the ride quality requires identification and characterization of the dynamics associated with the vehicle design and operating parameters. The ride dynamics of a vehicle may be characterized via either field measurements or analytical means. The analytical characterization of vehicle ride dynamics requires adequate representation of the random terrains and ride response evaluation of a realistic vehicle model. In view of the severity of ride vibration levels, and prolonged duration of occupational exposure, a large number of ride quality assessment methods have been proposed [40-43]. In this study, the ride dynamic response of the snowplow vehicle model subjected to excitations arising from non-deformable terrains is assessed using the guidelines proposed in ISO-2631 (1978) [41] and its revised version, ISO-2631 (1997) [43].

The ride quality assessment is performed using the analytical model developed in chapter 2, and validated using the road measured data in chapter 3. Since the ride dynamic behavior of a vehicle is influenced by a number of design and operating factors, such as terrain profile, vehicle speed, and vehicle design parameters associated with geometry, suspension systems, etc., a comprehensive parametric study is carried out to achieve a better understanding of their contribution to the overall ride quality. The ride

vibration environment of a snowplowing vehicle further depends on the nature of task being performed, such as transit operation, plowing, loading and sanding. The results of the parametric study can provide significant information on the effect of various parameters on the ride response and thus may yield a basis for selecting the design and operating parameters to achieve near optimal ride. In this chapter, parametric sensitivity analyses are carried out for two different tasks, transit and plowing, with an objective to identify desirable design and operating conditions for enhancement of ride quality.

4.2   RIDE QUALITY ANALYSIS

Numerous investigations on human response to vehicle vibration have been conducted to establish the acceptable levels of ride vibration for preservation of driver comfort, health, safety, and performance [30-43]. The influence of vibration exposure on the driver health, safety and fatigue has been related to the magnitude and frequency of transmitted vibration, and the daily exposure duration. In this study, the vibration levels transmitted to the seated driver of the vehicle, measured at the driver-seat interface, are assessed in relation to the *fatigue decreased proficiency limits* proposed in the International Standardization Organization, ISO-2631(1978) [41]. The International Standardization Organization has set forth exposure tolerance in view of preservation of health and safety, proficiency and comfort. The exposure limits are proposed for vertical and horizontal vibrations in terms of frequency-weighted rms acceleration as a function of exposure time in the frequency range of 1-80 Hz, as shown in Figure 1.13. The exposure limits, proposed in the International Standard reveal that the human body is

most sensitive to vertical vibrations in the frequency range of 4-8 Hz, and to horizontal vibration in the frequency range of 1-2 Hz.

The ride quality analyses are carried out for two specific operating conditions: (i) in a transit operation; and (ii) in a plowing operation. Equations (2.1) to (2.28) are solved for excitation arising from a random medium-rough road, as described in section 3.4.2 at a speed of 8 km/h. For plowing operation, the snow depth is considered as 0.5m, the maximum snow density of 0.35 gm/cc, and the minimum snow density of 0.09 gm/cc. Equation (3.14) is solved to determine the horizontal push force, which is integrated into the vehicle model. The resulting response is analyzed to determine the rms acceleration corresponding to 1/3 –octave band center frequencies. The weighting factors corresponding to X and Z axes, proposed in ISO 2631-1978 [40], are then applied to determine the weighted rms acceleration.

Figure 4.1 illustrates the rms acceleration of vibration at the driver-seat interface along the X and Z -axis respectively, when the snowplow vehicle is in plowing operation. The vibration transmitted along the X-axis is observed to be well below the 8 hours exposure duration. The vibration is also below the 8 hour exposure duration during 1-2 Hz which is the most fatigue sensitive range to the horizontal direction of human body. The human driver is known to be sensitive to vertical vibrations transmitted in the 4-8 Hz frequency range due to the primary resonances of the body. As shown in Figure 4.1, the magnitude of vertical vibration transmitted to the driver in this frequency range is considerably larger than that transmitted along the X axis. The weighted seat vertical rms

Seat Longitudinal RMS Acceleration (m/s²)

Frequency (Hz)

Seat Vertical RMS Acceleration (m/s²)

Frequency (Hz)

Figure 4.1: RMS acceleration at the seat compared with the exposure limits
proposed in ISO-2631 (1978)(Velocity: 8 Km/h, task: plowing)

121

acceleration response exhibits highest level of vibration in the vicinity of 5 Hz, which is attributed to the vertical cab mode resonance near 4.8 Hz. The weighted seat vertical rms acceleration response shown in Figure 4.1 also exhibits the peak level of vibration in the vicinity of 1.6 Hz and 12.5 Hz, which are attributed to the vertical seat mode resonance and the longitudinal cab mode resonance. The rms acceleration of vertical vibration transmitted to the driver exceeds the 4-hour exposure limit in the 4-8 Hz frequency range and approaches 2.5-hour exposure limit.

Figure 4.2 illustrates the rms acceleration of vibration at the driver-seat interface along the X and Z axis respectively, when the snowplow vehicle is in transit operation. The vibration transmitted along the X- axis is also observed to be well below the 8 hours exposure duration. The weighted seat vertical rms acceleration shown in Figure 4.2 also exhibits the peak levels of vibration in the vicinity of 1.5 Hz and 5 Hz, which are attributed to the vertical mode resonance of seat near 1.7 Hz and vertical mode resonance of cab near 5 Hz. The rms acceleration of vertical vibration transmitted to the driver is below the 8 hours exposure duration. From Figure 4.1 and Figure 4.2, it is concluded that the vibration transmitted along the X-axis is well below 8 hours exposure limit, when the snowplow is in plowing or transit operations. However, the vibration transmitted along the Z-axis is much lower when the snowplow is in transit operation than it is in plowing operation. When the snowplow vehicle is plowing snow, the acceptable exposure duration is only 2.5 hour. However, when the snowplow vehicle is transit, the exposure to vertical vibration can be acceptable for duration up to 8 hours.
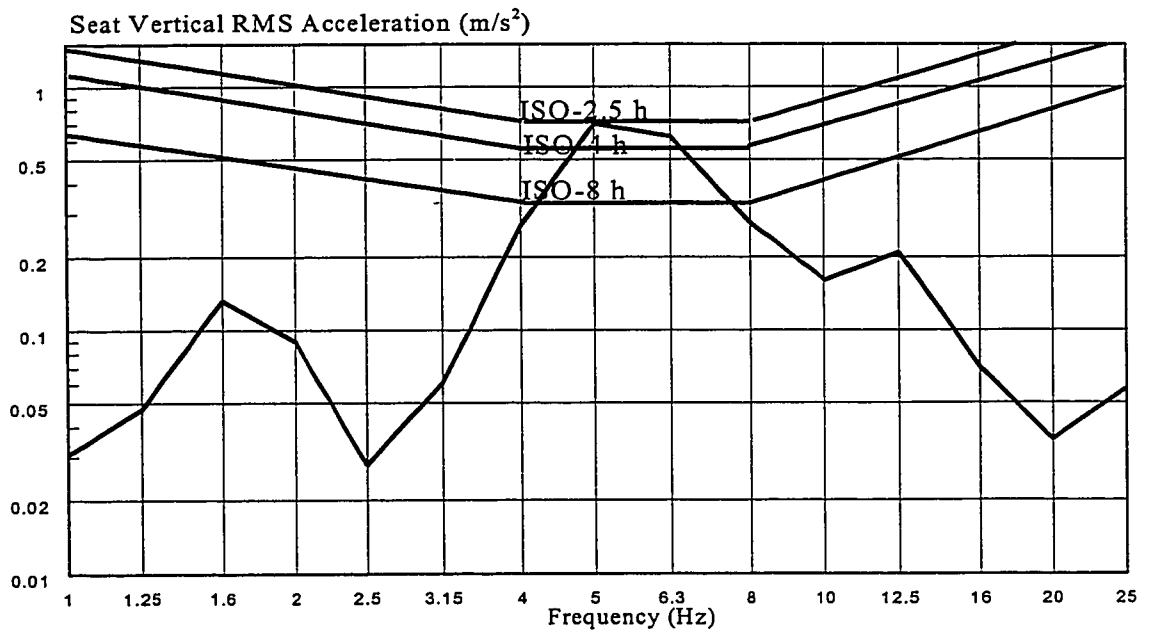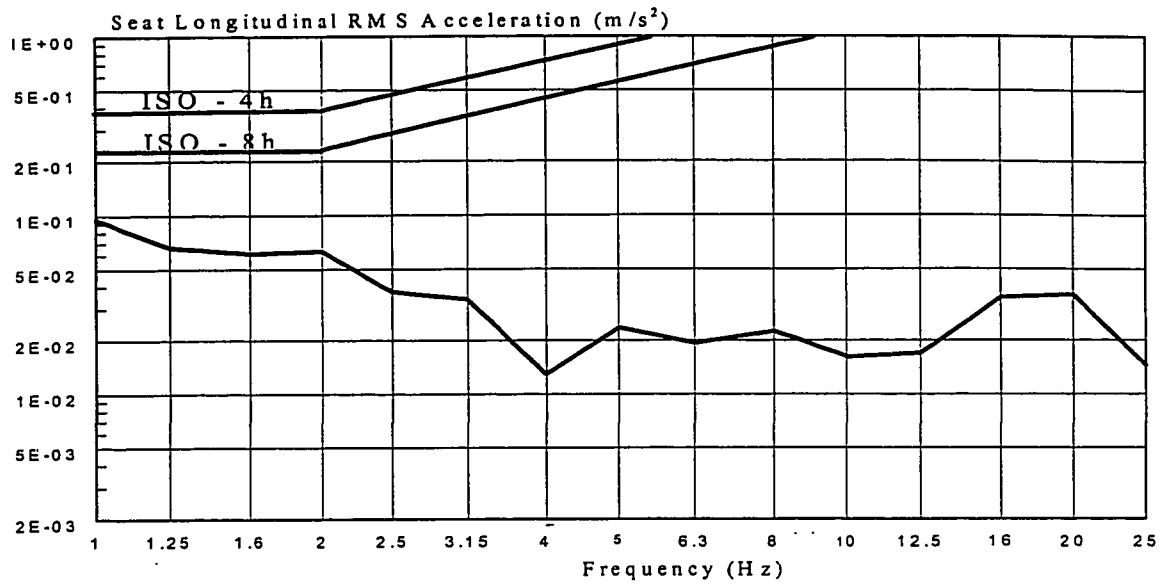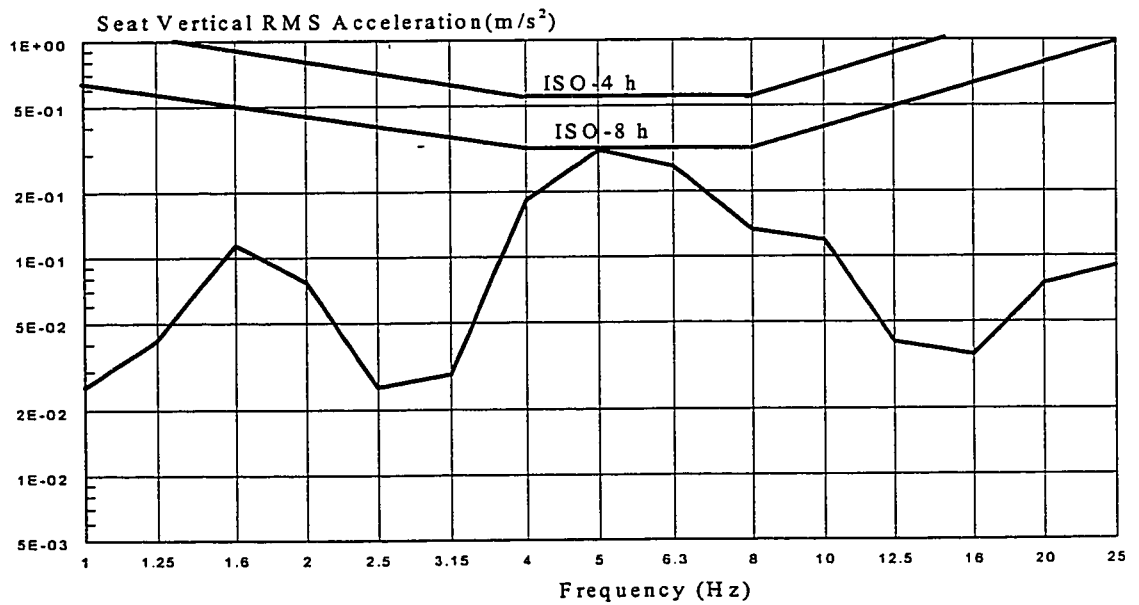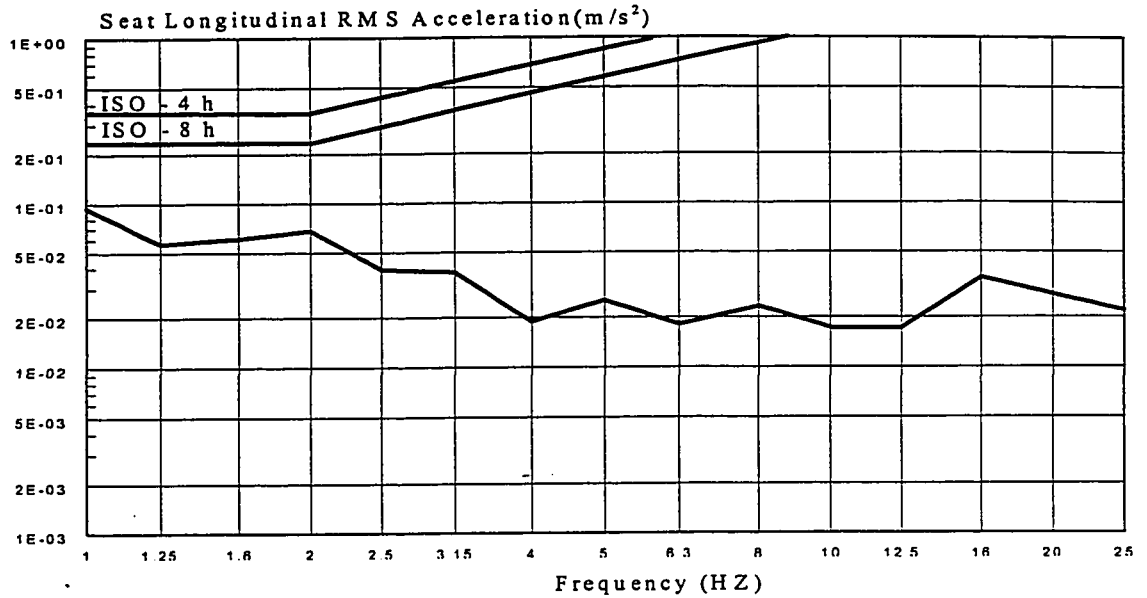
Figure 4.2 RMS acceleration at the seat compared with the exposure
limits proposed in ISO-2631 (1978).
(Velocity: 8 Km/h, task: transit)

123

4.3   INFLUENCE OF OPERATING FACTORS

The ride vibration response of a vehicle is strongly related to the operating conditions, such as terrain roughness, obstacle severity, vehicle speed and snow properties, which result in horizontal snowforce acting on the blade during plowing operation, as discussed in section 3.4.3. A thorough study of the influence of operating factors on the ride quality performance of the vehicle can provide significant insight into the operation of such vehicles. A parametric study is thus carried out by varying the selected parameters around the nominal operating parameters, when the vehicle is in snowplowing operation. The influence of variations in such parameters is then assessed in relation to the *fatigue decreased proficiency limits* proposed in ISO-2631 (1978) [41]. The influence of variation in these parameters is further assessed using the overall rms acceleration response along the vertical, longitudinal and pitch axes, using the frequency weighting proposed in the revised version of the ISO document, ISO-2631-1 (1997) [43]. The effectiveness of the suspension seat is evaluated in terms of Seat Effective Acceleration Transmissibility based upon the weighted (S.E.A.T.$_w$) and unweighted (S.E.A.T.) rms acceleration, defined as:

$$S.E.A.T. = \frac{\text{overall frequency - unweighted rms vertical acceleration at the driver - seat interface}}{\text{overall frequency - unweighted rms vertical acceleration at the seat base}}$$

$$S.E.A.T._w = \frac{\text{overall rms vertical acceleration at the driver - seat interface}}{\text{overall rms vertical acceleration at the seat base}}$$

The parametric study is performed by varying the operating parameters over a wide range considered to represent the variations in operating conditions. Table 4.1 lists the parameters and the range of variations considered in this study. The numbers

indicated in *bold* refer to the nominal values. The results of the parametric study are discussed in the following sections.

Table 4.1: Range of Operating Parameters Values.

Parameter	Value
Terrain profile	smooth, **medium**, rough
Vehicle speed (km/h) $\begin{cases} \text{plowing} \\ \text{transit} \end{cases}$	3, 5, **8**, 12 5, **8**, 12, 18
Snow depth (m)	0.0,0.3, **0.5**
Maximum snow peak density (gm/cc)	**0.35**, 0.25
Obstacle height (cm)	5,10,15

4.3.1 Influence of Terrain Roughness

The vehicle ride quality is strongly related to the track-terrain dynamic interactions, which is mostly influenced by the magnitude and frequency components of terrain roughness. The ride performance characteristics of the vehicle model are evaluated for three different terrain roughness. The coordinates of the measured terrain elevations are analyzed to derive a roughness index, which is further utilized to characterize three roads in terms of 'smooth', 'medium rough' and 'rough'. The roughness coordinates of three different roads, available at Concave [63], are considered in this study. The roughness (RI) index is computed from:

$$RI = \sum_{i=1}^{n} |\Delta Z_i| ; 0 < X < 1 \text{km} \tag{4.1}$$

where ΔZ_i is the elevation of the road profile from the mean value at every 0.3 m interval, n is the total number of data points and X is the longitudinal coordinate of the road, as illustrated in Figure 4.3. The RI values of three different roads, referred to as 'smooth', 'medium rough' and 'rough' are computed as 1.24m/km, 2.64m/km and 5.8m/km, respectively.
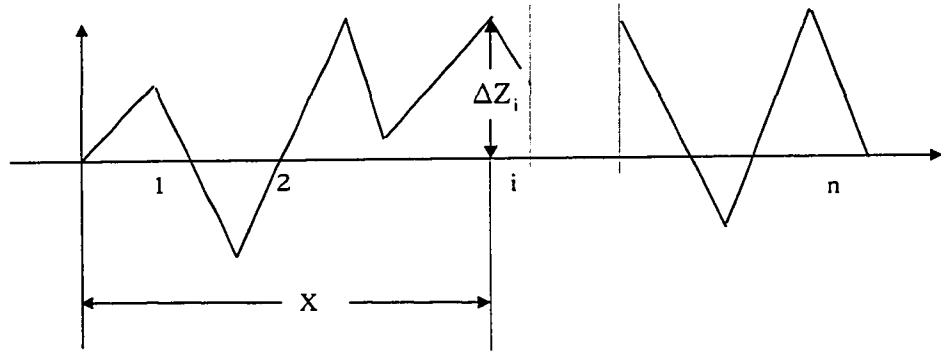
Figure 4.3: Elevation of road profile and computation of roughness index.

The comparison of weighted seat longitudinal and vertical acceleration with the *fatigue decreased proficiency limits* proposed in ISO-2631[40] for 1-16 hours exposure duration is shown in Figure 4.4. The results show that the vibration along the longitudinal and vertical directions increase considerably with the increase in the roughness of the terrain. The vibration transmitted along the X-axis is observed to be well below the 8 hours exposure duration for all the terrain profiles. While the vibration transmitted along the Z-axis is observed to be higher than 1 hour exposure duration, when the vehicle traverses on a rough terrain. When the vehicle traverses on a smooth terrain (RI=1.24 m/km), the vibration along the Z-axis is well below the 8 hours exposure duration.
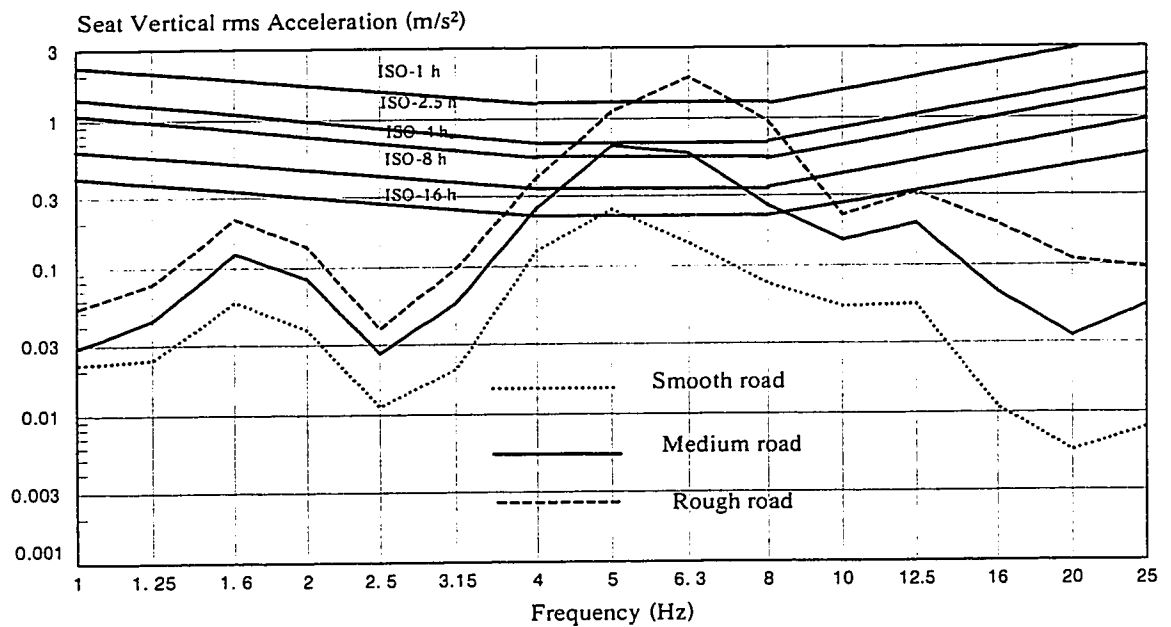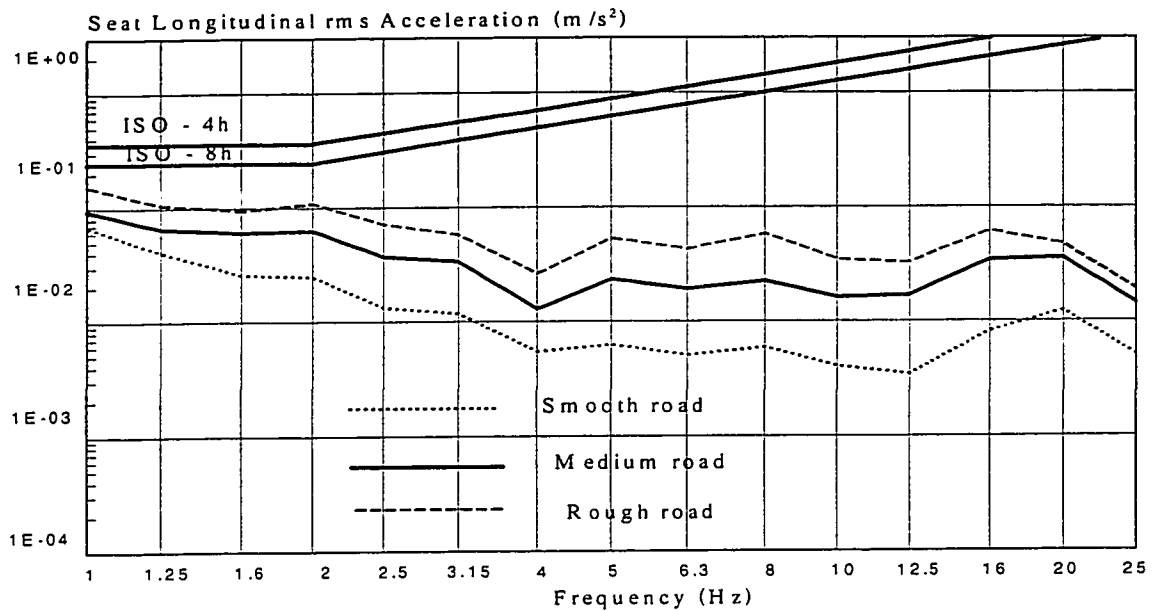
Figure 4.4: Influence of terrain roughness on the longitudinal and vertical rms acceleration response at the seat in relation to the exposure limits proposed in ISO-2631 (1978). (Task: plowing; Vehicle speed: 8 km/h)

Unweighted RMS Acceleration (m/s²-rad/s²)

Weighted RMS Acceleration (m/s²-rad/s²)
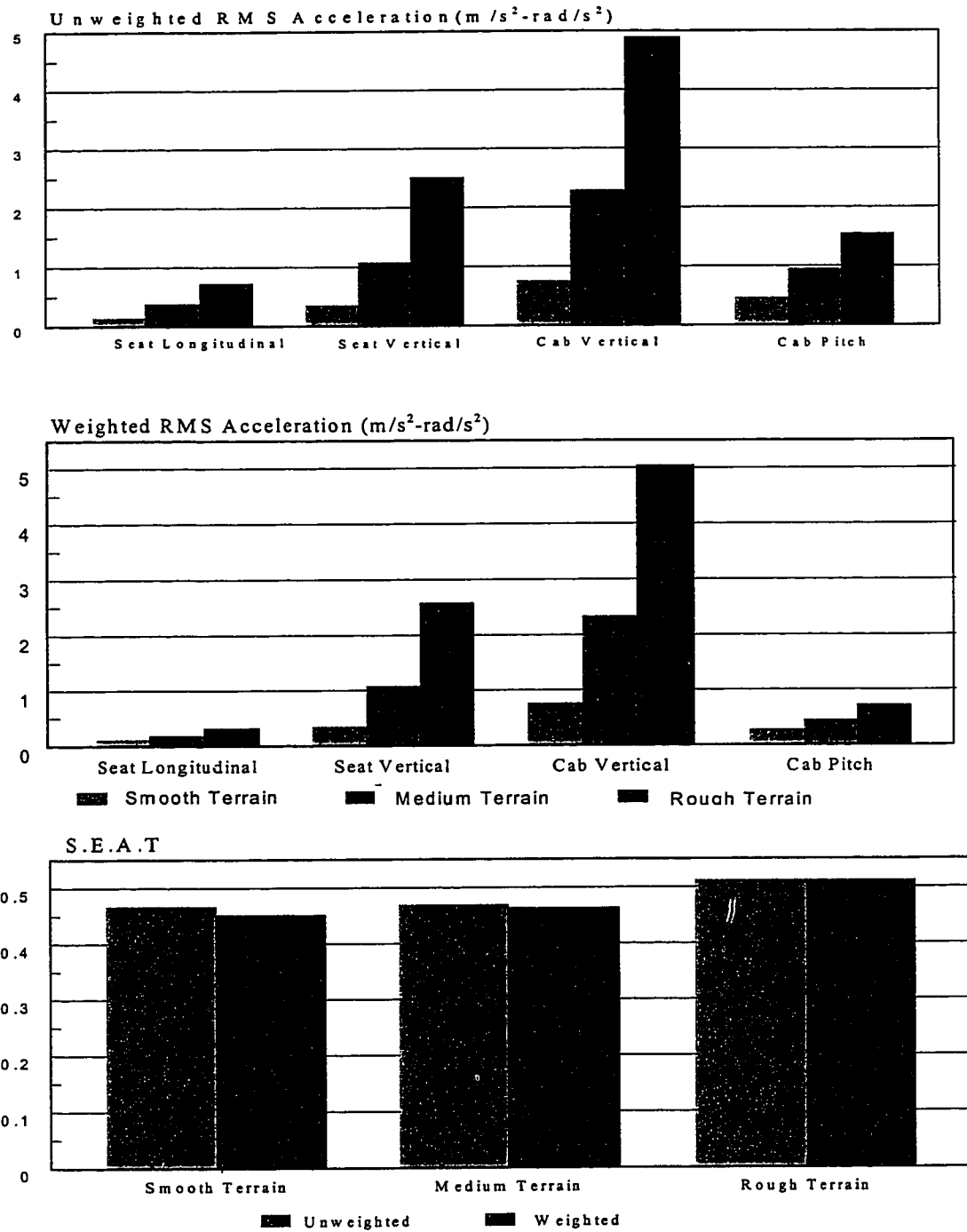
S.E.A.T

Figure 4.5: Influence of terrain profile on the overall rms acceleration
and S.E.A.T. values (Task: plowing, Vehicle speed: 8 km/h).

128

The influence of terrain profile on the longitudinal, vertical and pitch ride quality is further investigated through examination of overall rms acceleration. The frequency-weighting filters proposed in the revised ISO-2631 (1997) [43] are applied to determine the overall weighted rms acceleration along the three directions. Figure 4.5 illustrates the unweighted and weighted rms acceleration at the driver-seat interface and at the cab floor as a function of roughness of terrain profile. From the results, it is apparent that the overall (both weighted and unweighted) rms vertical acceleration at the cab increases considerably with the increase in the roughness of the random terrain profile. The increase in the overall rms acceleration of the seat is relatively high with the increase in the roughness of random terrain profile. Compared with the vertical vibration, the vibrations along the longitudinal and pitch are relatively insignificant. It should be noted that weighted rms acceleration along the vertical axis similar to the unweighted values, while the weighted pitch and longitudinal accelerations are considerably lower than the respective unweighted values. The vertical vibration predominantly occur in the 4-10 Hz bands, where the amplitude ratio of the weighting filter is either close to or greater than unity. The application of frequency weighting to the vertical vibration thus yields values similar to the unweighted values.

The S.E.A.T values, presented in Figure 4.5 reveal values ranging from 0.45 to 0.53. The S.E.A.T. value tends to increase with the increase in the terrain roughness. A S.E.A.T. value of 0.45 is attained when the vehicle traverses a smooth terrain, which increases to 0.53 under rough road. The effectiveness of the suspension seat in attenuating vertical vibration thus reduces by approximately 17%, when the vehicle is subject to excitation from a rough road.

4.3.2 Influence of Vehicle Speed

The ride quality of snowplow vehicle is strongly related to the operating speed of the vehicle. For this study, the influence of vehicle speed on the ride quality is investigated by varying the vehicle speed in the vicinity of the nominal value of 8 km/h. The ride quality of the snowplow vehicle is investigated for four different speeds: 3, 5, 8 and 12 km/h for the plowing task; and 5, 8, 12 and 18 km/h for the transit operation.

The acceleration response characteristics at the driver-seat interface are evaluated along the vertical and longitudinal axes. The frequency-weightings, proposed in ISO-2631 (1978) [40], are applied to the longitudinal and vertical acceleration response expressed in terms of rms acceleration in the respective 1/3 -octave frequency bands. The weighted rms acceleration response is assessed in relation to the fatigue decreased proficiency limits. Figure 4.6 illustrates the assessment of longitudinal and vertical ride response encountered at the driver seat during plowing tasks in relation to the fatigue decreased proficiency (FDP) limits as a function of the exposure duration. The results show that plowing tasks performed at a lower speed 3 km/h yield superior longitudinal ride in the entire speed range. The operation at 5 km/h yields increased levels of longitudinal acceleration in the 1-2 Hz frequency range, in which the human body is known to be most fatigue sensitive, and in 8 to 12.5 Hz bands. While an increase in the vehicle speed to 8 km/h yields better ride performance, further increase to 12 km/h results in poor ride performance along the longitudinal direction. The results in Figure 4.6 also show that plowing tasks performed at a lower speed 3 km/h yield superior vertical ride in the entire speed range. The operation at 5 km/h yields increased levels of vertical acceleration in the 8-10 Hz frequency range, which is the predominant frequency range of

Seat Longitudinal RMS Acceleration (m/s²)

1E+00
ISO - 4h
ISO - 8h

1E-01

1E-02

.... 3 Km/h

—·—·—·—·— 5 Km/h

——————— 8 Km/h

1E-03

——————— 12 Km/h

1E-04

1   1.25   1.6   2   2.5   3.15   4   5   6.3   8   10   12.5   16   20   25

Frequency (Hz)

Seat Vertical RMS Acceleration (m/s²)

3
ISO-1 h
1
ISO-2.5 h
ISO-4 h
ISO-8 h

0.3

0.1

.03   .... 3 Km/h

—·—·—·—·— 5 Km/h

.01   ——————— 8 Km/h

003   ——————— 12 Km/h

001

1   1.25   1.6   2   2.5   3.15   4   5   6.3   8   10   12.5   16   20   25

Frequency (Hz)

Figure 4.6: Influence of vehicle speed on the longitudinal and vertical RMS acceleration response at the seat in relation to the exposure limits proposed in ISO-2631 (1978). (Task: plowing; Terrain: medium rough)

131

Figure 4.7: Influence of vehicle speed on the overall rms acceleration and S.E.A.T. values (Task: plowing, Terrain: medium rough).

132

the wheels. An increase in the vehicle speed to 8 km/h and 12 km/h yields poor ride performance along the vertical direction in the 5-6 Hz frequency bands, which is the dominant frequency of the cab.

The influence of vehicle speed on the longitudinal, vertical and pitch ride quality is further investigated through examination of the overall rms acceleration. The frequency-weighting filters proposed in the revised ISO-2631 (1997) [43] are applied to determine the overall weighted acceleration along the three directions. Figure 4.7 illustrates the unweighted and weighted rms acceleration at the driver-seat interface and at the cab floor as a function of the vehicle speed. From the results, it is apparent that the overall (both weighted and unweighted) rms of vertical acceleration at the cab increase considerably with the increase in the vehicle speed. The suspension at the seat, however, tends to effectively attenuate the vertical vibration. The increase in overall rms acceleration of the seat is relatively small. It can be further observed that the vertical weighted accelerations are either similar to or greater than the unweighted acceleration. This is mostly attributed to the resonance of the cab and cab mounts in the vicinity of the 6.3 Hz and 8 Hz bands, where the weighting filter gain exceeds the unity value. The overall rms accelerations obtained along the longitudinal and pitch axes, however, reduce considerably when the weighting filter is applied. This reduction is attributed to the frequency characteristics of the filter and predominance of these vibrations at relatively high frequencies. The longitudinal ride quality, in terms of overall rms acceleration, tends to be poor at speeds of 5 km/h and 12 km/h, and relatively better at speeds of 3 and 8 km/h, as observed earlier in Figure 4.6. The pitch vibration tends to be lower at low as well as extremely high speed of 12 km/h.
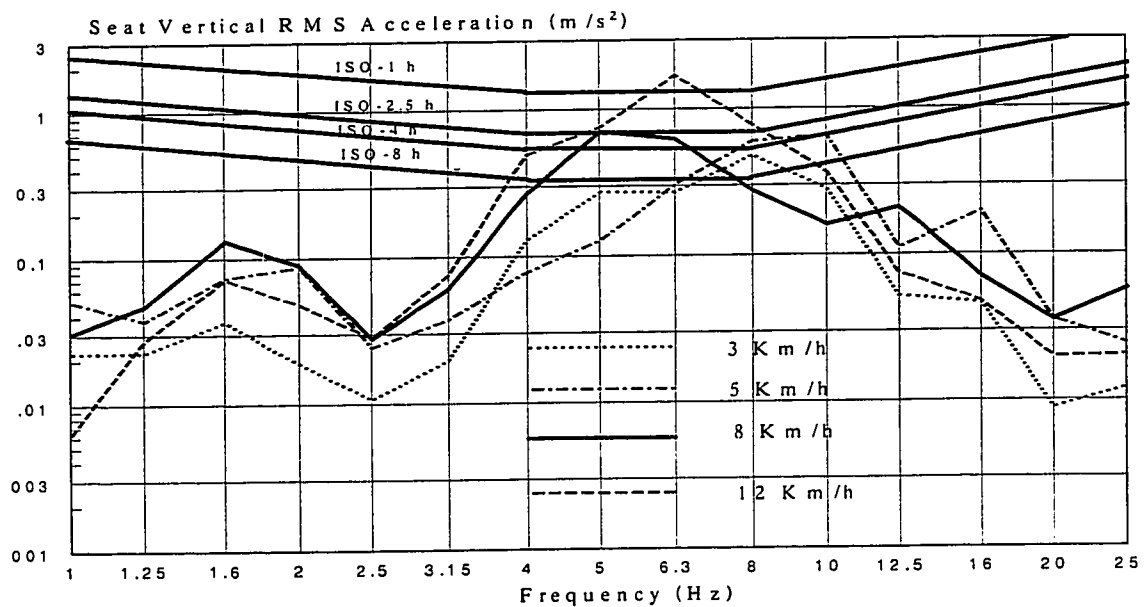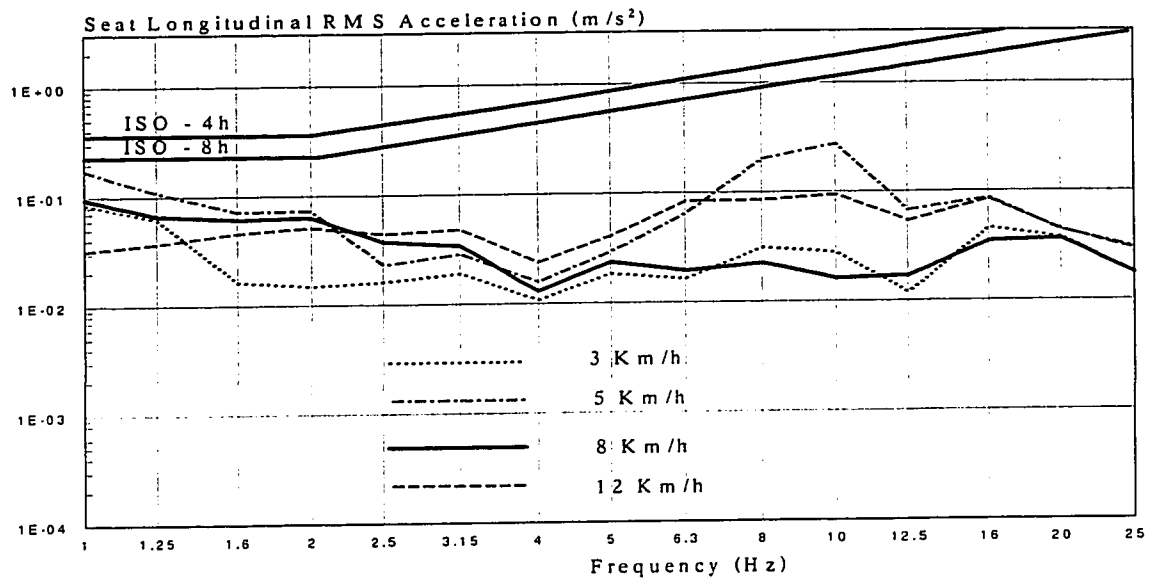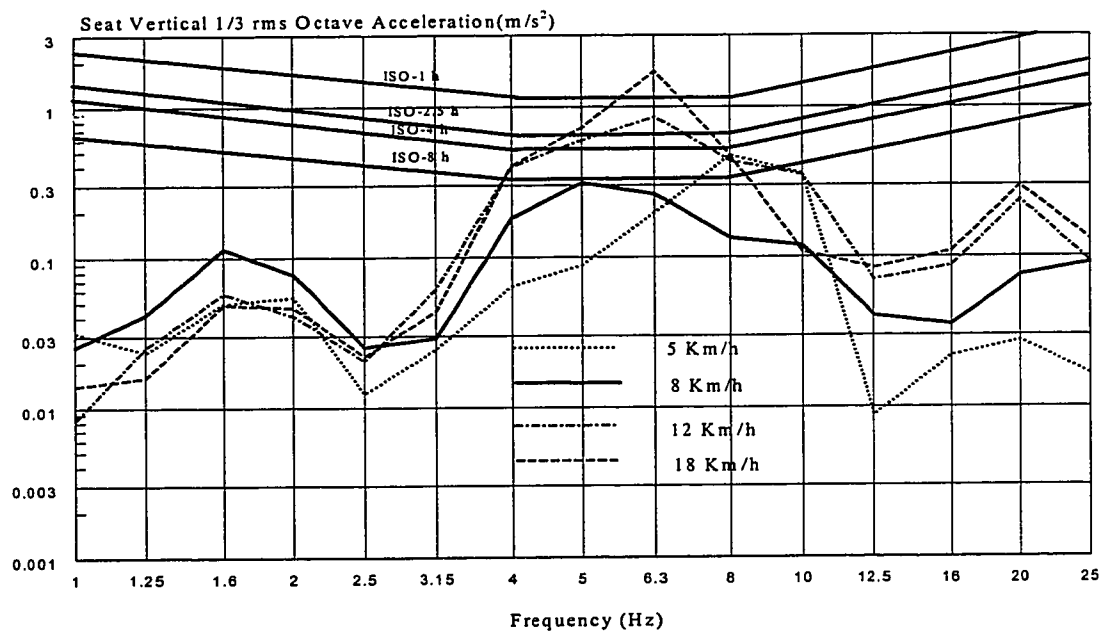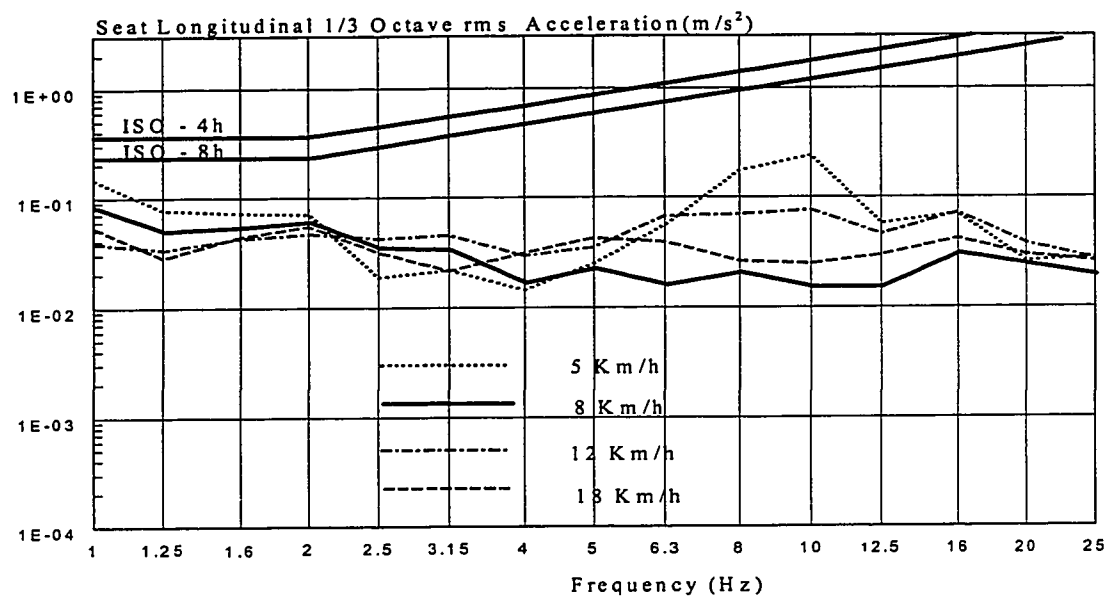
Figure 4.8: Influence of vehicle speed on the longitudinal & vertical rms seat acceleration response at the seat in relation to the exposure limits proposed in ISO-2631 (1978) (Task: transit; Terrain: medium rough)
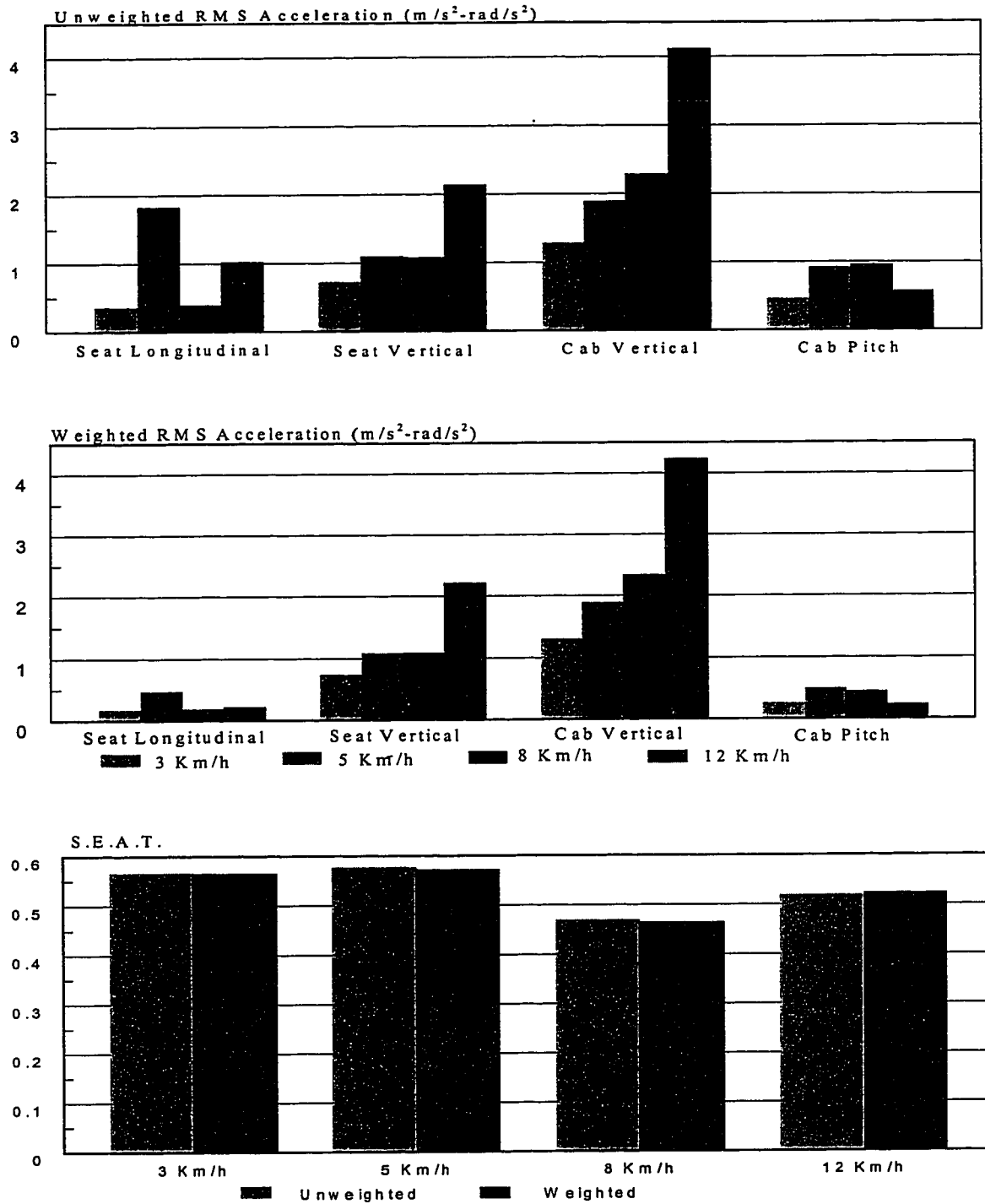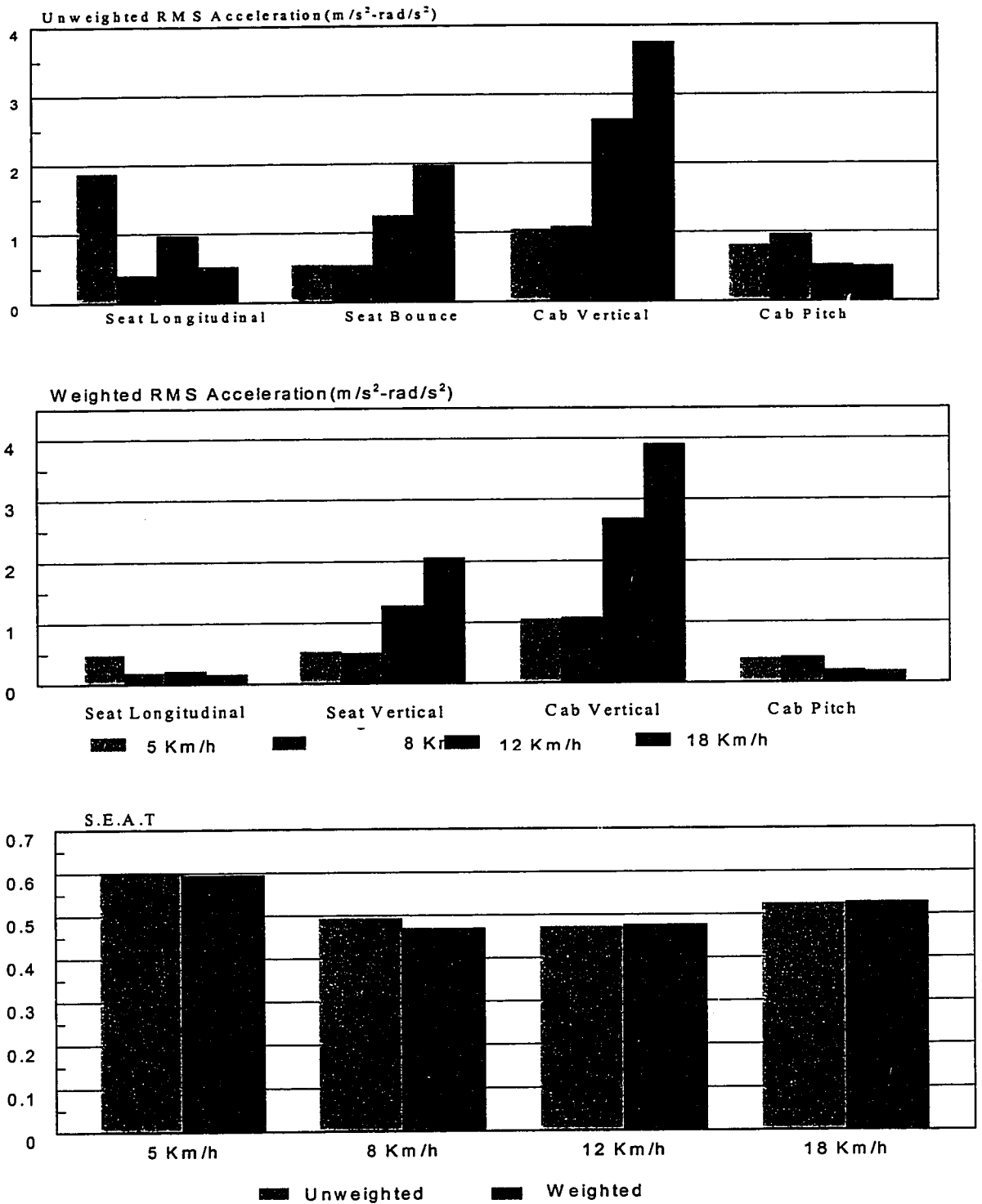
Figure 4.9: Influence of vehicle speed on the overall rms acceleration
and S.E.A.T. values (Task: transit, Terrain: medium rough)

As observed from S.E.A.T. values presented in Figure 4.7, the S.E.A.T. values based upon weighted and unweighted acceleration tend to be quite similar due to predominance of vertical vibration in the 4-10 Hz bands. The S.E.A.T. values vary in the 0.46 to 0.57 range. The suspension is observed to be most effective at a speed of 8 km/h resulting in S.E.A.T. value of 0.46, which approaches higher values at lower speeds.

Figure 4.8 illustrates a comparison of the weighted RMS seat acceleration response along the longitudinal and vertical axes encountered at the seat during transit operation with the FDP exposure limits as a function of the speed. A comparison of Figures 4.6 and 4.8 reveals that the levels of vertical vibration encountered during transit tasks are lower than those attained during plowing tasks, while the longitudinal vibration decreases slightly. The increase in vertical vibration can be attributed to the horizontal and vertical components of the plowing force. The corresponding decrease in the longitudinal vibration, however, is only minimal, which may be attributed to relatively high longitudinal stiffness of the cab mounts and constant velocity assumption.

The results show that the longitudinal vibration levels are relatively higher at a speed of 5 km/h in the 1-2 Hz and 8-12.5 Hz bands as observed earlier for a plowing task. A further increase in the vehicle speed to 18 km/h yields considerable reduction in the rms longitudinal acceleration, specially in the 1-2 Hz and 6.3-20 Hz bands. The levels of longitudinal vibration, however, remain well below the 8 hours exposure limit, irrespective of the vehicle speed. These levels may increase under transit disturbances arising from braking, acceleration and interactions with discontinuities in the sidewalks. The magnitudes of vertical rms acceleration obtained during a transit operation, in general, increase with increase in vehicle speed, specifically in the frequency bands in the

vicinity of vertical mode resonant frequency of the cab mounts. At a higher speed of 18 km/h, the levels of vertical vibration are assessed to be inadequate for an exposure duration of 1 hour. A reduction in the speed to 12 km/h yields satisfactory exposure duration of higher than 1 hour. The vertical vibration encountered at a speed of 8 km/h are judged to be satisfactory for 8 hours exposure, which is mostly attributed to superior attenuation performance of the seat at this speed. Further reduction in the speed to 5 km/h yields high levels of vibration in the 8-10 Hz bands due to the resonant vibrations of the road wheel suspension. The ride performance at this speed is thus considered adequate for exposure duration of 4 hours or slightly higher.

Figure 4.9 illustrates the overall rms accelerations due to vibration transmitted along the longitudinal, pitch and vertical axes. The figure presents the unweighted and frequency weighted rms accelerations due to longitudinal and pitch vibration of the seat, and vertical vibration at the seat and the cab floor. The Figure also illustrates the S.E.A.T values for the suspension seat considered in the study. A comparison of Figures 4.6 and 4.8, corresponding to plowing and transit operations respectively, reveals that the plowing tasks cause relatively higher vertical vibration of the cab and the seat. The effectiveness of the seat also tends to be slightly higher during a transit operation. The unweighted values of rms accelerations along the longitudinal axis at speeds of 5, 8 and 12 km/h are observed to be quite similar for both tasks. The vehicle, however, experiences slightly larger pitch vibrations under plowing operation at speeds of 5 km/h and 12 km/h. This is mostly caused by the additional moments imposed by the snow pushing force acting on the blade. From the comparison, it may be concluded that the

push force does not contribute considerably to the longitudinal ride performance of the vehicle.

The results further show that the overall rms values of vertical acceleration at the seat and the cab decreases slightly, when the speed is increased from 5 km/h to 8 km/h. A further increase in the vehicle speed to 12 and 18 km/h yields significant increase in the overall rms acceleration. The suspension seat provides most effective attenuation of vertical vibration at vehicle speed of 8 km/h and 12 km/h. The results also show that the overall rms values of longitudinal acceleration at the seat decrease significantly, when the speed is increased from 5 km/h to 8 km/h. However, further increase in the vehicle speed from 8 to12 km/h does not yield significant decrease in the overall rms acceleration. For the overall rms acceleration of pitch acceleration at the cab floor, the overall rms values tend to be very small when the speed is increased to 18 km/h. Therefore, it is concluded that the vehicle vertical ride quality deteriorates with higher speeds, whereas the vehicle longitudinal ride quality deteriorates with lower speeds. The seat attenuation performance is worst at 5 Km/h compared to the other speeds.

4.3.3 Influence of Snow Properties

The ride quality of snowplow vehicle employed in a plowing operation is related to the properties of the snow. As evident from equation (3.13), the total snow force generated in the compression zone is directly influenced by the snow density and snow depth in this zone. The influence of snow properties on the ride quality is investigated by varying the maximum snow peak density in the vicinity of the nominal value of 0.35 gm/cc and snow depth in the vicinity of the nominal value of 0.5 m. The ride quality of

the snowplow vehicle is investigated for two different values of maximum density: 0.35 and 0.25 gm/cc; and three different values of snow depth: 0.0, 0.3, 0.5 m.

Influence of Snow Density

The influence of snow density on the longitudinal, vertical and pitch ride quality is investigated through examination of the overall rms accelerations. The frequency-weighting filters proposed in the revised ISO-2631 (1997) [43] are applied to determine the overall weighted rms acceleration along the three directions. Figure 4.10 illustrates the unweighted and weighted rms accelerations at the driver-seat interface and at the cab floor as a function of maximum snow density. From the results, it is apparent that the overall (both weighted and unweighted) rms vertical accelerations at the cab and at the driver seat vary only slightly with change in the snow peak density considered in this study. A closer study of the overall values reveals that a reduction in the snow density yields slightly lower values of rms acceleration.

Influence of Snow Depth

The influence of snow depth on the longitudinal, vertical and pitch ride quality is also investigated through examination of the overall rms acceleration. Figure 4.11 illustrates the unweighted and weighted rms accelerations at the driver-seat interface and at the cab floor as a function of the snow depth. From the results, it is apparent that the overall (both weighted and unweighted) rms of longitudinal, vertical and pitch change very insignificantly, when the snow depth is decreased from 0.5m to 0.3m; the snowdepth of 0.3 m, however, yields slightly lower values of rms acceleration along both

Figure 4.10: Influence of maximum snow density on the overall rms accelerations
and S.E.A.T. values (task: plowing, vehicle speed: 8 km/h).

longitudinal and vertical direction. It should be noted that the horizontal push force is dependent upon the comparison of the snow and thus the depth in the compression zone. The variation in depth of fresh snow considered in this study may not cause significant change in the depth in the compression zone. The overall values of vertical rms acceleration also decrease when snow depth is 0.0 m. The effectiveness of the seat also tends to improve with the lower snow depth as evident from the S.E.A.T. values shown in the Figure 4.11.

4.3.4 Influence of Height of Obstacle

The transient vibration response of the snowplow vehicle may be strongly influenced by the severity of the obstacle, as it traverses during its operation. As discussed earlier, a side-walk snowplow encounters transient excitations due to discontinuities in the sidewalks. While the transient ride response is evaluated under semi-circle obstacles, the severity of such excitations is varied by varying the height of the obstacle. The transient response analysis is performed for three different obstacle heights: 5, 10 and 20 cm. The transient ride response is evaluated in terms of peak vertical acceleration at the driver-seat interface, derived from the response time-history shown in Figure 4.12. The results shown that the peak acceleration increases considerably with severity of the obstacle. A 5cm high obstacle yields peak acceleration of approximately $6 \, m/s^2$ and settling time of approximately 0.9 s. The peak accelerations under 10 cm and 20 cm high obstacles are obtained as $20 \, m/s^2$ and $100 \, m/s^2$, respectively. The settling time under severe obstacles also increase considerably.

141

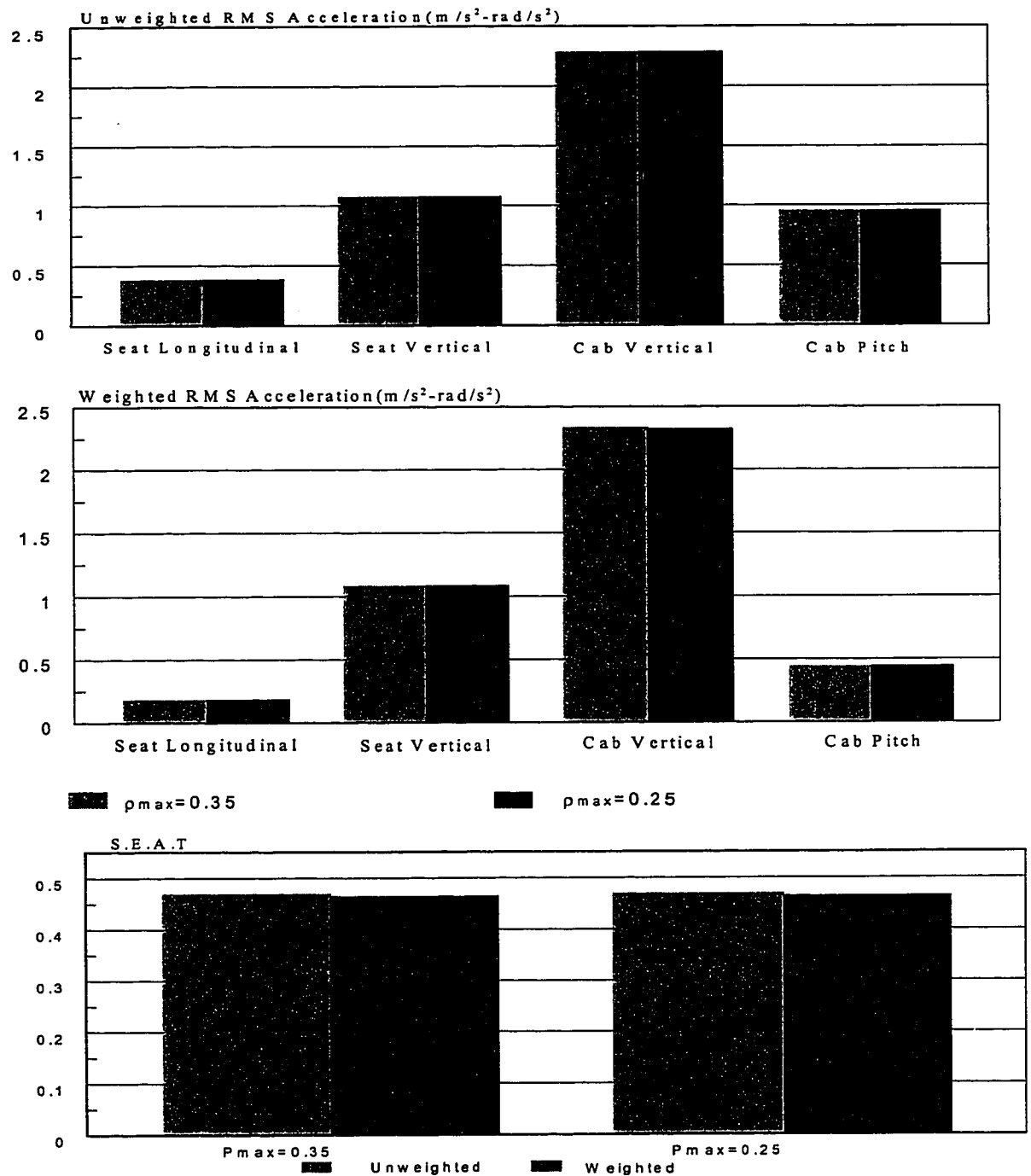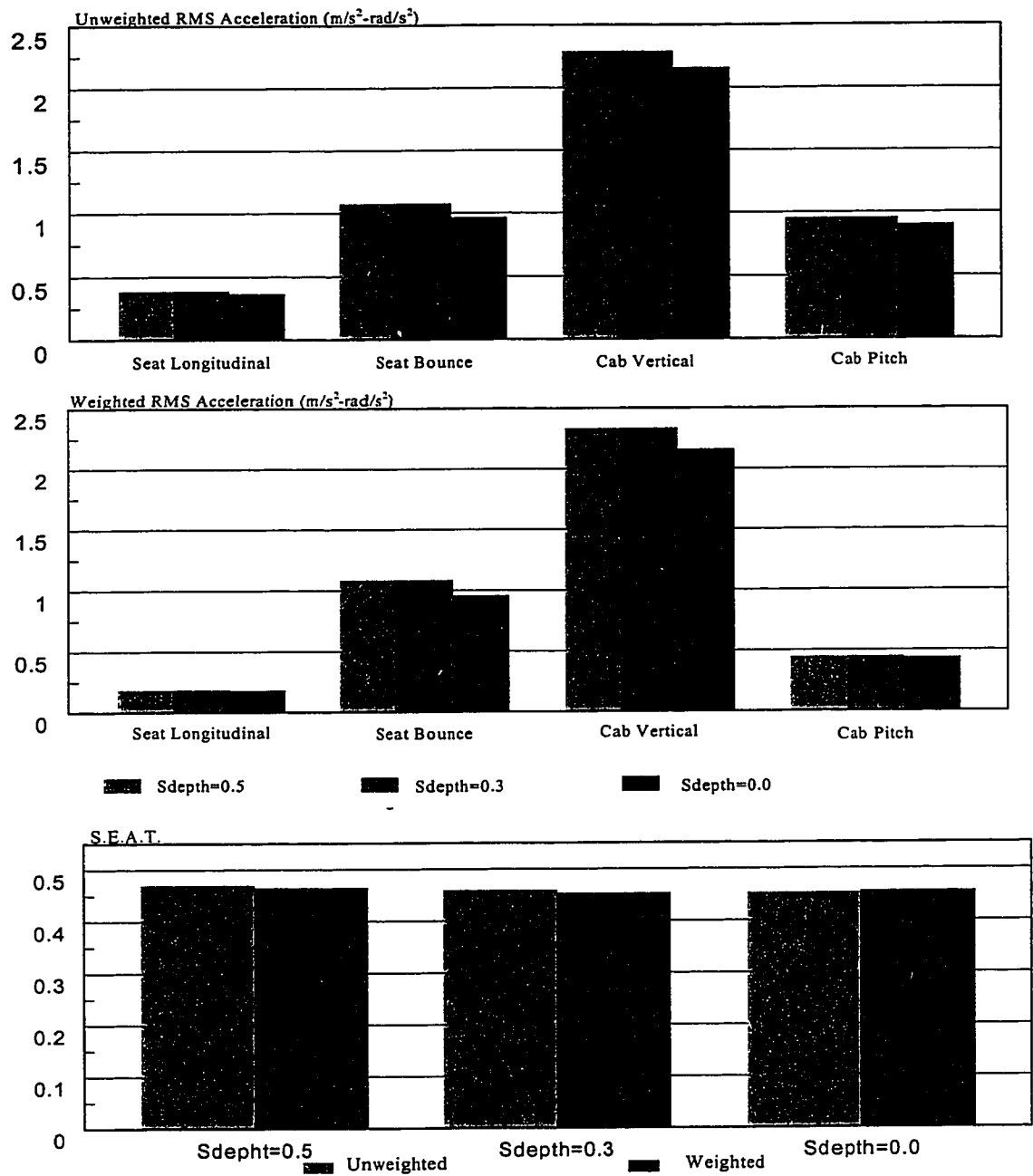Figure 4.11: Influence of snow depth on the overall rms acceleration and S.E.A.T. value. (task: plowing, vehicle speed: 8 km/h)

4.4 INFLUENCE OF DESIGN FACTORS

The results presented in section 4.3 clearly demonstrated that the ride quality of the snowplow vehicle is strongly influenced by various operating conditions in a highly complex manner. The ride quality of snowplow vehicle is also strongly related to many design factors such as seat suspension, cab suspension, wheel suspension stiffness, front wheel suspension stiffness, track stiffness and track pre-tension. A thorough study of influence of design factors on the ride quality performance of the vehicle can provide significant insight into the design of such vehicles to achieve improved ride quality. A parametric study is thus carried out by varying the selected parameters around the nominal values. The influence of variations in such parameters is then assessed in relation to the *fatigue decreased proficiency limits* proposed in ISO-2631 (1978) [40]. The influence of variation in these parameters is further assessed using the overall rms acceleration response along the vertical, longitudinal and pitch axes, using the frequency weighting proposed in the revised version of the ISO document, ISO-2631-1 (1997) [43]. The effectiveness of the suspension seat is evaluated in terms Seat Effective Acceleration Transmissibility based upon he weighted $(S.E.A.T._w)$ and unweighted (S.E.A.T.) rms acceleration. The parametric study is performed by varying the design parameters over a range considered to represent the feasible variations in design parameters. Table 4.2 lists the parameters and the range of variations considered in this study. The numbers indicated in *bold* refer to the nominal values. The results of the parameter study are discussed in the following sections.
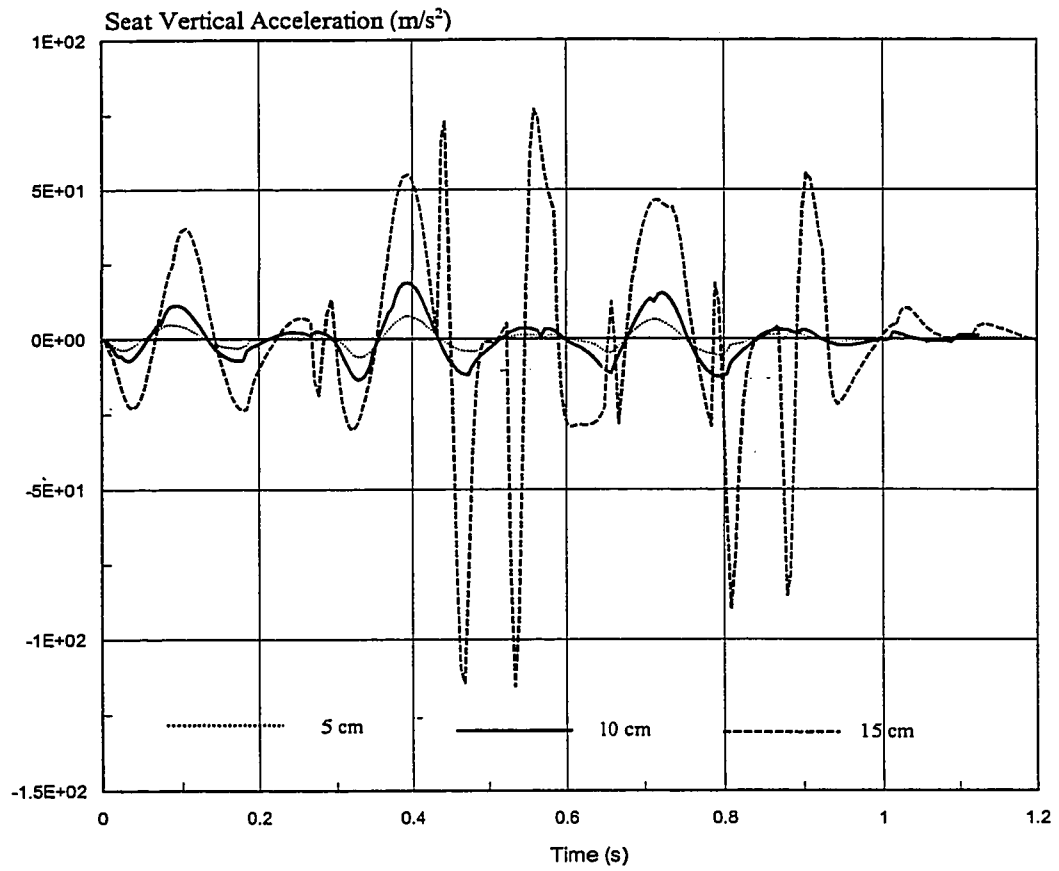
Figure 4.12: Influence of obstacle height on the seat vertical acceleration.
(Task: transit, Vehicle speed: 8 km/h).

Table 4.2: Range of Design Parameters Values.

Parameters	Values
Seat suspension $\begin{cases} \text{spring rate (N/m)} \\ \text{damping coefficent (Ns/m)} \end{cases}$	3675, 4900, 6152 592.5, 104.85; 790.0,139.8; 987.5, 174.75
Cab suspension $\begin{cases} \text{cab mount vertical stiffness (kN/m)} \\ \text{cab mount vertical damping coefficient (Ns/m)} \end{cases}$	245.23, 326.98, 408.72 150, 200, 250
Front wheel suspension (kNm/rad)	7.413, 9.884, 12.355
Wheel stiffness (kN/m/rad)	306.45, 459.68, 612.9, 766.13, 919.35
Track longitudinal stiffness (kN/m)	225, 300, 375
Track pre-tension (kN)	7.5, 10, 12.5

4.4.1 Influence of Seat Suspension Parameters

From the results presented in section 4.3, it is quite apparent that the suspension seat provides effective attenuation of vertical vibration, irrespective of the operating conditions. The effectiveness of a seat-suspension is vital for the comfort perception and protection of the driver from high magnitude ride vibration originating from the track-terrain interactions. Since effectiveness of a suspension seat is mostly dependent upon its spring rates (K_s) and damping parameters (C_A, C_B), the influence of variation in these parameters is further explored to seek improved attenuation performance. The paramteric study is performed by varying the seat suspension parameters in the vicinity of the nominal values of seat suspension stiffness of 4900 N/m and damping coefficient

145

$(C_A = 790 \, \text{Ns}/\text{m}, C_B = 139.8 \, \text{Ns/m})$. The ride quality of the snowplow vehicle is investigated for three different seat suspension stiffness and three different seat damping coefficients: 3675, 4900, 6125 N/m for the seat suspension stiffness and; (592.5, 104.85); (790.0, 139.8) and (987.5, 174.75) Ns/m for the damping coefficients.

Figure 4.14 illustrates the influence of seat suspension stiffness on the vertical ride response encountered at the driver seat during plowing tasks in relation to the fatigue decreased proficiency limits as a function of the exposure limits. The results show that variation in vertical seat suspension spring rate influence the seat vertical acceleration response in the 1.6 Hz frequency band attributed to the natural frequency of the seat. The suspension seat, however, does not affect the vehicle ride in in 4-8 Hz frequency range, where the vertical vibration is predominant. An increase in suspension stiffness to 6125 N/m yields increased levels of vertical acceleration in the vicinity of 1.6 Hz, and a softer seat suspension yields lower levels of acceleration in the vicinity of 1.6 Hz. Figure 4.14 illustrates the overall unweighted and weighted rms acceleration at the seat and the cab floor as a function of the spring rate K_s. The results clearly show an increase in overall rms accelerations of the seat and the cab. The Figure also shows that effectiveness of the seat, expressed in terms of its S.E.A.T value improves with decrease in the spring rate. The reduction in the S.E.A.T. value, however, is not significant for the variations considered in the study.

The influence of seat suspension damping coefficients on the vertical ride response at the seat and cab floor is investigated through examination of the overall rms acceleration. The damping coefficients are varied to study the influence of both the low
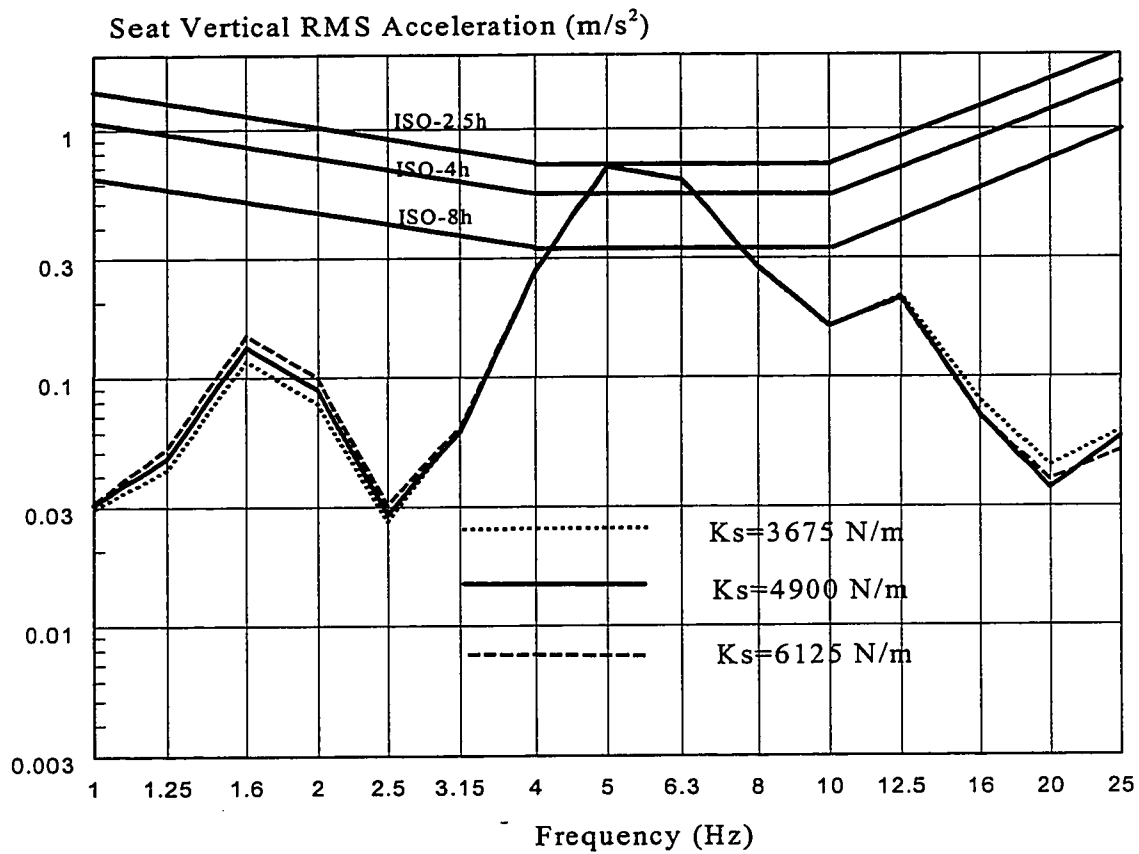
Figure 4.13: Influence of seat suspension stiffness on the vertical RMS acceleration responseat the seat (Task: plowing; Vehicle speed: 8km/h; Terrain: medium rough).
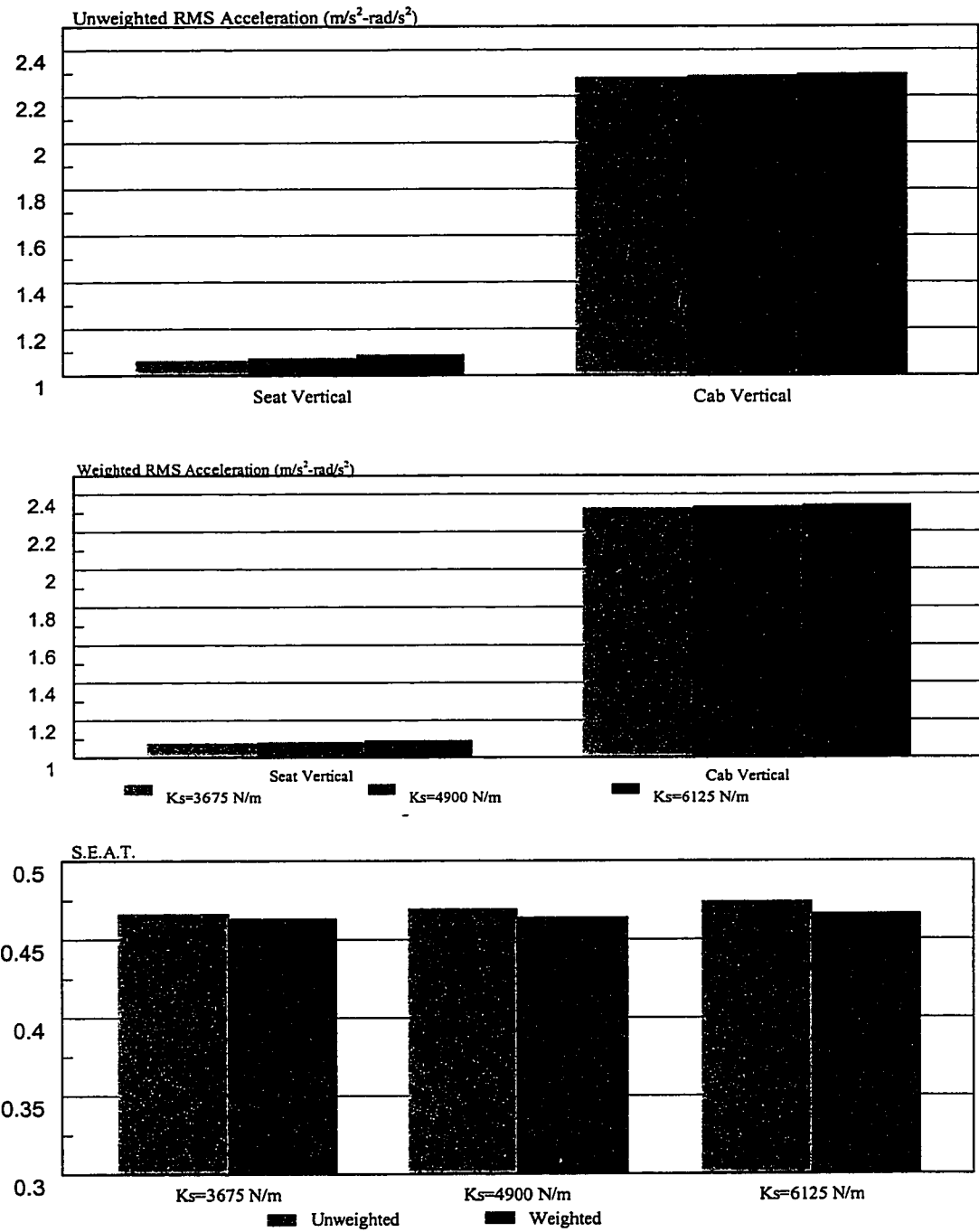
Figure 4.14: Influence of seat suspension stiffness on the overall RMS acceleration and S.E.A.T. values (task: plowing, vehicle speed: 8 Km/h).

speed or bleed damping coefficient (C_A) and high speed or blow-off damping coefficient (C_B), while the transition velocity is held constant. Figure 4.15 illustrates the unweighted and weighted vertical rms accelerations at the driver-seat interface and at the cab floor as a function of seat suspension damping coefficients. The results show that the overall (both unweighted and weighted) rms of vertical acceleration at the seat decreases considerably with increase in the damping coefficients; while the overall rms of vertical acceleration at the cab increases considerably with increase in suspension damping coefficients. High suspension damping tends to reduce the vertical vibration at the seat in the vicinity of the suspension natural frequency (1.6 Hz band). The overall rms of vertical acceleration thus reduces with increased damping . A heavily damped suspension seat, in general, yields poor vibration isolation at higher excitation frequencies. In the case of snowplow vehicle considered in this study, the predominant vibration occur in the 4-8 Hz frequency range. The increase in suspension damping appears to affect these vibration only slightly. The increased damping, however, causes increased vibration at the cab floor, and thus lower S.E.A.T. values, as shown in the Figure. The S.E.A.T. value for a lightly damped seat approaches 0.52 and that of heavily damped seat reduces to 0.41.

4.4.2 Influence of Cab Suspension Parameters

The analytical and field measured vibration response reveals dominant vertical vibration in the vicinity of vertical mode natural frequency of the cab. Since the cab is supported on very lightly damped elastic cab mounts, the high magnitude of vibration can be attributed to resonant vibration of a lightly damped system. Furthermore, apart from the seat suspension, the suspension at the cab forms the closest link with the driver. The
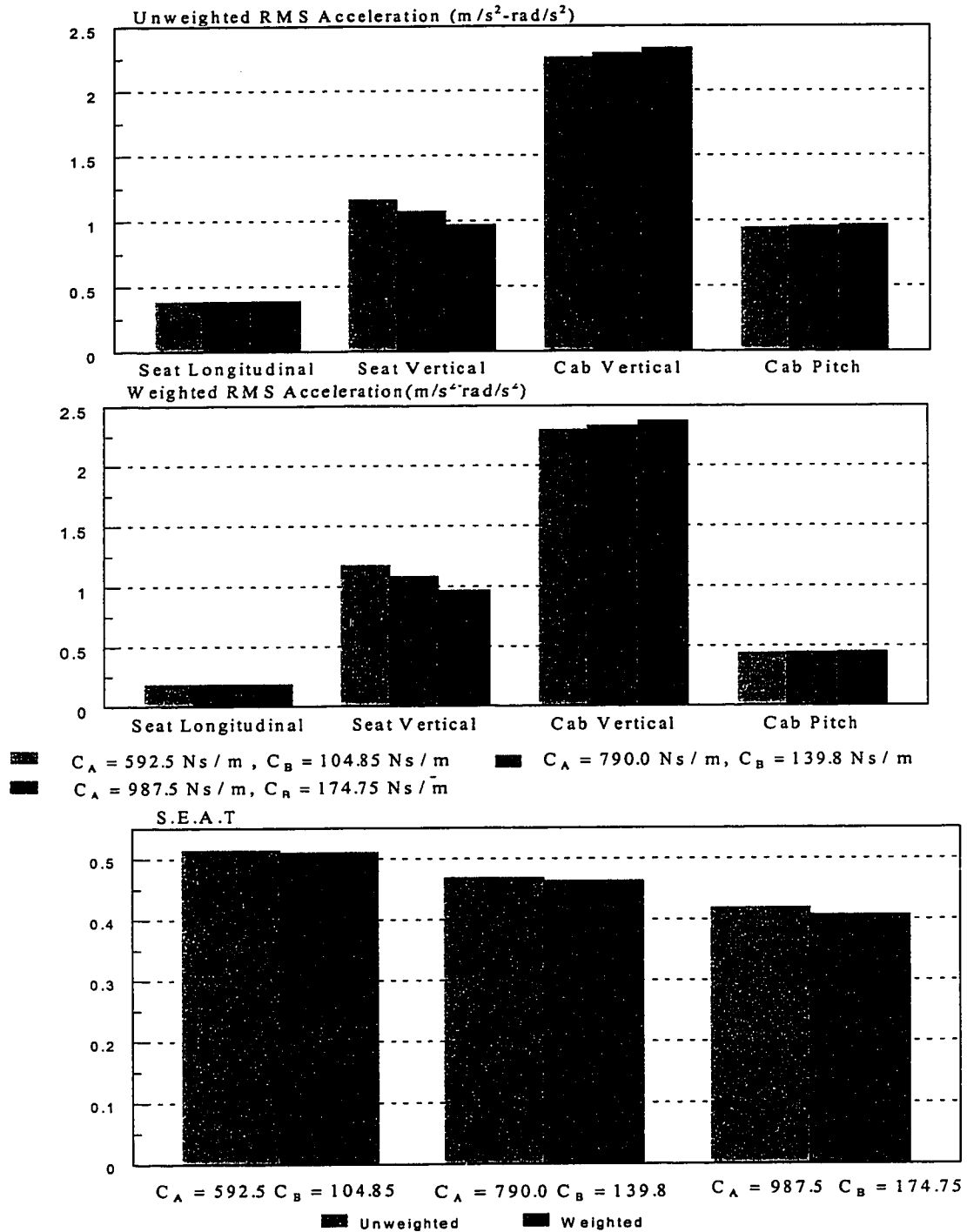
149

Figure 4.15: Influence of seat damping coefficients on the overall RMS accelerations and S.E.A.T. values (task: plowing, vehicle speed: 8 Km/h).

cab suspension design parameters are thus considered to be vital for enhancement of vehicle ride quality. The influence of vertical stiffness and damping of the cab mount on the ride quality are investigated, while the parameters are varied as outlined in Table 4.2.

The acceleration response characteristics at the driver-seat interface are evaluated along the vertical and longitudinal axes, and expressed in terms of rms accelerations in the respective 1/3- octave frequency bands. Figure 4.16 illustrates vertical and longitudinal weighted rms accelerations in relation to the fatigue decreased proficiency limits, as a function of the cab mount stiffness (K_{cz}). It should be noted that a variation in the vertical stiffness of the mount also yields proportional variation in its radial stiffness (K_{cx}). The results show a softer mount reduces the longitudinal acceleration transmitted to the driver in the 3.15-8 Hz bands, with increase in transmitted vibration in the 1.25-2 Hz bands. The soft mounts also yield lower vertical vibration in all the frequency bands above 3.15 Hz. This reduction in vibration levels is attributed to relatively lower natural frequencies of the cab supported on softer mounts. Stiffer mounts yields increased levels of vertical and longitudinal vibration at higher frequencies, and relatively lower levels of vibration in the 1-2 Hz bands, however, increases with stiffer cab mounts. The results further show that acceptable exposure duration can be increased significantly by reducing the cab mount stiffness.

The influence of variations in the cab mount stiffness coefficient on the longitudinal, vertical and pitch ride quality is further investigated through examination of the overall rms accelerations. Figure 4.17 illustrates the unweighted and weighted rms acceleration at the driver-seat interface and at the cab floor as a function of cab mount stiffness coefficient. While the overall rms longitudinal acceleration at the seat varies
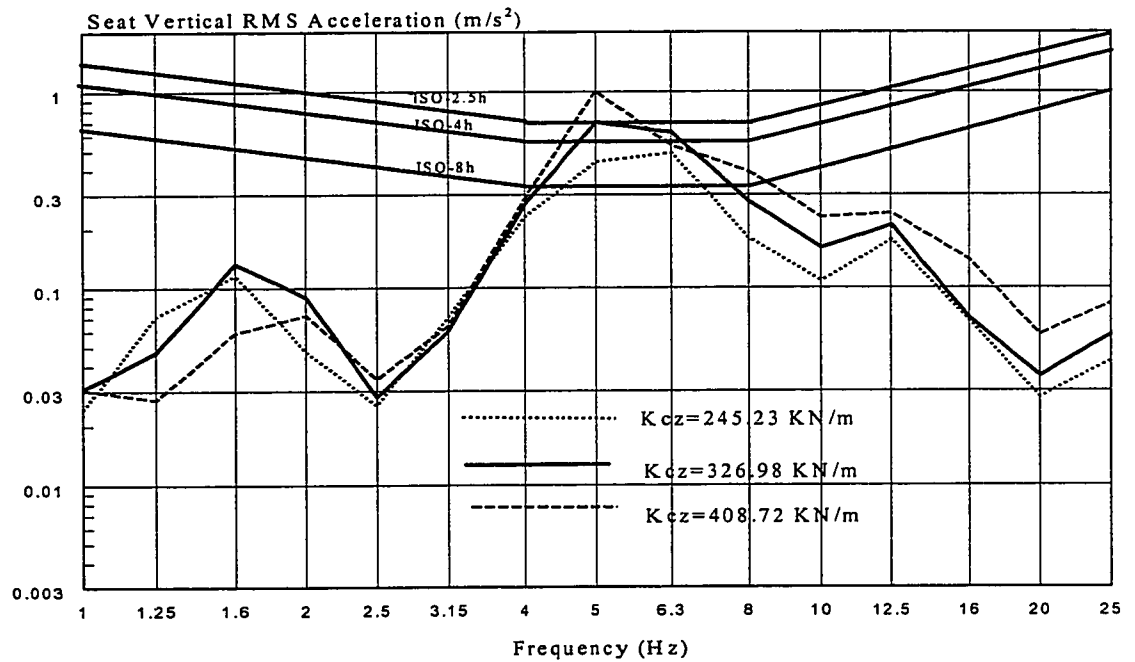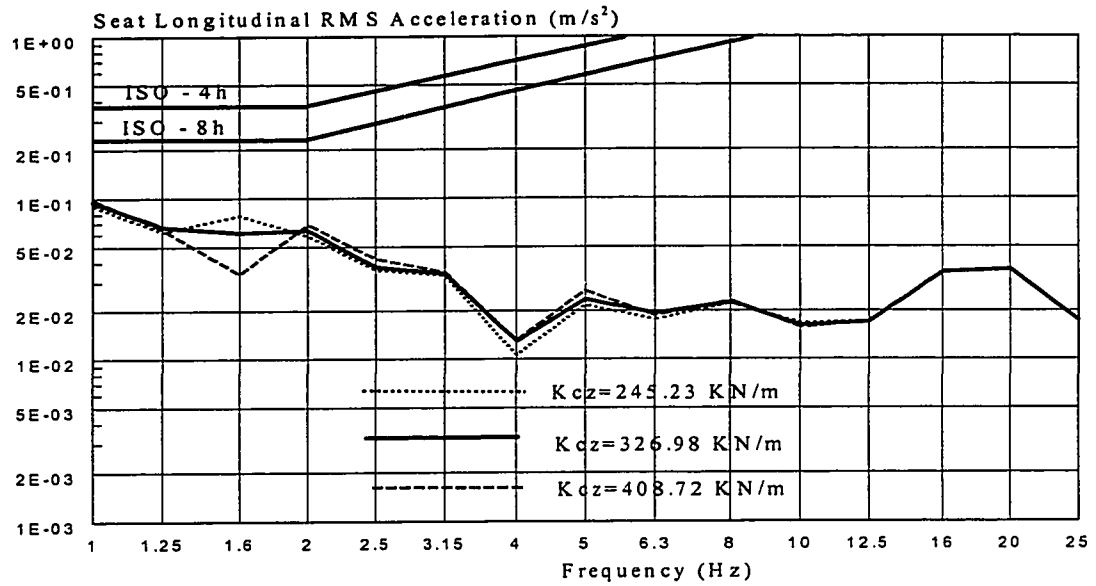
Figure 4.16: Influence of cab mount stiffness on the longitudinal and vertical acceleration response at the seat (Task: plowing; Vehicle speed: 8km/h).

Unweighted RMS Acceleration (m/s²-rad/s²)

Seat Longitudinal   Seat Vertical   Cab Vertical   Cab Pitch

Weighted RMS Acceleration (m/s²-rad/s²)

Seat Longitudinal   Seat Vertical   Cab Vertical   Cab Pitch

Kcz=245.23 KN/m   Kcz=326.98 KN/m
Kcz=408.72 KN/m

S.E.A.T

Kcz=245.23 KN/m   Kcz=326.98 KN/m   Kcz=408.72 KN/m
                       Unweighted   Weighted

Figure 4.17: Influence of cab mount stiffness on the overall RMS acceleration and S.E.A.T. values (task: plowing, vehicle speed: 8 km/h).

153

only slightly with variations in the cab mount vertical stiffness coefficient, vertical acceleration response at the seat and the cab are strongly affected. Similar to the observations made from Figure 4.16, the results show that the overall rms vertical acceleration of the cab and the seat can be reduced considerably by introducing softer cab mounts. The pitch acceleration response of the cab can also be reduced with soft suspension. The S.E.A.T. value of the seat also reduces with softer cab mounts, although the reduction is not significant. From the above results, it may be concluded that relatively softer cab mounts offer considerable potential to enhance the vehicle ride quality.

Figure 4.18 and 4.19 illustrate the influence of mounts damping on the pitch, longitudinal and vertical ride quality of the vehicle. The variation in mount damping does not influence the longitudinal vibration spectra, as shown in Figure 4.18. Mounts with increased damping properties help reduce the resonant vertical response of the cab slightly. Since the elastic mounts offer only low level damping properties, the enhancement of ride quality cannot be achieved through damping properties of such mounts. The overall rms acceleration of vertical and pitch vibration of the cab, however, decrease with increase in mounts damping, as shown in Figure 4.19. The longitudinal rms acceleration response, however, remains insensitive to cab mount damping characteristics. The vibration attenuation performance of the suspension seat also is not affected by the mount damping, as evident from the S.E.A.T. values shown in the Figure.

4.4.3   Influence of Front Wheel Suspension Stiffness

The front road wheel suspension employs an elastic rubber element in torsion.

154

Seat Longitudinal 1/3 Octave Acceleration (m/s²)

ISO - 4h
ISO - 8h

Ccz=150 Ns/m
Ccz=200 Ns/m
Ccz=250 Ns/m

Frequency (Hz)

Seat Vertical RMS Acceleration (m/s²)
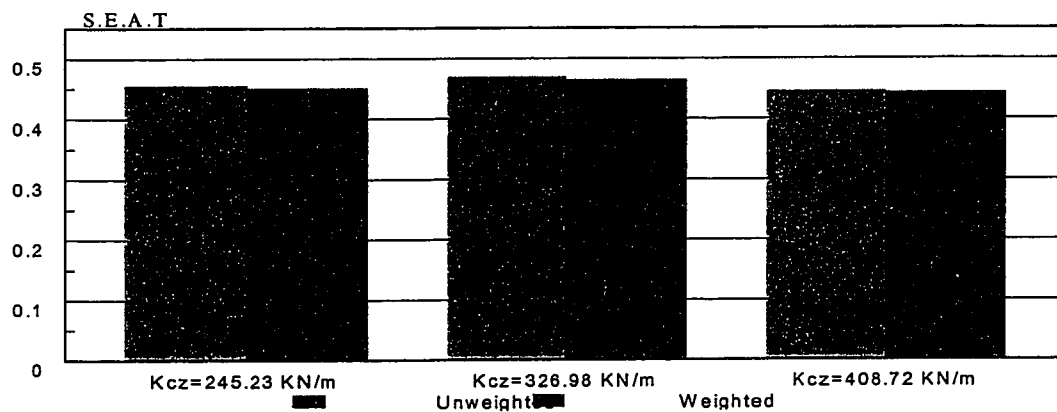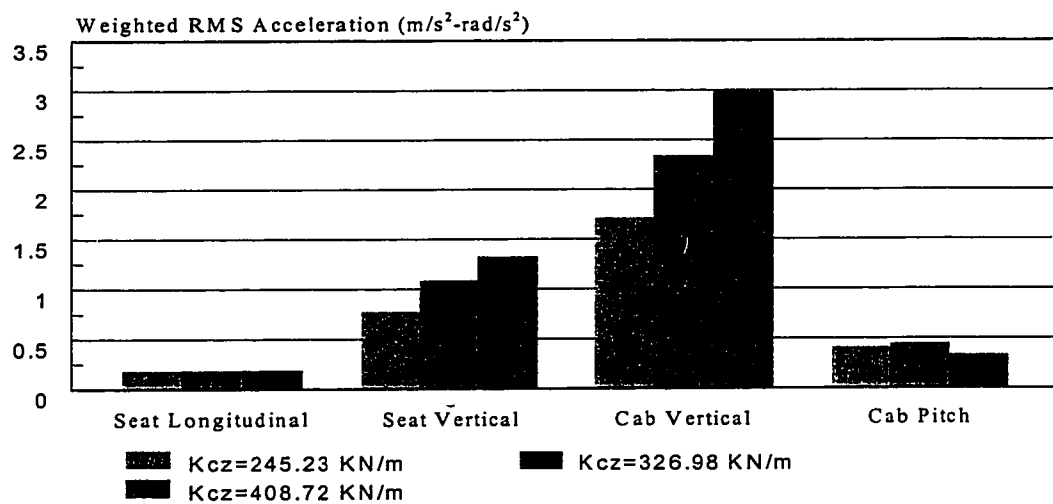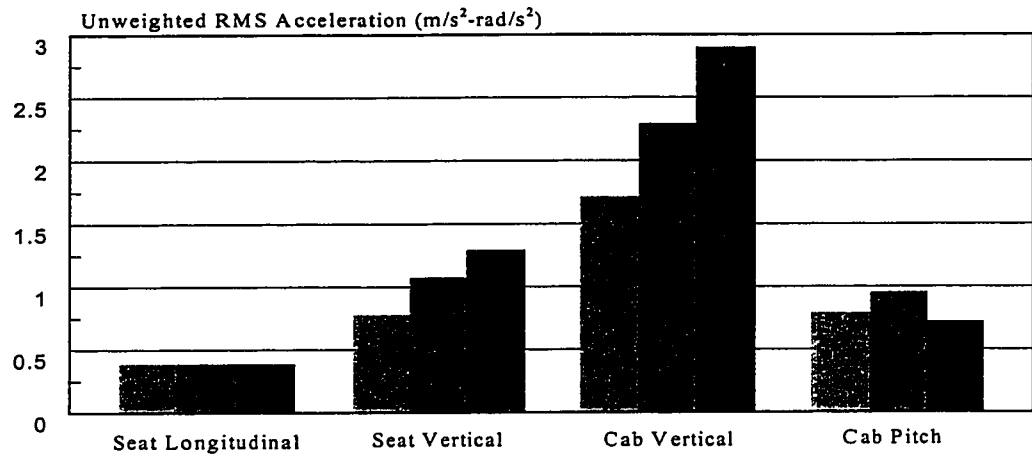
ISO-2.5 h
ISO-4 h
ISO-8 h

Ccz=150 Ns/m
Ccz=200 Ns/m
Ccz=250 Ns/m

Frequency (Hz)
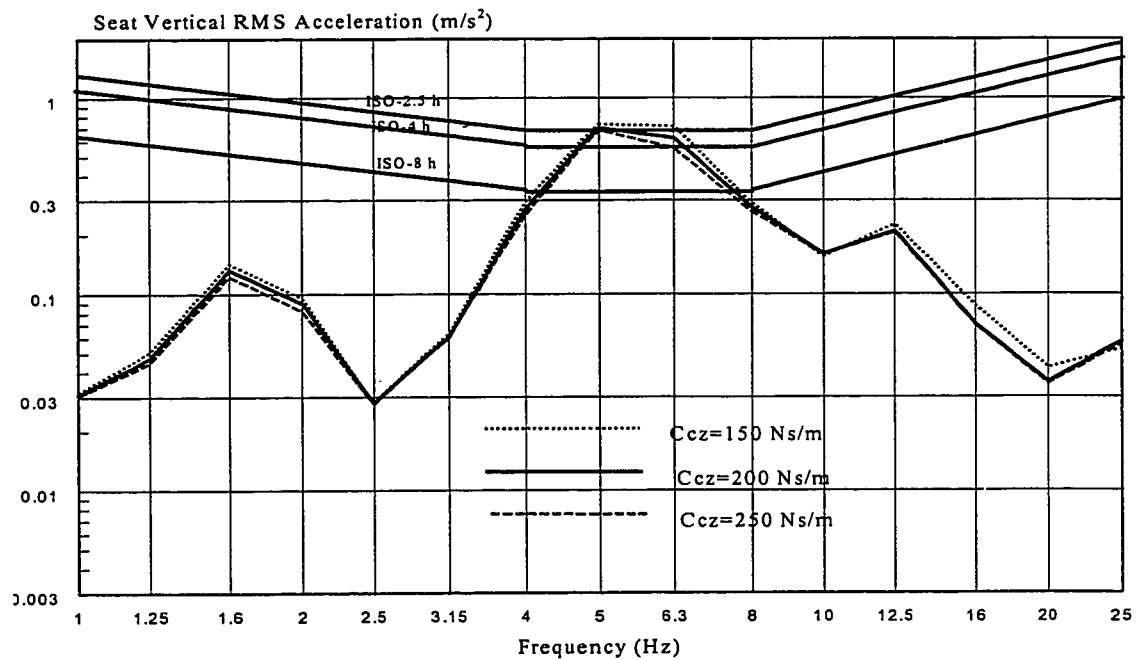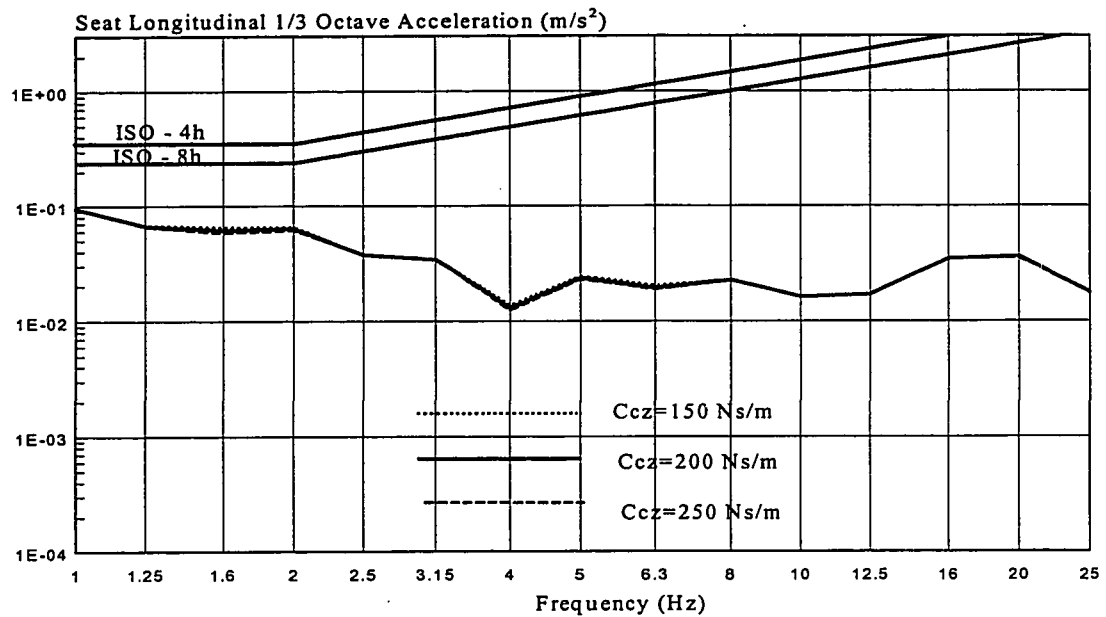
Figure 4.18: Influence of cab mount damping on the longitudinal and vertical RMS acceleration response at the seat in relation to the exposure limits proposed in ISO-2631 (1978) (Task: plowing; Vehicle speed: 8km/h)

155

Unweighted RMS Acceleration (m/s^2-rad/s^2)

Weighted RMS Acceleration (m/s^2-rad/s^2)

Ccz=150 Ns/m   Ccz=200 Ns/m   Ccz=250 Ns/m

S.E.A.T

Ccz=150 Ns/m   Ccz=200 Ns/m   Ccz=250 Ns/m
Unweighted   Weighted

Figure 4.19: Influence of cab mount damping on the overall RMS acceleration
and S.E.A.T. values (task: plowing, vehicle speed: 8 Km/h).

156

The influence of torsional stiffness of the rubber bushing on the ride performance of the vehicle is investigated for three different stiffness values: 7.41, 9.88, 12.36 kNm/rad. The acceleration response characteristi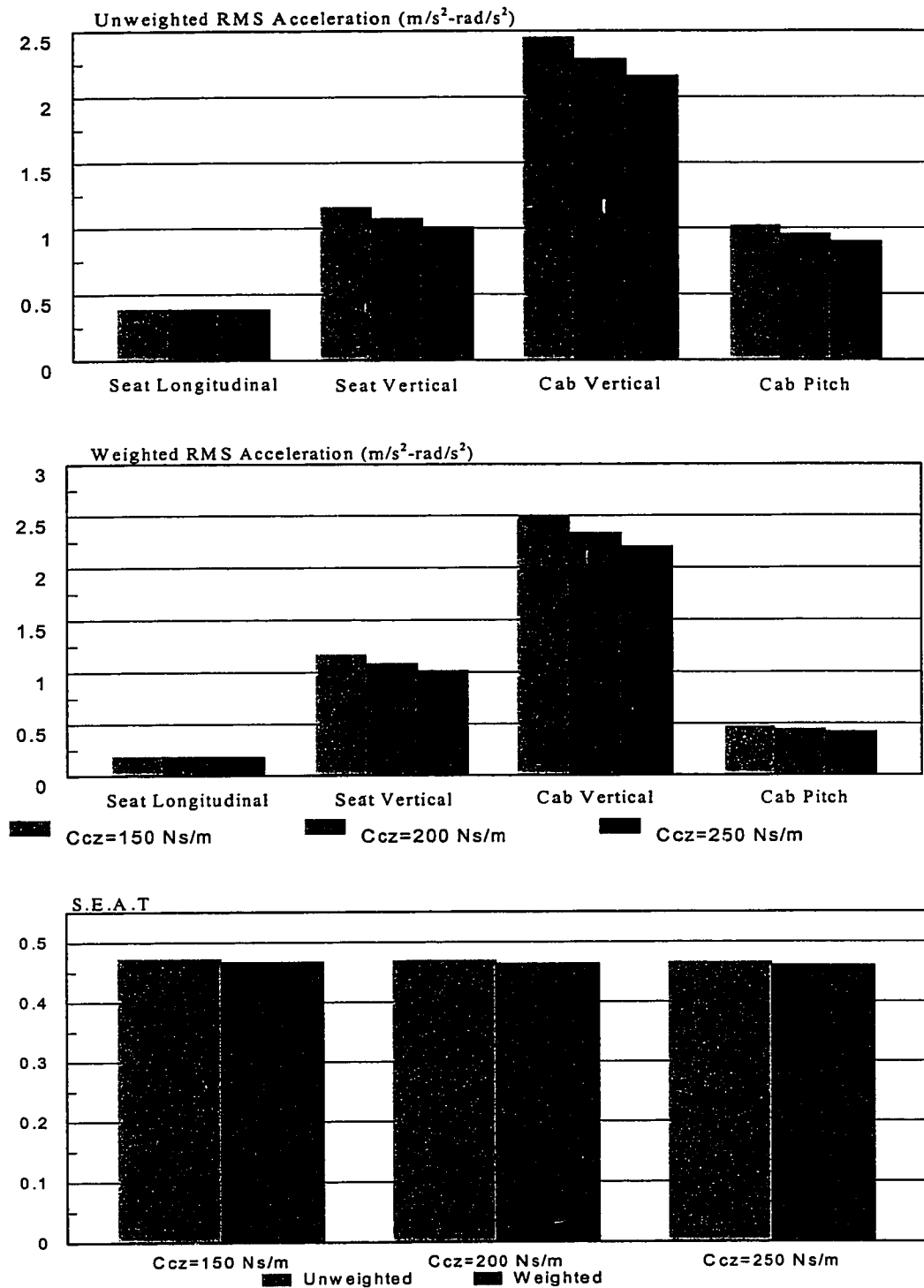cs at the driver-seat interface are evaluated along the vertical and longitudinal axes. Figure 4.20 shows a comparison of weighted longitudinal and vertical RMS acceleration at the seat with the exposure limits, as a function of front wheel suspension stiffness. The influence of front wheel suspension stiffness on the longitudinal, vertical and pitch ride quality is further investigated through examination of the overall rms acceleration, as shown in Figure 4.21. The results show that variation in torsional stiffness of the first road wheel suspension does not affect the longitudinal, pitch and vertical ride. An increase in the torsional stiffness, however, tends to increase the vertical acceleration response in the higher frequency bands (>10 Hz), around the resonant frequencies of the first road wheel. The overall rms vertical acceleration at the cab floor thus increases with increase in torsional stiffness. The S.E.A.T. value for the seat tends to decrease with higher torsional stiffness, which is primarily due to higher levels of cab vertical vibration at higher frequnencies.

4.4.4 Influence of Road Wheel Stiffness

The wheel-track-terrain interactions and thus the dynamic wheel forces transmitted to the chassis are directly related to the road wheel stiffness. The conventional vehicles employ solid rubber wheels, which are known to possess very high stiffness characteristics. These road wheels can be replaced by pneumatic tires resulting in considerably lower stiffness. Different rubber compounds and wheel sizes may also be
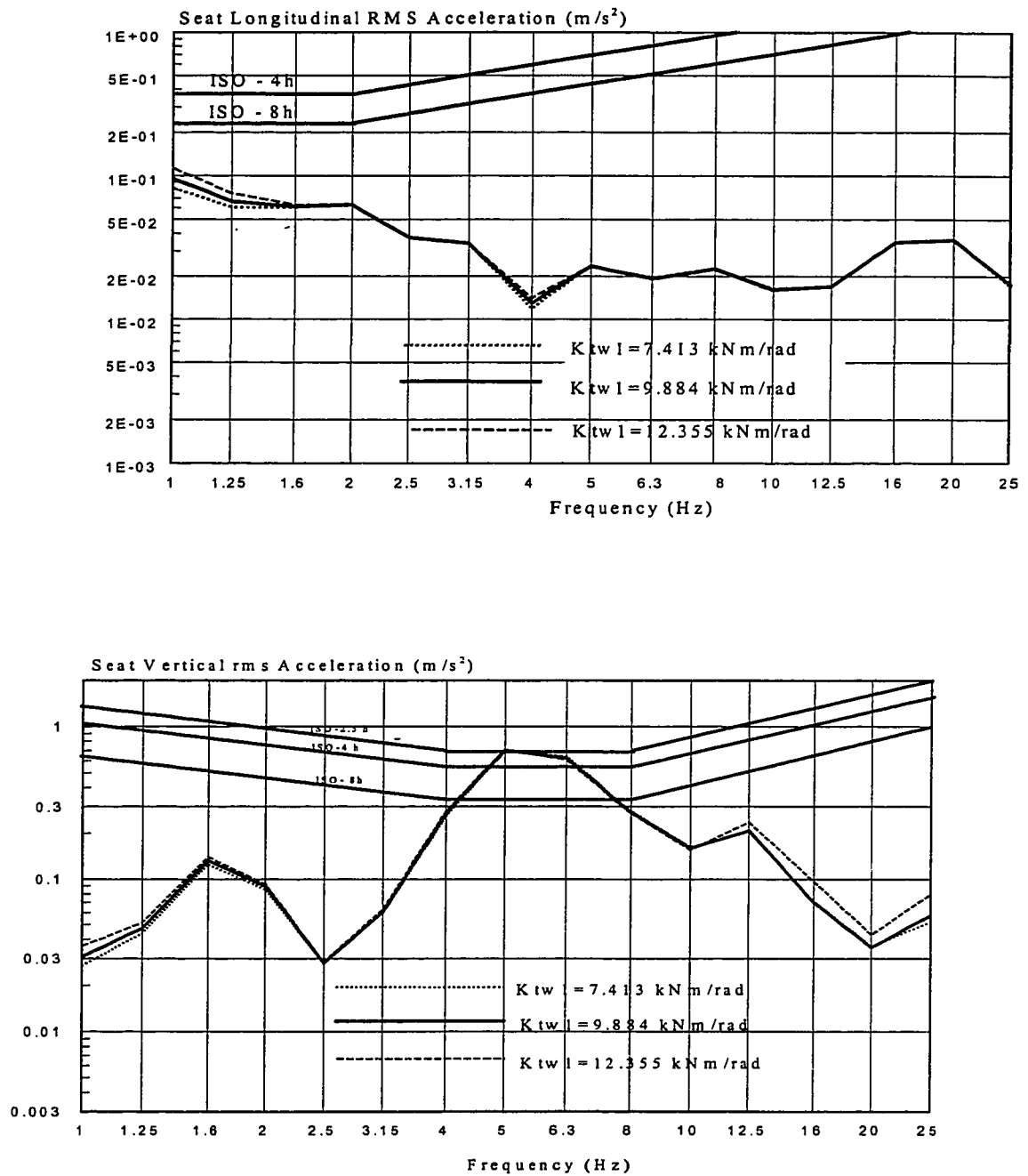
Figure 4.20: Influence of front wheel suspension stiffness on the seat acceleration response. (Task: plowing; Vehicle speed: 8km/h)
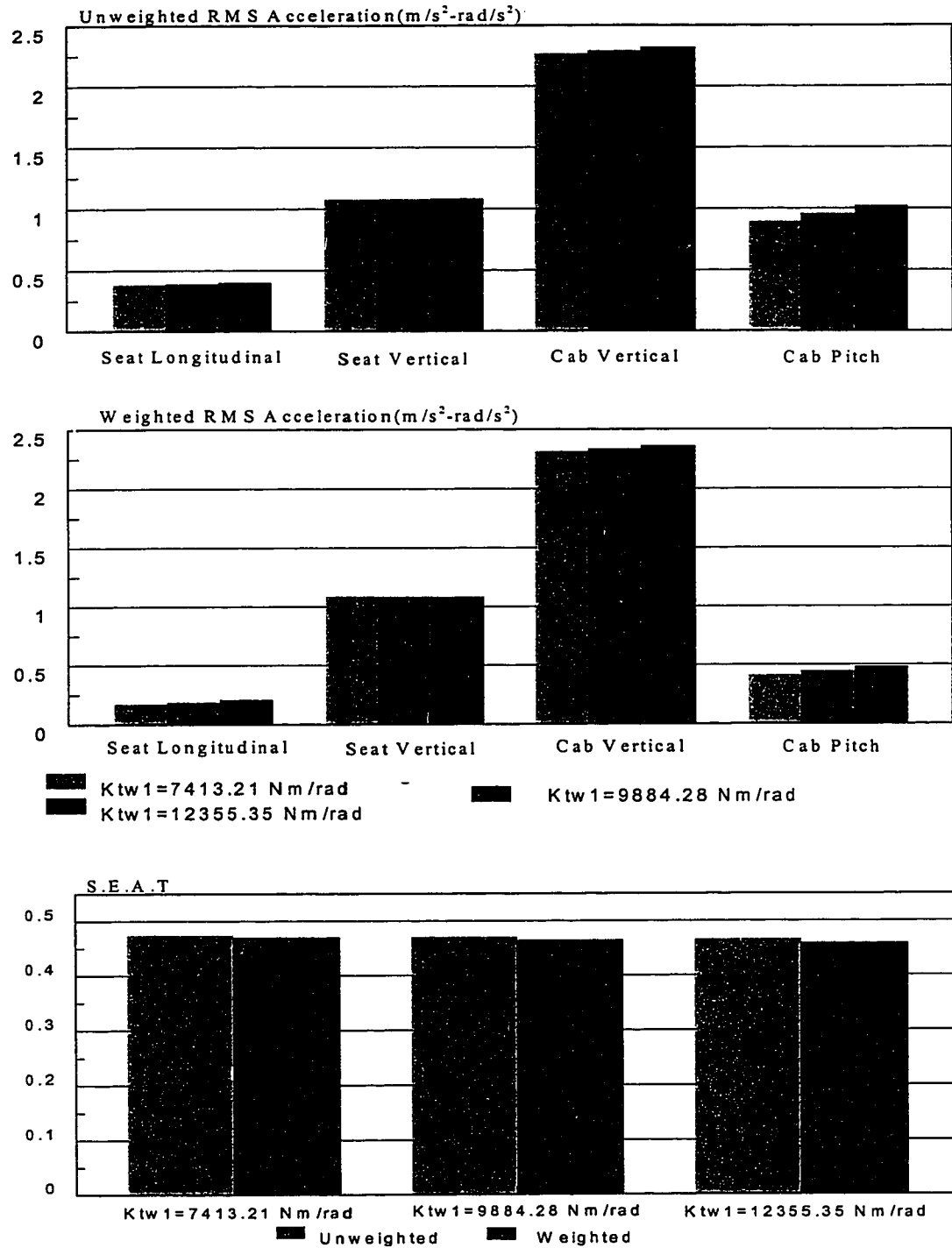
158

Figure 4.21: Influence of front wheel suspension stiffness on the overall RMS
acceleration and S.E.A.T. values (task: plowing, vehicle speed: 8 Km/h).

employed to achieve different stiffness characteristics. The influence of road wheel suspension stiffness on the ride quality is investigated by varying the nominal stiffness by ±25% and ±50%.

The acceleration response characteristics at the driver-seat interface are evaluated along the vertical and longitudinal axes, as shown in Figure 4.22. The results show that both longitudinal and vertical ride response of the vehicle is extremely sensitive to road wheel stiffness variations. A softer road wheel, in general, yields improved longitudinal vertical ride in 1-2 Hz frequency bands. This may be attributed to relatively lower natural frequency and thus higher damping ratios associated with wheel and wheel-track deflection models. Extremely low wheel stiffness (306.45 kN/m) however, yields considerable increase in the longitudinal acceleration response in the frequency bands greater than 4 Hz. High road wheel stiffness also deteriorates the longitudinal ride quality in these frequency bands. The soft road wheels are believed to induce larger pitch motion of the vehicle at relatively lower frequencies, while stiffer road wheels may cause increased longitudinal and vertical vibration. Extreme variation in the road wheel stiffness thus yield poor longitudinal ride. The vertical ride quality in the 2-4 Hz bands worsens with decrease in the road wheel stiffness, but improves considerably in the 8-16 Hz bands, as show in the Figure. While soft road wheels reduce the magnitude of vertical vibration in the 1-2 Hz and 8-16 Hz bands, the response in the 4-8 Hz bands remains relatively insensitive to wheel stiffness. This is most likely attributed to the resonant response of the cab in these frequency bands.

The significant influence of the wheel stiffness on the ride quality of the vehicle is further evident from the overall rms acceleration response shown in Figure 4.23. The
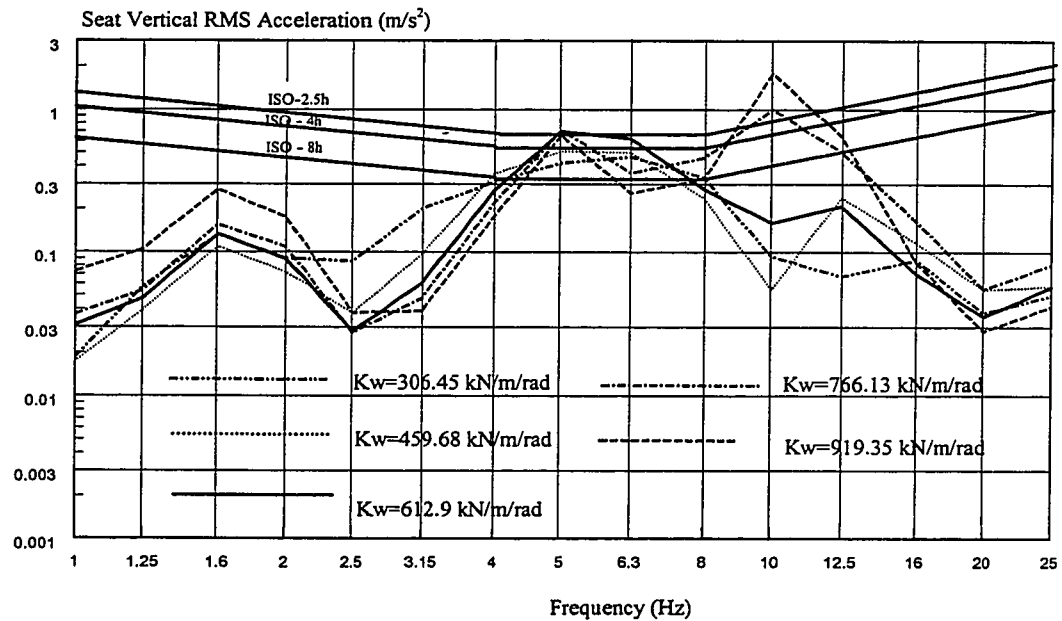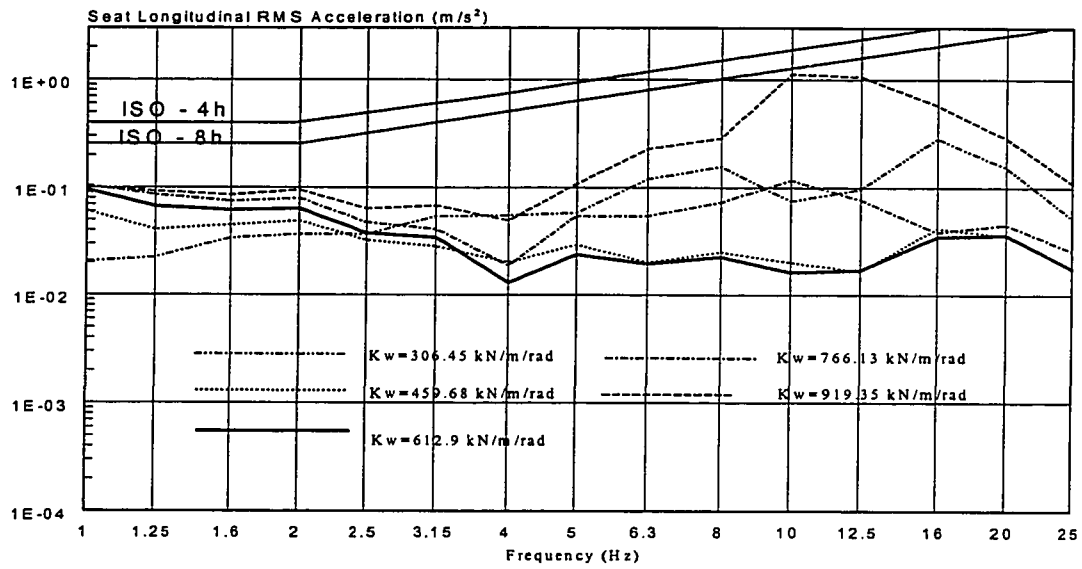
Figure 4.22: Influence of roadwheel stiffness on the RMS seat acceleration response (Task: plowing; Vehicle speed: 8km/h).
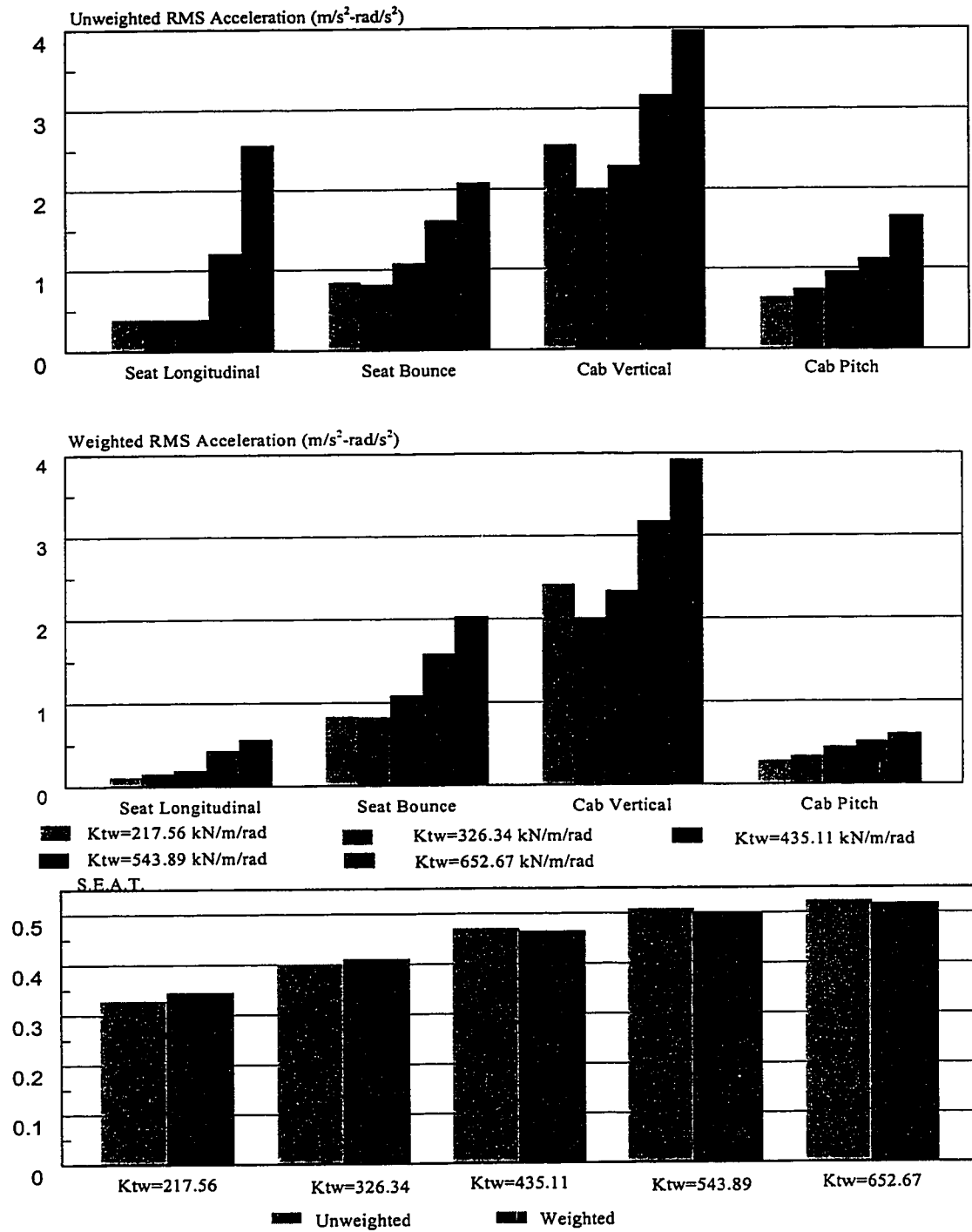
Figure 4.23: Influence of road wheel stiffness on the overall RMS acceleration response and S.E.A.T. values (task: plowing, vehicle speed: 8 km/h).

The longitudinal acceleration response increases considerably with increase in the wheel stiffness, which is mostly due to increase in the response in higher frequency bands. The weighted overall longitudinal acceleration, however, reveals relatively less increase for stiffer road wheels due to high attenuation of the weighting filter at higher frequencies. The overall rms acceleration along the pitch coordinate also increases with increase in the wheel stiffness.

The overall rms vertical acceleration at the cab floor increases considerably with increase in the wheel stiffness. This increase, however, is mostly due to amplification of vibration in the 1-2 Hz and 8-16 Hz bands. Extremely soft road wheels also yield a significant increase in rms acceleration of cab floor vertical vibration, which is attributed to increased vibration in the 2-4 Hz band. The vibration in these bands, however, are effectively attenuated by the suspension seat. The overall vertical rms acceleration at the seat thus reveals only minimal increase with soft road wheels. The effective attenuaton of vertical vibration in the 2-4 Hz by the seat also results in very low S.E.A.T. value, in the value of 0.35, as shown in Figure 4.23.

4.4.5 Influence of Longitudinal Stiffness of the Track

The variation in the longitudinal stiffness coefficient characterizing the track extensibility influence the longitudinal, vertical and pitch ride quality of the snowplow, as illustrated in Figures 4.24 and 4.25. A reduction in the track stiffness coefficient reduces the magnitudes of vertical forces arising from track-terrain interactions. The magnitudes of longitudinal and vertical acceleration at the seat thus decreases, as shown in the Figures. A soft track, however, affects the ride vibration in the frequency bands above 5
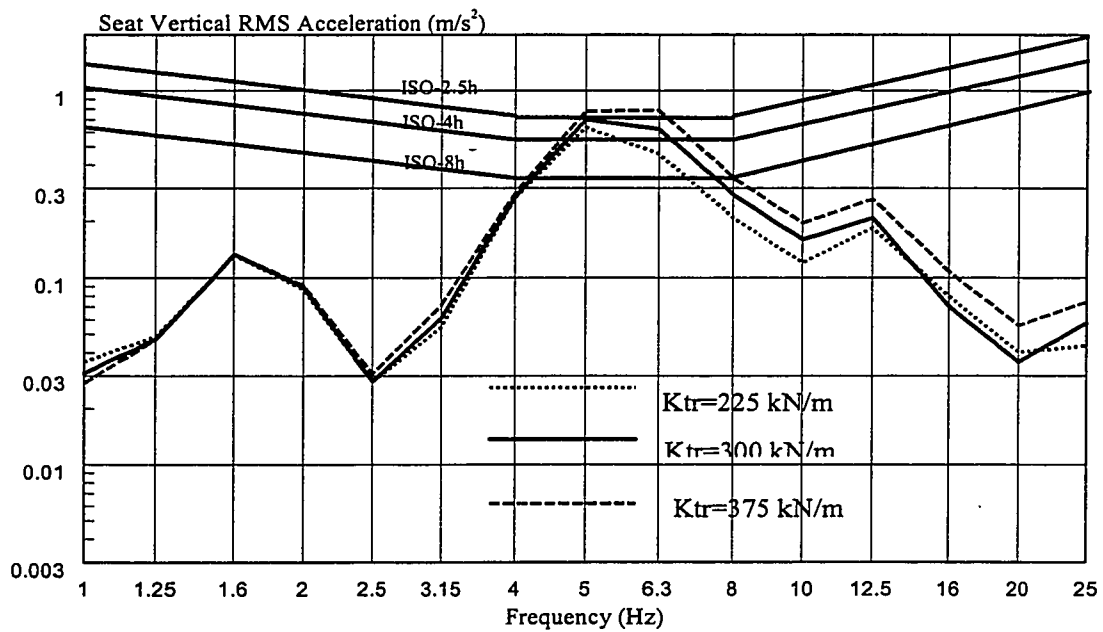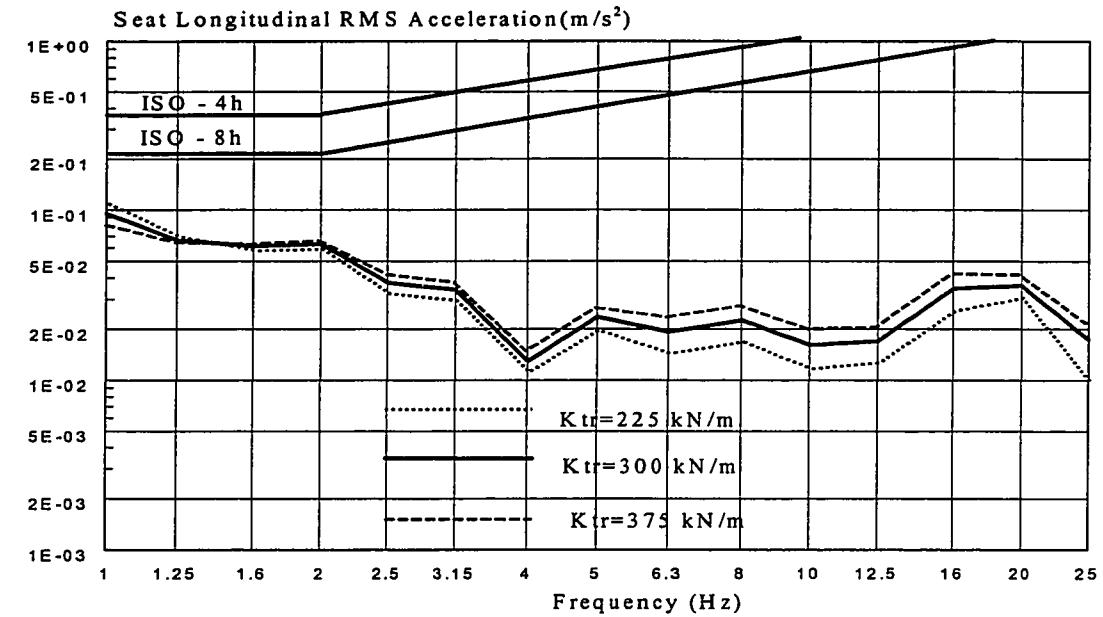
Figure 4.24: Influence of track stiffness on the longitudinal and vertical RMS acceleration response at the seat. (Task: plowing; Vehicle speed: 8km/h)

164

Unweighted RMS Acceleration (m/s^2-rad/s^2)

Weighted RMS Acceleration(m/s^2-rad/s^2)

Ktr=225 KN/m   Ktr=300 KN/m   Ktr=375 KN/m

S.E.A.T.

Ktr=225 KN/m   Ktr=300 KN/m   Ktr=325 KN/m
          Unweighted   Weighted

Figure 4.25: Influence of track stiffness on the overall RMS acceleration
and S.E.A.T. values (task: plowing, vehicle speed: 8 Km/h).

Hz. While the influence on the longitudinal ride is insignificant, a soft track can yield considerable improvement in vertical ride with slight deterioration in pitch response. The effectiveness of the seat is affected only slightly by variations in the longitudinal stiffness of the track, as observed from the S.E.A.T. values.

4.4.6   Influence of Track Pre-tension

Flexible tracks are frequently installed with certain pre-tension to minimize the slippage and sags. The variations in the track pre-tension affects the vehicle ride quality, as shown in Figures 4.26 and 4.27. A lower value of pre-tension yields lower longitudinal and vertical acceleration response in the higher frequency bands, as observed earlier for a longitudinal soft track. A low pre-tension, however, increases the longitudinal and vertical acceleration response in the 1-2.5 Hz bands. An increase in track tension yields increased levels of overall rms acceleration due to longitudinal and vertical vibration of the cab, and vertical vibration at the seat. The variations in the track pre-tension, however, affect the S.E.A.T. values only slightly. While low pre-tension and longitudinal stiffness of the track yields slight improvement in vehicle ride quality, the traction/braking performance of the vehicle may deteriorate. Enhancement of ride quality through variation in pre-tension and longitudinal stiffness of the track may thus be considered infeasible.

4.5   INFLUENCE OF GEOMETRY FACTORS

The ride quality of the snowplow vehicle may also be related to various dimensional parameters, such as location of driver seat and cab mount, trailing arm
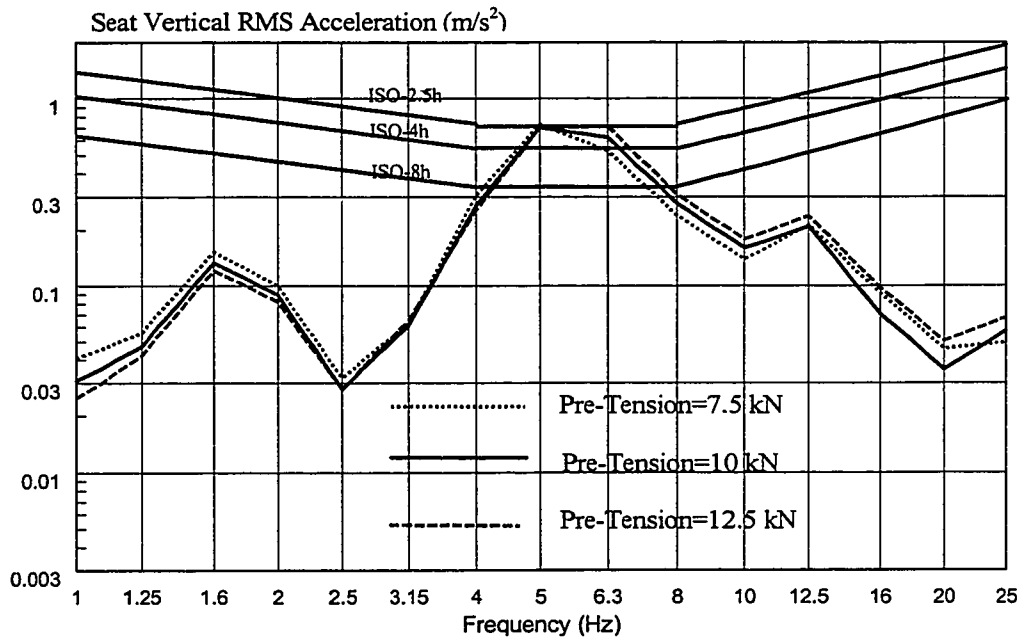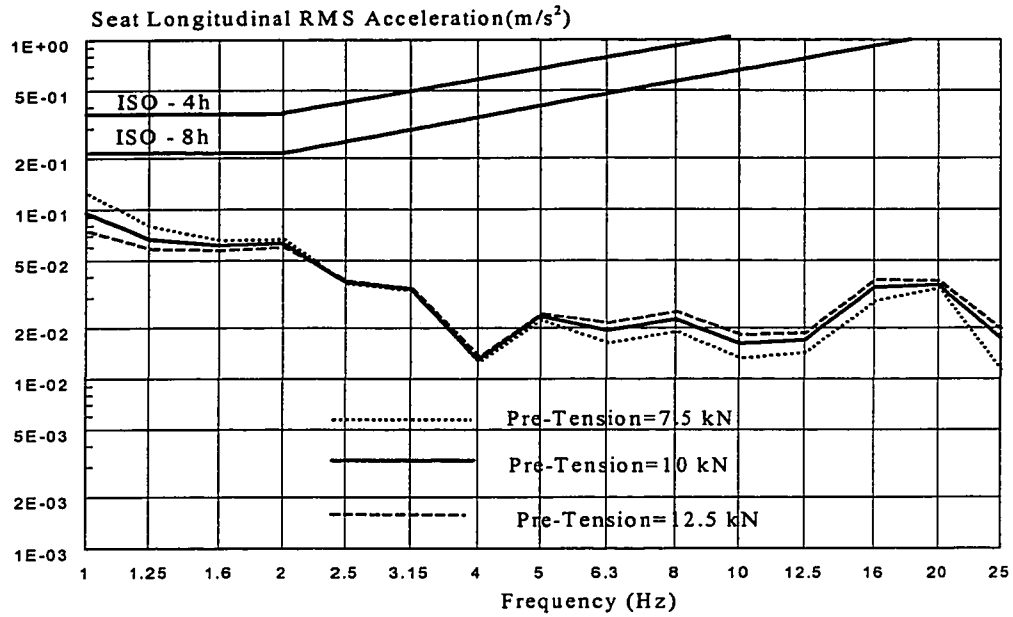
Figure 4.26: Influence of track pre-tension on the RMS seat acceleration response(Task: plowing; Vehicle speed: 8km/h).
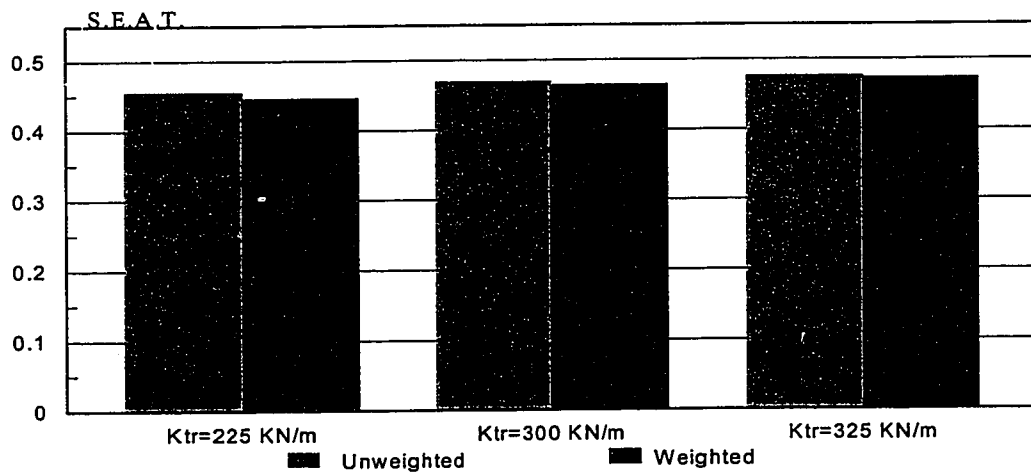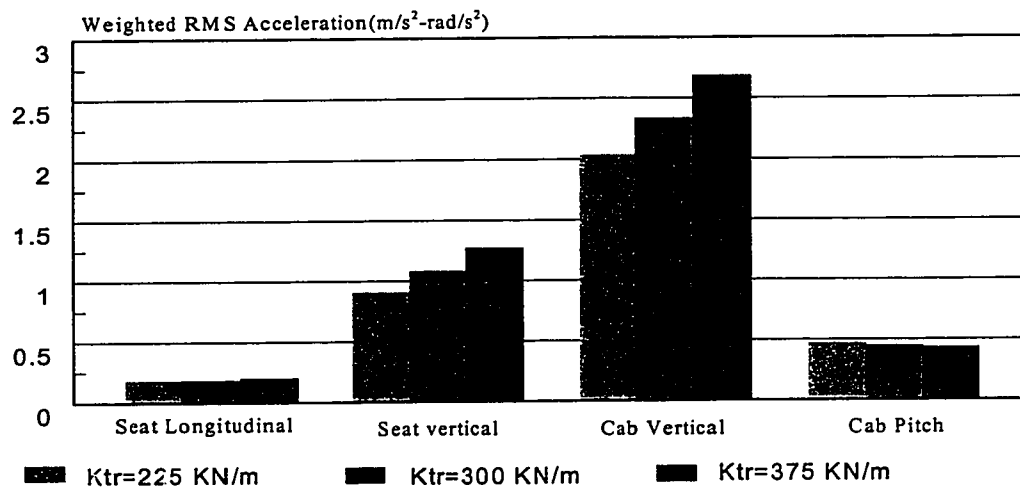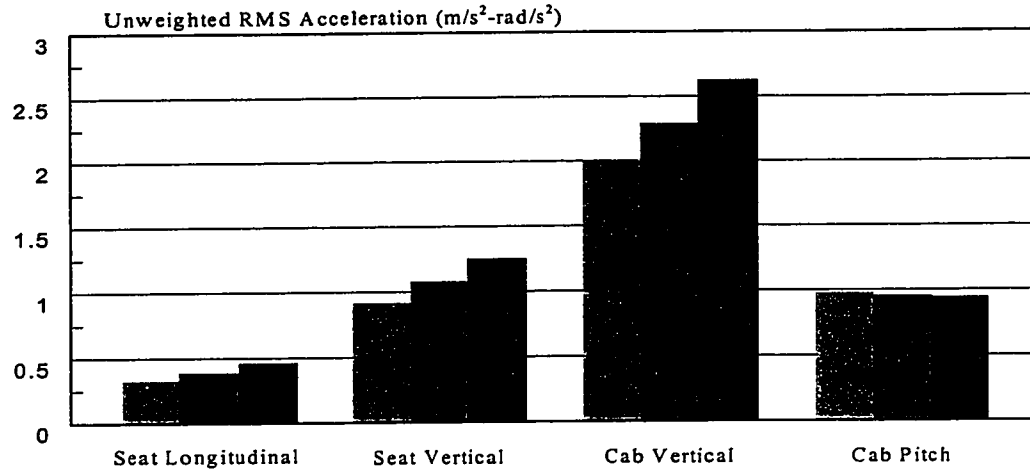
167
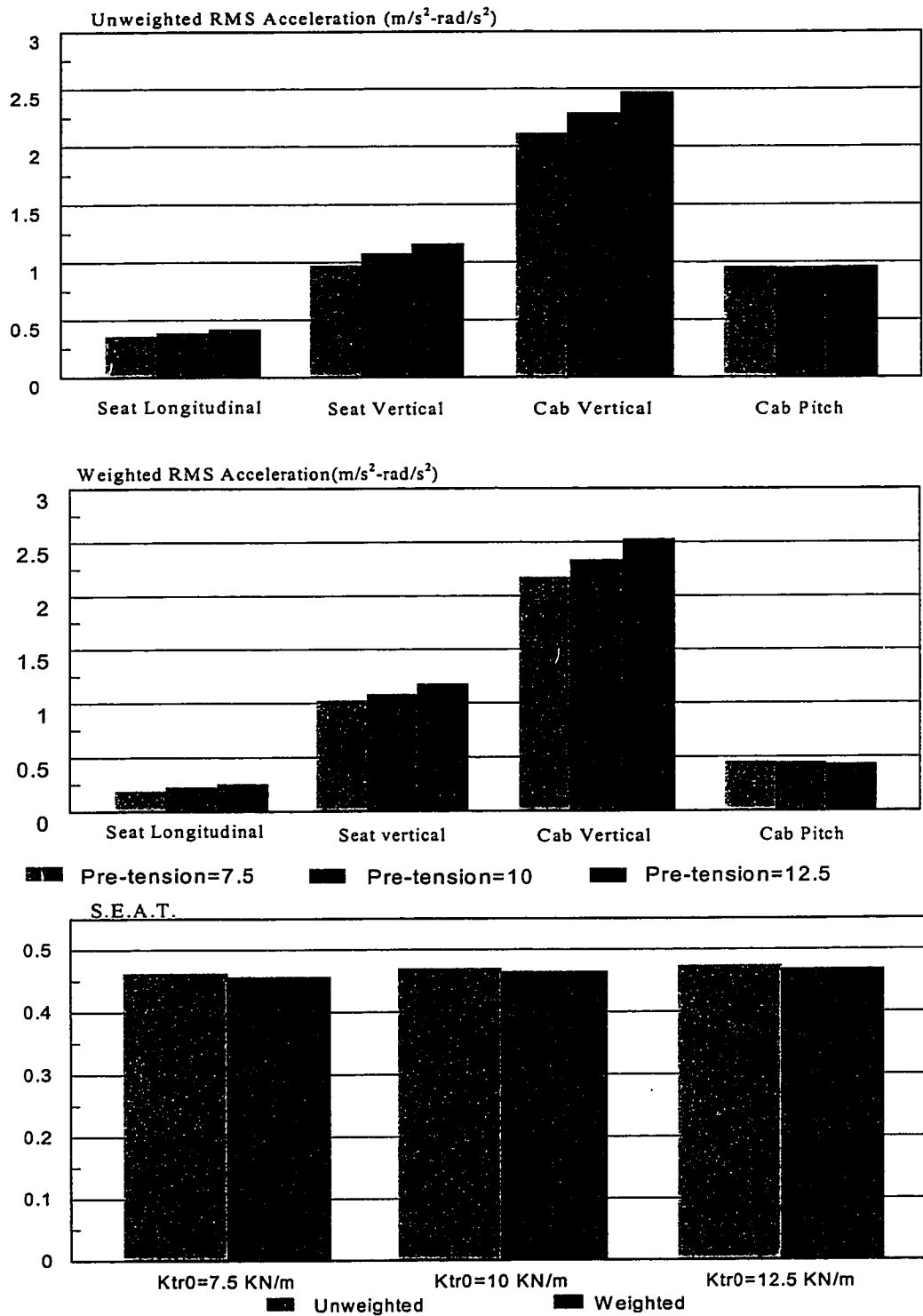
Figure 4.27: Influence of track pre-tension on the overall RMS acceleration and S.E.A.T. values (task: plowing, vehicle speed: 8 Km/h).

length and walking beam length. A parametric study is performed to study the influence of variations in these dimensional parameters on the vehicle ride quality. The ride quality of the vehicle is presented in terms of unweighted and weighted overall rms acceleration, and S.E.A.T. values.

Figure 4.28 illustrates the influence of variations in horizontal location of seat with respect to cab c.g. (a_o). The seat location is varied by ±0.05 m around the nominal value of 0.20 m. The results clearly show that such variations in the above range do not affect the vehicle ride quality.

The longitudinal spacing between the cab mounts (a_c) directly influences the effective pitch stiffness of the cab suspension and thus its pitch model natural frequency. The influence of variation in a_c on the overall rms acceleration response along the pitch and vertical axes is investigated by varying the nominal value of 1.308 m by ±0.327m. An increase in a_c yields higher effective pitch stiffness and thus the pitch mode natural frequency of the cab. The pitch mode natural frequency of the cab decreases when a_c is decreased to 0.981m. While the unweighted rms acceleration along the pitch coordinate decreases with both increase and decrease in a_c, the weighted acceleration value increases with lower value of a_c (Figure 4.29). This increase is attributed to lower pitch mode frequency and weighting filter characteristics. The S.E.A.T. value of the seat also increases due to predominant cab pitch vibration in the lower frequency range. The vertical ride response of the vehicle is only slightly influenced by spacing between the mounts.

The effective stiffness of the first road wheel suspension is related to torsional
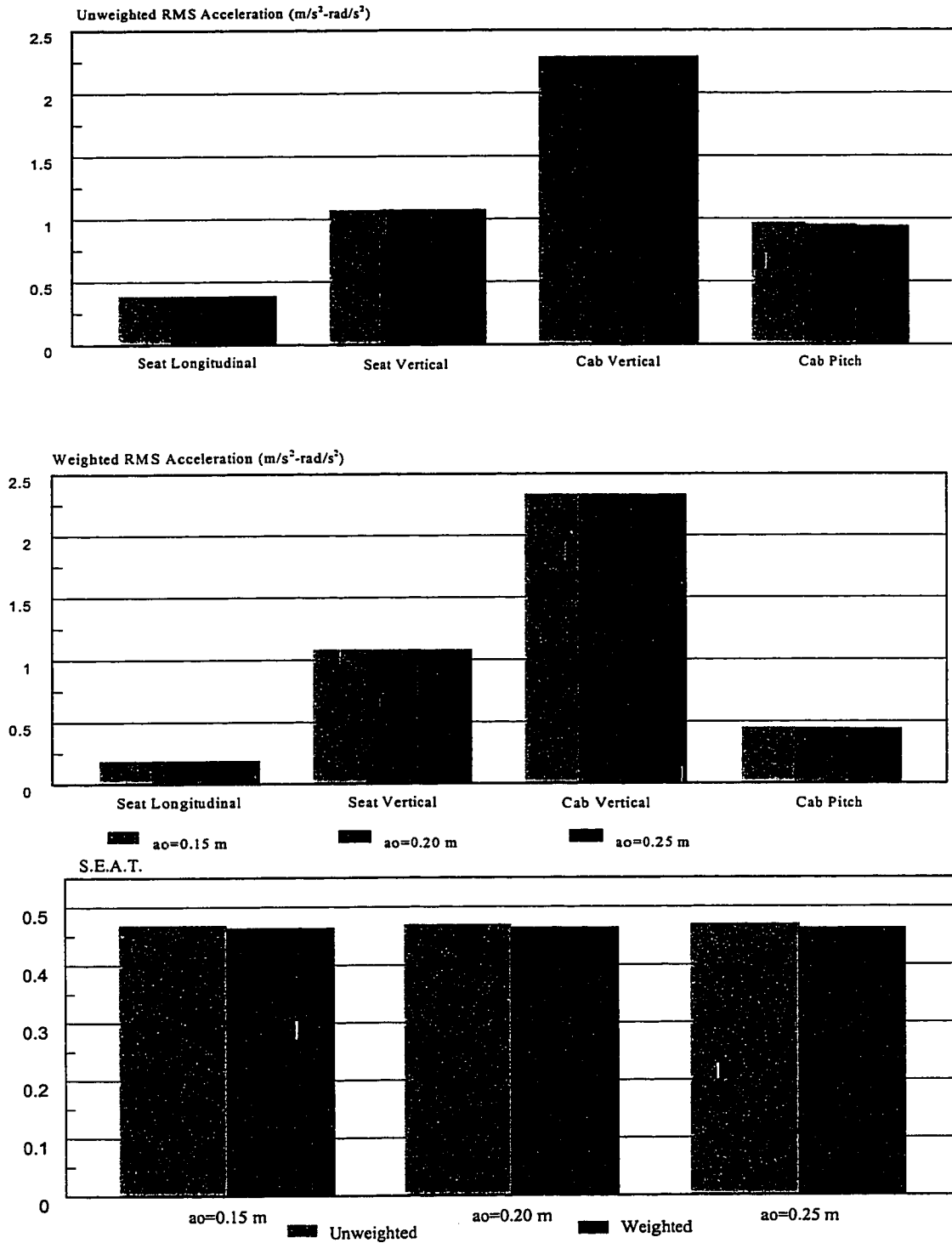
Figure 4.28: Influence of distance between cab c.g. and seat base on the overall RMS acceleration and S.E.A.T. values (task: plowing, vehicle speed: 8 Km/h).

Figure 4.29: Influence of longitudinal distance of cab mounts on the overall RMS acceleration and S.E.A.T. values (task: plowing, vehicle speed: 8 Km/h).

Figure 4.30: Influence of variation in the trailing arm length on the overall RMS acceleration and S.E.A.T. values (task: plowing, vehicle speed: 8 Km/h).

stiffness of the bushing and length of the trailing arm. The variation in the trailing arm length thus affect the vehicle ride quality considerably, as shown in Figure 4.30. The unweighted rms accelerations due to longitudinal, vertical and pitch vibration increase, when trailing arm length is reduced from 0.116 m to 0.087m. This increase may be attributed to lower effective stiffness and thus lower natural frequency of the road wheel suspension in the vicinity of vertical mode natural frequency of the cab. The deterioration in ride quality due to shorter trailing arm is further evident from the weighted rms acceleration response along all the axes. From the results, it may be concluded that a longer trailing arm yield considerable reduction in overall rms acceleration response and the S.E.A.T. values.

The variations in the length of walking beam employed in rear wheels suspenson also affect the vehicle ride, as shown in Figure 4.31. A reduction in the walking beam length does not influence the overall longitudinal and pitch rms acceleration. The corresponding overall rms acceleration of the cab and seat increase. An increase in the beam length yields an increase in the longitudinal and vertical ride quality, and the S.E.A.T. values. It should be noted that variation in the beam length directly relate to effective pitch mass moment of inertia due to rear road wheels, and wheel-track interactions in a complex manner.

4.6 SUMMARY

The ride quality of the snowplow vehicle is investigated for excitations arising from undeformable terrains. The *fatigue decreased proficiency limits* proposed by the International Standardization Organization (1978) is selected to assess the ride
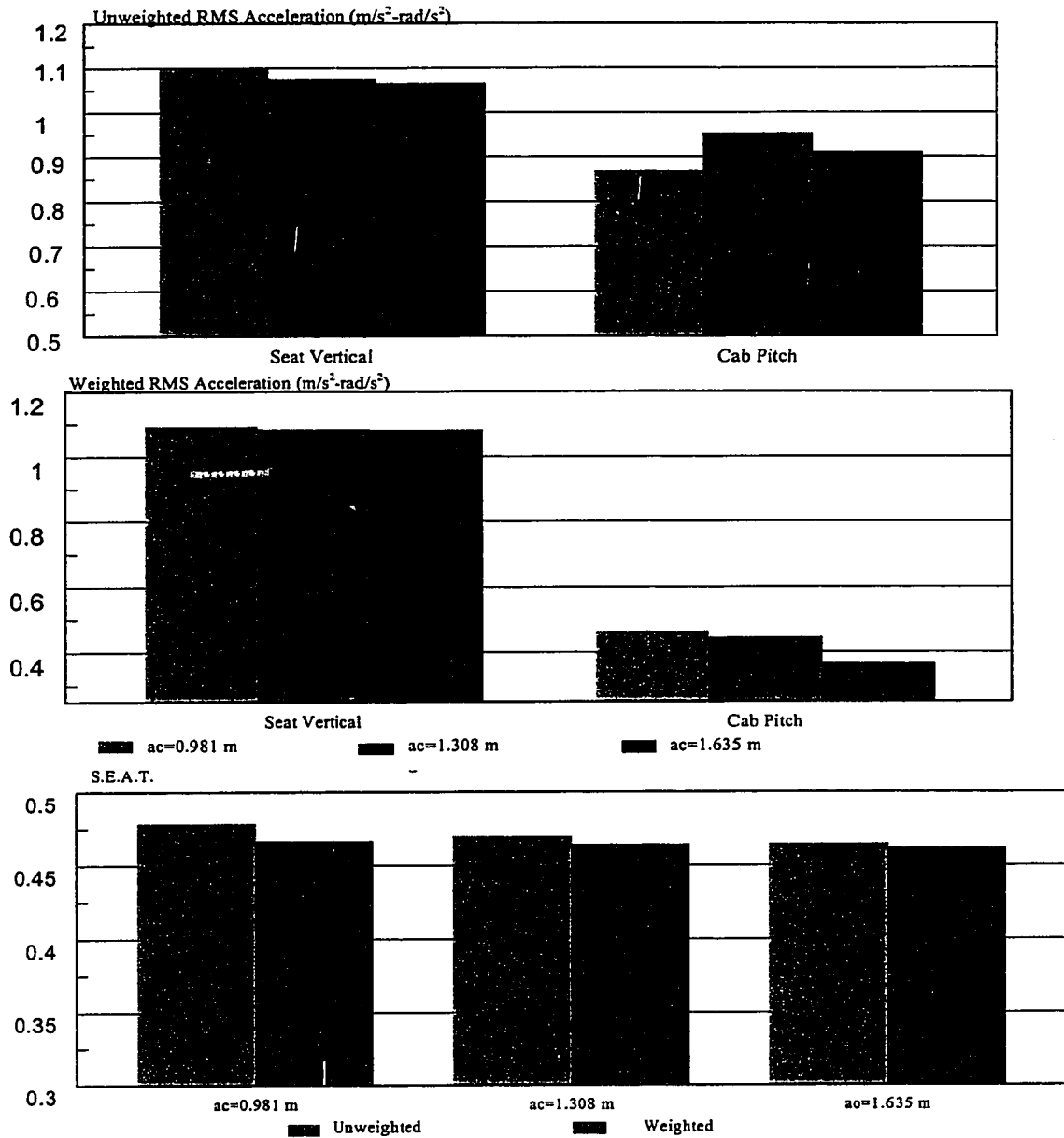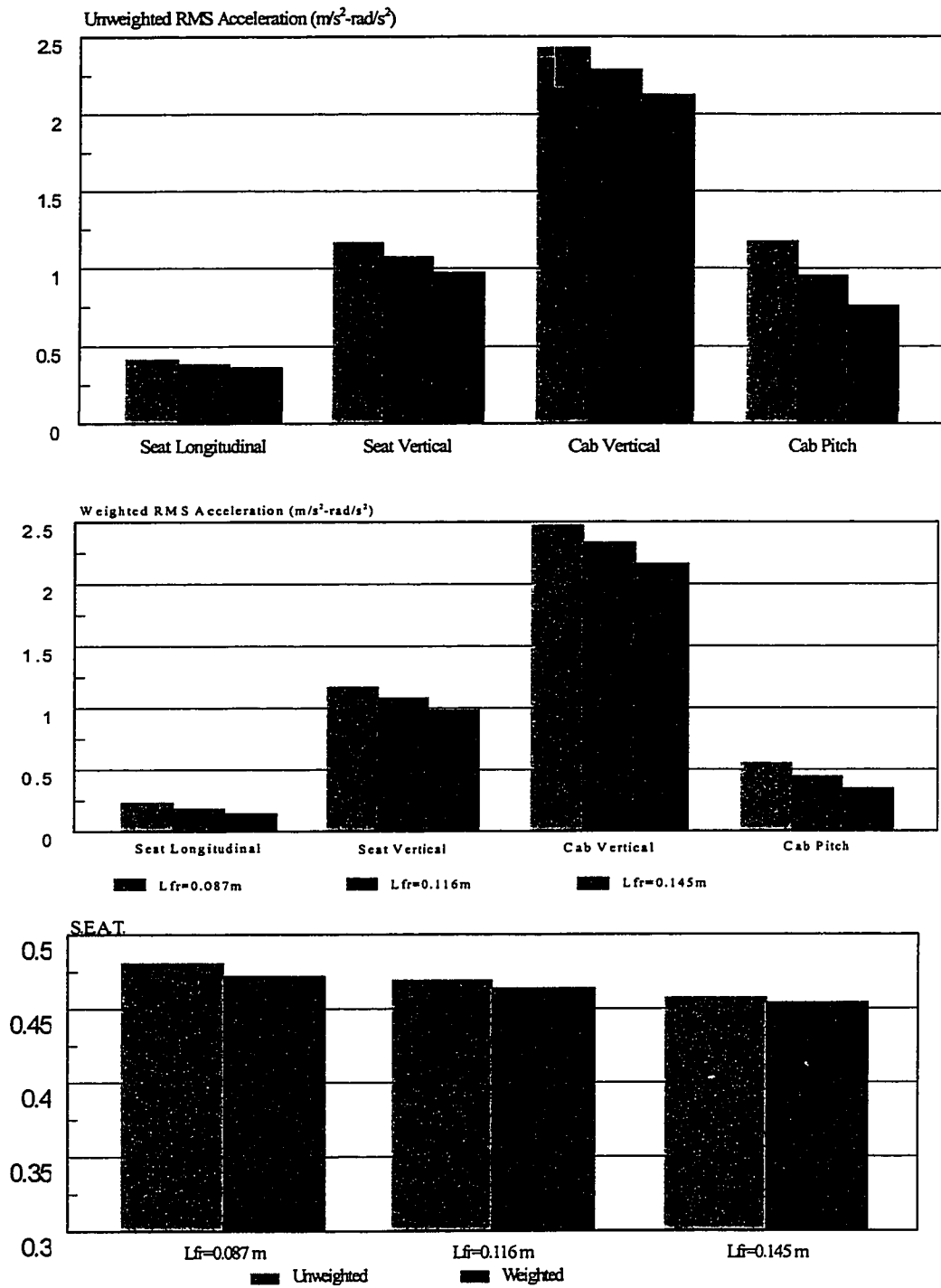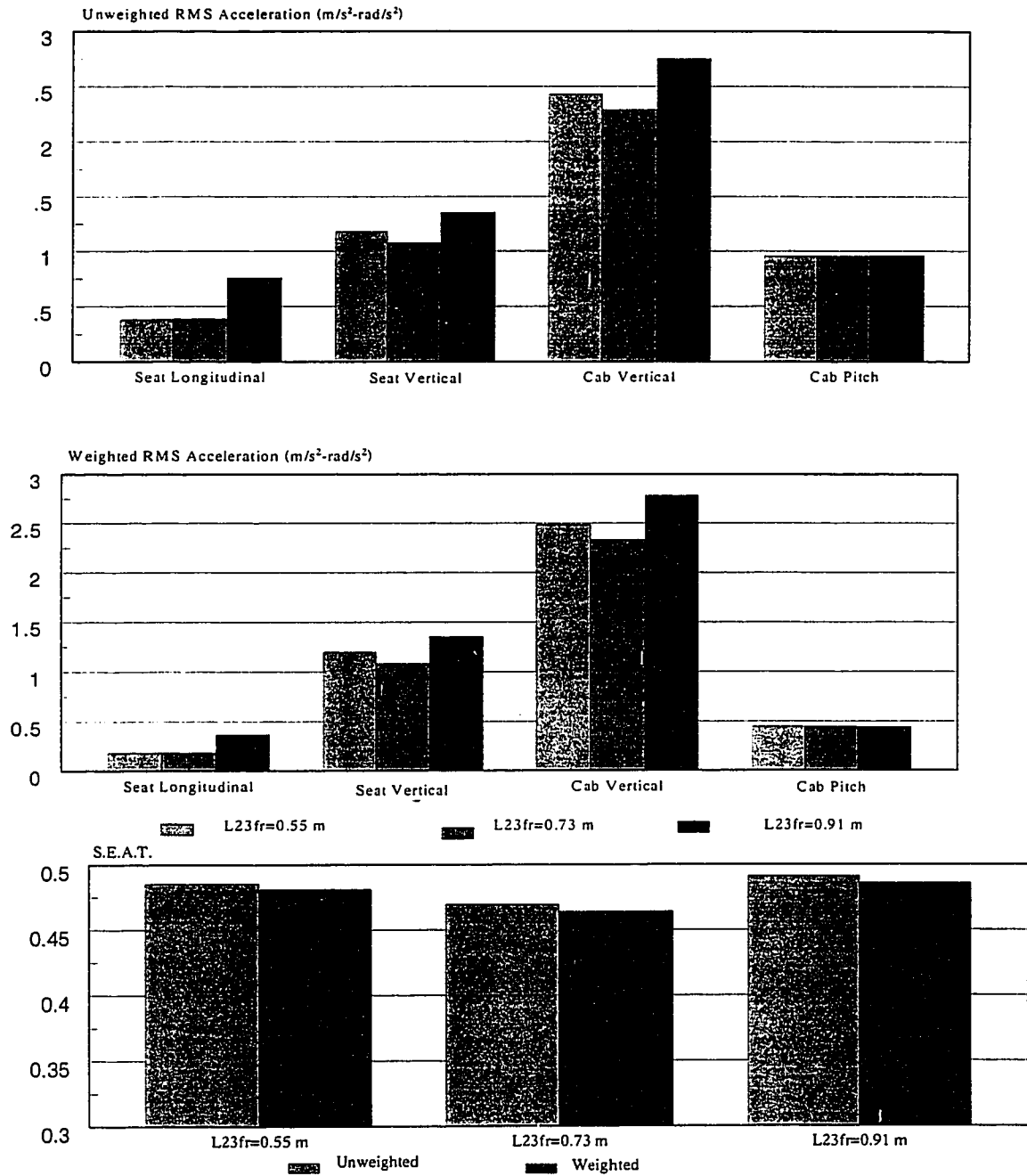
Figure 4.31: Influence of walking beam length on the overall RMS acceleration and S.E.A.T. values (task: plowing, vehicle speed: 8 Km/h).

174

quality of the snowplow vehicle. The ride quality of the snowplow configurations is also investigated for various operating conditions, and various design and dimensional parameters.

The results of the parametric study are summarized as follows:

- The ride quality of the vehicle deteriorates considerably with increase in terrain roughness and vehicle speed. The vehicle operation at a speed of 3km/h yields best ride quality.

- The driver is subject to considerably larger whole body vibrations during a plowing task than those encountered in a transit operation.

- The longitudinal ride quality of the vehicle can be considered satisfactory for 8 hours of exposure duration, while the vertical ride is satisfactory only for duration of 1.0 to 2.5 hours.

- The driver can experience significantly high levels of vehicle acceleration under excitation arising from transient obstacles. The magnitude of acceleration approaches as high as $100m/s^2$ for a 20 cm high semi-circle obstacle.

- An adequately damped soft seat suspension yields improved vertical rides in the low frequency bands. Too soft a suspension, however, can lead to higher levels of acceleration due to possible bottoming of the suspension. Too high a suspension damping can deteriorate the vertical ride in the isolation frequency range.

- Soft and adequately damped cab mounts are desirable to achieve improved vehicle ride along the longitudinal and vertical coordinates.

- While the front road wheel suspension does not affect the vehicle ride significantly, an increase in the trailing arm length can provide considerable ride improvement along all the three coordinates.

- Road wheel stiffness affects the vehicle ride most significantly. Road wheels with low stiffness provide considerable improvement in longitudinal ride in the 1-2 Hz band, and vertical ride in the 1-2 Hz and 8-16 Hz bands. The ride vibration levels,

175

however, increase in the 4-25 Hz, and 2-4 Hz for longitudinal and vertical vibration, respectively.

- Rubber track with low longitudinal stiffness also offer certain improvement in longitudinal and vertical ride quality, specifically in the frequency bands above 4 Hz.

- The contribution of variation in snow depth and density to the overall ride quality are observed to be minimal.

- The horizontal distance between the cab mounts affect the pitch ride quality due to variation in the effective pitch stiffness of the cab suspension.

CHAPTER 5

CONCLUSIONS AND RECOMMENDATIONS FOR FUTURE WORK

5.1 GENERAL

As set out in Chapter 1, the overall objectives of this dissertation research is to gain an understanding of the ride dynamic of a tracked snowplow vehicle. The specific objectives included development of a comprehensive mathematical model for ride analysis of snowplow vehicle, evaluation of ride vibration response of the snowplow vehicle subject to deterministic obstacles and random terrain excitations, validation of the analytical model, assessment of ride quality of the vehicle and to carry out comprehensive parametric sensitivity analyses. The computer model, thus evolved, could be employed as an effective design tool to study and to improve the ride quality and thus the mobility performance of snowplow vehicle. These objectives have been accomplished as presented in the preceding chapters. In the present chapter, highlights of the research work are summarized together with major conclusions and some recommendations for future work.

5.2 HIGHLIGHTS OF THE PRESENT WORK

In this thesis, the ride vibration and ride quality analysis of a tracked snowplow vehicle is carried out through analytical methods computer simulations. The proposed analytical model, is a time-domain ride simulation model formulated considering an in-plane analytical representation of the vehicle traversing over an arbitrary non-deformable terrain profile at a constant forward speed. The simulation model is a twelve-degrees-of-freedom dynamic system incorporating suspension kinematics and dynamics, and wheel-

track-terrain interactions. For the purpose of dynamic modeling, the sidewalk snowplow vehicle is divided into six major components: driver and seat suspension; cab suspension; road wheels suspension; hull; blade; and track. The vertical driver-seat-suspension system is developed upon integrating a single-DOF driver model to a two-DOF seat suspension, incorporating nonlinearities due to shock absorber damping, linkage friction and bump stops. The first road wheel and axle assembly is represented by a lumped mass with a trailing arm that undergoes a pitch rotation. The second and third road wheels, arranged in a tandem configuration, are represented by a walking beam with pitch DOF. Each road wheel resting on the track is represented by a continuous radial spring and an equivalent viscous damper model. The drive sprocket is also treated in a similar manner, when it comes in contact with the terrain under certain severe irregularities. The track is modeled as a continuous elastic belt capable of transmitting only tensile forces. The blade-road contact and plowing actions transmit considerable magnitudes of vertical and horizontal forces to the blade and the vehicle. The front blade assembly is thus represented by a rigid body with pitch degree-of-freedom. The total vehicle model is developed upon integrating the above sub-system models. The ride dynamic simulation model subjected to highly irregular terrain surface is formulated considering the non-linear dynamic wheel-track-terrain interactions. Thus this analytical model leads to complex formulations which are characterized through a set of highly nonlinear coupled differential equations.

Free vibration of the analytical model is performed to identify the important natural frequencies and modes of vibration, which are compared with the field measured dominant ride vibration frequencies. The comparison revealed reasonably good agreement between the computed and measured frequencies.

The ride vibration response behavior of the vehicle model is investigated under excitations arising from randomly rough terrain and plowing forces. The resulting cab and seat vibration response is analyzed and expressed in terms of PSD, 1/3-Octave band rms acceleration spectra, and overall (weighted and unweighted) rms acceleration along the pitch, longitudinal and vertical coordinates. The results obtained for two different tasks, plowing and transit operation, are compared with the envelopes of the field measured data to demonstrate its validity. The analytical results revealed a reasonably good agreement with the field test data.

The ride vibration response of a vehicle is strongly influenced by many operating, design and dimensional parameters. A parametric study is thus performed to gain an understanding on the contributions due to variation in these parameters to overall ride quality of the vehicle. The vibration levels transmitted to the seated driver of the vehicle, evaluated at the driver-seat interface, are assessed in relation to the *fatigue decreased proficiency limits* proposed by the International Standardization Organization [41]. Parametric studies are carried out to demonstrate the influence of operating, design and geometry factors on the ride dynamics and quality of snowplow vehicle, thus providing effective parameters to improve the ride quality of the snowplow vehicle.

5.3   CONCLUSIONS

The present research work has evolved into a methodology for development of an effective ride dynamic model of a sidewalk snowplow vehicle through systematic consideration and interaction of the subsystem dynamics. It has been shown that a simplified yet credible mathematical formulation of a complex tracked vehicle-terrain

dynamical system yields reasonably accurate ride predictions. Various conclusions drawn from the study are grouped in two categories, where the first category comprises the conclusions drawn from the analytical modeling strategies and their assessment based on the field validation of associated ride predictions. The second category of conclusions focus on the ride dynamic behavior of the snowplow vehicle in view of its operational and design parameters.

The major conclusions drawn from the analytical modeling approach are listed below:

- A two-dimensional ride dynamic formalism, assuming negligible contribution due to roll degree-of-freedom can be considered appropriate for ride analysis of such vehicles. Since vertical vibrations are known to be more severe than those along other axes, an in-plane model can yield accurate prediction of vertical vibration response.

- The wheel model based on the concept of a continuous ring of radial springs and an equivalent damper, represent better than the point contact modeling.

- The contribution due to visco-elastic behavior of the driver can be represented by a single-degree-freedom damped mass-spring model with natural frequency equal to the fundament resonance of the seated body ($\cong$5 Hz).

- The seat-suspension model can be accurately represented by a two-DOF lumped-parameter model, incorporating nonlinearities due to damping, bump-stops and Coulomb friction.

- The vertical force-deflection characteristics of the elastic cab mounts can be represented by a linear stiffness coefficient in the operating load range. The elastic mounts also offer compliance along the radial or horizontal direction.

- Analytical representation of trailing arm and walking arm suspension configuration necessitate appropriate considerations of their kinematic behavior.

- The continuous and homogenous elastic track employed in such vehicles can be appropriately modeled as a continuous elastic belt with certain pre-tension.

- Highly complex track-wheel-terrain interaction can be modeled using an adaptive contact principle based upon the coordinates of the wheel circumference and road profile, and track tension.

- The longitudinal forces developed by the track can be derived upon consideration of instantaneous track length incorporating bridging and wrap around length.

- Analytical model developed in the study resulted in acceptable correlation with the field measured data in the form of PSD and rms spectra of the pitch, longitudinal and vertical accelerations of the cab.

The major conclusions draw from the ride dynamic behavior of the study are summarized below:

- Assessment of vehicle ride quality attained at a speed of 8 km/h in relation to the guidelines proposed in ISO-2631 (1978) revealed the following:

  - The longitudinal ride quality of the vehicle is acceptable for over 8 hours of daily exposure, for both transit and plowing tasks.

  - The vertical ride quality of the vehicle during a plowing task performed at a speed of 8 km/h is acceptable only 2.5 hours exposure duration.

  - The vertical ride quality approaches acceptable limits for 8 hours exposure during transit operation.

- The vehicle ride quality deteriorates most significantly on rough terrains. Vehicle operation on icy roads may thus lead to unacceptable ride quality in view of longer daily occupational exposure duration.

- The vehicle ride can be significantly enhanced under operation at low speeds near 3 km/h.

- The horizontal snow pushing force varies linearly with the snow depth. The magnitude of the force imposed on relatively small blade area, however, is low. The force developed due to compression of the snow approaches only 600 N, when the fresh snow depth is 15 cm. The longitudinal and vertical ride quality of the vehicle thus remain relatively insensitive to variations in the depth and density of snow.

- The vertical ride quality and seat effectiveness can be enhanced by reducing its suspension stiffness and increasing the bleed and blow-off damping coefficients. Too low a suspension stiffness, however, can lead to frequent bottoming of the suspension and thus high levels of transmitted vibration.

- The vertical ride quality of the vehicle predominates in the 4-8 Hz frequency band due to vertical mode resonance of the cab and cab mounts. Since human body is most fatigue sensitive to vibration in this frequency range, the selection of cab mounts forms an important design task. Soft and adequately damped cab mounts are highly desirable to attain improved ride quality.

- The effective pitch stiffness of the cab suspension and thus its pitch ride quality can be enhanced by increasing the horizontal distance between the cab mounts.

- While variation in torsional stiffness of the first road wheel suspension do not affect the vehicle ride considerably, the effective suspension stiffness can be enhanced by increasing the trailing arm length. The vertical and pitch ride quality can thus be improved.

- The stiffness of road wheels affects the vehicle ride quality in most significant manner, specifically in the 1-2 Hz and 8-16 Hz bands. The solid rubber wheels, when replaced by pneumatic tires, can provide considerable improvement in the ride quality.

- It is vital to achieve adequate vibration isolation in the 4-8 Hz through appropriate design of cab mounts and road wheel stiffness. Pneumatic tires coupled with softer cab suspension offer the best ride improvement potential.

- Although a longitudinaly soft track can provide certain improvement in vehicle ride, the vehicle mobility may be limited due to reduced traction performance of soft track. The variation in track pre-tension do not affect the ride significantly.

5.4   RECOMMEDATIONS FOR FUTURE WORK

The present research work result in a computer simulation model which has been validated using the field test data. The potential usefulness of the computer model can be further enhanced upon consideration of the following:

- Although the in-plane simulation model developed in this study provides reasonable correlation with the measured data, it is unable to predict the vehicle ride along the lateral and roll axes. The ride quality along these axes may be important, since the vehicle frequently negotiates discontinuities in the sidewalks. It is thus recommended to enhance the model by incorporating lateral and roll degrees-of-freedom of the axles, chassis and the cab.

- The drive-train of the vehicle, directly installed on the chassis frame close to the cab, imposes considerable vibrations in the higher frequency bands. It is thus recommended to incorporate the drive-train components and their mounts in the model. Such a model can provide significant information related to the influence of drive-train vibration on the overall ride quality. The tool can then be employed to select appropriate engine and transmission mounts.

- More refined representation of the track bridging and wrap around is necessary to account for track separation.

- In view of excellent ride performance potentials of soft cab mounts and pneumatic wheels, it is highly recommended to undertake further analytical and experimental studies to establish quantitative benefits of such design variation.

REFERENCES

1. Hornich, R.J., "Effects of Vibrations on Operators", *Agricultural Engineering*, Dec. 1961, p.674.

2. Eppinger, R.H., King, A.I., and Lee, R.A., "Experimental and Mathematical Simulation of a Multi-wheeled Vehicle With and Without an Elastic Track", *Proceedings of the 2nd International Conference on Vehicle Mechanics*, Paris University, Paris, France, Sept. 6-9, 1971, pp. 275-286

3. Lessem, A.S., and Murphy Jr., N.R., "Studies of the Dynamics of Tracked Vehicles", *WES Technical Report* No. M-72-1, U.S. Army Engineer Waterways Experiment Station, Vicksburg, Miss., June 1972.

4. Murphy Jr., N.R. and Ahlvin, R.B., "AMC-74 Vehicle Dynamic Module," Technical Report No. M-76-1, US Army Engineer Waterways Experiment Station, Vicksburg, Miss., January 1976.

5. Lee, S.M., "The Study of Vibrations Generated by the Tracks of Tracked Vehicles", Keweenaw Research Center, Michigan Technological University, Houghton, Mich., July 1976.

6. "Noise and Vibration Reduction Program on the M-109 Self-Propelled Howitzer", *Report No. MPC-178*, Allison Division Army Tank-Automotive Plant, 1966.

7. Wheeler, P., "Tracked Vehicle Ride Dynamic Program". *SAE Technical Series Paper No. 770048*, International congress and Exposition, Detroit, Mich., 1977.

8. Meachom, H.C. Jr., Swain, J.P., Wilcox, J.P., and Doyle, G.R., "Track Dynamics Program", *TARADCOM Laboratory Technical Report NO. 12397*. U.S. Army Tank-Automotive Research and Development Command, Warren, Mich., Oct. 1978.

9. Hoogterp, F.B., "Interactive Vehicle Dynamics and Ride Evaluation Package", *TARADCOM Laboratory Technical Report No. 12413*, U.S. Army Tank-Automotive Research and Development Command, Warren, Mich., Nov. 1978.

10. Beck, R.R., and Wehage, R.A., "The Modeling and Simulation of Two Coupled M113 Armored Personnel Carriers", *Proceedings of the 10th Annuall Conference on Modeling and Simulation*, Pittsburgh, Penn., Vol. 10, Part 2, 1979, pp. 353-359.

11. Eberle, W.R., and Steele, M.M., "Investigation of Fluidically Controlled Suspension Systems for Tracked Vehicles", *TACOM Report No. 12072*, U.S. Army Tank-Automotive Command, Warren, Mich., Sept. 1975.

12. Salemka, R.M., and Beck, R.R., "Feasibility Analysis and Evaluation of an Adaptive Tracked Vehicle Suspension and Control System", *TACOM Final Report No. 11893(LL-146)*, U.S. Army Tank-Automotive Command, Warren, Mich., June 1975.

13. Bekker, M.G., Theory of Land Locomotion, University of Michigan Press, 1956.

14. Bekker, M.G., "Tracked Vehicles-Terrain Damage and Economy", *SAE Transactions Paper No. 800953*, 1980, pp. 2903-2917.

15. Wong, J.Y., Garber, M., and Preston-Thomas, J., "Theoretical Prediction and Experimental Substantiation of the Ground Pressure Distribution and Tractive Performance of Tracked Vehicles", Proceedings of the Institution of Mechanical Engineers, Vol. 1980, No.15, 1984, pp. 265-285.

16. Maclaurin, B., "Progress in British Tracked Vehicle Suspension Systems", *SAE Technical Series Paper No. 830442*, International Congress and Exposition, Detroit, Mich., Feb. 28 -Mar. 4, 1983.

17. Galaitsis, A.G., "TRAXION: A Model for Predicting Dynamic Track Loads in Military Vehicles", *ASME Transactions Journal of Vibration Acoustics, Stress, and Reliability in Design*, Vol. 106, April 1984, pp. 286-291.

18. Garnich, M.R. and Grimm, T.R., "Modeling and Simulation of a Tracked Vehicle." *ASME Proceedings of the International Computers in Engineering Conference and Exhibit on Advanced Automation*, Vol. 2, Las Vegas, Nevada, Aug. 12-15, pp. 591-600, 1984.

19. McCullough, M.K., and Haug, E.J., "Dynamics of High Mobility Track Vehicles", *ASME Report No*. 85-DET-95, 1985.

20. Krupka, R.M., "Mathematical Simulation of the Dynamics of a Military Tank", *SAE Technical Series Paper No. 850416*, International Congress and Exposition, Detroit, Mich., Feb. 25-Mar.1, 1985.

21. Creighton, D.C., "Revised Vehicle Dynamic Module: User's Guide for Computer Program VEHDYN II," *WES Technical Report No. SL-86-9*, U.S. Army Engineer Waterways Experiment Station, Vicksburg, Miss., May 1986.

22. Afonso, M.F.R., "Ride Dynamic Analysis of Tracked Vehicles," M.Eng. Thesis, Concordia University, Montreal, Quebec, 1989.

23. S.Rakheja, M.F.R. Afonso and S.Sankar, "Dynamic Analysis of Tracked Vehicles with Trailing Arm Suspension and Assessment of Ride Vibrations," *Int.J.of Vehicle Design*, Vol.13, No.1, 1992.

24. A.Dhir, S.Sankar, "Establishing Zero-Force and Static-equilibrium Configuration of Multi-Wheeled/Tracked Off-Road Vehicles For Ride Dynamic Simulation", *Proceedings of CSME forum*, Montreal, Quebec, June 1-4, pp.33-38, 1992.

25. A.Dhir and S.Sankar "An Adaptive Model of Wheel-Track-Terrain Interaction for Predicting Ride Performance of Tracked Vehicles." *Special issue No. 93-CSME-46*, EIC Accession No. 2363.

26. S.Sankar, A.Dhir, "Simulation and Field Testing of Tracked Vehicle Suspension Dynamics" *Transactions of the ASME*, 764/Vol. 116, December, 1994

27. Anil Dhir, M.F.R., "Ride Dynamics of High Mobility Wheeled/Tracked Off-Road Vehicles: Computer Simulation With Field Validation" M.Eng. Thesis, Concordia University, Montreal, Quebec, 1993.

28. Anil Dhir, Seshadri Sankar, "Analytical Track Models for Ride Dynamic Simulation of Tracked Vehicles" *J. of Terramechanics*, Vol.31, No.2, pp.107-138, 1994

29. Stikeleather, L.F., "Review of Ride Vibration Standards and Tolerance Criteria". *SAE Transactions Paper* No. 760413, 1976, pp. 1460-1467.

30. Van Deusen, B.D., "Human Response to Vehicle Vibration". *SAE Transactions Paper* No. 680090, 1968, pp. 328-345.

31. Dieckmann, D., "Einfluss Vertikaler Mechanischer Schwingungen auf den Menschen", *Internationale Zeitschrift Angewandte-Physiologie*, Vol. 16, 1957, pp. 519-564.

32. Goldman, D.E., " A Review of Subjective Responses to Vibratory Motion of the Human Body in the Frequency Range 1 to 70 cps," *Report No.4*, Naval Medical Research Institute, Mar. 1948.

33. Janeway, R.N., "Passenger Vibration Limits, " *SAE Journal*, Vol. 56, pp. 48-49, Aug. 1948.

34. Van Deusen, B.D., "Human Response to Vehicle Vibration," *SAE Paper No. 680090*, 1968.

35. Von Eldik Thieme, H.C.A., "Passenger Riding Comfort Criteria and Methods of Analyzing Ride and Vibration Data", *SAE Paper No.* 295 A, Mar. 1961.

36. Butkunas, A.A., "Power Spectral Density and Ride Evaluation", *SAE Transactions Paper No.* 660138, 1966, PP. 681-687.

37. VDI -2057, "Assessing the Effects of Vibration on Human Beings," *Verein Deutscher Ingenieure*, Translated and Published by Peter Peregrinus Ltd., 1963.

38. Lee, R., and Pradko, F., "Analytical Analysis of Human Vibration", *SAE Transactions Paper No.* 680091, 1968, pp. 346-370.

39. Pradko, L., Lee, R., and Kaluza, V., "Theory of Human Vibration Response", *ASME Paper No.* 66 WA/BHF -15, 1966.

40. ISO 2631, "Guide for Evaluation of Human Exposure to Whole Body Vibration", International Organization for Standardization, 1978

41. Military Standard 1472A, "Human Engineering Design Criteria for Military Systems, Equipment and Facilities", Department of Defence, Washington, D.C., 1970.

42. Smith, C.C., "On Using the ISO Standard to Evaluate the Ride Quality of Broad-Band Vibration Spectra in Transportation Vehicles," *Transactions ASME, Journal of Dynamic Systems, Measurements, and Control*, pp. 440-443, Dec. 1976.

43. ISO 2631, "Mechanical Vibration and Shock-Evaluation of Human Exposure to Whole Body Vibration", International Organization for Standardization, 1997

44. Claar II, P.W. and Sheth, P. "Off-road Vehicle Ride: Review of Concepts and Design Evaluations With Computer Simulations", *SAE Paper No. 801023*, 1980.

45. Rakheja, S. and Sankar, S. "Improved Off-Road Tractor Ride via Passive Cab and Seat Suspension", *Trans. ASME. J. of Vibration*, Aco., Stress and Reli. in Design, Vol. 106, No.2, pp.305-313, 1984

46. Young, R.E. and Suggs, C.W. "Seat-suspension System for Isolation of Roll and Pitch in Off-Road Vehicles", *Trans. ASAE*, Vol. 16, No.5, pp.973, 1973.

47. Stikeleather, L.F. "Operator Seats for Agricultural Equipment", *ASAE Distinguished Lecture Series*, No.7, 1981.

48. Griffin, M.J. "Biodynamic Response to Whole-Body Vibration", *Shock and Vibration Digest*, Vol. 13, No.8, pp.3-12, 1981.

49. Suggs, C.W., Stikeleather, L.F., Harrison, J.Y., and Young, R.E. "Application of Dynamic Simulator in Seat Testing", *Transaction ASAE*, Vol.13, No.3, pp. 378-381, 1970.

50. Xiaobo Yang, Subhash Rakheja, Paul-Emile Boileau and Ion Stiharu, "Comparison of Biodynamic Response Characteristics of Seated Driver Models", *Vehicle System Dynamics*, 30 1996.

51. S.Rakheja, Y.Afework and S.Sankar "An Analytical and Experimental Investigation of the Driver-Seat-Suspension System", *Vehicle System Dynamics*, 23 (1994) pp. 501-524.

52. Coermann, R.R., and Whittwer, A.L. "The Passive Dynamic Mechanical Properties of the Human Abdomen Thorax System and of the Whole-body System", *Aerospace Medicine*, Vol. 31, No.6, pp.443.

53. Flower, Wallace, "Analytical and Subjective Ride Quality Comparison of Front and Rear Cab Isolation System on a COE tractor", *SAE Prepr.*, paper 1978, No.780411.

54. Roley, D.G,m abd T.H.Burkhardt, "Performance Characteristics of Cab Suspensioin Models", *ASAE Prepr.*, 1975, ASAE Ann. Meet.

55. Bombardier Corporation, Specifications.1995

56. Bombardier Industrial drawings. 1995

58. David E. Kuemmel, "Managing Roadway Snow and Ice Control Operations", *Synthesis of Highway Practice 207*, Transportation Research Board, Washington DC, National Academy Press, 1994.

59. Malcom Mellor, "Snow Removal and Ice Control", Monograph III A3b, US Army Cold Regions Research and Engineering Laboratory, Hanover, NH/1965.

60. Terutoshi Kaku, "A Study on the Resistance of Snow Plowing and Running Stability of a Snow Removal Truck". Hokkaido Universit, Japan, 1980.

61. Walter W. Olson, Alan Kempaine and Dusan Milacic, Mark Osborne "Dynamic Modeling of Forces on Snowplow Equipped Trucks". Society of Automotive Engineers.

62. Masaharu Fukue, "Mechanical Performance of Snow Under Loading". Tokai University Press, 1977, pp.115.

63. Concave Research Center, Measured data of Snowplow vehicle.1998

64. Local highway data. 1997